3D and High Sensitivity Micrometric Mass Spectrometry Imaging

Tingting Fu

université PARIS-SACLAY

ÉCOLE DOCTORALE PHENIICS

UNIVERSITÉ PARIS SUD
Comprendre le monde, construire l'avenir

NNT : 2017SACLS218

3D and High Sensitivity Micrometric Mass Spectrometry Imaging

Thèse de doctorat de l'Université Paris-Saclay
préparée à L'Université Paris-Sud

École doctorale n°576 Particules Hadrons Énergie et Noyau : Instrumentation, Image, Cosmos et Simulation (PHENIICS)
Spécialité de doctorat: Physique des particules

Thèse présentée et soutenue à Orsay, le 22 septembre 2017, par

Tingting Fu

Composition du Jury :

Elias Khan Professeur, Université Paris-Sud (– IPNO)	Président
Andrew Ewing Professeur, Charmers Université de Technologie	Rapporteur
Isabelle Fournier Professeure, Université Lille 1 (– PRISM)	Rapporteur
Véronique Eparvier Ingénieure, CNRS (– ICSN)	Examinateur
Yves De Puydt Directeur, Tescan Analytics	Examinateur
Serge Della-Negra Directeur de Recherche, CNRS (– IPNO)	Directeur de thèse
Alain Brunelle Directeur de Recherche, CNRS (– ICSN)	Co-Directeur de thèse
David Touboul Chargé de Recherche, CNRS (– ICSN)	Invité

Thèse de doctorat

Remerciements

Je voudrais tout d'abord exprimer toute ma gratitude à Monsieur Alain Brunelle et Monsieur Serge Della-Negra pour m'avoir accueilli dans leurs équipes et avoir orienté et dirigé ce travail avec un intérêt constant. Un grand merci à Monsieur Alain Brunelle pour son soutien pendant les trois ans passés à l'ICSN. Merci pour m'avoir transmis tes compétences dans notre domaine de recherche et le sens de l'organisation du travail. Merci aussi pour ta disponibilité et gentillesse. Je remercie profondément aussi Monsieur Serge Della-Negra pour m'avoir appris une logique scientifique, pour tous les conseils et discussions pertinentes, ainsi que pour le soutien et les encouragements pour effectuer ce travail. Merci beaucoup aux deux meilleurs directeurs de thèse…

Je remercie très sincèrement le Professeur Elias Khan, le Professeur Andrew Ewing, la Professeure Isabelle Fournier, la Docteure Véronique Eparvier, le Docteur Yves De Puydt pour avoir accepté d'évaluer mon travail.

Je voudrais remercier particulièrement le Docteur David Touboul pour toutes les discussions scientifiques, pour l'initiation du travail sur la mesure de l'énergie interne des ions secondaire en SIMS, et m'avoir formé à la LC-MS.

Je remercie très cordialement mes collaborateurs le Docteur Christophe Duplais, le Docteur Nadine Amusant et le Docteur Emeline Houël pour les discussions sur l'analyse du bois de S. Rubra. Egalement, je remercie sincèrement le Docteur Gregory L. Fisher et ses collègues de Physical Electronics pour leur accueil chaleureux et leur aide pendant mon séjour aux États-Unis pour les expériences MS/MS TOF-SIMS.

Je voudrais remercier aussi Soizic Prado et Marine Vallet pour notre collaboration sur l'étude de la compétition entre les microorganismes, Jean-René Matin pour les discussions sur l'analyse de cerveaux de drosophile, et Valérie

Méchin pour avoir proposé de collaborer sur l'analyse de la lignification du Maïs. Ces travaux ne sont pas dans ma thèse, mais nos collaborations m'ont beaucoup appris sur la chimie et biologie de la nature.

Je tiens à remercier tous mes collègues de l'ICSN et de l'IPN. Merci à Quentin Vanbellingen pour m'avoir formé au ToF-SIMS à mon arrivée dans l'équipe, pour sa disponibilité et sa gentillesse. Merci à Manale Noun et Michael J. Eller pour l'aide et les enseignements que vous m'avez donés. Merci à Jean-Pierre Le Caer pour sa gentillesse et les expériences réalisées ensemble. Merci à Nicolas Elie pour l'aide informatique et technique au labo, pour sa gentillesse et sa disponibilité. Merci à Vincent Guérineau pour sa bonne humeur et son accompagnement pendant ces trois ans. Merci à Laurent Laboureur pour sa joyeuse compagnie et ses réponses à toutes mes 'petites questions' pendant ma thèse. Merci à Sébastiaan Van Nuffel pour les conseils et l'aide qu'il m'a prodigués pendant ma recherche d'emploi. Merci à Michèle Pautrat pour m'avoir accueillie avec extrême gentillesse et le temps passé ensemble au laboratoire.

Je tiens également à remercie les stagiaires qui ont travaillé dans l'équipe. Merci à Stéphanie Boutet, Cyrille Santerre, Anaïs Sam Lone, Carlos Rincon pour votre compagnie très agréable.

Je voudrais remercier aussi Claude Cabot, Céline Gaubert, Pascale Pichot, Isabelle Ribaud, Jean Lesrel pour votre gentillesse et les beaux moments que nous avons partagés.

En fin, bien sûr, je remercie ma chère famille pour le soutien que vous m'apporté depuis toujours.

Preface

A picture can say a thousand words. This is probably why scientists have never stopped trying to develop versatile imaging techniques or improving the resolution and sensitivity of existing techniques. Mass spectrometry imaging provides simultaneously chemical and spatial information of a variety of samples, from semiconductor to biological tissues, and even single cells. Among the various imaging techniques based on mass spectrometry, secondary ion mass spectrometry is the first technique used for surface imaging. After decades of development, TOF-SIMS is gaining increasing favor in biological imaging, especially for the high spatial resolution and minimum sample preparation.

Concerning the analysis of organic compounds, the major development in TOF-SIMS in the last few years is cluster ion source. Particularly, bismuth and gold ion beams enable routine imaging analysis of various chemical species including lipids, metabolites and pharmaceuticals in biological samples with high sensitivity and high spatial resolution of 1−2 μm. The recent use of argon gas cluster ion beam in TOF-SIMS for imaging purpose opens up several new possibilities: soft ionization of the analytes, enhancement of sensitivity, and 3D imaging. Compared to the aspect of application, fundamental study of the ionization/desorption process seems to be falling behind and requires to be continued despite its complexity. Thus understanding the ion production under different incident conditions is of special interest in this thesis.

On the other hand, ICSN has a long history of collaboration with researchers from Ecology of Guianan Forests (ECOFOG) where they are dedicated to understand and maintain the biodiversity of Amazon rain forest. Therefore, we have been utilizing TOF-SIMS to map chemical composition of wood samples from tree species growing in French Guiana. Previously, nutrients and toxic metabolites in *Dicorynia guianensis* Amsh. wood were imaged by TOF-SIMS to study the heartwood formation and defense mechanisms of this species. Here in this thesis, we aim to study the biosynthetic production of two bioactive metabolites rubrenolide and rubrynolide in *Sextonia rubra* (Lauraceae). Meanwhile, this wood species has also been used as a biological model to assess the parallel imaging MS/MS capability of the prototype PHI *nano* TOF II mass spectrometer.

Chapter 1 gives a general introduction to the history, principle and development of TOF-SIMS imaging technique. The instrumentation of IONTOF IV instrument, as well as the data acquisition and processing are described. New instrumentation emerged in the last few years are briefly summarized. TOF-SIMS imaging of plant metabolites is reviewed.

Chapter 2 aims to understand the ion production under impacts of massive argon cluster ions. The internal energy distribution of secondary ions is measured with a series of benzylpyridinium ions, the so called thermometer ions. Influence of beam energy, cluster size and velocity on internal energy distribution or fragmentation rate is established. Secondary ion yield, sample damage and emission efficiency from argon cluster impact are also compared with that from bismuth clusters.

The following three chapters concern the application of TOF-SIMS in mapping plant metabolites, but each with different objectives. To preserve this autonomy of each chapter, some experimental protocols (sample preparation and instrument description) are repeated in these chapters.

Chapter 3 describes the parallel imaging MS/MS technique with the prototype PHI *nano* TOF II mass spectrometer. The MS/MS imaging capability is evaluated with wood sample from *Sextonia rubra* (Lauraceae). The results show its feasibility in natural product analysis, in terms of sensitivity, MS/MS fragmentation, and parallel imaging.

Chapter 4 focuses on the biosynthetic investigation of the bioactive metabolites rubrenolide and rubrynolide in *Sextonia rubra* (Lauraceae). The parallel MS/MS imaging technique validated in Chapter 3 is utilized for in situ identification of related metabolites. 2D/3D TOF-SIMS imaging is performed to localize these metabolites in wood tissue at subcellular level. Based on LC, NMR, and imaging results, a new biosynthesis pathway is proposed. The solvent extraction of metabolites from wood and NMR analysis are done by the collaborators from ECOFOG.

Chapter 5 concerns the analysis of soft wood species— European larch *Larix decidua*. The radial distribution of mineral and lipophilic extractives is investigated by TOF-SIMS imaging to understand the chemical variation associated with heartwood formation.

List of abbreviations

BA: Burst Alignment

DE: Delayed Extraction

DESI: Desorption ElectroSpray Ionisation

EFI: Extended Focal Imaging

ELSD: Evaporative Light Scattering Detector

ESI: ElectroIpray Ionization

FAB: Fast Atom Bombardment

FTICR: Fourier Transform Ion Cyclotron Resonance

FTIR: Fourier Transform Near InfRared

FWHM: Full Width at Half Maximum

GC: Gas Chromatography

GCIB: Gas Cluster Ion Beam

GCIS: Gas Cluster Ion Source

gCOSY: Gradient COrrelation SpectroscopY

gHSQCAD: gradient Heteronuclear Single Quantum Coherence Adiabatic

gHMBC: gradient Heteronuclear Multiple-Bond Correlation Adiabatic

HPLC: High Performance Liquid Chromatography

LC: Liquid Chromatography

MS/MS: Tandem Mass Spectrometry

LMIG: Liquid Metal Ion Gun

MALDI: Matrix-Assisted Laser Desorption/Ionisation

MD: Molecular dynamics

MSI: Mass Spectrometry Imaging

MCP: Microchannel Plate

NMR: Nuclear Magnetic Resonance

PIDD: Primary Ion Dose Density

ROI: Region Of Interest

SEM: Scanning Electron Microscopy

SIMS: Secondary Ion Mass Spectrometry

SIs: Secondary ions

SY: Survival Yield

TDC: Time Digital Converter

TMS: TetraMethylSilane

TOF: Time of Flight

TRIFT: TRIple Focusing Time-of-flight

VDP: Variable Drift Path

BYP: Benzylpyridinium

CID: Collision Induced Dissociation (CID)

Table of Contents

Chapter 1 Introduction

1.1 SIMS: Secondary ion mass spectrometry

Secondary ion mass spectrometry (SIMS) is a mass spectrometric technique characterized by using energetic particles to cause secondary ion emission from a solid surface. The basic idea of using SIMS to generate spatially resolved chemical information was conceived in the 60s of last century by Castaing and Slodzian [1]. However, early studies with SIMS were confined to detection of inorganics or low molecular fragments due to the sample damage induced by energetic impacts. In 1973, Benninghoven [2] discovered that it was possible to observe molecular or quasi-molecular ion peaks in the mass spectra if the primary ion dose is maintained below a certain limit (10^{13} ions·cm^{-2}), the analysis of organic compounds started to come into being. Generally speaking, the static SIMS concept, together with the subsequent development of cluster ion sources which have dramatically enhanced the secondary ion yields, lead to today's biological SIMS imaging.

1.1.1 Principle

The particle-induced ion emission process in SIMS is most frequently described as a collision cascade in the target (Figure 1). Upon impact on the solid surface and the subsequent penetration, the primary ion transfers the momentum to target particles and sets the atoms in motion which will further cause other atoms in the target to move. Since the typical primary ions are in the keV range which is capable of breaking any chemical bond, intense fragmentation occurs at and near the impact site from where only fragments and elemental particles are emitted. Along the collision cascade trajectory, the activated atoms far from the collision site are less energetic and induce the emission of molecular and quasi molecular species. An unfortunate fact in SIMS is that most of the ejected particles are neutrals, whereas only ~ $10^{-6} - 10^{-1}$ of them are positively or negatively charged ions which are useful in mass spectrometry analysis. Due to the dissipation of primary ion energy, only particles from the first few layers (2−3 monolayers) are able to overcome the surface binding energy and be desorbed from the sample. For example, the ejection of secondary ions from organic materials is generally restricted to a depth of less than 100−200 Å [3,4], depending on the energy and mass of the projectiles as well as the nature of the target.

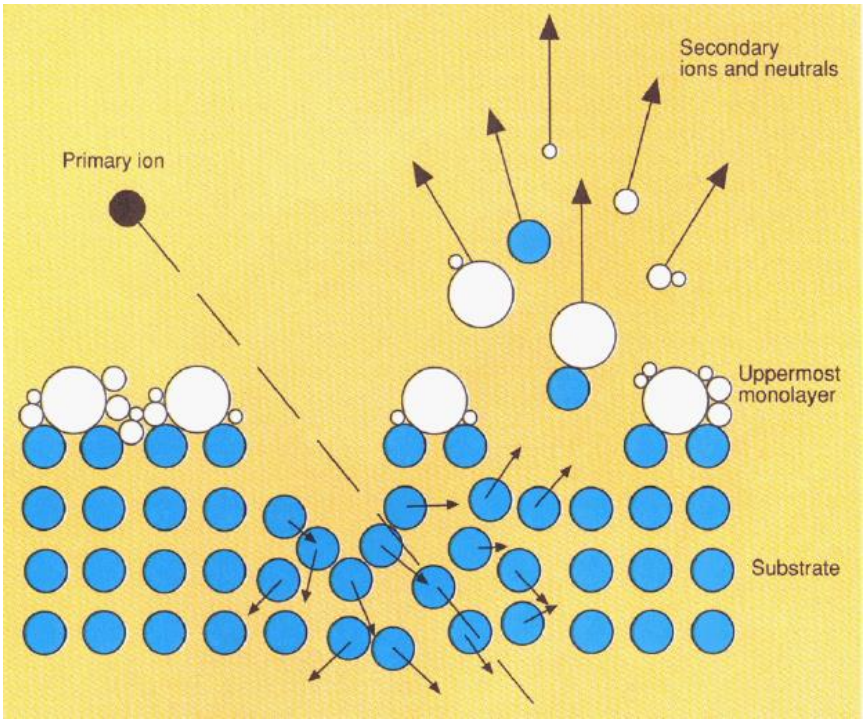

Figure 1: Secondary ions and neutrals emission induced by the primary ions via a collision cascade [5].

However, ionization/desorption in SIMS is a rather complex process, especially due to the fact that the mechanisms can be different when the impacting condition changes. For elastic collision, three sputtering regimes have been established to describe the secondary ion emission (Figure 2): the direct recoil (knock-on sputtering) for prompt collisional sputtering (low energy), the linear collision cascade for atomic impact (medium energy), and the thermal spike for dense or polyatomic impact (high energy) [6]. As to the subsequent ionization process, different models have been proposed according to the type of chemical species. For example, the ion-pair (A^+B^-) dissociation can be explained by the bond breaking model [7] where the incident energy is sufficient to break the ionic bonding. The ion emission from metal oxides is usually described by a less direct process: non-adiabatic dissociation of nascent ion molecules [8] where the impact of primary ions first leads to changes in internal energy and kinetic energy of the system before the ejection of ions or neutrals. A more universal model concerning the emission of organic molecules is desorption/ionization model which suggests the energy deposited in the target is converted to vibration energy. Thus, desorption of the particles is induced by vibrational excitation [9].

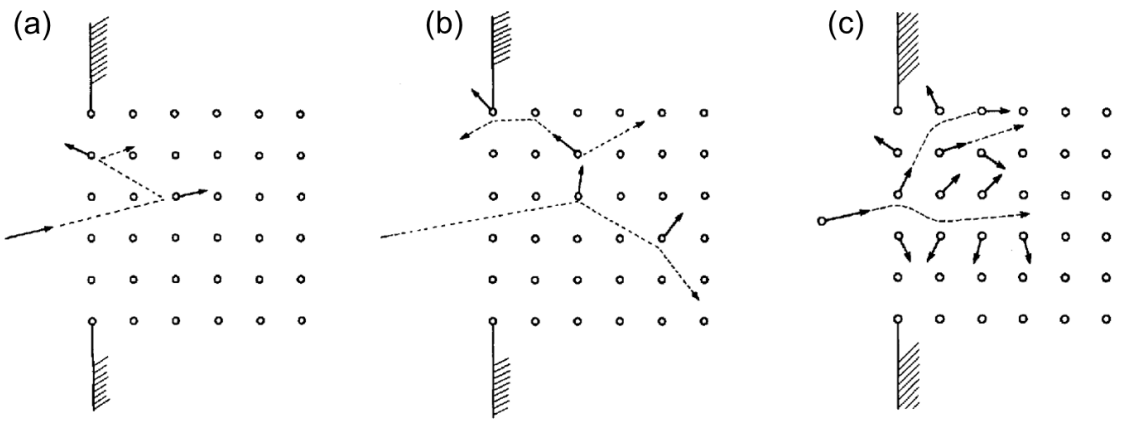

Figure 2: Three regimes of sputtering by elastic collisions. (a) The single-knock-on regime. Recoil atoms from ion-target collisions receive sufficiently high energy to get sputtered, but not enough to generate recoil cascades. (b) The linear cascade regime. Recoil atoms from ion-target collisions receive sufficiently high energy to generate recoil cascades. The density of recoil atoms is sufficiently low so that knock-on collisions dominate and collisions between moving atoms are infrequent. (c) The spike regime. The density of recoil atoms is so high that the majority of atoms within a certain volume (the spike volume) are in motion [6].

Although the above models do, to some extent, satisfactorily explain the secondary ion emission in SIMS, the sputtering and ionization processes are still not fully understood, especially when new phenomena appear as a result of introducing new projectiles such as massive argon clusters. In the second chapter of this thesis, the fragmentation of secondary ions which indicates the internal energy transfer from projectiles to secondary ions will be discussed to provide some insights into the ion formation in SIMS.

1.1.2 Terms and definitions

In order to evaluate and compare the efficiency of different cluster ion beams, several parameters are defined [10,11]: Primary ion dose density (PIDD), secondary ion yield Y, disappearance cross section σ, secondary ion emission efficiency E, and useful lateral resolution ΔL.

- Primary ion dose density (PIDD)

The Primary Ion Dose Density (PIDD), or otherwise called “fluence”, is the number of primary ions that reach the sample per unit area during the analysis:

$$PIDD = \frac{it}{qA} \tag{1.1.1}$$

where *i* is primary ion current; *t* is analysis time; *q* is the charge of primary ion and *A* is the bombarded area. This parameter defines the two SIMS analysis regimes: the "dynamics regime" where the PIDD is typically greater than 10^{16} ions·cm^{-2} and the static regime where the PIDD is kept below 10^{13} ions·cm^{-2}. As mentioned above, for analysis of organic materials, static SIMS has to be employed to ensure that each impact of the primary ion is on an intact area. Therefore, the sample damage caused by multiple irradiations is negligible. In dynamic SIMS, the high PIDD means there is a very high possibility that the primary ions will hit an area whose molecular structure has already been modified or damaged by the first impact. As a consequence, only small fragment ions and elemental species are obtained [12].

- Secondary ion yield *Y*

Secondary ion yield is an important parameter indicating the ion production efficiency by the primary ions. It is defined as the number of detected secondary ions (N_{SI}) divided by the number of primary ions (N_{PI}) hitting a certain area on the sample surface during the analysis:

$$Y = \frac{N_{SI}}{N_{PI}} \tag{1.1.2}$$

Under the same transmission efficiency, *Y* is principally determined by the property of the primary ions (energy, mass) and the nature of the samples (density, structure, chemical environment). In addition, since the ionization efficiency varies dramatically among the chemical species, secondary ion yield *Y* also depends on individual compounds [10].

- Disappearance cross section σ

Disappearance or damage cross section σ corresponds to the area damaged by the bombardment of a single primary ion. σ can be calculated by measuring the decrease in the secondary ion intensity as a function of the primary ion dose:

$$N(t) = N(t_0) \cdot \exp(-\sigma \frac{it}{qA}) \tag{1.1.3}$$

$$\frac{\ln N(t)}{\ln N(t_0)} = -\sigma \cdot PIDD \tag{1.1.4}$$

where $N(t)$ is the number of secondary ions detected at time t; $N(t_0)$ is the number of secondary ions detected at the beginning of the analysis; i, t, q and A are the same as that in equation 1.1.1. σ therefore is the slope of the decay curve of secondary ions. Similar to secondary ion yield, disappearance section also depends on the projectiles, sample system, as well as considered secondary ion species. In particle analysis, the σ measured from quasi-

molecular ions (typically about $10^{-15} - 10^{-12}$) are larger than that from fragment ions due to the surface modification during the erosion [13]. As shown in Figure 3, F_{supply} and $F_{sputter}$ indicate the flux of intact molecules into and out of the altered layer of thickness d, respectively. F_{damage} presents the damaged of the material caused by bond breaking and crosslinking (in the case of polymer). In this erosion model, a steady state can be reached where the consumption rate of the material and the supply rate from bulk to the altered layer reach equilibrium, then the disappearance section can be expressed in a more sophisticated equation [14]:

$$S(f) = S_{ss} + (S_0 - S_{ss})exp\left[-(\frac{Y}{nd} + \sigma_D)f\right] \tag{1.1.5}$$

where S_0 is the signal intensity at the beginning; S_{ss} is the signal intensity at steady state; Y is the total sputtering yield, n indicates the density of the molecules in the sample; d is the thickness of the altered layer; σ_d is the damage cross section associated with the molecules, f is the primary ion fluence. Then the value representing the exponential slope corresponds to the effective disappearance cross section:

$$\sigma_{eff} = \frac{Y}{nd} + \sigma_d \tag{1.1.6}$$

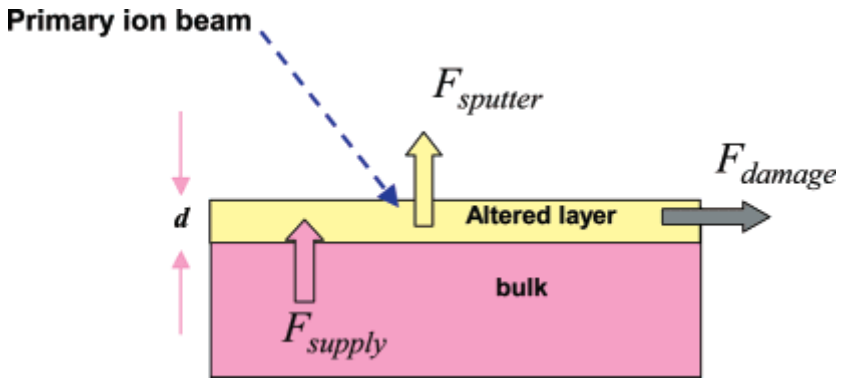

Figure 3: Schematic diagram of the erosion model. The variable F represents the indicated flux of intact molecules in to and out of the altered layer of thickness d [14].

It is noted that in the next chapter of this dissertation, we were dedicated to comparing the damage cross section for different primary ion beams and precise calculation was not pursued. Thus the steady state was not considered and the equation 1.1.4 was used for all the measurements.

- Secondary ion emission efficiency *E*

Secondary ion emission efficiency is the number of secondary ions detected per damaged area. It is calculated as the ratio of secondary ion yield *Y* over the disappearance cross section σ:

$$E = \frac{Y}{\sigma} \tag{1.1.7}$$

It can be reasoned from the above equation that secondary ionization emission efficiency can be improved by increasing the secondary ion yield or/and reducing the disappearance cross section.

- Useful lateral resolution ΔL

Useful lateral resolution is ΔL, is the minimum length of a pixel needed to produce a detectable signal, typically with signal-to-noise ratio (S/N) > 3. Thus, in the case of Poisson counting statistics,

$$\Delta L = S/N \sqrt{\frac{A}{I}} \tag{1.1.8}$$

where I is the intensity of the signal; A is the area of one pixel. Therefore, ΔL is a parameter essentially related to secondary ion emission. The attainable useful lateral resolution depends both on the spot size of the incident beam and the intensity of the signal. Thus, for a given primary ion beam, this value can vary between the samples and chemical species (related to ionization/desorption efficiency).

1.1.3 Primary ions

In the early years, inert gas ions such as He^+, Ar^+ and Xe^+ were commonly used in SIMS due to their relatively simple design and operation [15]. However, it proved quite challenging then to focus the gas ions to small spots usefully for imaging purposes and retain sufficient beam current at the same time. The development of liquid metal ion sources (Ga^+, Cs^+) in the 1970s [16] has effectively overcome this difficulty and provides metal ion beam with spot size less than 100 nm, enabling high resolution imaging of inorganics from a variety of materials [12] as well as low molecular weight fragments from cell membranes [17, 18]. Nevertheless, due to the low secondary ion yield, attempts to obtain molecular information with the atomic ions under static conditions (PIDD $<10^{13}$ ions·cm^{-2}) had been rather frustrated until late 1990s.

In the course of developing new ion sources to improve secondary ion yields in SIMS analysis, a very important phenomenon concerning secondary ion yield—the nonlinear

enhancement effect under polyatomic ion impact started to draw attention in the 1970s when Andersen and Bay [19] observed an enhancement in sputtering yield using diatomic molecular projectiles instead of atomic ions. Here the nonlinear enhancement refers to the fact that the secondary ion yield obtained from the impact of a cluster ion consisting of *n* atoms is larger than that from *n* individual atoms impacting the target with the same velocity [20]. After the first observation with diatomic ions, other polyatomic projectiles such as CF_3^+ [21] and SF6/SF6$^-$ [22] were subsequently investigated and found to produce similar enhancement effect. The first systematic study of this cluster effect was conducted previously by the IPNO group in collaboration with Texas A&M group around 1990s. The influence of the number of constituents in the cluster projectile on secondary ion yield was examined on a variety of polyatomic projectiles: $C_{24}H_{12}^+$, $(CsI)_nCs^+$ (n= 0−2), Au_n^{q+} (n= 1−5, q= 1−2), C_{60}^+ [23, 24, 25]. In addition to confirmation of the nonlinear enhancement, the results further revealed that the number of constituents was a more important parameter compared with the mass of the cluster and the enhancement was most significant from atomic impact to diatomic impact (Figure 4).

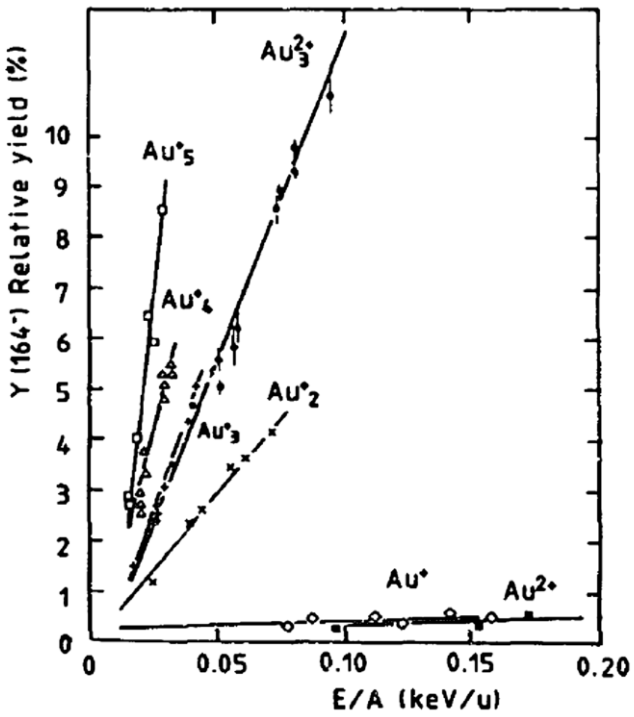

Figure 4: Molecular ion (*m/z* 164.2, $[M-H]^-$) yield from a phenylalanine target as a function of energy per mass unit (E/A) of gold clusters Au_n^{q+} (n= 1−5, q= 1−2) [24].

Based on the above studies of nonlinear effect by polyatomic projectiles, a significant breakthrough in molecular imaging with SIMS took place when cluster ion sources were practically introduced at the beginning of the millennium. In 2003, a commercial gold liquid

metal ion source was developed jointly by Vickerman group and Ionoptika company [26]. The Au_3^+ projectile was shown to dramatically increase the molecular ion yields and was soon applied to map lipids in mouse brain [27,28] and tissues [29]. Soon enough, the ION-TOF company came out with a bismuth liquid metal ion gun delivering Bi_n^{q+} (n= 1−7, q= 1−2) primary ions [30,31]. Compared with gold, bismuth has lower melting point and ionization energy which permits the ion gun works at the lower source current, resulting in lower energy deficit for the ion emission. Therefore, the bunching is relatively easier and the time resolution of the pulsed beam is better. Indeed, during the comparison (Figure 5), Bi_3^+ was found to have similar performance as Au_3^+ but with a much higher attainable beam current because of the improved bunching process. For imaging purpose, Bi_5^{2+} could provide excellent sensitivity with submicron useful lateral resolution but requires longer acquisition time due to the inferior beam current (Figure 5C). Until today, Au_3^+ and Bi_3^+ remain the most popular primary ion beams for high resolution molecular imaging and are available in most of commercial TOF-SIMS instruments.

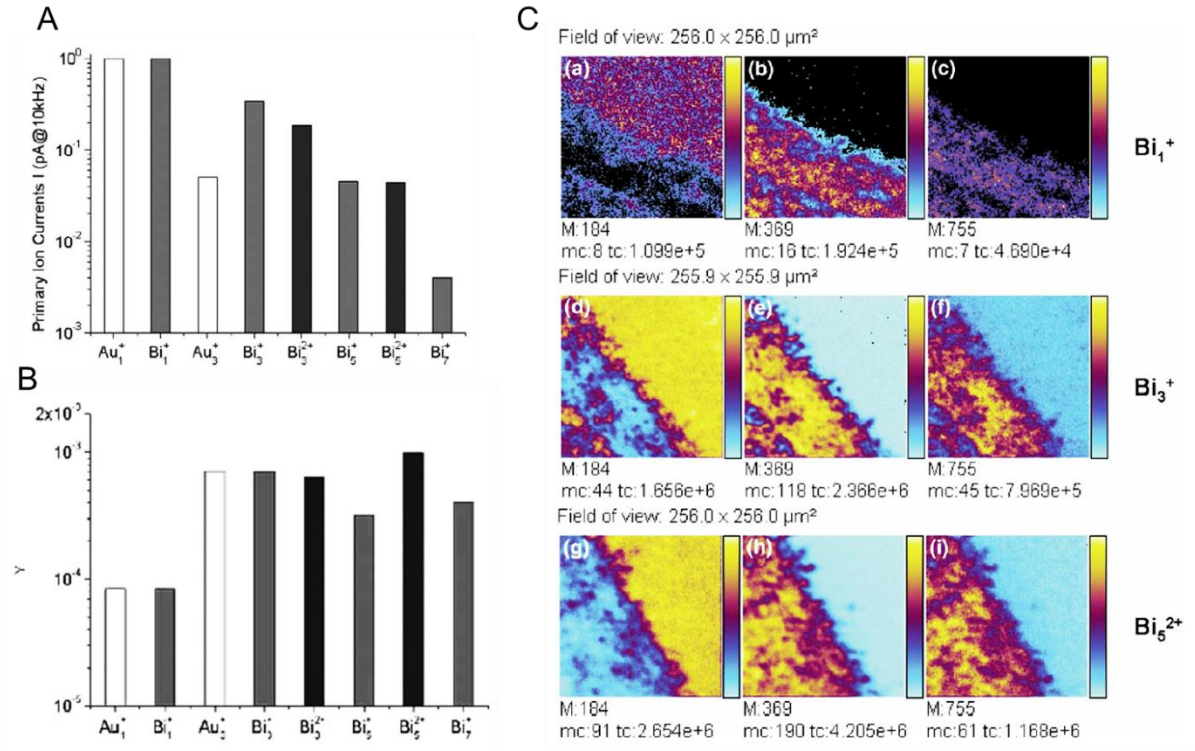

Figure 5: Comparison between gold and bismuth clusters in attainable target beam current (A) and secondary ion yield ($[M-H]^-$ ions of cholesterol in the corpus callosum of a rat brain tissue section (B), and the imaging capability comparison between different bismuth projectiles: Bi^+, Bi_3^+, and Bi_5^{2+} (C). The images were acquired on the corpus callosum area of a rat brain tissue section with 256 × 256 pixels and an PIDD of 10^{12} ions·cm^{-2}. Acquisition time was about 4 min for Bi^+, 10.5 min for Bi_3^+, and 100 min for Bi_5^{2+}, respectively [31].

Although Au_3^+ and Bi_3^+ have greatly improved the capability of high resolution biological imaging, it should be noted that the static limit still need to be applied to avoid the accumulation of sample damage. Other promising primary ions for biological analysis include C_{60} and massive argon clusters. Practical C_{60} ion source was introduced by Vickerman group in 2003 [32,33]. In consistent with previous observations, C_{60} projectiles have shown significantly enhanced secondary ion yields from organic substrates, especially for molecular ions [34,35]. Compared with Au_3^+ and Bi_3^+, C_{60} ion beam is difficult to be focused to a small spot size required for high resolution imaging. Consequently, considerable effort has been devoted to investigating its application in depth profiling and 3D imaging [36,37], owning to the high sputter yield and minimum subsurface chemical damage.

Large argon cluster ion beam was initially developed by the Kyoto group during the 1990s for surface processing such as smoothing, cleaning and thin film deposition [38,39]. Utilizing Ar_n^+ ions as primary ion beam for analytical purpose began with the same group about ten years ago. The analysis of amino acid and small peptide revealed that large argon clusters were not only able to cause effective secondary ion emission but also possible to realize fragment-free ionization under proper conditions [40,41]. Later, small proteins were also successfully detected with argon cluster TOF-SIMS [42,43]. However, similar to C_{60} ion source, Ar-GCIB is principally utilized as sputter beam in depth profiling and 3D imaging [44,45] because of the difficulty in focusing large gas clusters for imaging purpose.

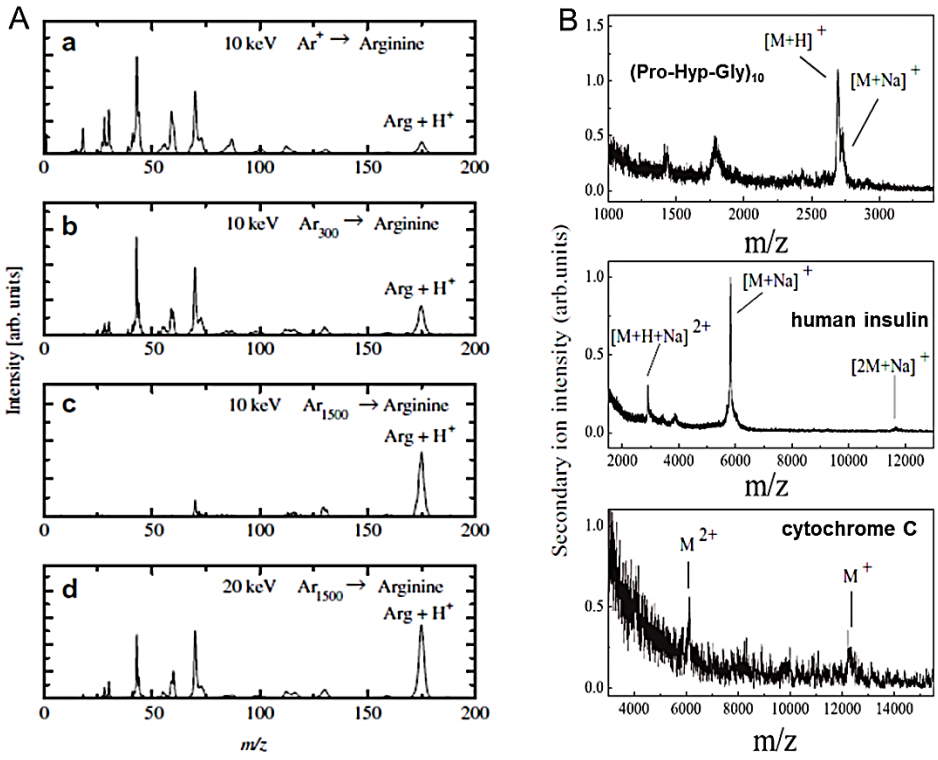

Figure 6: Molecular analysis with argon cluster ion source. (A) Mass spectra of positively charged secondary ions for an arginine target bombarded with different argon clusters [40]. (B) Mass spectra of thin film of $(Pro\text{-}Hyp\text{-}Gly)_{10}$ (top), human insulin (middle) and cytochrome C (bottom) on silicon from the bombardment of 5 keV Ar_{1400} [42].

1.2 Time of flight analyzer

Initially, SIMS instruments were coupled with magnetic [1] or quadrupole analyzer [46]. The introduction of time-of-flight analyzer [47] has provided a much larger mass range with improved transmission efficiency and good mass resolution for SIMS analysis.

1.2.1 Principle

Time-of flight analyzer is based on the simple principle that when ions with different *m/z* but with the same kinetic energy are travelling through a field free path, they will be separated by their *m/z* due to the velocity difference and reach the end of this zone (where lies the ion detector) at different time. Hence, these ions will be time-resolved and the *m/z* of each ion can be determined by measuring the time difference between its emission and detection after a field-free flight. The history and development of different kinds of TOF analyzer to improve the mass resolution have been comprehensively reviewed by Radionova, *et al.* recently [48].

As shown in Figure 7, a typical time-of-flight analyzer consists of two zones: the acceleration zone with a uniform static electric field E_s and a field free zone (E_L=0) of length L (usually 1 to 2 m).

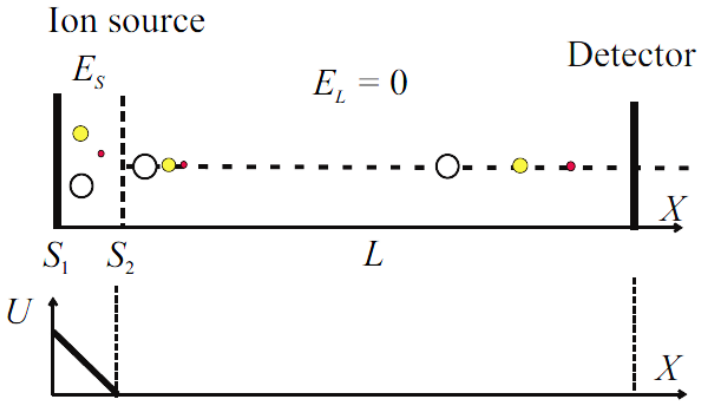

Figure 7: Scheme of a linear time-of-flight analyzer with potentials along the ion optical axis (bottom) [48].

In the acceleration zone, a potential difference U is applied between the target and the extractor. Then the electric field which accelerates the charged particle (with a distance x_{acc} from the extractor) is:

$$E = \frac{U}{x_{acc}} \tag{1.2.1}$$

The force resulting from this electric field is:

$$F = zeU = m\frac{d^2x}{dt^2} \tag{1.2.2}$$

where m is the mass of the particle; z is the number of charges carried by the particle; e is the electric charge of an electron, namely 1.602×10^{-19} C. Then the acceleration time for the particle in the electric field can be deduced:

$$t_{acc} = 2x_{acc}\sqrt{\frac{m}{2zeU}} \tag{1.2.3}$$

Once in the field free zone, the particle is no more subjected to electric field. The velocity will become constant and the kinetic energy is given by the simple relation:

$$E_k = \frac{1}{2}m{v_0}^2 = zeU \tag{1.2.4}$$

The velocity in the field free region is:

$$v_0 = \sqrt{\frac{2zeU}{m}} \tag{1.2.5}$$

The time of flight in the field free path t_L equals to:

(1.2.6)

Then substituting for v_0 leads to:

$$t_L = \frac{L}{v_0}$$

$$t_L = \mathrm{L}\sqrt{\frac{m}{2zeU}} \tag{1.2.7}$$

Therefore, the total time required for the particle to reach the detector is:

$$t = t_{acc} + t_L = (2x_{acc} + L)\sqrt{\frac{m}{2zeU}} \tag{1.2.8}$$

With this equation, the *m/z* of the charged particle can be obtained by measuring this total time of flight. It also clearly shows that heavy ions will have a longer flight time than light ions, leading to mass resolving of the emitted ions. If we use proportionality constant *K* to represent the instrument settings including the acceleration distance x_{acc}, the length of the field free tube L and the electric potential difference U, which do not change in a given instrument, then for a particle carrying *z* charges,

$$t = (2x_{acc} + L)\sqrt{\frac{m}{2zeU}} = K\sqrt{\frac{m}{z}} \tag{1.2.9}$$

Then,

$$\frac{m}{z} = \frac{1}{K}t^2 \tag{1.2.10}$$

$$dm = \frac{1}{K} \cdot 2tdt \tag{1.2.11}$$

$$\frac{m}{dm} = \frac{t}{2dt} \tag{1.2.12}$$

Therefore, the mass resolution *R* equals is given as:

$$R = \frac{m}{\Delta m} = \frac{t}{2\Delta t} \tag{1.2.13}$$

The mass resolution obtained with a TOF analyzer can be affected by several factors: the pulse duration of the primary beam which introduces a time gap in ionization/desorption between the ions; the ejection process which result in a velocity distribution of the emitted ions; the topography of sample surface which directly influences the time of flight. All the above factors will result in one same consequence that the same ions arrive at the detector at different time, thus broadening the ion peak when using a time to digital converter (TDC).

To improve the mass resolution, most of current TOF instruments are equipped with a electrostatic reflector to correct the initial kinetic energy distribution. Meanwhile, an extraction delay of the ions can also effectively improve mass resolution by focusing the ion in time before entering the TOF tube.

1.2.2 TOF analyzer with electrostatic mirror (Reflectron)

The use of a reflectron, or ion mirror to improve the mass resolution was first proposed by Alihanov in 1956 [49]. A reflectron consists of a series of electrodes with increasing potentials to generate a uniform electric field, in which the ions will be reflected towards the detector. The principle is to refocus in time the secondary ion beam so that they can reach the detector at the same time. Figure 8 shows the ion optics of TOF analyzer with a one-stage ion mirror (with a length of h_r). Regions l_1 and l_2 are two field-free zones. For ions with the same *m/z*, the ones with higher kinetic energy or higher speed will penetrate deeper into the reflectron, resulting in a longer traveling path. In contrast, the ones with lower kinetic energy will penetrate a shorter distance before turn around, which leads to a shorter path to the detector. As a result, the time distribution of the ions will be narrowed and consequently better mass resolution can be obtained.

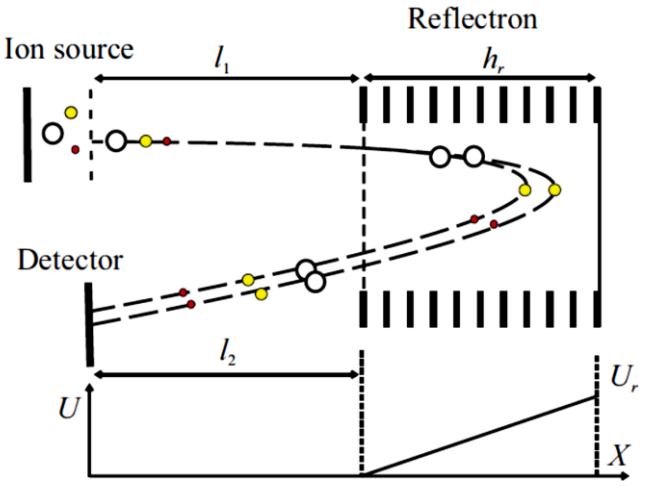

Figure 8: Schematic of the ion optics of a one-stage ion mirror with potentials along the ion optical axis (bottom) [48].

To further improve the resolution, another two ion mirror techniques, two-stage reflectron [50] and quadratic-field reflectron were developed in the 1970s. With two-stage reflectron, spatial and kinetic energy distributions can be effectively corrected, and it is possible to achieve second-order time focusing. However, the employment of more grids brings possible disadvantages such as loss of sensitivity and transmission, and TOF analyzers with grid-free ion mirrors were subsequently developed [51,52].

1.2.3 Delayed extraction

An alternative method to improve the mass resolution is to narrow the initial velocity distribution of the ions before they enter the TOF analyzer. This can be realized by applying an extraction delay of the ions. For example, in a double-stage extraction system as shown in Figure 9, after leaving the target (1), the ions will travel in a field free area (2) as no potential difference is applied. Then after a certain delay t_d, a slight potential difference is applied between the target and the intermediate grid (ΔU = 6 kV, for example). The ions are thus weakly accelerated before reaching the intermediate grid. Since the ions with higher initial velocity will penetrate further into the field free region (closer to the intermediate grid) during the time τ, they will be less accelerated than the same ions with lower velocity. In this way, the ions can be grouped to narrow the distribution of kinetic energy before entering the TOF analyzer, which will ultimately lead to better mass resolution.

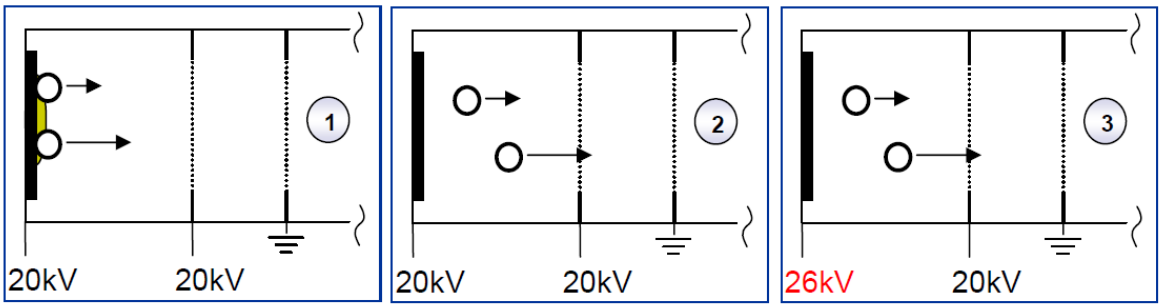

Figure 9: Principle of delayed extraction. 1. At t = 0, the ions are leaving the target after excitation by the ion source; 2. During a certain period t, the ions travel though a field free area as the voltage applied on the intermediate grid is the same as that of the target; 3. After a delay, a potential difference is applied. The ions are slightly accelerated (U = 6 kV) before the intermediate grid before being strongly accelerated (U = 20 keV) to the second grid.

In practical, this method has been most successfully applied in MALDI-TOF instruments and for many years [53,54], whereas in TOF-SIMS, delayed extraction drew less attention due to the relatively narrow distribution of the kinetic energy [55,56]. Owing to a recent systematic study of the effect of delayed extraction on mass spectra by Vanbellingen, *et al.* [57], this method began to be more widely employed in TOF-SIMS analysis to improve the mass resolution [58,59]. Nowadays, delayed extraction method has been integrated into the data acquisition software of TOF-SIMS instruments by ION-TOF GmbH. All the high resolution images shown in this thesis were obtained with an employment of this delayed extraction method.

1.3 TOF-SIMS IV instrument (ION-TOF)

The TOF-SIMS instrument utilized in my thesis is from a TOF-SIMS IV from ION-TOF GmbH (Münster, Germany). It is equipped with two ion sources: Bi-LMIG delivering Bi_n^{q+} (n= 1−7, q= 1−2) ions with kinetic energies of 25 k × q eV and argon GCIB producing massive argon clusters Ar_n^+ (n=500−10000) with kinetic energies ranging from 5 keV to 20 keV, a TOF analyzer with one-stage reflectron and a hybrid detector which is composed of a single microchannel plate (MCP), a scintillator and a photomultiplier. Figure 10 illustrates the instrumentation and schematic view of the principle of this instrument. The main components of the instruments are described in detail in the following paragraphs.

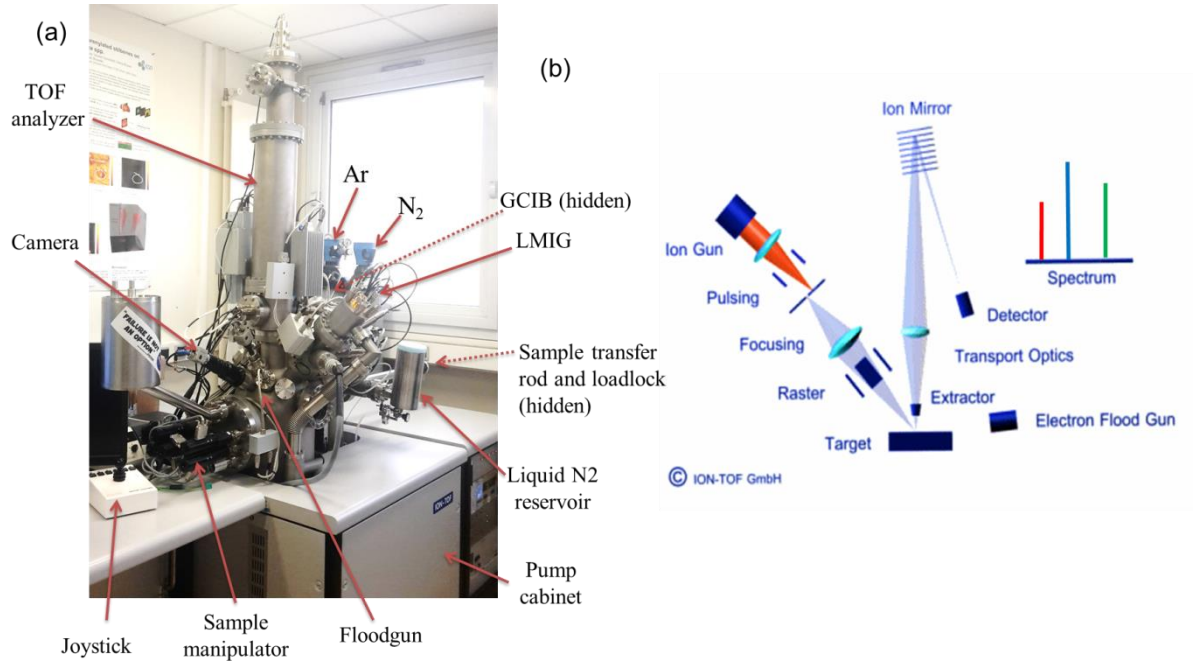

Figure 10: (a) Photo of TOF-SIMS IV instrument in ICSN laboratory. (b) Principle of TOF-SIMS (from ION-TOF GmbH).

1.3.1 Ion source

- Liquide metal ion gun (LMIG)

The LMIG gun is made up of several modules that are responsible for ion production, extraction, focusing, mass selection and beam centering, respectively. Figure 11 displays a schematic view of the ion production from a LMIG emitter. To generate a metallic ion beam, the metal is first heated to liquid state by the heater filament. Then a Taylor cone can be formed due to the potential difference between the emission apex and the extractor. The emitted ions are usually extracted to a standard potential between 7000 and 11000 V (depending on the emitter). From this kind of LMIG emitter, most of the produced ions are monatomic and singly charged species. Nevertheless, clusters and doubly charged ions can also be formed. In the case of bismuth LMIG, Bi^+, Bi_2^+, Bi_3^+, Bi_3^{2+}, Bi_4^+, Bi_5^+, Bi_5^{2+}, Bi_6^+, and Bi_7^+ are present with varying intensities [30]. In addition, for practical reasons, Bi/Mn alloy (less than 1% of Mn) is used instead of pure bismuth. As a result, Mn ions are also among the emitted ion species. Therefore, after being focused by the source lens, an ion selection process needs to be carried out to obtain the desired ion beam.

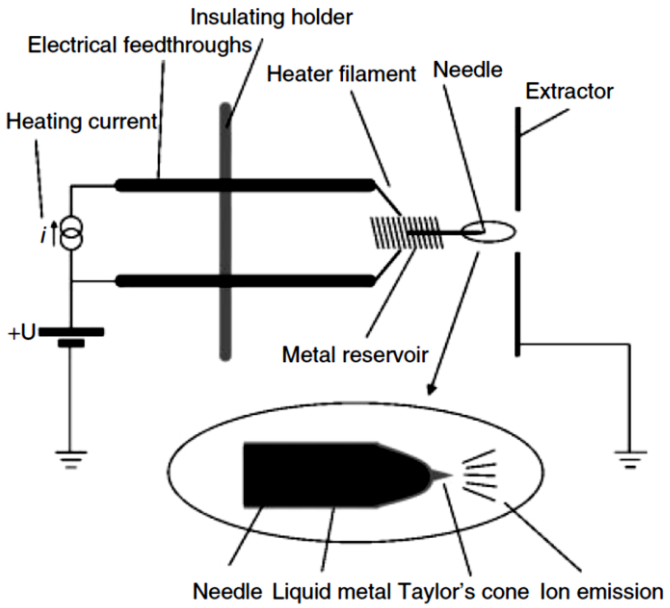

Figure 11: Schematic view of a LMIG emitter [11].

Figure 12 shows the principle of ion selection and beam pulsing by using a dual set of blanking plates. After entering the first deflection plate, ions with different *m/z* travel at different velocities. Thus they are time resolved between the two deflection plates. By calculating the time that takes a particular ion to reach the center of the second plate and applying to these plates a deflection pulse at this time delay, the ions with desired *m/z* can be selected. To narrow the time gap between the emitted ions (to improve mass resolution), the primary ion beam need to be pulsed for a very short duration, usually 1 ns or less. However, such short pulse duration results in dramatically decreased beam intensity. In many cases, much longer pulse duration is employed (~16 ns for Bi_3^+ ions in the TOF-SIMS IV instrument to get a target current of 0.4 pA at 10 kHz), but with an addition buncher placed right after the deflection plates to compress the ions. Ion selection can also be accomplished by using a Wien filter which involves the application of a crossed electric and magnetic field to achieve velocity selection of the ions. Wien filter ensures a high transmission of the ion beam. However, compared with the dual blanking plates system, it could not achieve good mass resolution selection.

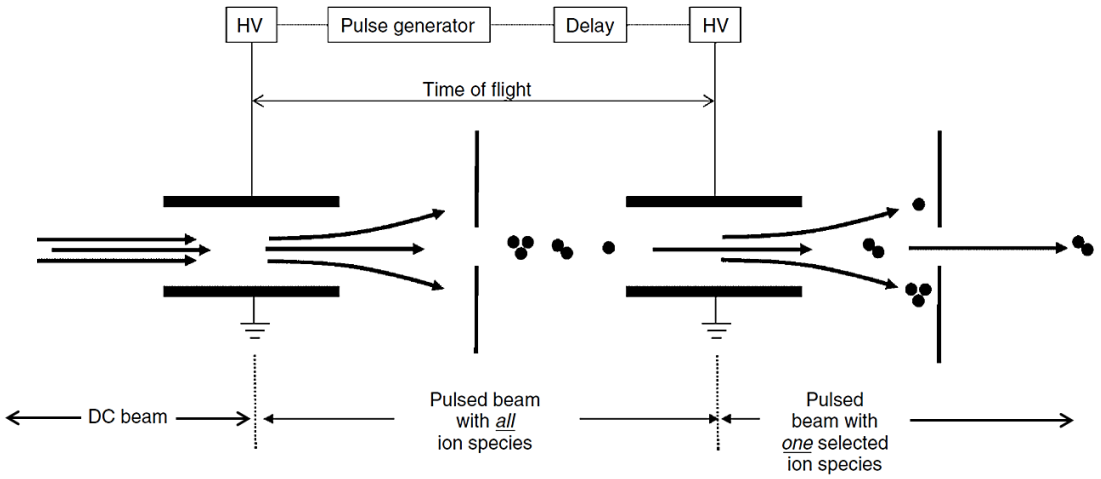

Figure 12: Schematic view of dual deflection plates pulsing and mass section system [11].

Depending on different focusing strategies of the primary ion beam, several operation modes are available: HCBU (high current bunch) mode, BA (burst alignment) mode, collimated mode, and burst mode. In HCBU mode, the primary ions are compressed by using a buncher to get very short pulse duration. By this way, high mass resolution (> 5000) can be obtained without loss of beam intensity (Figure 13a). However, the compressed ions cannot be focused to very small beam size and the attainable spatial resolution is about 2−3 µm. In BA mode, no buncher is applied after the dual deflection plates. The primary ions can be focused to a few hundred nanometers so that submicron spatial resolution is achievable. If the bean is further narrowed by apertures, namely in collimated mode, the spatial resolution can reach ~ 100 nm. Nevertheless, these methods require long pulse duration to get sufficient beam current, which leads to very limited mass resolution (Figure 13b). Compared to the above the HCBU and BA modes, burst mode is a compromise mode which provides both good mass resolution and spatial resolution. In this mode, the pulsed primary beam is chopped to several short, unbunched pulses of ~ 1.5 ns to maintain the good mass resolution (Figure 13c). The disadvantage of burst mode is that it only allows analysis of low mass molecules. In practical analysis, HCBU is the most frequently used mode due to the good beam intensity (thus short acquisition time) and simplicity of beam manipulation. Otherwise, HCBU and BA modes can be combined to take advantage of the high mass resolution of HCBU mode and high spatial resolution of BA mode, respectively [60]. Or, as mentioned previously [57], an extraction delay of the secondary ions can be applied to improve the mass resolution where BA mode is required for high spatial resolution imaging.

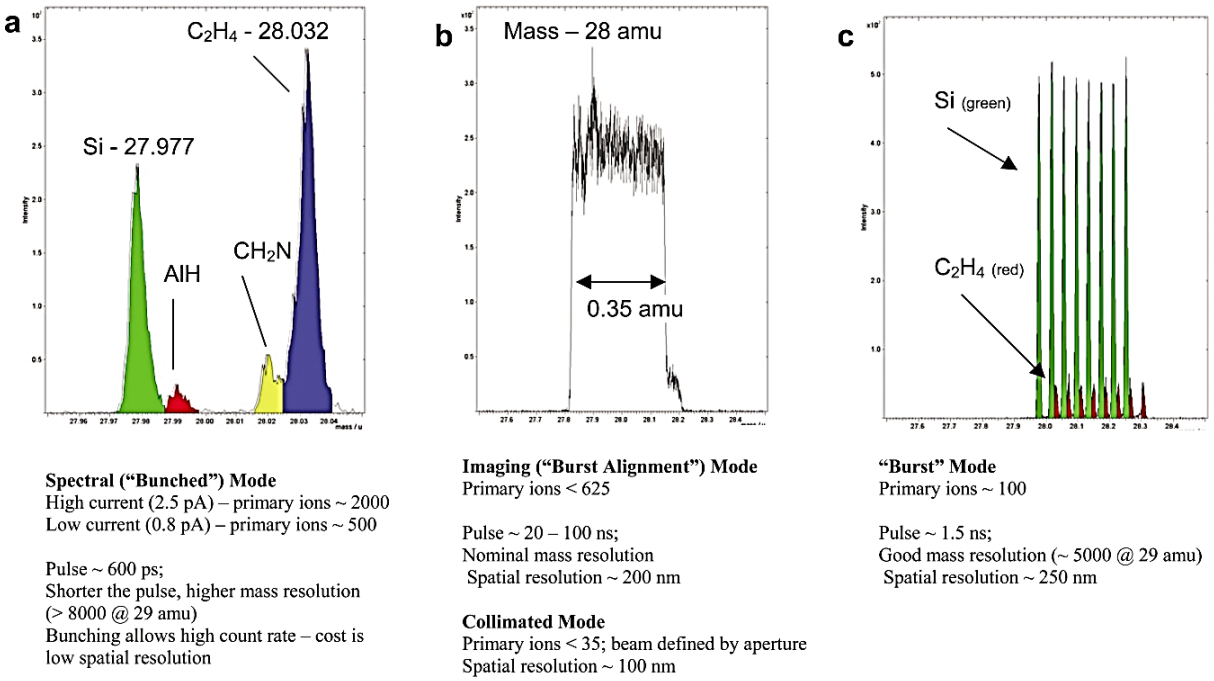

Figure 13: Comparison of different operation modes of primary ion beam [61]. (a) HCBU (high current bunch) mode. (b) BA (burst alignment) and collimated mode. (c) Burst mode.

- Gas cluster ion beam (GCIB)

The principle of gas cluster ion beam (GCIB) generation is shown in Figure 14. In gas cluster ion source, neutral gas clusters are generated by adiabatic gas expansion. When the high pressure gas expands through a Laval nozzle, temperature in the expansion chamber decreases dramatically due to the energy transformation, i.e. thermal energy to kinetic energy. Meanwhile, large clusters could be formed by condensation and nucleation. Then the condensed gas clusters are collimated by a skimmer before entering the ionization chamber where the neutral clusters are ionized by electron impact. The obtained cluster ions can be directed to the target by subsequent extraction, acceleration and beam focusing process. Noticeably, during the production of gas cluster ion beam, the cluster size and beam intensity can be affected by source gas pressure, ionizer (energy and emission), and acceleration energy [62,63]. Thus, those parameters need to be taken into account when tuning the ion beam.

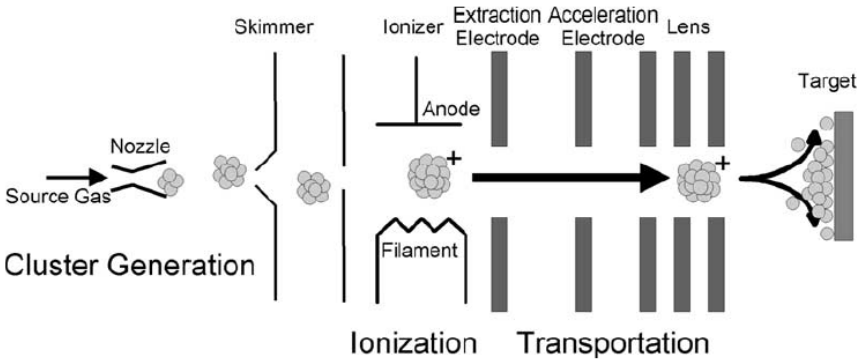

Figure 14: Schematic diagram of gas cluster ion beam generation [39].

The gas clusters generated from the ion source are composed of individual clusters with various sizes, ranging from a few hundreds to several thousands. For practical analysis, cluster size selection need to be performed after the ionization to meet experimental requirements. In the ION-TOF GCIB ion column (Figure 15), cluster size section is achieved by the combination of a Wien filter and a 90° deflection unit. The Wien filter is located behind the ion source to remove low mass species (small clusters). 90° deflection unit comprise a static deflection (static high voltage) and a 90 degree pulser (pulsed high voltage) which help to direct the ion beam to the analytical chamber and allow mass separation by momentum deflection [64,65].

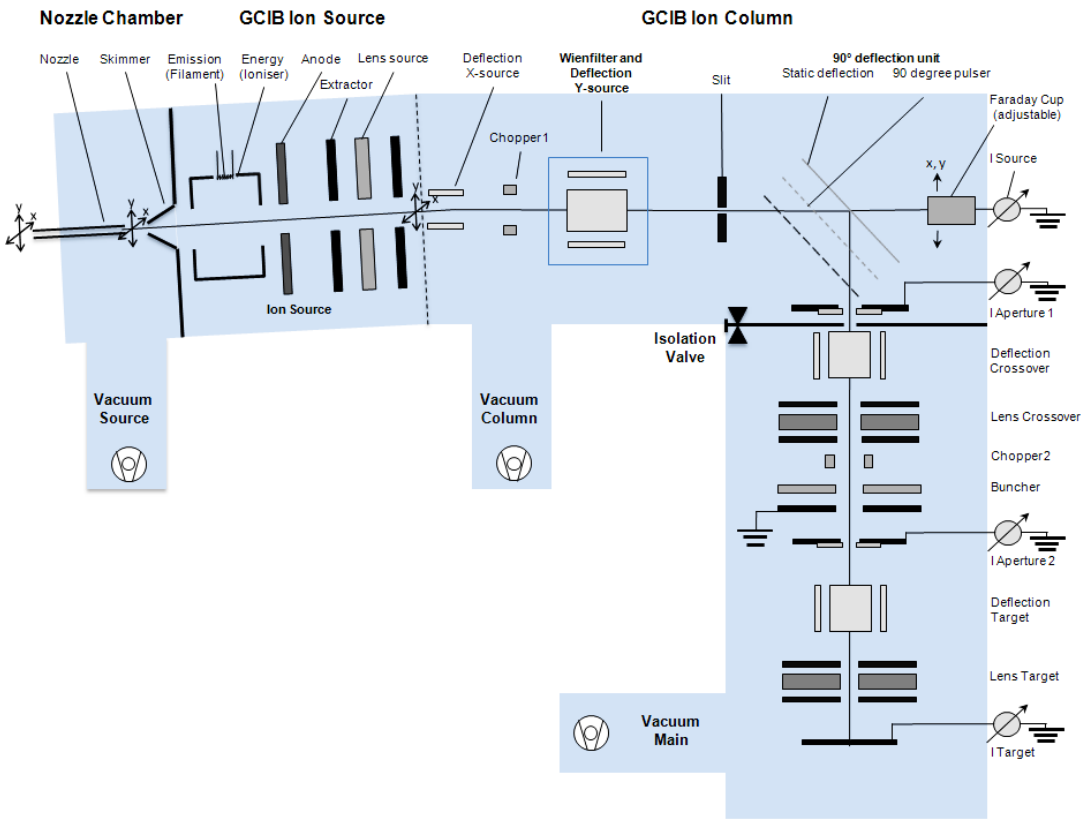

Figure 15: Schematic drawing of the ION-TOF GCIB ion column (from ION-TOF SurfaceLab).

1.3.2 Analyzer

The secondary ion separation in the TOF-SIMS IV mass spectrometer is a time-of-flight analyzer with a single-stage reflectron (Figure 16). Once desorbed, the secondary ions are extracted towards the entrance of the TOF tube by applying a potential difference (2 kV). The ions beam is then focused by the analyzer lens composed of three electrodes. The deflection unit is used to center the ion beam on the detector. The optional blanking plates located at the beginning of the field-free region can be used to select a fraction of the ion beam or a single ion for other purposes, post-source decay analysis [66], for example. A gridless reflectron is employed to perform time focusing of the ions while an additional adjustable reflectron voltage (VDP, variable drift path) permits to compensate for the temporal degradation induced by the post-acceleration in front of the ion detector. VDP tuning enables fine adjustment of energy focusing to maintain full mass resolution in different operation modes.

At the end of the flight path, the secondary ions are post-accelerated at 10 kV onto the MCP to ensure a sufficient conversion of ions to electrons. The number of electrons is multiplied by a factor of about 1000 by the electron collision cascade amplification in the MCP. Then in a scintillator the electrons are converted into photos which can be detected by a

photomultiplier. The finally obtained pulses are analyzed by a threshold discriminator which determines the time with high temporal precision, the signal thus obtained is transmitted to a time-to-digital converter.

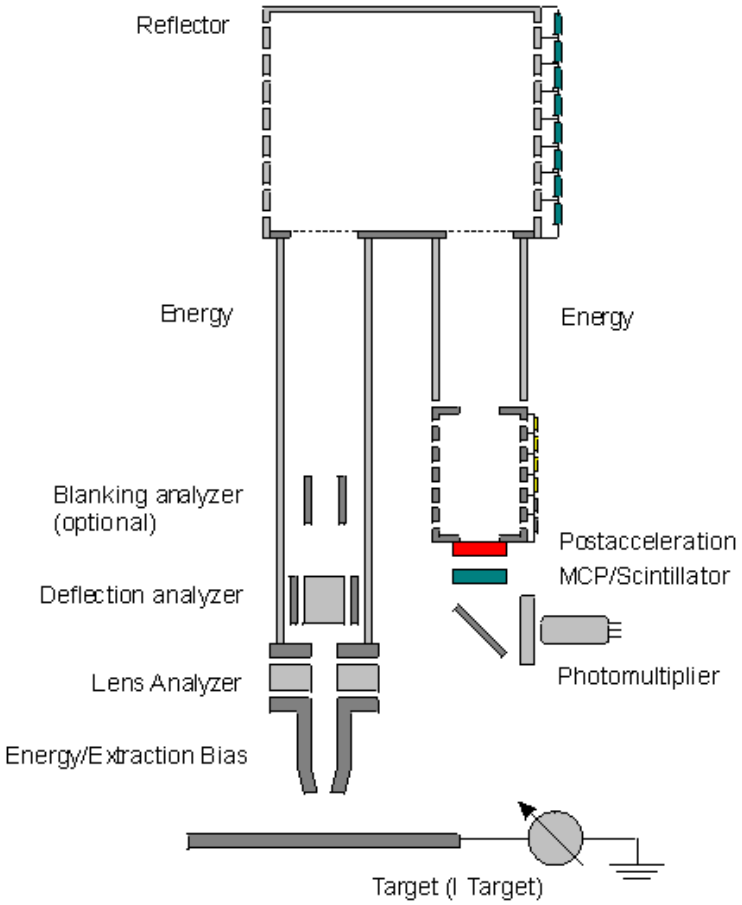

Figure 16: Schematic illustration of the TOF analyzer in TOF-SIMS IV (from ION-TOF SurfaceLab).

1.3.3 Flood gun

In analysis of insulating samples, extra charges from the primary ions will accumulate on the surface, leading to changes in surface potential which disturb secondary ion emission and modify the ion energy and therefore time of flight. In order to compensate these extra charges, low energy electrons produced from a flood gun are applied between two analysis cycles (see Figure 17). In TOF-SIMS IV, the flood gun mainly consists of a filament heated with a standard current of 2.4 A−2.6 A, a Wehnelt electrode for optimization of the electron beam current, and extraction electrodes. The energy of the electrons is determined by the voltage applied to the filament, which is adjustable between 0 and 21 V.

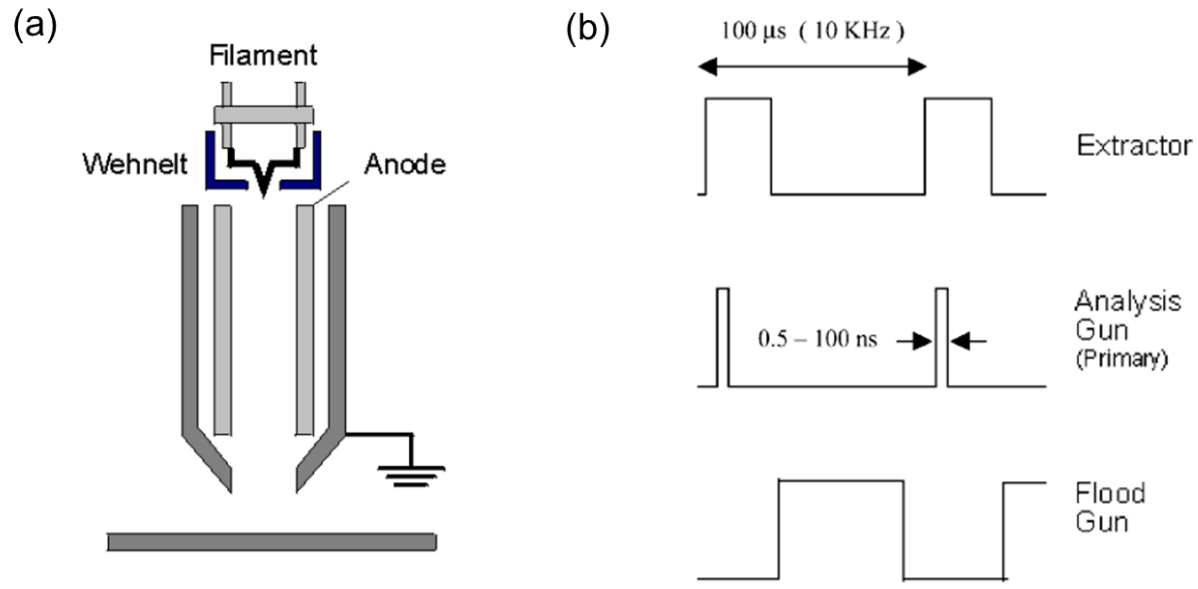

Figure 17: (a) Schematic view of flood gun (from ION-TOF SurfaceLab) and (b) Timing details of the operation of primary gun, extractor and flood fun [61].

Although the employment of flood gun can significantly improve the surface charging issues, it has to be kept in mind that these low energy electrons might be able to cause damage to some electron-sensitive samples such as polymer [67]. Thus, an adjustment of the electron fluence according to the property of samples is recommended.

1.4 TOF-SIMS imaging

Depending on how the spatial information is acquired from the sample surface, mass spectrometry imaging can be achieved with either microscope or microprobe method (see Figure 18). Microscope approach involves the use of ion-optical microscope elements to record the spatial origin of the secondary ions. Thus the spatial resolution is independent of the size of the primary ion beam but determined by the ion optics and resolution of the detector. The decoupling of spatial resolution from the ion beam allows a large area being analyzed without moving the sample or the beam. This imaging approach dominates the early SIMS instruments dedicated to surface imaging [1], as well as the triple focusing time-of-flight (TRIFT) mass spectrometer [68]. Microprobe imaging employs a focused ion beam to raster an area divided by a given number of pixels. Mass spectrum generated from each pixel is correlated with the position of the pixel so that the spatial information can be reconstructed from the mass spectra after data acquisition. In microprobe mode, spatial resolution largely depends on the spot size of the primary ion beam and the acquisition time is relatively longer since the ion beam has to move from pixel to pixel to accomplish the measurement of a

certain area. Nowadays, microprobe method is the most common imaging mode in TOF-SIMS and MALDI-TOF.

The TOF-SIMS instruments from ION-TOF GmbH are operated with microprobe approach, thus the following description about 2D and 3D TOF-SIMS imaging only concerns this imaging mode.

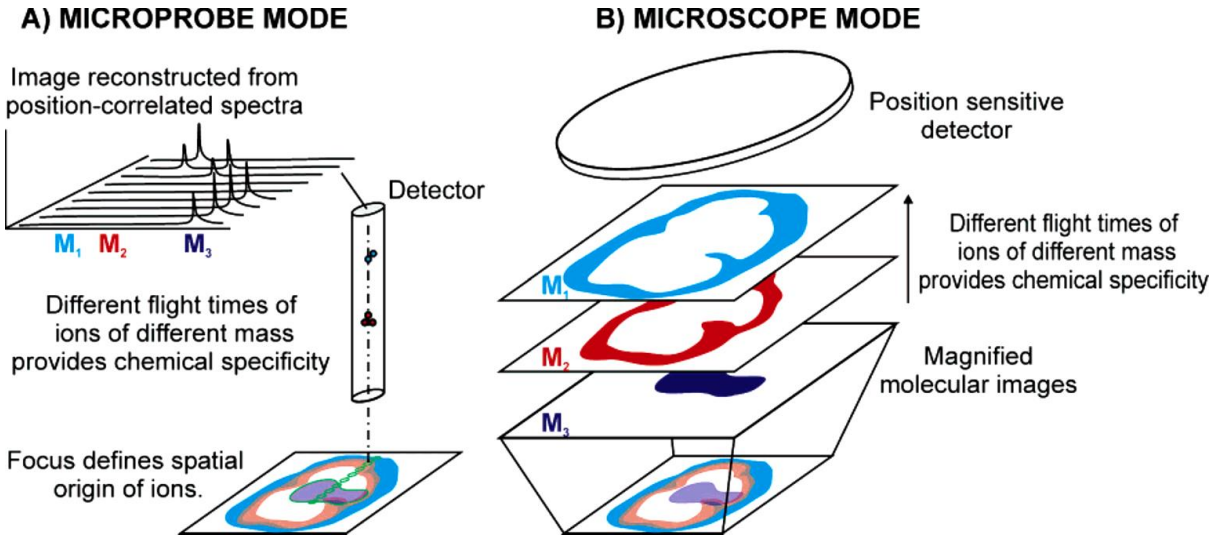

Figure 18: Schematics view of the microprobe and microscope approaches in mass spectrometry imaging [69].

1.4.1 2D TOF-SIMS imaging

In TOF-SIMS, 2D imaging is performed with a single ion beam, either metal ion beam or gas cluster ion beam. For an area smaller than 500 µm × 500 µm, the ion beam is rastered over the sample from pixel to pixel while the sample is kept still during the acquisition, thus the beam scan mode. The raster of the beam is realized by electrostatic deflection plates with an excellent precision of ~ 1ppm. Nevertheless, the raster size is limited to the field of secondary ion extraction optics which is about 500 µm × 500 µm. For large area analysis (usually in the order of cm^2), the total analytical area is divided into several patches (analytical areas that are rastered by the ion beam without move of the sample) and the sample holder is moved from one patch to another by mechanic motors, known as stage scan mode. Within each patch, the ion beam is operated in the same way as in beam scan mode, meaning that the patch size has also to be less than 500 µm × 500 µm. Then large area images can be constructed by stitching ion images from all the patches. In stage scan mode, the mechanical motor has limited precision, thus minimum number of patches and scans of acquisition are favored to minimize the frequency of sample movement. To maintain a sufficient ion dose, the pulses per pixel has to be increased to a compromise value (empirically 4−10 pulses per pixel) as not to cause

severe surface charging. Meanwhile, a larger pixels size is used for the sake of reasonable acquisition time.

1.4.2 3D TOF-SIMS imaging

3D mass spectrometry imaging can be essentially achieved by two approaches. The first one requires "dissecting" the sample into many successive sections, each of which is then subjected to 2D mass spectrometry imaging. Finally, 3D images can be reconstructed by stacking together all the 2D images. Thus, obvious drawbacks of this method are time- and labor-consuming as well as giant data size. It is currently employed in ambient MSI techniques such as MALDI [70,71] and DESI [72]. In an alternative approach, the sample remains intact when introduced to the mass spectrometer. During the analysis, a sputter ion beam is applied to ablate the materials layer by layer in a way that chemical information of each layer surface can be obtained by another analysis beam. 3D images then can be generated by stacking the data from each layer (2D ion images) (see Figure 19). This process is called depth profiling which is commonly used in TOF-SIMS to obtain information underneath the surface. This depth profiling method requires minimum sample preparation and the analytical time depends on how deep the sample is to be analyzed, namely the amount of material that needs to be removed. In TOF-SIMS, 3D imaging can be realized by using a single beam or dual beams.

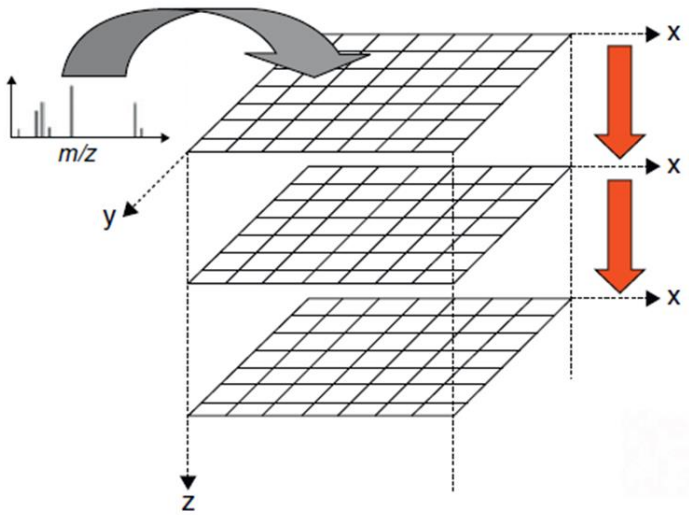

Figure 19: Schematic of the formation of the 3D data set by the stacking of sequential 2D images from the depth profile [73].

- 3D imaging with a single beam

In this case, the single ion beam is used as both the analysis beam and the putter beam, which, in a certain way, simplifies the instrumental configuration for 3D imaging. The issue lies in that large cluster ion beam is required to cause effective sputtering to remove the material while keep the underneath material undamaged. The ion beams suitable for such kind of sputtering process are principally C_{60}^+ and Ar_n^+ clusters, which are difficult to be focused to a satisfying beam size for imaging purpose without loss of beam intensity. To date, 3D imaging by using a single beam have been mainly performed with C_{60} ion beam of which the beam size is ~10 µm [74]. For such analysis, the C_{60} ion beam is operated in DC mode to get sufficient intensity for sputtering.

- 3D imaging with dual beams

In dual beams method, two ion beams are utilized, one for analysis and another for sputtering away damaged materials (Figure 20). The most prevailing configuration in current 3D TOF-SIMS imaging is Au_3^+ or Bi_3^+ clusters being used as analysis beam for the sake of high spatial resolution and C_{60}^+ or Ar_n^+ ion beam as sputter beam for high efficient sputtering. As to the sputter rate, no significant difference is found between C_{60} and Ar clusters [75]. However, Ar clusters have been clearly shown to provide better depth resolution which is about 5 nm with 2.5 keV Ar_{1700}^+ clusters compared to ~ 15 nm with 40 keV C_{60}^+ clusters [76].

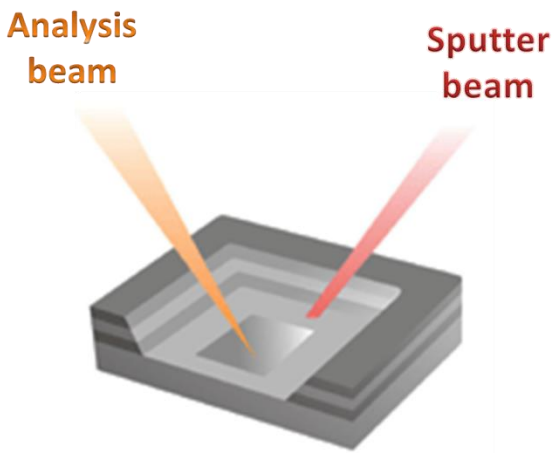

Figure 20: Scheme of 3D TOF-SIMS imaging with dual beam method.

1.5 Data processing

The raw data acquired with TOF-SIMS contains mass spectrum of each pixel of the analytical area in each scan, thus the mass spectra are correlated with the spatial information of the sample and from which the ion density images can be reconstructed. To improve the data

quality and get full interpretation of the data, further processing need to be carried out with corresponding software (for example SurfaceLab for data recorded on TOF-SIMS instruments from ION-TOF GmbH and TOF-DR for apparatus from ULVAC-PHI.

1.5.1 Corrections

For the sake of data quality, the shifts induced by the changes of instrumental parameters during the measurement as well as by the sample itself can be corrected by the following functions.

- Lateral shift correction

In the case of long measurements, the position of the primary ion beam can be shifted during the acquisition leading to blurry ion images. To compensate for these eventual shifts, lateral shift correction can be performed to calibrate the beam position in each scan to that in the first scan or other selected scans. As we can see from Figure 21, after this beam position calibration (right), the ion image becomes sharper, thus the image quality is improved.

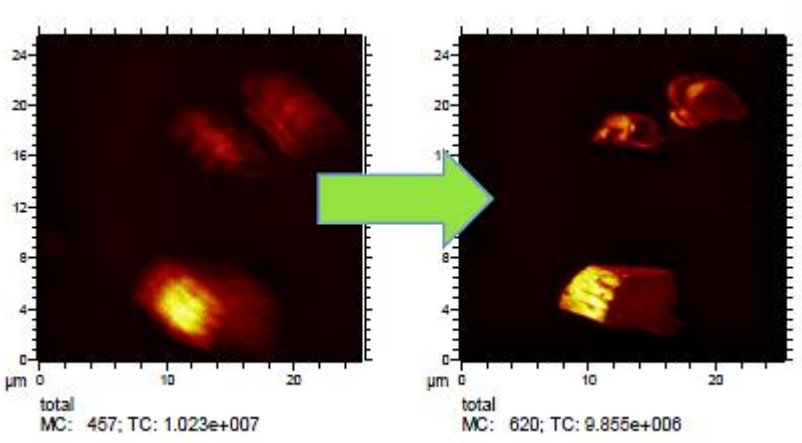

Figure 21: Ion images obtained before (left) and after (right) lateral shift correction (from ION-TOF SurfaceLab).

- Advanced TOF correction

For analysis of topographic samples, surface topography leads to broad kinetic energy distribution of the secondary ions. As a result, the mass resolution can be drastically degraded [77,78]. The advanced TOF correction function in the software can be applied to improve mass resolution by correcting the flight time of secondary ions ejected from each pixel.

- Mass shift correction

Mass shift correction function is specially developed for samples consisting of both inorganic and organic layers. During depth profiling, the change in potential difference at the interface between inorganic and organic layer causes mass shifts of the ions and thus deformed ion peaks in the spectra. To improve the shape of the ion peak, this mass shift can be corrected the mass shift correction function.

- 3D correction using flat substrate (height correction)

In 3D measurements, if the sample surface is not flat, the resulting images reconstructed in the software can be distorted and may not represent the real sample structure. Thus, this height difference in the sample needs to be corrected. By applying the 3D correction or height correction, the 3D images can be corrected by specifying a flat substrate.

It has to be noted that performing these corrections can be very time consuming due to long calculations of various correction factors. Therefore, these functions can be selected to carry out as needed. In this thesis, all the high resolution images acquired with long acquisition time are corrected with lateral shift correction.

1.5.2 Image processing

In the data processing software, many functions are available to help process the images and interpret the data:

- ROI editor

ROI editor is used to extract mass spectrum of a region of interest (ROI) from a complete ion image. The size and shape of the ROI can be determined either manually or by setting the intensity threshold. Performing ROI on the ion images is very useful in revealing the chemical composition in a particular feature of the sample. Noticeably, it sometimes can reveal the ion peaks that have been buried by noise in the total mass spectra.

- RGB overlay

To facilitate the comparison of distributional difference between two or three chemical species, ion image of each species can be defined to a specific color (red, green, blue) and then overlaid, resulting in two-color overlay or three-color overlay images.

- Addition

Addition function is used to sum the ion images of chemical species with the identical localization. It is particularly useful in cases where the ion intensities of several co-localized species are not sufficient to provide individual interpretable images.

In addition, other frequently used functions include adjustment of the intensity scale to increase the image contrast, binning the adjacent pixels to increase the signal intensity, measuring beam size with line scan, etc.

1.6 New developments in TOF-SIMS instrumentation

Owing to the development of efficient cluster ion beams and the improvement in secondary ion transmission and detection, TOF-SIMS has achieved substantial success in characterizing a variety of samples. Nevertheless, there is no doubt that considerable issues still exist in this analytical technique, especially when applied to biological imaging. First of all, secondary ion intensity is still a very important consideration in analysis of biological samples. To date, most of the analysis is performed within the static limit where the primary ion dose is less than 1×10^{13} ions·cm^{-2}. Recent studies have shown that it is possible to surpass this limit by using C_{60}^+ or Ar_n^+ large cluster ion beam. However, with conventional TOF-SIMS instrument, a short primary ion pulse is mandatory to achieve good mass resolution. As a consequence, the beam intensity is sacrificed and the low duty cycle of the pulsed beam leads to incredibly long acquisition time [79]. The second issue is the lack of structural characterization capability. Uncertainties frequently arise when it comes to ion peak attribution, which is especially frustrating in analysis of complex samples. In addition, mass resolution in TOF-SIMS analysis has been moderate (< 10,000) due to the kinetic energy distribution of the secondary ion induced by emission process and topography of the sample. Fortunately, considerable efforts have been performed by the SIMS community to solve these issues and several new instrumentations have been developed in the last decade.

- J105 −3D Chemical Imager

J105−3D Chemical Imager was developed by the Vickerman group in collaboration with Ionoptika Ltd. (Southampton, UK) in 2008 [80]. The main objective of this development is to overcome the requirement to use a pulsed primary ion beam in conventional TOF-SIMS. Figure 22 illustrates the schematic of this J105−3D Chemical Imager. The primary ion beam works in a continuous way so that good beam intensity can be guaranteed. In order to retain a good mass resolution, a set of buncher plates are used to focus the secondary ions in time at the entrance of a quadratic field ToF mass analyser. This design significantly increases the duty cycle and enables 3D imaging and also large area analysis of biological tissues at a reasonable time scale. Besides, tandem MS analysis is realized with a ToF–ToF configuration by placing a collision cell between the buncher and reflectron. Initially equipped with an Ionoptika C_{60} ion beam, the instrument was later fitted with a 40 kV GCIB system providing both C_{60}^+ and Ar_n^+ cluster ions [81]. The MS/MS analysis and imaging of lipids in drosophila

brained with this instrumentation using 40 keV Ar_{4000}^{+} ion beam has been reported recently [82].

The same instrumental concept also yielded another configuration, the Q-Star MALDI mass spectrometer developed by the Winograd group at Penn State [83]. This instrument uses the same continuous C_{60} ion beam and combines MALDI and SIMS analysis in one spectrometer by using an optimized hybrid quadrupole orthogonal TOF analyzer.

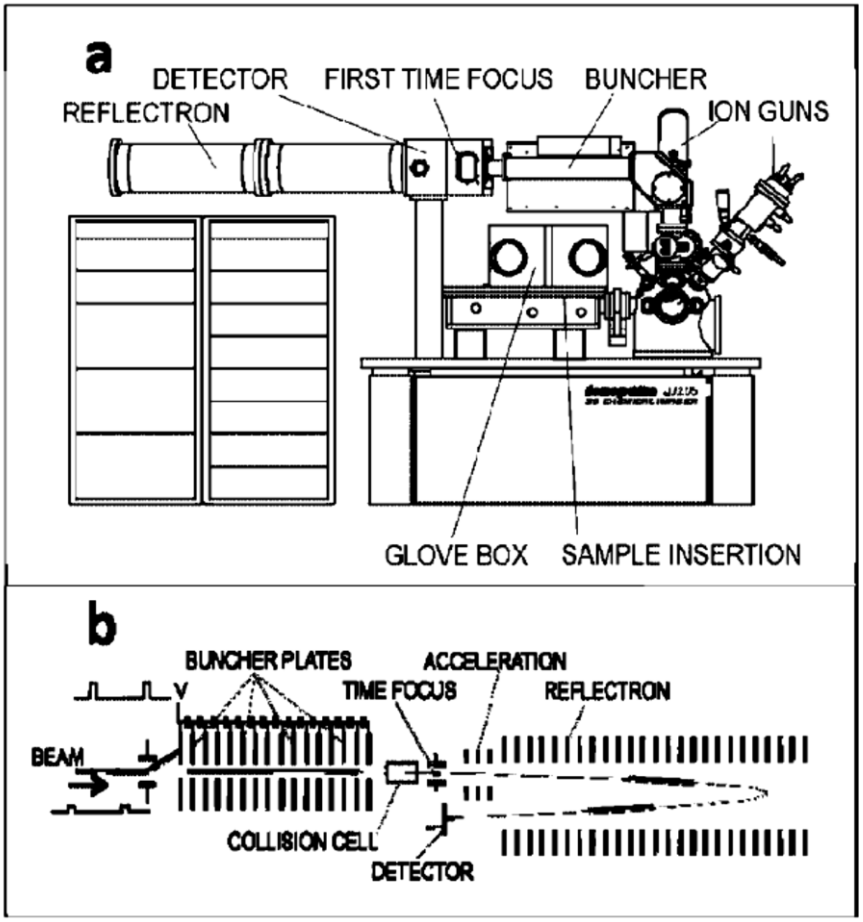

Figure 22: Schematics of (a) the J105−3D Chemical Imager and (b) the coupling of the buncher to the harmonic reflectron.

- PHI *nano* TOF II

PHI *nano* TOF II is a very recent design dedicated to parallel imaging MS/MS analysis. It was developed by Physical Electronics Inc. in collaboration with Maastricht University in 2016 [84,85]. PHI *nano* TOF II is based on the triple ion focusing time-of-flight (TRIFT) spectrometer. The parallel MS/MS imaging capability is achieved by placing a precursor selector right after the third electrostatic analyzer (ESA) where the secondary ions are completely time resolved. The precursor selector is designed such that the desired precursor

ion is reflected into a collision cell for fragmentation followed by a linear TOF for separation and a MS2 detector for ion detection while the rest secondary ions continue their trajectory to reach the MS1 detector. By this way, MS and MS/MS analysis and imaging are realized simultaneously. The instrument has been shown able to perform MS/MS structural characterization of various chemical species.

This technique has been used to perform in situ identification of wood metabolites in chapter 3 and chapter 4. Detailed description about the design and performance of this instrumentation can be found in Chapter 3.

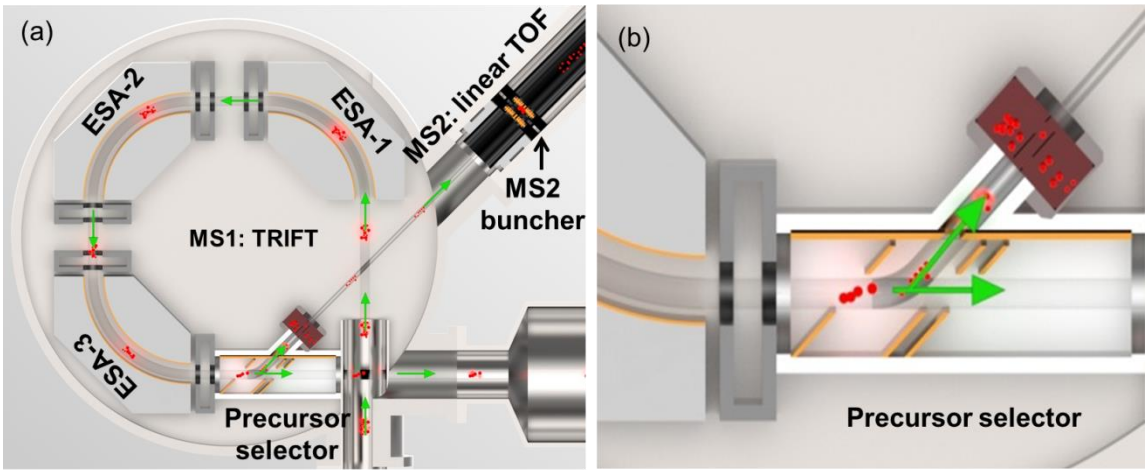

Figure 23: (a) Schematic illustration of the Parallel Imaging MS/MS spectrometer. (b) schematic illustration showing an enlargement of the precursor selector and the activation cell of the MS2 spectrometer [84].

- 3D OrbiSIMS

A so-called revolutionary development in TOF-SIMS is the 3D OrbiSIMS developed by National Physical Laboratory (NPL, UK) and ION-TOF GmbH. This hybrid instrument combines a TOF analyzer for rapid analysis and an Orbitrap mass spectrometer (Q Exactive^{TM} Extension, Thermo Fischer Scientific) for obtaining high sensitivity and high mass resolution. It has been claimed that excellent mass resolution of 240,000 at *m/z* 200 and mass accuracy less than 1 ppm are attainable. Moreover, this configuration permits to determine the molecular structure by MS/MS capability. Commercialization and completion of the 3D OrbiSIMS platform is still in progress.

Previously, a similar coupling of C_{60} SIMS source to a 12 T solariX FTICR mass spectrometer was also reported in 2011 [86]. The mass resolution is better than 100,000 and

mass accuracy is less than 2 ppm. However, the ion transfer optics needs to be optimized to increase secondary ion transmission efficiency for better sensitivity and spatial resolution.

1.7 TOF-SIMS imaging of plant metabolites

Plants have been frequently described as nature's most skilled chemist for their astounding ability in synthesizing a vast array of different metabolites [87]. Those secondary metabolites are essential in various biological activities such as protecting the plants, communicating with the surrounds, and so on. Information on their spatial distribution will be essential to understand the plant metabolism and the corresponding biological process within specific tissues [88]. Compared with conventional spectroscopy techniques, mass spectrometry imaging (MSI) shows superior capability of mapping a wide range of plant metabolites without requirement of any kind of labeling.

TOF-SIMS imaging of wood tissues is among the earliest examples where spatial information of plant metabolites is disclosed by MSI [89,90]. In 2005, Imai, *et al.* [89] first applied TOF-SIMS to localize heartwood extractives ferruginol in Sugi (*Cryptomeria japonica*) wood tissues and revealed that this compound was almost homogeneously distributed in the cell wall on both cross section and tangential section of the heartwood. In 2008, spatial distribution of specific metabolites from Hinoki cypress (*Chamaecyparis obtusa*), hinokinin, hinokiresinol, hinokione, and hinokiol were examined by TOF-SIMS to distinguish sapwood from heartwood in discolored wood from ancient architectural material [91]. The imaging results show that these compounds were exclusively localized in ray parenchyma cells and maximum intensity of the compounds was observed in the transition zone. It was also revealed that these compounds persisted in the wood even the tree was felled in ancient time. On the same wood species [92], elements (Na, Mg, Al, K, and Ca) and lignin distributions in sapwood, transition zone, and heartwood, respectively were also investigated. Lignin was found almost uniformly distributed from sapwood to heartwood, whereas the distribution of elements varied greatly between the different areas. Later, TOF-SIMS was applied to localize flavonoids in seed samples (peas and *Arabidopsis thaliana*) [93] and showed that flavonoids were mainly present in the seed coats (Figure 24). In order to assess the performance of a cryo-TOF-SIMS/SEM system, the distribution of ferruginol in *Cryptomeria japonica* wood species was reinvestigated in 2011. It was revealed that ferruginol was more abundant in the cell walls of some tracheid cells in this frozen-hydrated sample [94]. Very recently, this cryo-TOF-SIMS/SEM system has been successfully employed to visualize the distribution of alkaloids in freeze-fixed stem of *Magnolia Kobus* species [95]. The water-soluble alkaloid salicifoline was mostly found in living phloem tissues as well as in ray cells, lignifying fibres and vessels in the xylem (Figure 25).

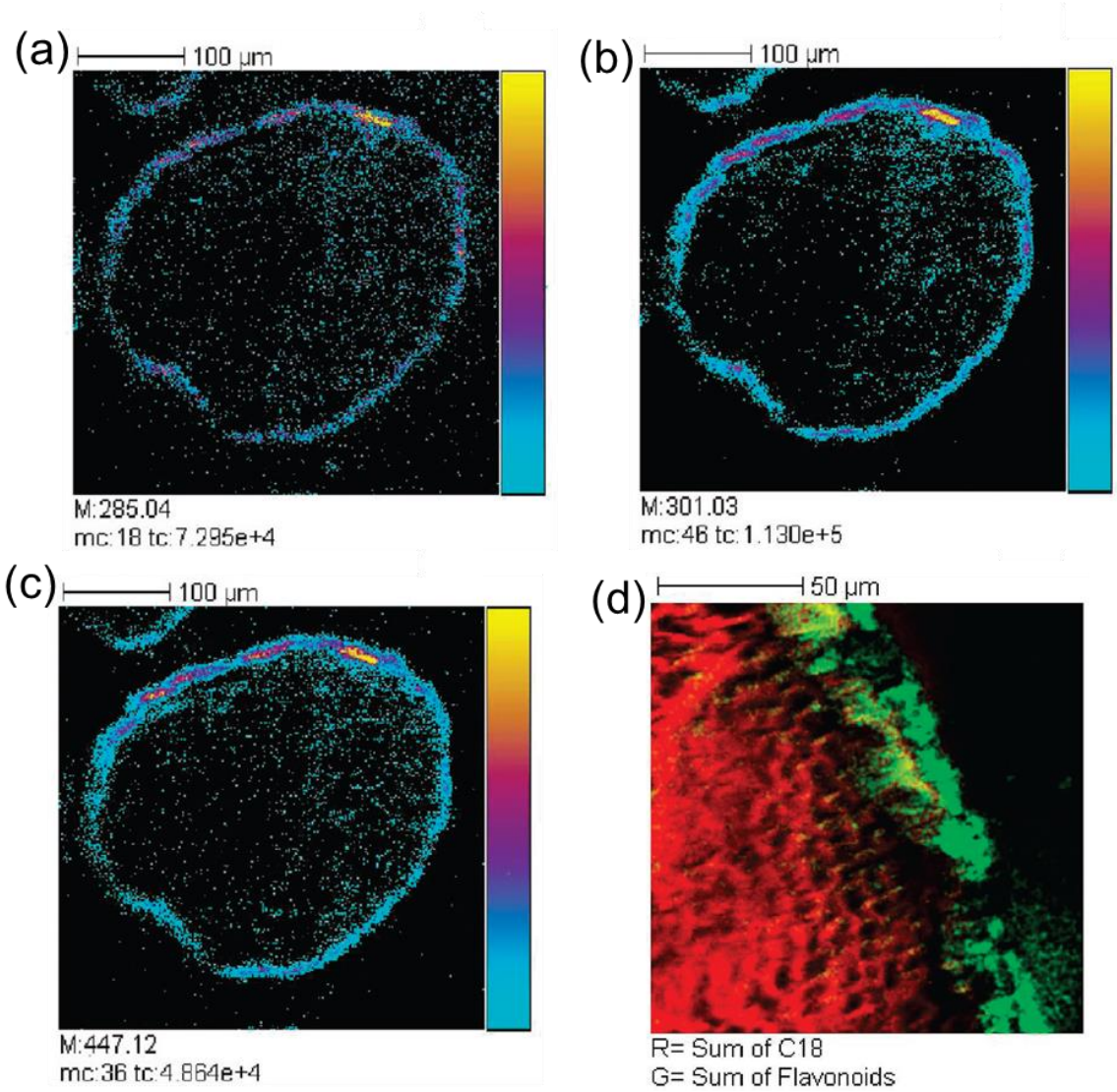

Figure 24: TOF-SIMS negative ion images of an *A. thaliana* seed section, embedded in a polyester resin: (a) *m/z* 285.04. (b) *m/z* 301.03. (c) *m/z* 447.1 (field of view 400 µm × 400 µm, 256 × 256 pixels, pixel size 1.56 µm, fluence 1.5×10^{12} ions·cm^{-2}). (d) High spatial resolution negative ion image recorded close to the seed coat of an *A. thaliana seed* section embedded in a polyester resin (field of view 150 µm × 150 µm, 256 × 256 pixels, pixel size 586 nm, fluence 4×10^{12} ions·cm^{-2}). Two-color overlay: red, sum of C18 fatty acid carboxylate ions; green, sum of flavonoid ions [93].

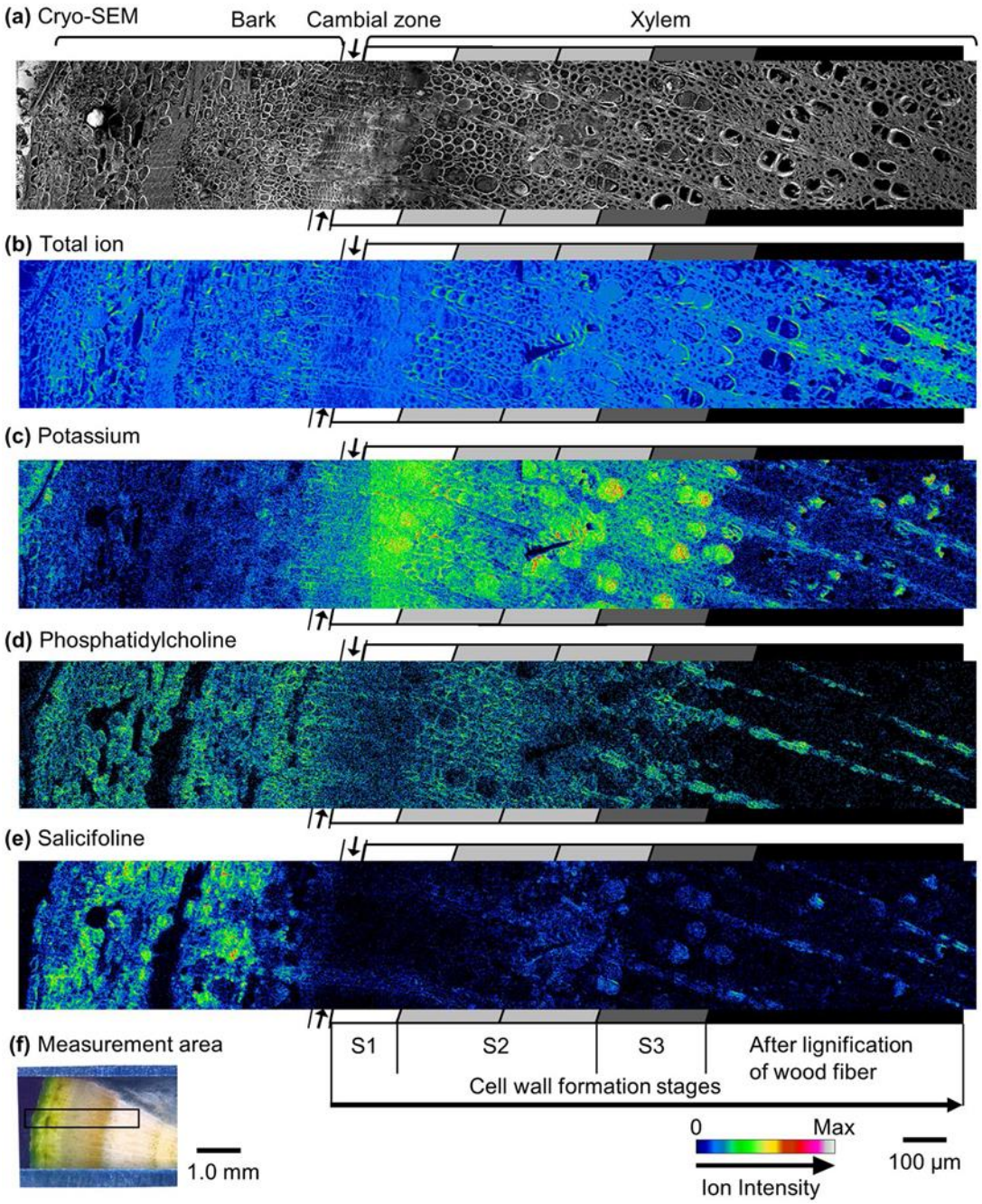

Figure 25: (a) Cryo-SEM image taken after cryo-TOF-SIMS measurement and appropriate freeze etching. Cryo-TOF-SIMS positive ion images of the (b) total ion, (c) potassium, (d) phosphatidylcholine, and (e) salicifoline. (f) Optical microscopic image of a freeze-fixed stem of M. kobus in a sample holder showing the measurement area (approximately 2.4 × 0.4 mm). Scale bars are 100 µm for a, b, c, d, and e and 1.0 mm for f. Arrows above and below the sides of the images of a, b, c, d, and e indicate the cambial zone. Grey scaled tetragons at both sides of the images a, b, c, d, and e indicate the cell wall formation stages of wood fibres [95].

It is noted that all the above wood species studied by TOF-SIMS imaging are soft wood species. Wood metabolites distribution in hard wood species was reported only recently by Vanbellingen, *et al.* [58]. In tropical tree species *Dicorynia guianensis*, toxic metabolite tryptamine and inorganic compound silica were mapped from sapwood to heartwood with high spatial resolution of ~ 400 nm (Figure 26).

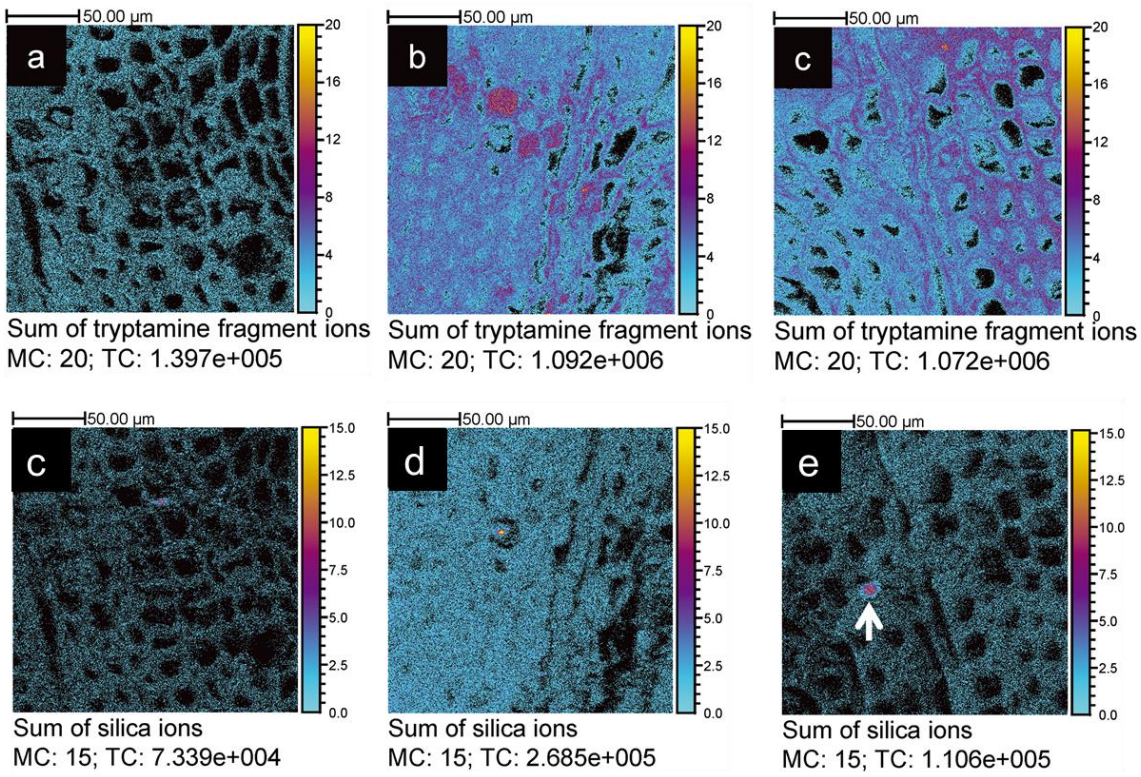

Figure 26: Distribution of tryptamine and silica on the transverse surface of *D. guianensis*. (a) & (c): sapwood. (b) & (d): transition zone. (c) & (e): heartwood. Images have been cropped to zoom on areas of interest of 200 µm× 200 µm size. The white arrows show the silica grain [58].

Although it is recognized that TOF-SIMS has the best spatial resolving capability, the recent reviews [96,97,98,99] about MSI analysis of plant metabolites have clearly demonstrated that the number of studies using TOF-SIMS imaging is far less than MALDI and DESI imaging. Frequently, TOF-SIMS has been criticized for the low secondary ion intensity. However, owing to instrumental development in the last few years, many aspects concerning the performance of TOF-SIMS imaging have been improved, and future mapping of plant metabolites will surely benefit from the high spatial resolution and 3D imaging capability.

References

[1] Castaing, R.; Slodzian, G. Microanalyse par émission ionique secondaire. *Journal of Microscopy* **1962**, *1*, 395−410.

[2] Benninghoven, A. Surface investigation of solids by the statical method of secondary ion mass spectroscopy (SIMS). *Surface Science* **1973**, *35*, 427−437.

[3] Whitlow, H. J.; Hautala, M.; Sundqvist, B. U. R. *International Journal of Mass Spectrometry and Ion Processes* **1987**, *78*, 329−340.

[4] Bolbach, G.; Viari, A.; Galera, R.; Brunot, A.; Blais, J. C. Organic film thickness effect in secondary ion mass spectrometry and plasma desorption mass spectrometry. *International Journal of Mass Spectrometry and Ion Processes* **1992**, *112*, 93−100.

[5] Benninghoven, A.; Hagenhoff, B.; Niehuis, E. Surface MS: probing real-world samples. *Analytical Chemistry* **1993**, *65*, 630A−640A.

[6] Sigmund, P. Sputtering by ion bombardment: theoretical concepts. In *Sputtering by particle bombardment I: physical sputtering of single-element solids*; Behrisch, R., Ed.; Springer-Verlag Berlin Heidelberg, **1981**.

[7] Yu, M. L. A bond breaking model for secondary ion emission. *Nuclear Instruments and Methods in Physics Research Section B: Beam Interactions with Materials and Atoms* **1986**, *18*, 542-548.

[8] Gerhard, W.; Plog, C. Secondary ion emission by nonadiabatic dissociation of nascent ion molecules with energies depending on solid composition. *Zeitschrift für Physik B Condensed Matter* **1983**, *54*, 59–70.

[9] Cooks, R. G.; Busch, K. L. Matrix Effects, Internal Energies and MS/MS Spectra of Molecular Ions Sputtered from Surfaces. *International Journal of Mass Spectrometry and Ion Physics*, **1983**, *53*, 111–124.

[10] Kotter, F.; Benninghoven, A. Secondary ion emission from polymer surfaces under Ar^+, Xe^+ and SF_5^+ ion bombardment. *Applied Surface Science* **1998**, *133*, 47–57.

[11] Brunelle, A.; Touboul, D.; Laprévote, O. Biological tissue imaging with time-of-flight secondary ion mass spectrometry and cluster ion source. *Journal of Mass Spectrometry* **2005**, *40*, 985−999.

[12] Pacholski, M. L.; Winograd, N. Imaging with Mass Spectrometry. *Chemical Review* **1999**, *99*, 2977−3005.

[13] Rading, D. From sample to data. IONTOF workshop, Mons, **2016**.

[14] Cheng, J.; Wucher, A.; Winograd, N. Molecular depth profiling with cluster ion beams. *Journal of Physical Chemistry B* **2006**, *110*, 8329−833.

[15] Vickerman, J. C.; Briggs, D. ToF-SIMS: Materials analysis by mass spectrometry, 2nd Ed. Surface Spectra/IM Publs, Manchester/Chichester, **2001**.

[16] Krohn, V. E.; Ringo, G. R. Ion source of high brightness using liquid metal. *Applied Physics Letters* **1975**, *27*, 479−481.

[17] Cannon, D. M.; Pacholski, M. L.; Winograd, N.; Ewing, A. G. Molecule specific imaging of freeze-fractured, frozen-hydrated model membrane systems using mass spectrometry. *Journal of American Chemical Society* **2000**, *122*, 603−610.

[18] Ostrowski, S. G.; Van Bell, C. T.; Winograd, N.; Ewing, A. G. Mass spectrometric imaging of highly curved membranes during tetrahymena mating. *Science* **2004**, *305*, 71−73.

[19] Andersen, H. H.; Bay, H. L. Nonlinear effects in heavy-ion sputtering. *Journal of Applied Physics* **1974**, *45*, 953−954.

[20] Wucher, A. Molecular secondary ion formation under cluster bombardment: A fundamental review. *Applied Surface Science* 2006, *252*, 6482–648.

[21] Reuter W. Secondary ion emission from metal targets under carbon trifluoride ion (CF_3^+) and oxygen ion (O_2^+) bombardment. *Analytical Chemistry* **1987**, *59*, 2081–2087.

[22] Appelhans, A. D.; Delmore, J. E. Comparison of polyatomic and atomic primary beams for secondary ion mass spectrometry of organics. *Analytical Chemistry* **1989**, *61*, 1087–1093.

[23] Blain, M. G.; Della-Negra, S.; Joret, H.; Le Beyec, Y.; Schweikert, E. A. Secondary-ion yields from surfaces bombarded with keV molecular and cluster Ions. *Physical Review Letters* **1989**, *63*, 1625−1628.

[24] Benguerba, M.; Brunelle, A.; Della-Negra, S.; Depauw, J.; Joret, H.; Le Beyec, Y.; Blain, M. G.; Scweikert, E. A.; Ben Assayag, G.; Sudraud, P. Impact of slow gold clusters on various solids: nonlinear effects in secondary ion emission. *Nuclear Instruments and Methods in Physics Research B* **1991**, *62*, 8−22.

[25] Baudin K, Bolbach G, Brunelle A, Della-Negra S, Ha°kansson P, Le Beyec Y. Secondary ion emission under cluster impact at low energies (5–60 keV); influence of the number of atoms in the projectile. *Nuclear Instruments and Methods in Physics Research B* **1991**, *88*, 160−163.

[26] Davies, N.; Weibel, D. E.; Blenkinsopp, P.; Lockyer, N.; Hill, R.; Vickerman, J. C. Development and experimental application of a gold liquid metal ion source. *Applied Surface Science* **2003**, *203−204*, 223−227.

[27] Touboul, D.; Halgand, F.; Brunelle, A.; Kersting, R.; Tallarek, E.; Hagenhoff, B.; Laprévote O. Tissue molecular ion imaging by gold cluster ion bombardment. *Analytical Chemistry* **2004**, *76*, 1550−1159.

[28] Sjövall, P.; Jausmaa, J.; Johansson, B. Mass spectrometric imaging of lipids in brain tissue. *Analytical Chemistry* **2004**, *76*, 4271–4278.

[29] Touboul, D.; Brunelle, A.; Halgand, F.; De La Porte, S.; Laprévote, O. Lipid imaging by gold cluster time-of-flight-secondary ion mass spectrometry: application to Duchenne muscular dystrophy. *Journal of Lipid Research* **2005**, *46*, 1388–1395.

[30] Kollmer F. Cluster primary ion bombardment of organic materials. *Applied Surface Science* **2004**, *231−232*,153−158.

[31] Touboul, D.; Kollmer, F.; Niehuis, E.; Brunelle, A.; Laprévote, O. Improvement of biological time-of-flight-secondary ion mass spectrometry imaging with a bismuth cluster ion source. *Journal of American Society for Mass Spectrometry* **2005**, *16*, 1608–1618.

[32] Wong, S. C. C.; Hill, R.; Blenkinsopp; Lockyer, N. P.; Weibel, D. E.; Vickerman, J. C. Development of a C60+ ion gun for static SIMS and chemical imaging. *Applied Surface Science* **2003**, *203−204*, 219−222.

[33] Weibel, D.; Wong, S.; Lockyer, N.; Blenkinsopp, P.; Hill, R.; Vickerman, J. C. A C_{60} primary ion beam system for time of flight secondary ion mass spectrometry: Its development and secondary ion yield characteristics. *Analytical Chemistry* **2003**, *75*, 1754–1764.

[34] Kersting, R.; Hagenhoff, B.; Kollmer, F.; Mollers, R.; Niehuis, E. Influence of primary ion bombardment conditions on the emission of molecular secondary ions. *Applied Surface Science* **2004**, *231−232*, 261−264.

[35] Fletcher, J. S.; Conlan, X. A.; Jones, E. A.; Biddulph, G.; Lockyer, N. P.; Vickerman, J. C. TOF-SIMS analysis using C60. Effect of impact energy on yield and damage. Analytical Chemistry 2006, 78, 1827−1831.

[36] Fletcher, J. S.; Lockyer, N. P.; Vickerman, J. C. Developments in molecular SIMS depth profiling and 3D imaging of biological systems using polyatomic primary ions. *Mass Spectrometry Reviews* **2011**, *30*, 142−174.

[37] Fletcher, J. S. Latest applications of 3D ToF-SIMS bio-imaging. *Biointerphases* **2015**, *10*, 018902-1.

[38] Matsuo, J.; Abe, H.; Takaoka, G. H.; Yamada, I. Gas cluster ion beam equipments for industrial applications. *Nuclear Instruments and Methods in Physics Research B* **1995**, *99*, 244−247.

[39] Yamada, I.; Matsuo, J.; Toyoda, N.; Kirkpatrick, A. Materials processing by gas cluster ion beams. *Materials Science and Engineering R* **2001**, *34*, 231–295.

[40] Ninomiya, S.; Nakata, Y.; Ichiki, K.; Seki, T.; Aoki, T.; Matsuo, J. Measurements of secondary ions emitted from organic compounds bombarded with large gas cluster ions. *Nuclear Instruments and Methods in Physics Research B* **2007**, *256*, 493–496.

[41] Ninomiya, S.; Nakata, Y.; Honda, Y.; Ichiki, K.; Seki, T.; Aoki, T.; Matsuo, J. A fragment-free ionization technique for organic mass spectrometry with large Ar cluster ions. *Applied Surface Science* **2008**, *255*, 1588–1590.

[42] Mochiji, K.; Hashinokuchiy, M.; Moritani, K.; Toyoda, N. Matrix-free detection of intact ions from proteins in argon-cluster secondary ion mass spectrometry. *Rapid Communication in Mass Spectrometry* **2009**, *23*, 648–652.

[43] Oshima, S.; Kashihara, I.; Moritani, K.; Inui, N.; Mochiji, K. Soft-sputtering of insulin films in argon-cluster secondary ion mass spectrometry. *Rapid Communication in Mass Spectrometry* **2011**, *25*, 1070–1074.

[44] Bich, C.; Havelund, R.; Moellers, R.; Touboul, D.; Kollmer, F.; Niehuis, E.; Gilmore, I. S.; Brunelle, A. Argon cluster ion source evaluation on lipid standards and rat brain tissue samples. *Analytical Chemistry* **2013**, *85*, 7745−7752.

[45] Körsgen, M.; Pelster, A.; Dreisewerd, K; Arlinghaus, H. F. 3D ToF-SIMS analysis of peptide incorporation into MALDI matrix crystals with sub-micrometer resolution. *Joural of American Society of Mass Spectrometry* **2016**, *27*, 277−284.

[46] Magee, C. W.; Harrington, W. L.; Honig, R. E. Secondary ion quadrupole mass spectrometer for depth profiling–design and performance evaluation. *Review of Scientific Instruments*, **1978**, *49*, 477−785.

[47] Chait, B. T.; Standing, K. G. A time-of-flight mass spectrometer for measurement of secondary ion mass spectra. *International Journal of Mass Spectrometry and Ion Physics*, **1981**, *40*, 185−193.

[48] Radionova, A.; Filippov, I.; Derrick, P. J. In pursuit of resolution in time-of-flight mass spectrometry: A historical perspective. *Mass spectrometry reviews* **2015**, 35, 738−757.

[49] Alihanov, S. G. A new impulse method of measuring ion masses. *Journal of Technical Physics* **1956**, *31*, 517–521.

[50] Mamyrin, B. A.; Karataev, V. I.; Shmikk, D. V.; Zagulin, V. A. The mass reflectron, a new nonmagnetic time-of-flight mass spectrometer with high resolution. *Zh Eksp Teor Fiz* **1973**, *64*, 82–89.

[51] Frey, R.; Schlag, E. W. Time-of-flight mass spectrometer using an ion reflector. Patent US 4731532 A1, **1986**.

[52] Kutscher, R.; Grix, R.; Li, G.; Wollnik, H. A transversally and longitudinally focusing time-of-flight mass spectrometer. *International Journal of Mass Spectrometry and Ion Processes* **1991**, *103*, 117–128.

[53] Brown, R. S.; Lennon, J. J. Mass resolution improvement by incorporation of pulsed ion extraction in a matrix-assisted laser desorption/ionization linear time-of-flight mass spectrometer. *Analytical Chemistry* **1995**, *67*, 1998–2003.

[54] Vestal, M. L.; Juhasz, P.; Martin, S. A. Delayed extraction matrix-assisted laser desorption time-of-flight mass spectrometry. *Rapid Communications in Mass Spectrometry* **1995**, *9*, 1044–1050.

[55] Cheng, J.; Winograd, N. Depth profiling of peptide films with TOF-SIMS and a C60 probe. *Analytical Chemistry* **2005**, *77*, 3651–3659.
[56] McDonnell, L. A.; Heeren, R. M. N. Imaging mass spectrometry. *Mass Spectrometry Reviews* **2007**, *26*, 606–643.
[57] Vanbellingen, Q. P.; Elie N.; Eller, M. J.; Della-Negra, S.; Touboul D.; Brunelle A. Time-of-flight secondary ion mass spectrometry imaging of biological samples with delayed extraction for high mass and high spatial resolutions. *Rapid Communications in Mass Spectrometry* **2015**, *29*, 1187–1195.
[58] Vanbellingen, Q. P.; Fu T.; Bich, C.; Amusant, N.; Stien, D.; Della-Negra, S.; Touboul, D.; Brunelle, A. Mapping Dicorynia guianensis wood constituents by submicron resolution cluster-TOF-SIMS Imaging. *Journal of Mass Spectrometry* **2016**, *51*, 412–423.
[59] Shon, H. K.; Yoon, S.; Moon, J. H.; Lee, T. G. Improved mass resolution and mass accuracy in TOF-SIMS spectra and images using argon gas cluster ion beams. *Biointerphases* **2016**, *11*, 02A321.
[60] Lindgren, J.; Uvdal, P.; Sjövall, P.; Nilsson, D. E. Engdahl, A.; Schultz, B. P.; Thiel, V. Molecular preservation of the pigment melanin in fossil melanosomes. *Nature Communications* **2012**, *3*, 824.
[61] Sodhi, R. N. S. Time-of-flight secondary ion mass spectrometry (tof-sims): versatility in chemical and imaging surface analysis. *Analyst* **2004**, *129*, 483–487.
[62] Seki, T.; Matsuo, J.; Takaoka, G. H.; Yamada, I. Generation of the large current cluster ion beam. *Nuclear Instruments and Methods in Physics Research B* **2003**, *206*, 902−906.
[63] Matsuo, J.; Okubo, C.; Seki, T.; Aoki, T.; Toyoda, N.; Yamada, I. A new secondary ion mass spectrometry (SIMS) system with high-intensity cluster ion source. *Nuclear Instruments and Methods in Physics Research B* **2004**, *219−220*, 463−467.
[64] Niehuis, E.; Heller, T.; Feld, H.; Benninghoven, A. High Resolution TOF Secondary Ion Mass Spectrometer. Secondary Ion Mass Spectrometry SIMS V, Springer Series in Chemical Physics 44, Benninghoven, A., (Eds: Colton, R. J.; Simons, D. S.; Werner, H. W.), Springer Verlag, Berlin, **1986**, 188-190.
[65] Kayser, S.; Rading, D.; Moellers, R.; Kollmer, F.; Niehuis, E. Surface spectrometry using large argon clusters. *Surface Interface Analysis* **2013**, *45*, 131–133.
[66] Touboul, D.; Brunelle, A.; Olivier Laprévote. Structural analysis of secondary ions by post-source decay in time-of-flight secondary ion mass spectrometry. *Rapid Communications in Mass Spectrometry* **2006**, *20*, 703–709.
[67] Gilmore, I. S.; Seah, M. P. Electron flood gun damage in the analysis of polymers and organics in time-of-flight SIMS. *Applied Surface Science* **2002**, *187*, 89−100.

[68] Schueler, B.; Sander, P.; Reed, D. A. A time-of-flight secondary ion microscope. *Vacuum* **1990**, *41*, 1661−1664.

[69] Luxembourg, S. L.; Mize, T. H.; McDonnell, L. A.; Heeren, R. M. A. High-Spatial resolution mass spectrometric imaging of peptide and protein distributions on a surface. *Anallytical Chemistry* **2004**, *76*, 5339−5344.

[70] Andersson, M.; Groseclose, M. R.; Deutch, A. Y.; Caprioli, R. M. Imaging mass spectrometry of proteins and peptides: 3D volume reconstruction. *Nature Methods* **2008**, *5*, 101–108.

[71] Sinha, T. K.; Khatib-Shahidi, S.; Yankeelov, T. E.; Mapara, K.; Ehtesham, M.; Cornett, D. S.; Dawant, B. M.; Caprioli, R. M.; Gore, J. C. Integrating spatially resolved three-dimensional MALDI IMS with in vivo magnetic resonance imaging. *Nature Methods* **2008**, *5*, 57–9.

[72] Eberlin, L. S.; Ifa, D. R.; Wu, C.; Cooks, R. G. Three-Dimensional vizualization of mouse brain by lipid analysis using ambient ionization mass spectrometry. *Angewandte Chemie International Edition* **2010**, *49*, 873−876.

[73] Fletcher, J. S.; Lockyer, N. P.; Vaidyanathan, S.; Vickerman, J. C. TOF-SIMS 3D biomolecular imaging of *Xenopus laevis* oocytes using buckminsterfullerene (C_{60}) primary ions. *Analytical Chemistry* **2007**, *79*, 2199−220.

[74] Lu, C.; Wucher, A.; Winograd, N. Molecular depth profiling of buried lipid bilayers using C_{60}-SIMS. *Analytical Chemistry* **2011**, *83*, 351–358.

[75] Rabbani, S.; Barber, A. M.; Fletcher, J. S.; Lockyer, N. P.; and Vickerman, J. C. TOF-SIMS with Argon Gas Cluster Ion Beams: A Comparison with $C60^{+}$. *Analytical Chemistry* **2011**, *83*, 3793−3800.

[76] Winograd, N.; Mao, D.; Miyayama, T.; Niehuis, E., Rading, D., Moellers, R. Argon cluster ion beams for organic depth profiling: results from a VAMAS interlaboratory study. *Analytical Chemistry* **2012**, *84*, 7865−7873.

[77] Lee, J. L. S.; Gilmore, I. S.; Seah, M. P.; Fletcher, I. W. Topography and field effects in secondary ion mass spectrometry – Part I: conducting samples. *Journal of the American Society for Mass Spectrometry* **2011**, *22*, 1718−1728.

[78] Lee, J. L. S.; Gilmore, I. S.; Seah, M. P.; Levick, A. P.; Shard, A. G. Topography and field effects in secondary ion mass spectrometry Part II: insulating samples. *Surface Interface Analysis* **2012**, *44*, 238–245

[79] Walker, A. V. Why Is SIMS underused in chemical and biological analysis? Challenges and opportunities. *Analytical Chemistry* **2008**, *80*, 8865–8870.

[80] Fletcher, J. S.; Rabbani, S.; Henderson, A.; Blenkinsopp, P.; Thompson, S. P.; Lockyer, N. P.; Vickerman, J. C. A new dynamic in mass spectral imaging of single biological cells. *Analytical Chemistry* **2008**, *80*, 9058−9064.

[81] Angerer, T. B.; Blenkinsopp, P.; Fletcher, J. S. High energy gas cluster ions for organic and biological analysis by time-of-flight secondary ion mass spectrometry. *International Journal of Mass Spectrometry* **2015**, *377*, 591−598.

[82] Phan, N. T. N.; Munem, M.; Ewing, A. G.; Fletcher, J. S. MS/MS analysis and imaging of lipids across Drosophila brain using secondary ion mass spectrometry. *Analytical and Bioanalytical Chemistry* **2017**, *409*, 3923–3932.

[83] Carado, A.; Passarelli, M. K.; Kozole, J.; Wingate, J. E.; Winograd, N., Loboda, A, V. C_{60} SIMS with a hybrid-quadrupole orthogonal time-of-flight mass spectrometer. *Analytical Chemistry* **2008**, *80*, 7921−7929.

[84] Fisher, G. L.; Bruinen, A. L.; Ogrinc Potočnik, N.; Hammond, J. S.; Bryan, S. R.; Larson, P. E.; Heeren, R. M. A. A New Method and Mass Spectrometer Design for TOF-SIMS Parallel Imaging MS/MS. *Analytical Chemistry* **2016**, *88*, 6433−6440.

[85] Fisher, G. L.; Hammond, J. S.; Larson, P. E.; Bryan, S. R.; Heeren, R. M. A. Parallel imaging MS/MS TOF-SIMS instrument. *Journal of Vacuum Science & Technology B* **2016**, *34*, 03H126.

[86] Smith, D. F.; Robinson, E. W.; Tolmachev, A. V.; Heeren, R. M.; Pasa-Tolic, L. C60 secondary ion fourier transform ion cyclotron resonance mass spectrometry. *Analytical Chemistry* **2011**, *83*, 9552–9556.

[87] Hussain, M. S.; Fareed, S.; Ansari, S.; Rahman, M. A.; Ahmad, I. Z.; Saeed, M. Current approaches toward production of secondary plant metabolites. *Journal of Pharmacy and Bioallied Sciences* **2012**, *4*, 10–20.

[88] Lee,Y. J.; Perdian, D. C.; Song, Z.;Yeung, E. S.; Nikolau, B. J. Use of Mass spectrometry for imaging metabolites in plants. *Plant Journal* **2012**, 70, 81–95.

[89] Imai, T.;Tanabe, K.; Kato,T.; Fukushima, K. (2005). Localization of ferruginol, a diterpenephenol, in *Cryptomeria japonica* heartwood by time-of-flight secondary ion mass spectrometry. *Planta* **2005**, *221*, 549–556.

[90] Mullen, A. K.; Clench, M. R.; Crosland, S.; Sharples, K. R. Determination of agrochemical compounds in soya plants by imaging matrix-assisted laser desorption/ionization mass spectrometry. *Rapid Communications in Mass Spectrometry* **2005**, *19*, 2507–2516.

[91] Saito, K.; Mitsutani, T.; Imai, T.; Matsushita, Y., Fukushima, K. Discriminating the indistinguishable sapwood from heartwood in discolored ancient wood by direct molecular

mapping of specific extractives using time-of-flight secondary ion mass spectrometry. *Analytical Chemistry* **2008**, *80*, 1552–1557.

[92] Saito, K.; Mitsutani, T.; Imai, T.; Matsushita, Y.; Yamamoto, A.; Fukushima, K. Chemical differences between sapwood and heartwood of *Chamaecyparis obtusa* detected by ToF-SIMS. *Applied Surface Science* **2008**, *255*, 1088–1091.

[93] Seyer, A.; Einhorn, J.; Brunelle, A.; Laprévote, O. Localization of flavonoids in seeds by cluster time-of-flight secondary ion mass spectrometry imaging. *Analytical Chemistry* **2010**, *82*, 2326–2333.

[94] Kuroda, K.; Fujiwara, T.; Imai, T.; Takama, R.; Saito, K.; Matsushita, Y.; Fukushima, K. The cryo-TOF-SIMS/SEM system for the analysis of the chemical distribution in the freeze-fixed Cryptomeria japonica wood. *Surface Interface Analysis* **2013**, *45*, 215–219.

[95] Okumura, W.; Aoki, D.; Matsushita, Y.; Yoshida, M.; Fukushima, K. Distribution of salicifoline in freeze-fixed stems of Magnolia kobus as observed by cryo-TOF-SIMS. *Scientific Reports* **2017**, *7*, 5939.

[96] Matros, A.; Mock, H. P. Mass spectrometry based imaging techniques for spatially resolved analysis of molecules. *Frontiers in Plant Science* **2013**, *4*, 89.

[97] Bjarnholt, N.; Li, B.; D'Alvise, J.; Janfelt, C. Mass spectrometry imaging of plant metabolites–principles and possibilities. *Nature Product Report* **2014**, *31*, 818–837.

[98] Sumner, L. W.; Lei, Z.; Nikolau, B. J.; Saito, K. Modern plant metabolomics: advanced natural product gene discoveries, improved technologies, and future prospects. *Nature Product Report* **2015**, *32*, 212−229.

[99] Dong, Y.; Li, B.; Malitsky, S.; Rogachev, I.; Aharoni, A.; Kaftan, F.; Svatoš, A.; Franceschi, P. Sample preparation for mass spectrometry imaging of plant tissues: A review. *Frontiers in Plant Science* **2016**, 7, 60.

Chapter 2 Internal energy distribution of secondary ions under argon and bismuth cluster bombardments

2.1 Abstract

The emission/ionization process under massive argon cluster bombardment was investigated by measuring the internal energy distributions of a series of benzylpyridinium ions. Ar_n^+ clusters with kinetic energies between 10 and 20 keV and cluster sizes ranging from 500 to 10000 were examined to establish the influence of cluster size, energy and velocity on the internal energy distribution of the secondary ions. It is shown that the internal energy distribution of secondary ions principally depends on the energy per atom or the velocity of the cluster ion beam ($E \propto v^2$). Under low velocity impact ($E/n < 10$ eV), the mean internal energy and fragmentation yield increase rapidly with the incident energy of individual constituents. Beyond 10 eV/atom impact (up to 40 eV/atom), the internal energy reaches a plateau and remains constant. Results were compared with those generated from bismuth cluster impacts and it turns out the mean internal energies obtained under keV bismuth cluster impacts correspond well to the plateau values for argon clusters. However, a big difference was found between argon and bismuth clusters concerning the damage or disappearance cross section. A distinctively small disappearance cross section of 4.44×10^{-15} cm^{-2} was measured under 20 keV Ar_{2000}^+ impact, which is more than 20 times smaller than that obtained under 25 keV Bi_5^+ bombardment, thus quantitatively showing the low damage effect of large argon clusters.

2.2 Introduction

Secondary ion mass spectrometry (SIMS) has been applied to analyze organic substances under static condition. That is, low primary ion dose ($<10^{13}$ ions/cm^2) has to be used to ensure that every impact is on an intact area to avoid sampling of damaged surfaces [1]. As a result, very small proportion of the surface material is sputtered and of which less than 1% is ionized [2], leading to very low secondary ion yield. Consequently, considerable efforts have been put into the development of more efficient polyatomic ion beams to increase sputter efficiency and secondary ion yield. Among the most widely exploited cluster ion beams, SF_6 neutral beam [3] and SF_5^+ ion beam [4] were demonstrated to greatly enhance secondary ion yield and reduce sample damage in characterizing organic polymers. The non-linear enhancement of secondary ion yields by Au_n^{q+} was reported by Benguerba *et al.* [5] and later Bi_n^{q+} by Touboul *et al.* [6], both of which have been intensively applied to molecular imaging ever since. In particular, much attention has been drawn to C_{60} ion beam since it became a routine ion source in TOF-SIMS [7]. C_{60} bombardment illustrates greatly enhanced secondary ion yields especially for molecular ions and significantly smaller damage cross section, which result in a number of applications in depth profiling and 3D imaging [8,9,10]. Nevertheless,

despite the secondary ion yield enhancement with the above cluster ion projectiles, the molecular damage caused by the energetic ion beams is still prominent and the largest intact molecules that can be detected in current TOF-SIMS is generally no bigger than 1000 Da. Thus, most of the time, analyses of biomolecules such as peptide and protein are simply precluded in current biological TOF-SIMS imaging.

A rather promising ion source is massive argon cluster ion beam. Gas cluster ion beam (GCIB) was initially developed by the Kyoto group for surface processing [11]. The utilization of large Ar clusters as primary ion beam on organics was first proposed by Ninomiya *et al.* [12,13] and was proved to be able to ionize amino acid and small peptide without causing fragmentation. Soon afterwards, detection of intact molecular ions of small proteins without using matrix was reported by Mochiji *et al.* [14] and Oshima *et al.* [15]. Moreover, multimers of amino acid molecules were also detected under impact of large argon cluster with low energy per atom [16]. These studies imply that a soft ionization process might take place under the impact. Large Ar clusters are typically composed of hundreds to thousands constitutes, resulting in extremely low energy per atom *E/n*. Thus, it is suggested that the soft sputtering associated with large Ar clusters is due to the low incident energy of the constitutional atoms arriving on the target. Those low energy projectiles induce a very short range of penetration into the solid material so that the energy is deposited within the first layers of surface without causing damage of the underneath layers. However, in general, the ionization/desorption of the analytes involved in such bombardment is still poorly understood.

We herein propose to study the ionization and fragmentation process in SIMS by examining the internal energy distribution of the secondary ions (SIs), namely the internal energy imparted to desorbed ions by projectiles during the impacts. Survival yield method was applied to measure internal energy distributions of SIs produced from argon and bismuth clusters bombardments, respectively. This approach has been used to determine the internal energy of species produced from fast atom bombardment (FAB) [17,18], matrix-assisted laser desorption/ionization (MALDI) [19], electrospray ionization (ESI) [20,21], which are well-recognized methods of “soft” ionization, as well as gold nanoparticle impact at high energy [22, 23]. Thus, the softness of the ionization process under massive argon cluster bombardment was evaluated and compared with small bismuth clusters.

2.3 Experimental

2.3.1 Sample preparation

Benzylpyridinium (BYP) salts were generously provided by Prof. D. Rondeau (Univ. de Bretagne Occidentale, Brest, France) except the *p*-cyanobenzylpyridinium salt which was purchased from Otava Chemicals Ltd. (Kyiv, Ukraine). They were separately prepared in MeOH/H_2O (1:1) and mixed together before TOF-SIMS analyses so that several BYP species could be analyzed at the same time. To simplify analyses of the mass spectra, *p*-CH_3, *p*-OCH_3, *p*-NO_2, *p*-Cl, *p*-F substituted BYP ion solutions were mixed together to form one solution, while *p*-CN, *m*-CH_3, *m*-OCH_3 substituted BYP ions and 1-benzylpyridinium were mixed to obtain another. This also permits to perform the measurements with the same projectiles under exactly the same condition of impact and detection efficiency. 0.5 µL of each mixed solution was deposited onto a gold plate and allowed to dry in air before being introduced into mass spectrometer.

2.3.2 TOF-SIMS analysis

All analyses were performed with a commercial TOF-SIMS IV (ION-TOF GmbH, Münster, Germany) mass spectrometer equipped with a bismuth liquid metal ion gun (LMIG) and argon gas cluster ion source (GCIS). In the present instrumental setup [24,25], Bi-LMIG is able to deliver pulsed and mass selected Bi_n (n = 1−7) ions with single or double charges. The Bi_n^{q+} ions were accelerated to kinetic energies of either 25 × q keV or 12.5 × q keV. The pulse durations of the primary ion beams were adjusted to keep a relatively low Poisson correction factor around or less than 1.1 so that saturation detection was negligible. Consequently, the target currents of the Bi_n^{q+} beams measured at 10 kHz were generally below 0.1 pA. All the primary ions were bunched for the sake of a good mass resolution of 5300 at *m/z* 204. The GCIB ion column could produce giant argon cluster ions of which the sizes vary from few hundreds up to 10000. A 90° pulsing system was used to generate short pulsed ion beams with a mass resolution of 60−120. Details about the performance of this setup have been described previously [26]. In this report, different beam energies were investigated: the 20 keV energy argon clusters were selected to study the size dependence of internal energy distribution of secondary ions because of the attainable wide range of argon cluster sizes and certain 10 keV, 15 keV and 20 keV argon clusters were selected to examine the influence of cluster size and energy at given velocities (*E/n* = 2 eV, 5 eV, 10 eV, 20 eV). The beam currents of argon cluster ions were typically below 0.05 pA at 10 kHz. The incident angle was 45° for both bismuth and argon cluster ion beams. Secondary ions were extracted into a single-stage reflectron-type analyzer with kinetic energies of 2 keV and then post-accelerated to 10 keV before reaching a hybrid detector composed of a single

microchannel plate followed by a scintillator and a photomultiplier. The electron floodgun was switched off during all the acquisitions because the low energy electrons could slightly overestimate the internal energy distribution.

Mass spectra of Bi_n^{q+} impacts were recorded on an area of 100 μm × 100 μm divided by 128 pixel × 128 pixel, with ion doses of 6×10^8–4×10^{10} ions/cm^2. Ar_n^+ bombardments were carried out on a larger area of 500 μm × 500 μm with ion doses lower than 8×10^8 ions/cm^2. Measurements of disappearance cross sections were performed on 100 μm × 100 μm areas with 128 × 128 pixels for each area. The employed ion doses depended on the decreasing slope of secondary ion intensity *versus* primary ion fluence and were about 10^{13} ions/cm^2 for Bi clusters and > 10^{14} ions/cm^2 for Ar clusters, respectively. The area integration of parent and fragment peaks was processed with SurfaceLab 6.5 (ION-TOF GmbH, Münster, Germany).

2.4 Results

2.4.1 Determination of internal energy distribution

The survival yield (SY) method for determination of internal energy distribution was described in detail by De Pauw et al. [27]. Briefly, a series of so-called thermometer ions with different dissociation energies are first analyzed to indicate the internal energy generated by the SIs during the ionization process. Then, survival yields of thermometer ions are calculated using the formula $SY = I(M^+) / [I(M^+) + I(F^+)]$, where M^+ is the molecular ion and F^+ the fragment, followed by plotting the SYs as a function of dissociation energies. Benzylpyridinium salts are ideal thermometer ions owing to their very similar structure, the well-known dissociation pathway leading to benzyl cation as the only detectable fragment, and calculated dissociation energies related to the property of substituent groups. In current case, two critical conditions are assumed: no parent ion remains (SY = 0) when the dissociation energy is zero and no fragment ions are produced (SY = 1) when the dissociation energy is 4 eV. Then the data points were fitted with a sigmoidal curve with fixed maximum SY of 1. Differentiating the sigmoidal curve gives the internal energy distribution of the desorbed thermometer ions. Five benzylpyridinium salts covering a wide range of dissociation energies were used for the measurement of internal energy distribution (Table 1). The dissociation energies employed here are calculated at CCSD(T)/BSII//B3LYP/BSI level which could provide more accurate values [22].

Table 1: Benzylpyridium ions used for the measurement of internal energy distribution.

R[a]	*m/z* (M^+)[b]	*m/z* (F^+)[c]	Dissociation E (eV) [22]
p-CH_3	184.11	105.07	2.267
p-OCH_3	200.11	121.06	1.840
p-NO_2	215.08	136.04	2.843
m-CH_3	184.11	105.07	2.417
H	170.10	91.05	2.500

[a] Substituent group of the BYP ions. [b] M^+ for molecular ion. [c] F^+ for fragment ion.

Figure 1 presents the survival yields generated from the 20 keV Ar_{500}^+ bombardments, where an overestimation of the survival yield of *p*-nitrobenzylpyridinium ion is observed after fitting the data points with a sigmoidal curve. This overestimation is probably due to the occurrence of an alternative fragmentation pathway apart from the typical one which goes through the lowest activation barrier (cleavage of C-N bond in benzylpyridine). Indeed, in the corresponding mass spectrum (Figure 1b), the ion at *m/z* 169.1 which can be assigned to $C_{12}H_{11}N^+$ is very likely another fragment of *p*-NO_2 BYP ion [28]. However, *p*-nitrobenzylpyridinium ion represents the "tough" thermometer ions with high critical energies which could provide very high SY value and contribute to the sigmoidal fitting. Thus the survival yield of *p*-NO_2 BYP ion is retained for the internal energy distribution calculation since same experimental conditions will be applied to all the projectiles and precise measurement is not pursued here. It is noted that this overestimation effect can be neglected when the incident velocity is low ($E/n < 4$ eV), whereas from $E/n > 5$ eV, the sigmoidal fit and distribution width can be slightly modified.

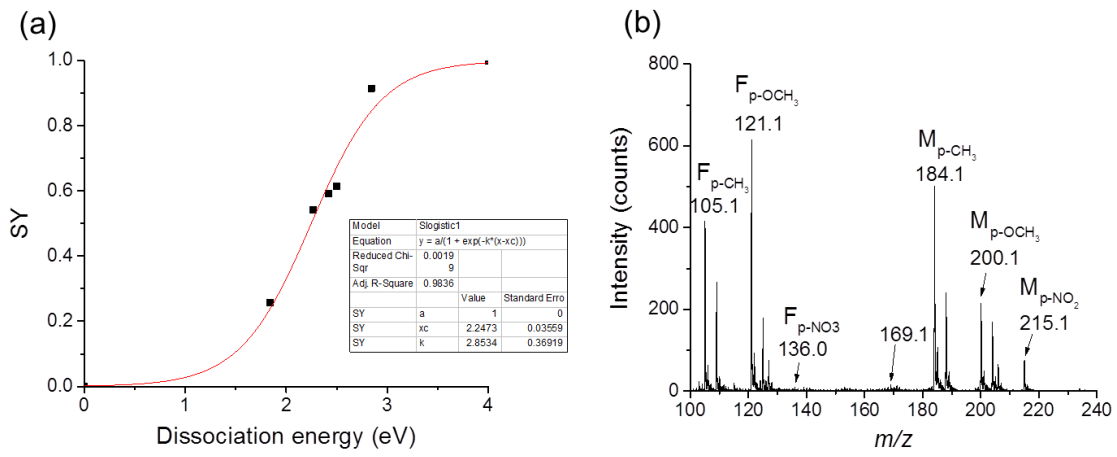

Figure 1: (a) Survival yields of five benzylpyridium ions obtained from 20 keV Ar_{500}^{+} bombardments, plotted as a function of dissociation energy. (b) Mass spectrum of a mixture of *p*-CH_3, *p*-OCH_3, *p*-NO_2, *p*-Cl, *p*-F substituted BYP ions acquired under the bombardment of 20 keV Ar_{500}^{+} ions.

2.4.2 Internal energy distribution of thermometer ions under argon cluster bombardment

In current TOF-SIMS instrumentation, the attainable argon cluster size ranges from few hundreds up to 10000, thus enabling the examination a wide range of cluster ions. At a fixed kinetic energy of 20 keV, argon clusters with cluster sizes of 500−10000 were investigated to establish the influence of cluster size on the internal energy distributions of thermometer ions. The derived plots shown in Figure 2 suggest that the cluster size of impacting argons plays an important role in the internal energy distribution. An obvious shift of internal energy distribution towards lower energy is observed as the cluster size increases. In addition, the narrow distributions at lower energy range generated from bombardments of giant clusters especially when n = 10000 in the present work indicate a softer ionization process compared with smaller cluster bombardments. The broad distributions of SIs under impacts of Ar_{3000}^{+} and Ar_{4000}^{+} are possibly due to the modification of sigmoidal fit by the data point from *p*-NO_2 BYP ion. Representative mass spectra recorded under impacts of 20 keV Ar_n^{+} clusters with different sizes (n = 500, 1000, 2000, 4000, 6000 and 8000) are illustrated in Figure 3. It is demonstrated that the relative intensity of fragment ions decreases gradually when increasing the number of constitutional atoms in the argon clusters, which means less fragmentation occurs under larger cluster impacts. Meanwhile, the peak width increases with the cluster size, implying a broader kinetic energy distribution of the SIs under the bombardment of larger cluster ions. The drop in the ion intensity is due to the decrease of primary ion intensity as the cluster size increases.

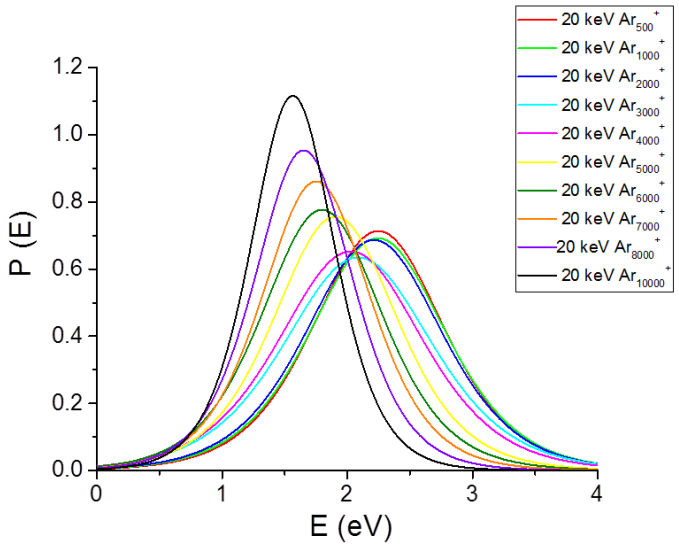

Figure 2: Internal energy distributions of SIs under impact of 20 keV argon clusters.

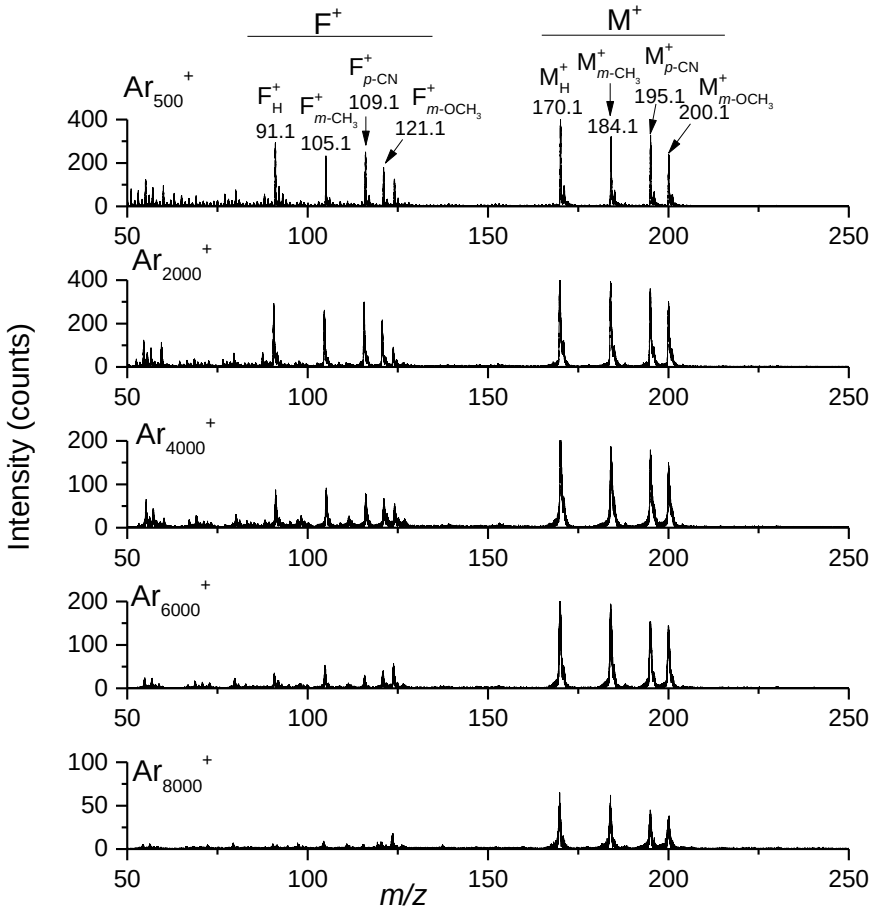

Figure 3: Mass spectra of thermometer ions under impact of 20 keV argon clusters of different cluster sizes. F^+: Fragment ions; M^+: Molecular ions.

Apart from cluster size, another relevant parameter that characterizes a cluster ion beam is energy per atom *E/n* which stands for the velocity of the clusters. Since the internal energy measured with survival yield method presents the internal energy imparted to the desorbed molecular ions by the projectiles during bombardments, the internal energy distribution can be affected by both impact energy of individual constituents *E/n* and total energy E. Therefore, to determine the decisive factors account for internal energy distribution, argon clusters with different total kinetic energies and cluster sizes were investigated. Figure 4 displays the internal energy distributions of SIs under impact of argon clusters with *E/n* of 2 eV, 5 eV, 10 eV and 20 eV, respectively. Interestingly, it is revealed that the argon clusters which share the same velocity but carry different energies and constitutional numbers result in approximately the same distribution. This observation indicates that the internal energy distribution mainly depends on the *E/n* of the clusters, independent of the total kinetic energy and cluster size. The variation in the distribution width shown in Figure 4a is probably due to the cluster distribution of the selected ion beams. It is worth noticing that the average internal energy of the thermometer ions increases with the impact velocity, from 1.56 eV generated under 2 eV/atom impact to 2.24 eV under 20 eV/atom impact.

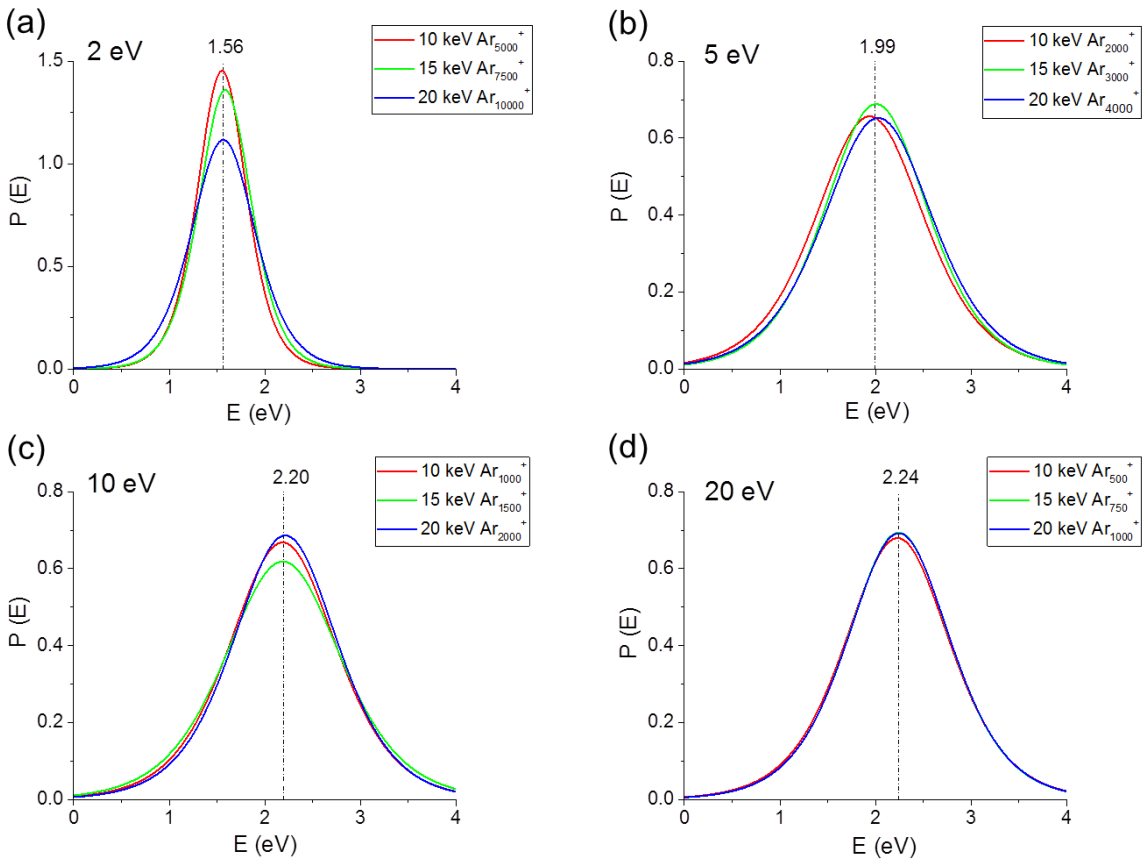

Figure 4: Internal energy distributions under impact of argon clusters with different total kinetic energy and cluster sizes but same velocities (energy per atom *E/n*): a: *E/n* = 2 eV; b: *E/n* = 5 eV; c: *E/n* = 10 eV; d: *E/n* = 20 eV.

In order to establish the influence of incident velocity on the internal energy distribution of SIs under argon cluster bombardments, we then plotted the mean internal energy as a function of energy per atom *E/n* of the 20 keV argon clusters. As shown in Figure 5, below *E/n* = 10 eV, the internal energy increase rapidly as the energy per atom increases. While for *E/n* > 10 eV, the mean internal energy of the SIs stays more or less constant in spite of the increasing incident energy. The raise of internal energy at low velocity impact can be easily explained by the increase in energy deposition when clusters with higher *E/n* hit the target, whereas the plateau observed at high impinging energy can be reasoned to result from dissipation of the projectile energy and only certain amount of the energy caused effective sputtering and energy transfer processes.

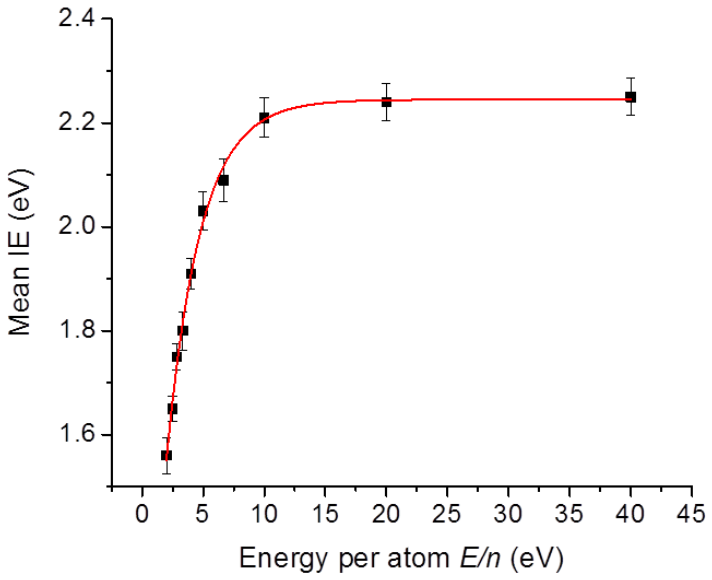

Figure 5: Mean internal energy (IE) of the secondary ions as a function of the energy per atom (*E/n*) of 20 keV argon clusters.

Examination of secondary ion yield under the low *E/n* impact is illustrated by *p*-OCH_3 BYP ion in Figure 6. The lowest energy per atom investigated here is 2.5 eV which is still able to afford an effective sputtering process providing an ion yield of 1.18×10^{-2} for the molecular ion (Figure 6a). This may partly benefit from the readily charged target molecular ions, while it is more likely due to the enhancement effect of cluster ions. The low energy but extremely dense impacts cause more efficient sputtering than individual atoms. It is noted that effective sputtering was also observed under impact of clusters with *E/n* = 2.0 eV (20 keV Ar_{10000}^{+}). However, the cluster ion current was too low to afford an accurate value of secondary ion yield.

Figure 6 also demonstrates that the molecular ion yield of *p*-OCH_3 BYP ion decrease rapidly as *E/n* increases from 2.5 to 10 eV while the fragment ion yield exhibits an opposite trend, indicating an increase of fragmentation extent as the impact velocity increases. Nevertheless, the decrease of molecular ion yield may also be partly due to the metastable decay occurred during the flight to the detector [29]. In the case of *p*-OCH_3 BYP ion which has very low dissociation energy, the sum of molecular and fragment ion yields is revealed to be generally constant irrespective of the *E/n* of the impacting clusters (Figure 6c), whereas for the thermometer ions with higher dissociation energies, the fragment ion yields are so low that the plots of summed ion yields versus *E/n* are governed basically by the behavior of molecular ions. The dependence of fragment ion intensity/molecular ion intensity ratio on the energy per atom is in line with the plot depicting mean internal energy as a function of *E/n* of

the argon clusters. It is worth noticing that all the 10 keV, 15 keV and 20 keV argon clusters with same energy per atom gave very similar ion yield values, demonstrating the beam velocity dependence of the secondary ion yields.

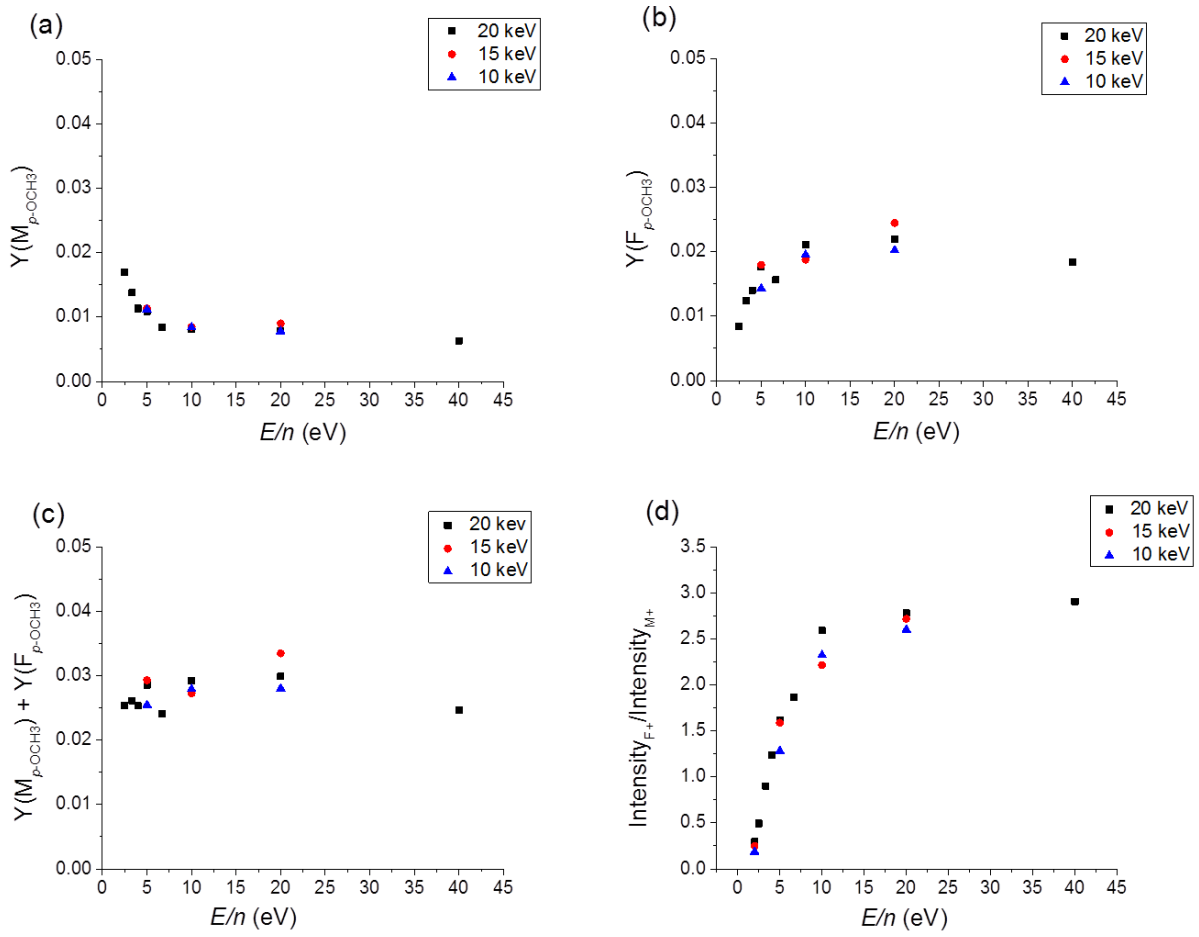

Figure 6: Influence of energy per atom *E/n* of argon clusters on the ion yield of (a) *p*-OCH_3 BYP molecular ion ($M_{p\text{-}OCH3}$), (b) *p*-OCH_3 BYP fragment ion ($F_{p\text{-}OCH3}$), (c) sum of $M_{p\text{-}OCH3}$ and $F_{p\text{-}OCH3}$, and (d) relative intensity of *p*-OCH_3 fragment ion ($F_{p\text{-}OCH3}$) over molecular ion ($M_{p\text{-}OCH3}$).

2.4.3 Internal energy distribution of secondary ions under bismuth cluster bombardment

With the same instrumental configuration as employed in preceding investigations, internal energy distributions of SIs under small bismuth cluster impacts were examined for comparison. Figure 7 displays the internal energy distributions of thermometer ions under 25 keV or 50 keV Bi_n^{q+} cluster bombardments. It is revealed that the internal energy distributions obtained from different bismuth clusters are more or less similar in terms of both the mean internal energy and the width of the distribution. Further examination of Bi_n^{q+} ion beam accelerated by 12.5 kV voltage gave nearly identical results with a mean internal

energy of 2.2−2.4 eV (Table 2). Rather surprising at first thought that the internal energy imparted from Bi clusters to the SIs is independent of the beam energy, however, this finding is in consistent with the results from high energy per atom (E/n > 10 eV) argon cluster impacts where the mean internal energy remains constant at ~ 2.24 eV. Since the energy per atom of the examined Bi clusters is far beyond 10 eV, all the data points shall fall onto the plateau and provide similar mean internal energy.

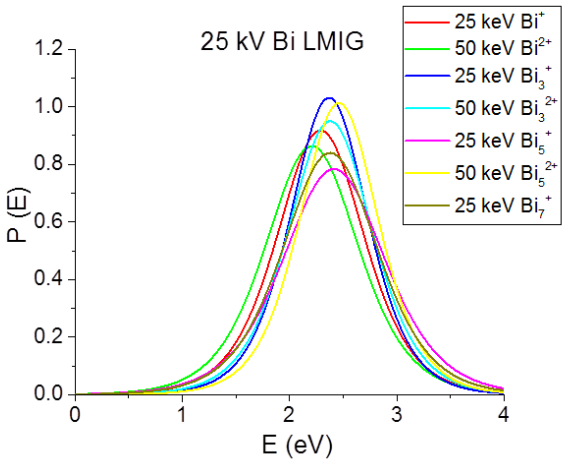

Figure 7: Internal energy distribution of thermometer ions under impacts of Bi_n^{q+} clusters with kinetic energies of 25 keV (q = 1) and 50 keV (q = 2).

Table 2: Mean internal energies (IE) obtained for different Bi clusters with accelerating voltages of 25 kV and 12.5 kV, respectively.

Primary ion	Mean IE (eV)	
	25 kV	12.5 kV
Bi^+	2.29 ± 0.02	2.33 ± 0.01
Bi^{2+}	2.21 ± 0.02	2.24 ± 0.01
Bi_3^+	2.37 ± 0.01	2.37 ± 0.02
Bi_3^{2+}	2.38 ± 0.02	2.45 ± 0.03
Bi_5^+	2.41 ± 0.04	2.34 ± 0.03
Bi_5^{2+}	2.46 ± 0.03	2.39 ± 0.02
Bi_7^+	2.38 ± 0.03	2.31 ± 0.02

2.4.4 Secondary ion yield, disappearance cross section and ion efficiency under bismuth and argon cluster bombardments

To further understand the low energy impact of massive argon clusters, several values such as secondary ion emission yields *Y*, disappearance cross section σ and secondary ion efficiency *E* (defined as *Y*/σ) obtained under argon cluster bombardment were compared with those from small bismuth cluster bombardments. The definitions and determination of those values have been comprehensively described elsewhere [24,30]. Table 3 summarizes the cluster species and the corresponding *Y*, σ, *E*, and mean internal energy (IE) values generated for *p*-OCH_3 BYP ion. It should be noted that only one argon cluster species is investigated here, due to the significantly small damage cross section which leads to the requirement of extremely long acquisition time to observe the decrease of ion intensity. Upon comparison, it is revealed that the secondary ion yields obtained under 20 keV Ar_{2000}^+ cluster impact are of the same order of magnitude as those measured from bismuth cluster impacts. Meanwhile, although there is a dramatic difference in energy per atom between bismuth cluster (keV regime) and argon cluster (eV regime), the amount of energy transferred to the analytes

during the bombardments proves to be very similar. However, it is worth noticing that the disappearance cross section for large argon cluster bombardment (4.44×10^{-15} cm^2) is over 20 times smaller than that for 25 keV Bi_5^+ cluster bombardment (9.17×10^{-14} cm^2), resulting in a much higher secondary ion efficiency of 3.47×10^{12} cm^{-2}. These values directly show that large argon cluster sputtering induce greatly reduced sample damage, consistent with previous comparison studies with C_{60}^+ projectile [31,32].

Table 3: Yields *Y*, disappearance cross section σ, secondary ion efficiency *E* and mean internal energy IE generated for *p*-methylbenzylpyridinium ion (*m/z* 184.11) under bismuth and argon clusters bombardments.

Voltage	PI	Current (@100 µs)	*Y*	σ (cm^2)	*E* (cm^{-2})	Mean IE (eV)
25 kV	Bi^+	0.330 pA	5.49×10^{-4}	3.87×10^{-14}	1.42×10^{10}	2.29 ± 0.02
	Bi^{2+}	0.184 pA	4.52×10^{-3}	3.03×10^{-14}	1.49×10^{11}	2.21 ± 0.02
	Bi_3^+	0.022 pA	4.40×10^{-2}	1.62×10^{-13}	2.72×10^{11}	2.37 ± 0.01
	Bi_3^{2+}	0.012 pA	6.02×10^{-2}	2.58×10^{-13}	2.34×10^{11}	2.38 ± 0.02
	Bi_5^+	0.028 pA	2.55×10^{-2}	9.17×10^{-14}	2.78×10^{11}	2.41 ± 0.04
	Bi_5^{2+}	0.026 pA	4.18×10^{-2}	7.38×10^{-14}	5.66×10^{11}	2.46 ± 0.03
	Bi_7^+	0.006 pA	4.48×10^{-2}	1.11×10^{-13}	4.04×10^{11}	2.38 ± 0.03
20 kV	Ar_{2000}^+	0.05 pA	1.54×10^{-2}	4.44×10^{-15}	3.47×10^{12}	2.21 ± 0.04

2.5 Discussion

Driven by the benefit of soft ionization in biomolecule analysis, a few experimental studies [12,13,16] as well molecular dynamic simulations [33,34,35] have been carried out to determine the effect of cluster size on the molecular ion production. In accordance with previous reports about argon cluster bombardments on amino acid species, the present work shows that increasing the number of constituents in the argon cluster could effectively reduce fragmentation of the organic molecules to an extent that very few or no fragment ions are present in the mass spectra (Figure 3). As a result, the mass spectra become much simpler and in some extent could better reveal the chemical information of the samples. However, it has also been shown that the secondary ion yield decrease distinctively within a certain *E/n*. In

particular, Gnaser *et al.* [16] have demonstrated that the molecular intensities of amino acids are relatively constant beyond E/n = 10 eV while drop dramatically in the low energy regime (E/n < 10 eV). This phenomenon was tentatively explained by the decrease in the number of free protons produced during the bombardment, thus reducing the protonation of sputtered molecules. In other words, the molecular ion production is mainly determined by the ionization efficiency under low energy impact. This assumption is confirmed by our observation that the ion yield of thermometer ions decrease with E/n of the impinging projectiles. Since there is almost no ionization barrier for the thermometer ions (BYP cations), the fragmentation will takes place as soon as the received internal energy exceeds the dissociation energy, leading to the decrease of molecular ion yield.

Internal energy represents the internal energy generated by SIs under the bombardment and determines the fragmentation extent of the molecules. Therefore, examination of internal energy distributions of the thermometer ions could evaluate the softness of the ionization process of cluster bombardments. Results show that larger argon clusters (E/n < 5 eV) give lower and narrower internal energy distributions, implying a softer ionization process (Figure 2 and 4). The plot of internal energy *versus* the energy per atom of argon clusters shown in Figure 5 indicates that the fragmentation increases with the incident energy of individual constituents when E/n is less than 10 eV, whereas a saturation state arises with E/n exceeding 10 eV. Similar threshold value was observed experimentally [16] as well as in MD simulations where a relatively higher value of 15−20 eV was predicted [35]. While such saturation phenomenon is not yet well understood, it may however be due to increase of energy dissipation under higher energy impact as in the case of C_{60} projectiles [36]. Therefore, only the projectile energy deposited in a certain volume could contribute to this energy transfer. Thus, it can be concluded that for organic sputtering by large argon clusters, soft ionization could be realized under impact of large argon clusters with E/n < 5 eV. Below 10 eV, fragmentation increases rapidly with E/n before arriving at a saturation state when E/n > 10 eV.

Under keV bismuth cluster impacts, all the Bi_n^{q+} species gave similar internal energy distributions with mean internal energy values close to those obtained under E/n > 10 eV argon cluster impact, underlying a similar saturation phenomenon of the fragmentation. Therefore, the relatively constant mean internal energy values obtained from bismuth cluster impact might correspond to the plateau part in the plot shown in Figure 5 and this plot may possibly present the universal behavior of the cluster impact in TOF-SIMS. However, further investigation of a wider range of projectiles will be required to verify this hypothesis.

2.6 Conclusion

The energy deposition during large argon cluster bombardment is addressed by measuring the internal energy distribution of the desorbed SIs, which represents the fragmentation extent or softness of the ionization process of cluster impact. Impacting energy of individual argon atoms in the cluster is found to be the decisive factor of internal energy distribution of secondary ions. In the investigated energy regime (2.0−40 eV), very few fragmentation takes place (soft ionization) for $E/n < 5$ eV; below 10 eV/atom impact, fragmentation increases dramatically as an increasing amount of energy being imparted to the SIs. When the impacting energy exceeds 10 eV/atom, fragmentation of the molecules reaches a saturation state. The high energy bombardments of small bismuth clusters give generally constant mean internal energies which may correspond to the saturation state of fragmentation as observed with argon cluster impacts. In addition, compared with bismuth clusters, argon cluster impact provides similar secondary ion yield but much higher secondary ion efficiency owing to the significantly smaller disappearance cross section.

2.7 Acknowledgements

This work was supported by the Agence Nationale de la Recherche (grant ANR-2015-CE29-0007-01 DEFIMAGE). TF would like to acknowledge financial support from China Scholarship Council (CSC, No. 201406310013).

Reference

[1] Benninghoven, A.; Jaspers, D.; Sichtermann, W. Secondary-ion emission of amino acids. *Applied Physics* **1976**, *11*, 35-39.

[2] Benninghoven, A.; Hagenhoff, B.; Niehuis, E. Surface MS: probing real-world samples. *Anal. Chem.* **1993**, *65*, 630–640A.

[3] Appelhans, A. D.; Delmore, J. E.; Dahl, D. A. Focused, rasterable, high-energy neutral molecular beam probe for secondary ion mass spectrometry. *Analytical Chemistry* **1987**, *59*, 1685–1691.

[4] Gillen, G.; Roberson, S. Preliminary evaluation of an SF_5 polyatomic primary ion beam for analysis of organic thin films by secondary ion mass spectrometry. *Rapid Communication in Mass Spectrometry* **1998**, *12*, 1303–1312.

[5] Benguerba, M.; Brunelle, A.; Della-Negra, S.; Depauw, J.; Joret, H.; Le Beyec, Y.; Blain, M. G.; Schweikert, E. A.; Ben Assayag, G.; Sudraud, P. Impact of slow gold cluster on

various solids: nonlinear effects in secondary ion emission. *Nuclear Instruments and Methods in Physics Research B* **1991**, *62*, 8–22.

[6] Touboul, D.; Kollmer, F.; Niehuis, E. Brunelle, A.; Laprévote, O. Improvement of biological time-of-flight-secondary ion mass spectrometry imaging with a bismuth cluster ion source. *Journal of American Society for Mass Spectrometry* **2005**, *16*, 1608–1618.

[7] Weibel, D.; Wong, S.; Lockyer, N.; Blenkinsopp, P.; Hill, R.; Vickerman, J. C. A C_{60} primary ion beam system for time of flight secondary ion mass spectrometry: Its development and secondary ion yield characteristics. *Analytical Chemistry* **2003**, *75*, 1754–1764.

[8] Fletcher, J. S.; Lockyer, N. P.; Vickerman, J. C. Developments in molecular SIMS depth profiling and 3D imaging of biological systems using polyatomic primary ions. *Mass Spectrometry Reviews* **2011**, *30*, 142–174.

[9] Robinson, M. A.; Graham, D. J.; Castner, D. G. ToF-SIMS depth profiling of cells: z-correction, 3D imaging, and sputter rate of individual NIH/3T3 fibroblasts. *Analytical Chemistry* **2012**, *84*, 4880−4885.

[10] Tian, H.; Six, D. A.; Krucker, T.; Leeds, J. A.; Winograd, N. Subcellular chemical imaging of antibiotics in single bacteria using C_{60}-secondary ion mass spectrometry. *Analytical Chemistry* **2017**, *89*, 5050−5057.

[11] Yamada, I.; Matsuo, J.; Toyoda, N.; Kirkpatrick, A. Materials processing by gas cluster ion beams. *Materials Science and Engineering R* **2001**, *34*, 231–295.

[12] Ninomiya, S.; Nakata, Y.; Ichiki, K.; Seki, T.; Aoki, T.; Matsuo, J. Measurements of secondary ions emitted from organic compounds bombarded with large gas cluster ions. *Nuclear Instruments and Methods in Physics Research B* **2007**, *256*, 493–496.

[13] Ninomiya, S.; Nakata, Y.; Honda, Y.; Ichiki, K.; Seki, T.; Aoki, T.; Matsuo, J. A fragment-free ionization technique for organic mass spectrometry with large Ar cluster ions. *Applied Surface Science* **2008**, *255*, 1588–1590.

[14] Mochiji, K.; Hashinokuchiy, M.; Moritani, K.; Toyoda, N. Matrix-free detection of intact ions from proteins in argon-cluster secondary ion mass spectrometry. *Rapid Communications in Mass Spectrometry* **2009**, *23*, 648–652.

[15] Oshima, S.; Kashihara, I.; Moritani, K.; Inui, N.; Mochiji, K. Soft-sputtering of insulin films in argon-cluster secondary ion mass spectrometry. *Rapid Communications in Mass Spectrometry* **2011**, *25*, 1070–1074.

[16] Gnaser, H.; Ichiki, K.; Matsuo, J. Strongly reduced fragmentation and soft emission processes in sputtered ion formation from amino acid films under large Ar_n^+ ($n \leq 2200$) cluster ion bombardment. *Rapid Communications in Mass Spectrometry* **2012**, *26*, 1–8.

[17] De Pauw, E.; Pelzer, G.; Marien, J.; Natalis, P. Internal energy distribution of ions emitted in secondary ion mass spectrometry. *Springer Proceedings in Physics* **1986**, *9*, 103–108.

[18] Derwa, F.; De Pauw, E.; Natalis, P. New basis for a method for the estimation of secondary ion internal energy distribution in 'soft' ionization techniques. *Organic Mass Spectrometry* **1991**, *26*, 117–118.

[19] Luo, G.; Marginean, I.; Vertes, A. Internal energy of ions generated by matrix-assisted laser desorption/ionization. *Analytical Chemistry* **2002**, *74*, 6185–6190.

[20] Collette, C.; De Pauw, E. Calibration of the internal energy distribution of ions produced by electrospray. *Rapid Communications in Mass Spectrometry* **1998**, *12*, 165–170.

[21] Touboul, D.; Jecklin, M. C.; Zenobi, R. Ion internal energy distributions validate the charge residue model for small molecule ion formation by spray methods. *Rapid Communications in Mass Spectrometry* **2008**, *22*, 1062–1068.

[22] DeBord, J. D.; Verkhoturov, S. V.; Perez, L. M.; North, S. W.; Hall, M. B.; Schweikert, E. A. Measuring the internal energies of species emitted from hypervelocity nanoprojectile impacts on surfaces using recalibrated benzylpyridinium probe ions. *The Journal of Chemical Physics* **2013**, *138*, 214301.

[23] DeBord, J. D.; Fernandez-Lima, F. A.; Verkhoturov, S. V.; Schweikert, E. A.; Della-Negra, S. Characteristics of positive and negative secondary ions emitted from Au_3^+ and Au_{400}^{+4} impacts. *Surface and Interface Analysis* **2013**, *45*, 134–137.

[24] Brunelle, A.; Touboul, D.; Laprévote, O. Biological tissue imaging with time-of-flight secondary ion mass spectrometry and cluster ion sources. *Journal of Mass Spectrometry* **2005**, *40*, 985–999.

[25] Touboul, D.; Kollmer, F.; Niehui, E.; Brunelle, A.; Laprévote, O. Improvement of biological time-of-flight secondary ion mass spectrometry imaging with a bismuth cluster ion source. *Journal of the American Society for Mass Spectrometry* **2005**, *16*, 1608–1618.

[26] Kayser, S.; Rading, D.; Moellers, R.; Kollmer, F.; Niehuis, E. Surface spectrometry using large argon clusters. *Surface and Interface Analysis* **2013**, *45*, 131–133.

[27] Gabelica, V.; De Pauw, E. Internal energy and fragmentation of ions produced in electrospray sources. *Mass Spectrometry Reviews* **2005**, *24*, 566–587.

[28] Barylyuk, K. V.; Chingin, K.; Balabin, R. M.; Zenobi, R. Fragmentation of Benzylpyridinium "Thermometer" Ions and Its Effect on the Accuracy of Internal Energy Calibration. *Journal of the American Society for Mass Spectrometry* **2010**, *21*, 172–177.

[29] Luxembourg, S. L.; Heeren, R. M. A. Fragmentation at and above surfaces in SIMS: Effects of biomolecular yield enhancing surface modifications. *International Journal of Mass Spectrometry* **2006**, *253*, 181–192.

[30] Kötter, F.; Benninghoven, A. Secondary ion emission from polymer surfaces under Ar^+, Xe^+ and SF_5^+ ion bombardment. *Applied Surface Science* **1998**, *133*, 47–57.

[31] Rabbani, S.; Barber, A. M.; Fletcher, J. S.; Lockyer, N. P.; and Vickerman, J. C. TOF-SIMS with Argon Gas Cluster Ion Beams: A Comparison with $C60^+$. *Analytical Chemistry* **2011**, *83*, 3793–3800.

[32] Shard, A. G.; Havelund, R.; Seah, M. P.; Spencer, S. J.; Gilmore, I. S.; Winograd, N.; Mao, D.; Miyayama, T.; Niehuis, E.; Rading, D.; Moellers, R. Argon cluster ion beams for organic depth profiling: results from a VAMAS interlaboratory study. *Analytical Chemistry* **2012**, *84*, 7865−7873.

[33] Rzeznik, L.; Czerwinski, B.; Garrison, B. J.; Winograd, N.; Postawa, Z. Molecular dynamics simulations of sputtering of organic overlayers by slow, large clusters. *Applied Surface Science* **2008**, *255*, 841–843.

[34] Rzeznik, L.; Czerwinski, B.; Garrison, B. J.; Winograd, N.; Postawa, Z. Microscopic insight into the sputtering of thin polystyrene films on Ag{111} induced by large and slow Ar clusters. *Journal of Physical Chemistry C* **2008**, *112*, 521–531.

[35] Delcorte, A.; Garrison, B. J.; Hamraoui, K. Dynamics of molecular impacts on soft materials: from fullerenes to organic nanodrops. *Analytical Chemistry* **2009**, *81*, 6676–6686.

[36] Russo, M. F.; Garrison, B. J. Mesoscale energy deposition footprint model for kiloelectronvolt cluster bombardment of solids. *Analytical chemistry* **2006**, *78*, 7206–7210.

Chapter 3 Tandem MS imaging and *in situ* identification of bioactive wood metabolites in Amazonian tree species *Sextonia rubra*

3.1 Abstract

The use of ionic column with new cluster ion sources (e.g. Bi_3^+, Au_3^+, C_{60}^+ and Ar_n^+) in TOF-SIMS (Time of Flight-Secondary Ion Mass Spectrometry) has led to a great improvement in molecular signals and permits to map chemical distribution on various biological samples. However, further biological applications are severely hampered by the lack of tandem MS capability for structural characterization, which is crucial when it comes to molecules identification in complex biological samples. Driven by this necessity, a new TOF-SIMS parallel imaging MS/MS spectrometer has been recently developed by Physical Electronics. In this report, the superior MS/MS spectrometric and imaging capability of this new development for natural product study was demonstrated for the first time through *in situ* identification of bioactive metabolites rubrynolide and rubrenolide in Amazonian tree species *Sextonia rubra* (Lauraceae). Despite the low abundance of the metabolites in the wood sample, unambiguous identification of these molecules has been achieved with high efficient MS/MS analysis. In addition, tandem MS imaging minimizes mass interferences and reveals specific localization of these metabolites in ray parenchyma cells, providing important new insight into their biosynthetic production within plant tissues.

3.2 Introduction

Biological TOF-SIMS imaging has undergone rapid advances in the last two decades. This is principally due to the development of various cluster ion beams which have brought multiple benefits including substantial ion yield enhancement by Au_3 [1,2], Bi_3 [3,4], and particularly buckminsterfullerene C_{60} [5] and large argon cluster [6]; extended mass range up to 10 kDa [7,8]; submicrometer imaging resolution in routine analyses [9,10]; as well as capability of three dimensional analysis [11]. Nevertheless, it remains undoubtable that current mass spectrometry imaging analysis of biological samples is still dominated by matrix-assisted laser desorption ionization (MALDI) technique [12]. Besides the inferior ability in generating high mass range spectra, a major limitation in TOF-SIMS is the lack of structural analysis for ion peak annotation [13]. Moreover, mass accuracy in TOF-SIMS is limited by the kinetic energy and emission angle distributions of the desorbed ions [14], which makes unambiguous assignments extremely challenging. Consequently, tandem mass spectrometry is highly desired for molecular identification, especially in the case of biological samples with complex chemical environment.

An early attempt of performing tandem mass spectrometry measurement with TOF-SIMS was achieved by Touboul, *et al.* using post source decay (PSD)-like method [15]. Here no collision cell was integrated and the fragmentation spectrum depended on the metastable

decomposition of the selected precursor ions. Based on a commercial hybrid-quadrupole orthogonal TOF mass spectrometer, Carado, *et al.* [16,17] developed a hybrid MALDI/C_{60}-SIMS which was capable to provide CID fragmentation and relative high mass resolution of 12 000-15 600 with a moderate lateral resolution of 25-30 µm. This hybrid system was later improved by Lanni, *et al.* [18] to image complex biological samples at 10 µm lateral resolution. Meanwhile, the Vickerman group designed the J105 3D Chemical Imager which exploited a linear buncher-TOF and a quasi-continuous C_{60} primary ion beam [19,20]. The new dedicated instrument offers MS/MS and high throughput cell imaging capabilities [21], and has recently been applied to identify intact lipids in *Drosophila* brain using argon cluster ion source [22]. More recently, Smith, *et al.* reported the coupling of C_{60} SIMS source to a FTICR mass spectrometer which allows MS/MS capability with excellent mass resolution (> 100,000, $m/\Delta m$ 50%) and mass accuracy (< 2 ppm) [23].

Different from the above instrumental concept pursuing conventional tandem fragmentation by sacrificing all the other irrelevant ions, the recent design of a new TOF-SIMS parallel imaging MS/MS spectrometer by Fisher and coauthors [24,25], in contrast, enables parallel and lossless collection of MS and MS/MS spectra. This attribute ensures that any analytical volume of the sample would be used to the best. The parallel imaging MS/MS prototype spectrometer is based on the triple ion focusing time-of-flight (TRIFT) analyzer where a precursor selection device allows the selection of the precursor ions with a window of about 1 Da. Furthermore, this system is fully comparable with conventional TOF-SIMS instruments in terms of sample handling, ion source operation and lateral resolution limit which proved to be problematic in other cases [23,26].

As a further exploration of the analytical potential of this new technology, we herein report the application of the tandem MS imaging technique in *in situ* identification of plant metabolites in Amazonian tree species *Sextonia rubra* (Mez) van der Werff (Lauraceae) [27]. In the search of natural products of interest, *S. rubra* is a relevant model, of which the heartwood contains two major bioactive secondary metabolites rubrenolide (**1**) and rubrynolide (**2**) (Figure 1) [28]. Rubrynolide shows particularly potent termiticidal activity [29] while both rubrenolide and rubrynolide exhibit activity against pathogenic fungi [30] and mosquito larvae [31]. These bioassays suggest that that these two compounds play a key role in heartwood resistance against wood destroying organisms [32]. Therefore, the *in situ* structural identification will help to better understand the production of these metabolites within plant tissues, which might further contribute to the elucidation of their biosynthetic pathways.

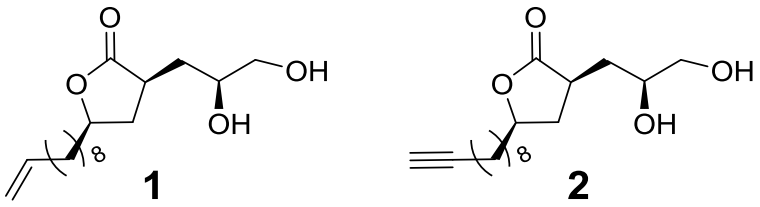

Figure 1: Structures of rubrenolide **1** and rubrynolide **2**.

3.3 Experimental

3.3.1 Plant material

Samples were collected from a *S. rubra* adult tree in the Paracou forest in French Guiana (5°15' N, 52°55'W) in December 2015. Wood increment cores were taken at breast height and stored in freeze condition (-18 °C) until experimentations (TOF-SIMS and extraction of the compounds). Each increment core contains both sapwood and heartwood which were separated when performing the extraction and ultramicrotoming.

3.3.2 Isolation of rubrenolide and rubrynolide

For extraction and isolation of chemical species, the wood sample was collected from commercial forest waste and identified by professional forest prospectors. Wood materials were ground into small particles of 0.5 mm in a Retsch ZM 200 mill (Oise, France). Extraction of the chemical species from the *S. rubra* heartwood was performed according to previously described procedures [30]. Briefly, 200 g of wood were extracted three times at room temperature for 48 h with ethyl acetate (3 × 500 mL). The ethyl acetate extract was then purified by column chromatography (EtOAc). Isolation of heartwood compounds rubrynolide and rubrenolide was carried out with 40 mg of the purified fraction diluted in 1.5 mL of water/acetonitrile 50:50 using a linear gradient of water/acetonitrile (50:50 to 0:100 over 15 min) and remaining at 100% acetonitrile during 5 min. The eluates from the column were monitored at 210 and 240 nm, and the chromatographic profiles confirmed with ELSD detection in analytical mode using the same solvent method at 1 mL/min. Fractions containing the same constituents were gathered and evaporation allowed for isolation of compounds rubrynolide (14.1 mg, 35.2% w/w) rubrenolide (8.1 mg, 20.2% w/w). Both compounds were isolated in pure form.

3.3.3 LC-MS analysis

Purified rubrenolide and rubrynolide were prepared in methanol at a concentration of 0.1 mg/mL. LC-MS/MS experiments were performed on a HPLC Ultimate 3000 system (Dionex, Voisins-le-Bretonneux, France) coupled with an Agilent 6540 Q-ToF (Agilent Technologies, Waldbronn, Germany) mass spectrometer equipped with electrospray ion

source. LC analysis was carried out in an Accucore RP-MS column (100 × 2.1 mm, 2.6 µm, Thermo Scientific, Courtaboeuf, France) with a mobile phase consisting of water (A) and acetonitrile (B). 0.1% formic acid was added to both phases. Compounds were eluted at a flow rate of 0.4 mL/min with a gradient from 5 %B to 100% B in 25 min and then 100% B for 3 min. All the mass spectra were recorded in positive ion mode with the following parameters: spray voltage set at 3.5 kV, capillary temperature at 325 °C, capillary voltage at 45 V and fragmentor voltage at 120 V. The collision energy was fixed at 15 eV for MS/MS fragmentation. Internal calibration was achieved with two calibrants (*m/z* 121.0509 and *m/z* 922.0098) providing a high mass accuracy better than 2 ppm. Mass resolution (FWHM, full width at half maximum) was chosen at 20,000 for *m/z* 922 in MS and MS/MS spectra.

3.3.4 Wood surface preparation

The transition zone area of a wood increment core was first cut off by an electric saw. The small wood block (~ 0.7 cm × 0.7 cm × 0.7 cm) was then trimmed with a razor blade to generate a transverse cutting surface of approximately 1 mm × 2.5 mm which was left to be cut with ultramicrotome (EM UC6, Leica Microsystèmes, SAS, Nanterre, France) using diamond knife (DIATOME Cryotrim 45°, Leica Microsystèmes, SAS, Nanterre, France). A high cutting speed of 50 mm/s was used considering the hard transverse wood surface and the cutting feed was set at 200 nm. The clearance angle was kept constant at 6° during the sectioning. Optical image of the wood surface was acquired at 10 × magnification with an Olympus BX51 microscope (Rungis, France) using extended focal imaging (EFI) scanning mode.

3.3.5 MS/MS TOF-SIMS analysis

The parallel imaging MS/MS analyses were performed with the prototype TRIFT spectrometer on a PHI *nano*TOF II TOF-SIMS instrument (Physical Electronics, Minnesota, U.S.A.). A detailed description of the instrumental design can be found in ref. 24 and 25. Briefly, after desorption, the secondary ions are extracted into a TRIFT spectrometer which consists of three electrostatic analyzers (ESA). After the third ESA, an electrostatic precursor selector is positioned so that the mass resolved ions can either fly through this crossover and be detected by the MS1 detector or be deflected into a collision cell for fragmentation (see Figure 2). The fragment ions as well as the remaining precursor are then bunched and accelerated into a linear TOF analyzer before reaching the MS/MS detector. The precursor selection window is about 1 Da at *m/z* 500. In each duty cycle, the deflection proportion of the precursor ion can be defined as desired so that it is possible to maintain a fractional portion of the precursor ions in MS1 spectrum.

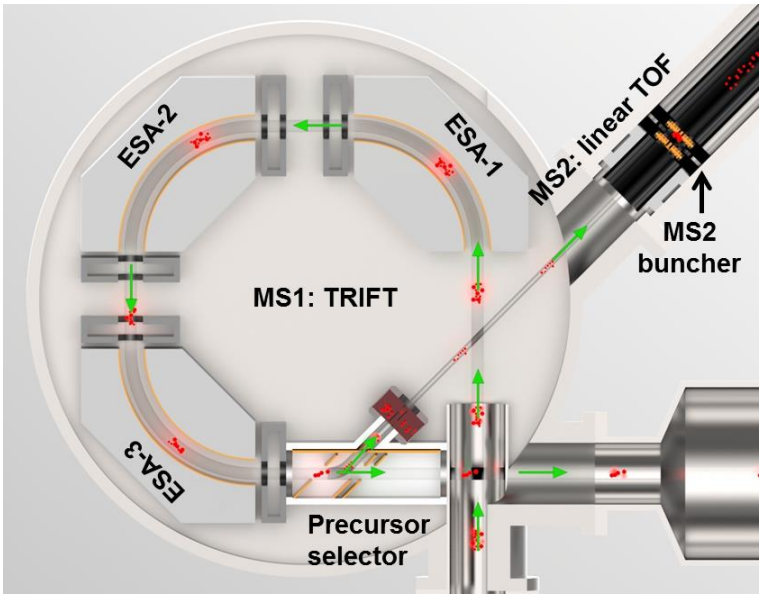

Figure 2: Schematic illustration of the parallel imaging MS/MS spectrometer. Adapted from ref. 24.

In the current report, all the spectra and images were recorded with 30 keV Bi_3^+ primary ion beam of which the DC current was ~ 11 nA in all cases. The ion beam was operated in both bunched mode and unbunched mode, with the former for high mass resolution spectra acquisition and the latter for high lateral resolution images recording. During the analysis, low energy electrons (15 eV) were applied for charge compensation. FOV (field-of-view) of each analytical area was 150 µm × 150 µm or 200 µm × 200 µm which was divided by 256 × 256 image pixels. In MS/MS acquisitions, the deflection fraction of the precursors into collision cell was 100% given the low abundance of target metabolites in the wood sample. In the precursor selector, precursor ions were deflected at ~1.5 keV, implying a keV collision event with the argon gas in the collision cell. The MS/MS acquisition time for each molecule was about 22 min and the primary ion beam density was 2×10^{13} ions/cm^2 where stable ion emissions were recorded in the profiles. Mass spectra were acquired over a mass range of 0-1000 in positive ion mode and mass calibration was achieved with internal fragments from wood structural polymer. Data processing was performed using PHI TOF-DR (Physical Electronics, Minnesota, U.S.A.) software.

3.4 Results and discussion

3.4.1 Structural characterization of isolated rubrynolide and rubrenolide by LC-MS/MS

The bioactive metabolites rubrynolide and rubrenolide isolated from the wood extract were first analyzed by LC-MS/MS. Figure 3 presents their LC profiles and the corresponding mass spectra. With the experimental conditions described above, the two metabolites were eluted at 11.463 min and 13.509 min, respectively. In the mass spectrum extracted from the peak at 11.463 min, *m/z* 297.2060, *m/z* 319.1879 and *m/z* 615.3881 were attributed to protonated rubrynolide ($C_{17}H_{29}O_4^+$, $\Delta_{m/z}$ = − 0.47 ppm) and its sodiated monomer ($C_{17}H_{28}O_4Na^+$, $\Delta_{m/z}$ = − 0.14 ppm) and dimer $C_{17}H_{28}O_4Na^+$, $\Delta_{m/z}$ = 2.27 ppm), respectively. Similarly, the mass peaks corresponding to $[M+H]^+$ (*m/z* 299.2213, $\Delta_{m/z}$ = − 1.30 ppm), $[M+Na]^+$ (*m/z* 321.2038, $\Delta_{m/z}$ = 0.53 ppm), and $[2M+Na]^+$ (*m/z* 619.4188, $\Delta_{m/z}$ = 1.23 ppm) ions of rubrenolide ($C_{17}H_{30}O_4$, MW 298.213 g/mol) were also assigned (Figure 3d). To provide further structural characterization and to facilitate the comparison with the following *in situ* TOF-SIMS MS/MS spectra, Q-TOF MS/MS fragmentation of the molecular ions were carried out. MS/MS spectrum of the ion at *m/z* 299.2224 ($[M+H]^+$, rubrenolide) is illustrated as a representative in Figure 3e. According to the chemical structure of rubrenolide (**2**), the losses of water molecules in the high mass range occur from the hydroxyl groups and the γ-lactone ring opening [33]. The presence of hydrocarbon fragments with 12 Da or 14 Da mass intervals in the low mass range correspond to the fragmentation of the long carbon chain. Peak attributions of the fragment ions shown in the spectrum are made within 5 ppm mass accuracy.

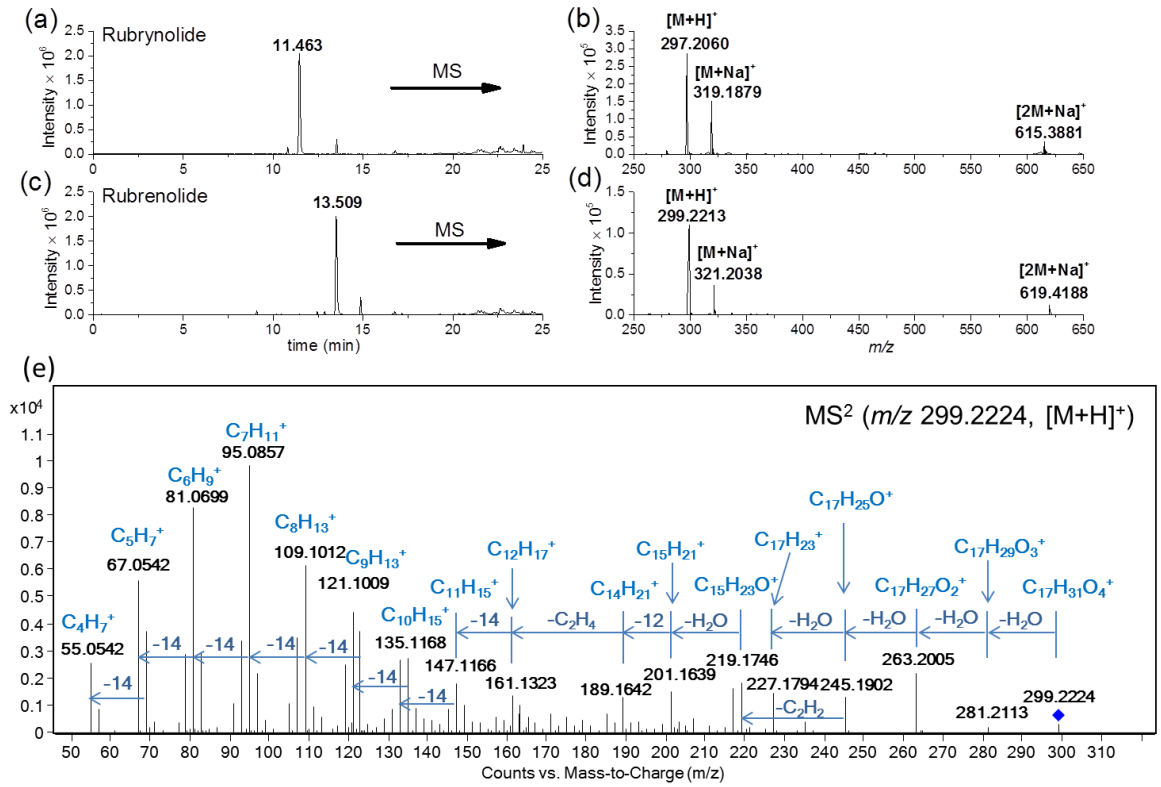

Figure 3: LC-MS analyses of the bioactive compounds. (a) Liquid chromatogram of rubrynolide. (b) ESI-Q-TOF mass spectrum of rubrynolide. (c) Liquid chromatogram of rubrenolide. (d) ESI-Q-TOF mass spectrum of rubrenolide. (e) ESI-Q-TOF MS/MS spectrum of protonated rubrenolide (*m/z* 299.2224).

3.4.2 *In situ* detection and localization

In situ mass spectrometric detection was performed on a transition zone wood sample from *S. rubra* with the knowledge that transition zone is associated with the biosynthesis of many heartwood metabolites during heartwood formation [34]. In addition, it has been observed that the amount of metabolites is most abundant around the transition area [35]. Figure 4 shows the mass spectrum obtained from a 150 µm × 150 µm analytical area. The primary ion beam was bunched to get high mass resolution spectrum. Despite the topography effect of the wood tissues, a high mass resolution of 10,000 at *m/z* 263 was readily attained. As illustrated in the inset, the quasi-molecular ions of rubrynolide and rubrenolide were detected at very low intensity, which is likely due to low ionization efficiency and low abundance of the metabolites in the wood tissue. Nevertheless, after internal mass calibration, a good mass accuracy < 10 ppm allowed the peak attribution with high confidence. The corresponding ion images of these two metabolites are presented in Figure 5 which reveals that rubrynolide and rubrenolide are co-localized around mainly ray parenchyma cells and small vessels (white arrows in Figure 5c and 5d). Ray parenchyma cells are the only living cells at the heartwood periphery and many optical [36,37] and mass spectrometric [35] observations suggest that

heartwood metabolites are primarily produced in this cell type. Therefore, our imaging results indicate that rubrynolide and rubrenolide are most probably biosynthesized in ray parenchyma cells before being actively or passively transferred to nearby cells and tissues.

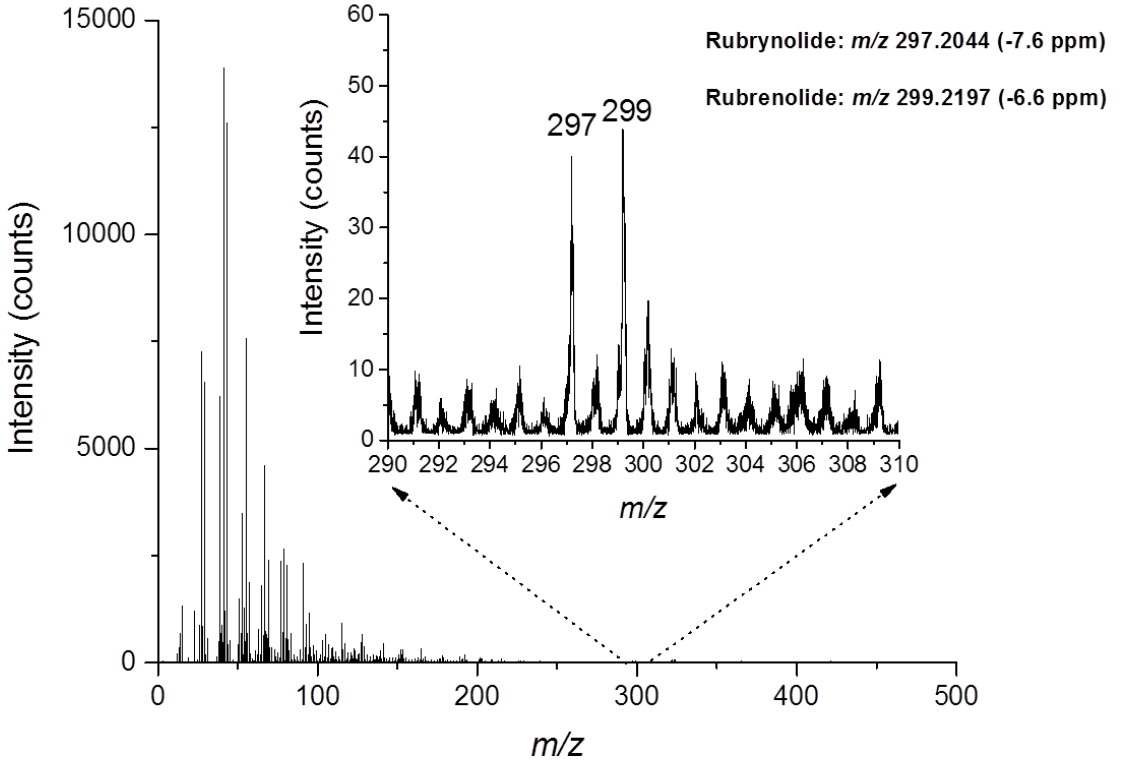

Figure 4: Mass spectrum of *S. rubra* wood sample from transition zone (positive ion mode). The inset shows the spectrum of low abundance bioactive metabolites rubrynolide (*m/z* 297) and rubrenolide (*m/z* 299).

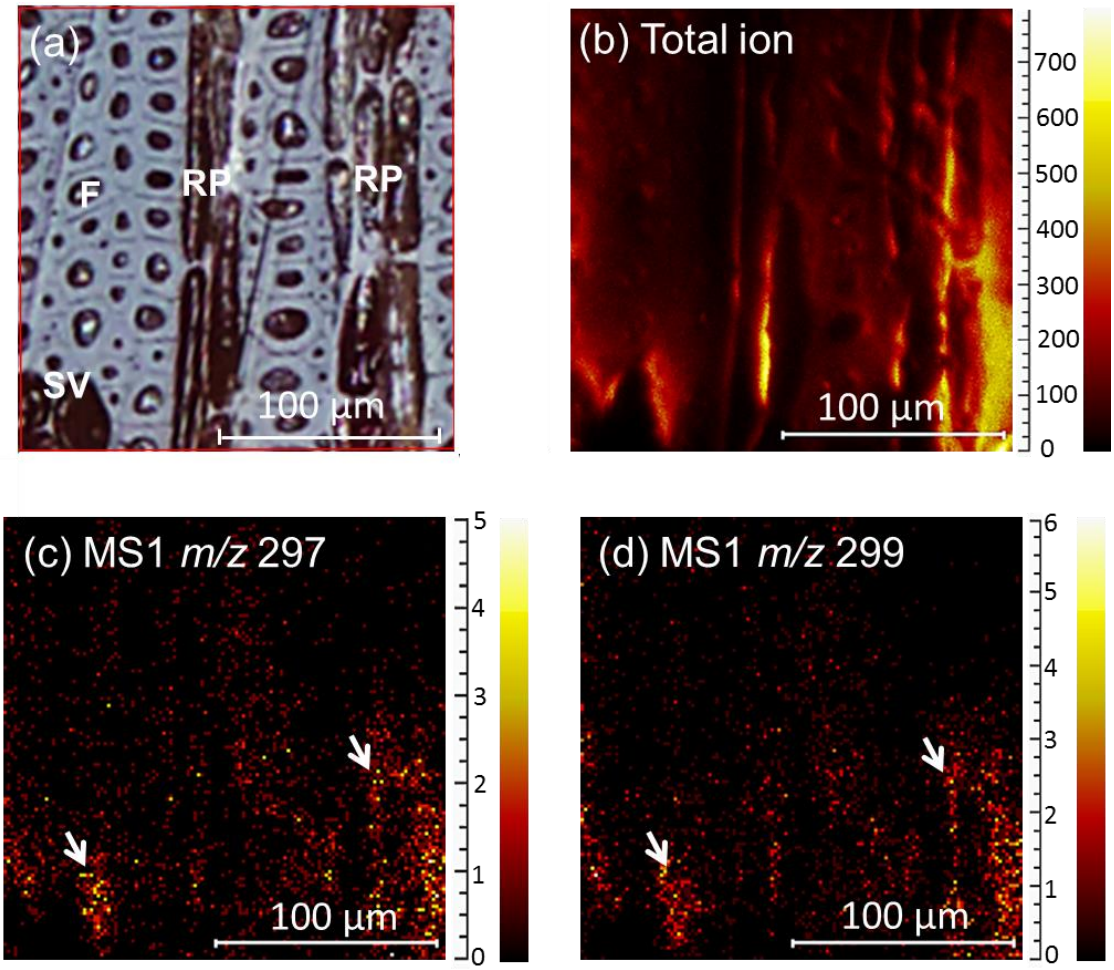

Figure 5: (a) Optical image of the analytical area on the transition zone wood sample. RP: ray parenchyma cell; F: fiber cell. SV: small vessel. (b) Total ion image. (c) MS1 ion image of rubrynolide (*m/z* 297). (d) MS1 ion image of rubrenolide (*m/z* 299). The analyzed area is 150 µm × 150 µm divided by 256 × 256 pixels. Ion images are compressed to 128 × 128 pixels to increase the contrast. White arrows indicate the distribution of rubrynolide and rubrenolide in small vessel and ray parenchyma cell.

3.4.3 *In situ* MS/MS identification of rubrynolide and rubrenolide

To guarantee a sufficient amount of precursor ions for MS/MS fragmentation, the primary ion beam was operated in continuous mode and the ions at *m/z* 297 and *m/z* 299 were thoroughly deflected into the collision cell. Here MS1 and MS/MS data were collected simultaneously where we can clearly observe the missing of precursor ions in the MS1 spectra (data not shown). The resulting tandem mass spectra show characteristic fragments of rubrynolide and rubrenolide (Figure 6). As expected, successive loss of the two hydroxyl groups in rubrenolide molecule is well demonstrated after collision-induced dissociation (CID), leading to the fragment ions at *m/z* 281 ($C_{17}H_{29}O_3^+$) and *m/z* 263 ($C_{17}H_{27}O_2^+$), respectively (Figure 6a). The abundant fragments in the low mass range are also in good accordance with those

from Q-TOF MS/MS spectrum and are attributed accordingly. These fragments display a serial mass loss of 12 Da or 14 Da which is the typical fragmentation pattern observed with compounds bearing long hydrocarbon chains. The fragmentation of rubrynolide results in very similar fragment ions except the mass difference derived from the terminal unsaturation. The exotic peak at *m/z* 209 which is not observed in low CID spectra probably arises from different fragmentation mechanisms associated with high energy collisions or simply from possible interference peaks.

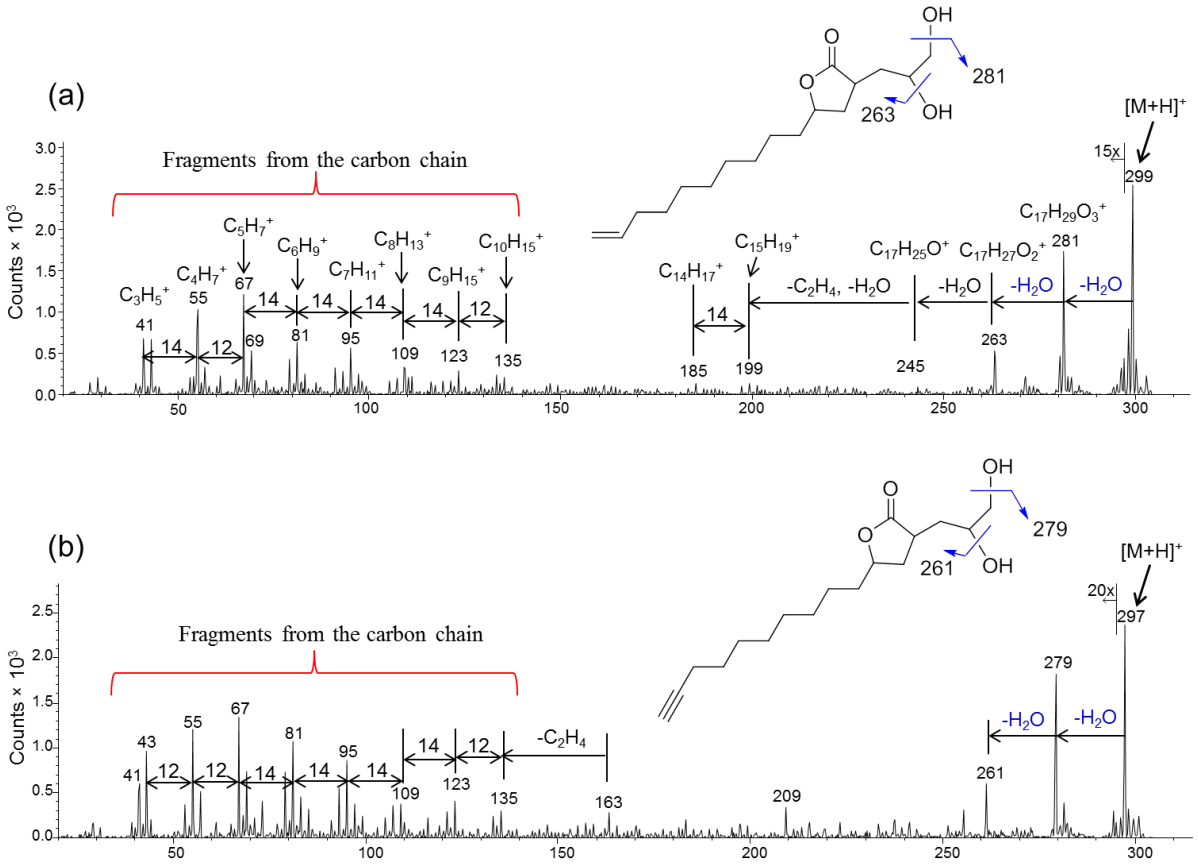

Figure 6: TOF-SIMS MS/MS spectra of (a) *m/z* 299 ($[M+H]^+$, rubrenolide) and (b) *m/z* 297 ($[M+H]^+$, rubrynolide). The blue-colored arrows in the structures indicate the characteristic loss of hydroxyl groups.

The MS/MS data were acquired on the same area as presented in Figure 5. Ion images of rubrenolide and rubrynolide were obtained by collecting all the ions produced from the fragmentation (Figure 7). It is worth noticing that the selection of monoisotopic ions of the precursor effectively excludes the background interferences, leading to more reliable localization information of the target biomolecules. As shown in the ion images, rubrenolide and rubrynolide are colocalized principally in and around the ray parenchyma cells, which reinforces the hypothesis that ray parenchyma cells are involved in the production of these two bioactive metabolites.

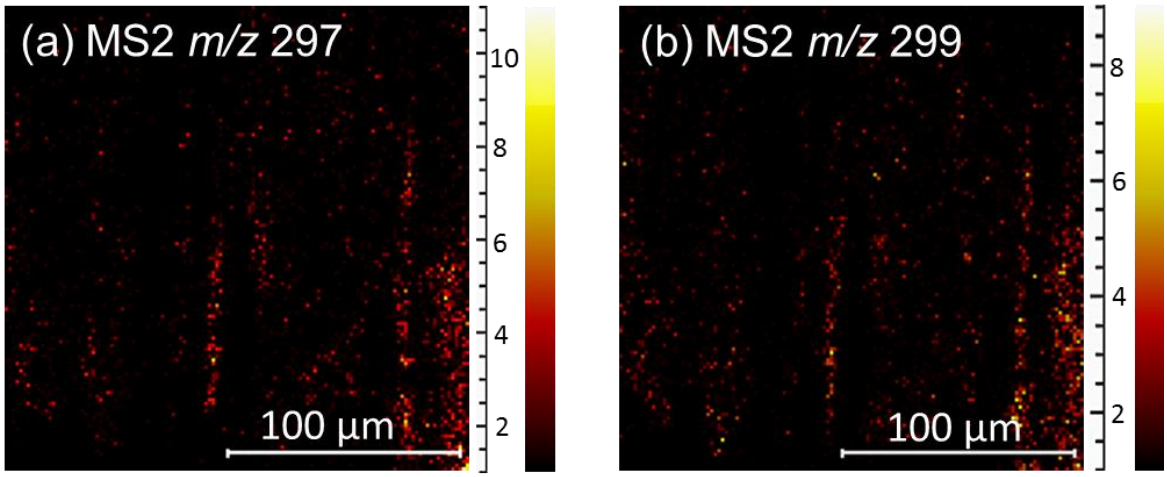

Figure 7: MS2 ion image of (a) rubrynolide (*m/z* 297) and (b) rubrenolide (*m/z* 299). The analytical area is the same as that in Figure 5. The ion images are compressed from 256 × 256 pixels to 128 × 128 pixels to increase the contrast.

3.5 Conclusion

The new parallel MS/MS imaging technique has been successfully applied to perform *in situ* identification of bioactive metabolites in tropical wood species *S. rubra*. The MS/MS fragmentation provides unambiguous identification of the metabolites. Moreover, MS/MS ion images have superior image contrast and could more precisely localize the low abundance biomolecules, which is frequently the case with natural products. Both MS1 and MS/MS ion images demonstrate the colocalization of rubrenolide and rubrynolide principally in and around ray parenchyma cells. Based on previous studies, it is suggested that these two bioactive metabolites are biosynthesized in ray parenchyma cells.

The lack of tandem mass spectrometry capability has long been an issue in applying TOF-SIMS imaging to biological studies. Here we show that this new parallel MS/MS imaging spectrometer can be a powerful tool in characterization, identification and localization of low abundance natural products in complex biological samples.

3.6 Acknowledgements

We acknowledge an Investissement d'Avenir grant of the Agence Nationale de la Recherche (CEBA: ANR-10-LABX-25-01). TF would like to acknowledge financial support from China Scholarship Council (CSC, No. 201406310013). This work has benefited from the facilities and expertise of the Electron Microscopy facilities of Imagerie-Gif (http://www.i2bc.parissaclay.fr/spip.php?article282).

3.7 Supporting information

3.7.1 MS/MS spectrum of reference purified rubrenolide

Reference tandem spectrum was obtained with isolated rubrenolide and rubrynolide sample on the parallel MS/MS imaging spectromter. Purified rubenolide powder was dissolved in ethyl acetate and deposited on a clean silicon wafer.

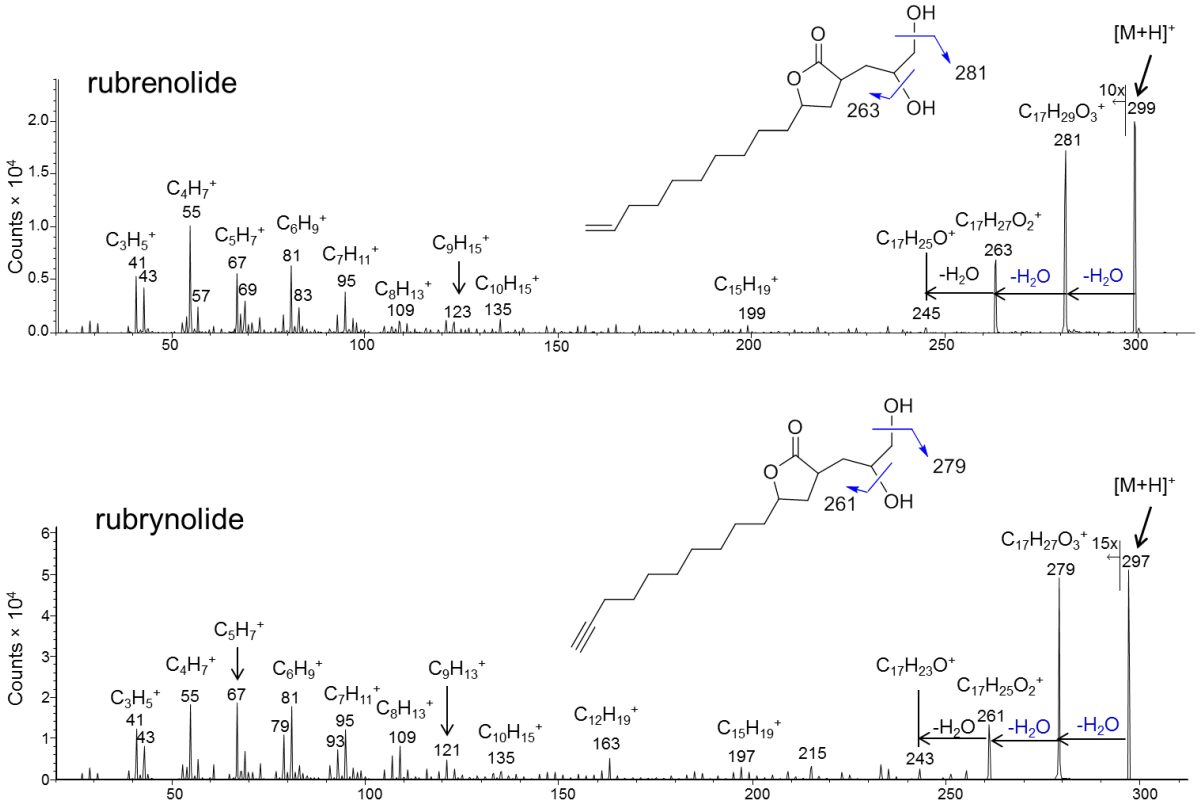

Figure S1: MS/MS spectrum of purified rubrenolide and rubrynolide acquired on the parallel MS/MS imaging spectrometer. The blue colored arrows in the structure indicate the characteristic loss of hydroxyl groups.

References

[1] Benguerba, M.; Brunelle, A.; Della-Negra, S.; Depauw, J.; Joret, H.; Le Beyec, Y.; Blain, M. G.; Schweikert, E. A.; Ben Assayag, G.; Sudraud, P. Impact of Slow Gold Cluster on Various Solids: Nonlinear Effects in Secondary Ion Emission. *Nuclear Instruments and Methods in Physics Research Section B* **1991**, 62, 8–22.

[2] Davies, N.; Weibel, D. E.; Blenkinsopp, P.; Lockyer, N.; R. Hillb, Vickerman, J. C. Development and experimental application of a gold liquid metal ion source. *Applied Surface Science* **2003**, *203-204*, 223–227.

[3] Kollmer, F. Cluster Primary Ion Bombardment of Organic Materials. *Applied Surface Science* **2004**, *231-232*, 153–158.

[4] Touboul, D.; Kollmer, F.; Ewald Niehuis; Brunelle, A.; Laprévote, O. Improvement of Biological Time-of-Flight-Secondary Ion Mass Spectrometry Imaging with a Bismuth Cluster Ion Source. *Journal of American Society for Mass Spectrometry* **2005**, *16*, 1608–1618.

[5] Weibel, D.; Wong, S.; Lockyer, N.; Blenkinsopp, P.; Hill, R.; Vickerman, J. C. A C60 Primary Ion Beam System for Time of Flight Secondary Ion Mass Spectrometry: Its Development and Secondary Ion Yield Characteristics. *Analytical Chemistry* **2003**, *75*, 1754–1764.

[6] Tanaka, M.; Moritani, K.; Hirota, T.; Toyoda, N.; Yamada, I.; Inui, N.; Mochiji, K. Enhanced surface sensitivity in secondary ion mass spectrometric analysis of organic thin films using size-selected Ar gas-cluster ion projectiles. *Rapid Communication in Mass Spectrometry* **2010**, *24*, 1405–1410.

[7] Winograd, N. The Magic of Cluster SIMS. *Analytical Chemistry* **2005**, *77*, 142A–149A.

[8] Mochiji, K.; Hashinokuchiy, M.; Moritani, K.; Toyoda, N. Matrix-free detection of intact ions from proteins in argon-cluster secondary ion mass spectrometry. *Rapid Communication in Mass Spectrometry* **2009**, *23*, 648–652.

[9] Brunelle, A.; Touboul, D.; Laprévote, O. Biological tissue imaging with time-of-flight secondary ion mass spectrometry and cluster ion sources. *Journal of Mass Spectrometry* **2005**, *40*, 985–999.

[10] Bich, C.; Touboul, D.; Brunelle, A. Cluster TOF-SIMS imaging as a tool for micrometric histology of lipids in tissue. *Mass Spectrometry Reviews* **2014**, *33*, 442–451.

[11] Fletcher, J. S.; Lockyer, N. P.; Vickerman, J. C. Developments in molecular SIMS depth profiling and 3D imaging of biological systems using polyatomic primary ions. *Mass Spectrometry Reviews* **2011**, *30*, 142–174.

[12] McDonnell, L. A.; Heeren, R. M. A. Imaging mass spectrometry. *Mass Spectrometry Reviews* **2007**, *26*, 606–643.

[13] Touboul, D.; Brunelle, A. What more can TOF-SIMS bring than other MS imaging methods? *Bioanalysis* **2016**, *8*, 367–369.

[14] Green, F. M.; Gilmore, I. S.; Seah, M. P. *Journal of the American Society for Mass Spectrometry* **2006**, *17*, 514–523.

[15] Touboul, D.; Brunelle, A.; Laprévote, O. Structural analysis of secondary ions by post-source decay in time-of-flight secondary ion mass spectrometry. *Rapid Communications in Mass Spectrometry* **2006**, *20*, 703–709.

[16] Carado, A.; Passarelli, M. K.; Kozole, J.; Wingate, J. E.; Winograd, N.; Loboda, A.V. C60 secondary ion mass spectrometry with a hybrid quadrupole orthogonal time-of-flight mass spectrometer. *Analytical Chemistry* **2008**, *80*, 7921–7929.

[17] Carado, A.; Kozole, J.; Passarelli, M.; Winograd, N.; Loboda, A.; Wingate, J. Cluster SIMS with a hybrid quadrupole time-of-flight mass spectrometer. *Applied Surface Science* **2008**, *255*, 1610–1613.

[18] Lanni, E. J.; Dunham, S. J.; Nemes, P.; Rubakhin, S. S.; Sweedler, J. V. Biomolecular Imaging with a C60-SIMS/MALDI Dual Ion Source Hybrid Mass Spectrometer: Instrumentation, Matrix Enhancement, and Single Cell Analysis. *Journal of American Society for Mass Spectrometry* **2014**, *25*, 1897–1907.

[19] Fletcher, J. S.; Rabbani, S.; Henderson, A.; Blenkinsopp, P.; Thompson, S. P.; Lockyer, N. P.; Vickerman, J. C. A New Dynamic in Mass Spectral Imaging of Single Biological Cells. *Analytical Chemistry* **2008**, *80*, 9058–9064.

[20] Hill, R.; Blenkinsopp, P.; Thompson, S.; Vickerman, J.; Fletcher, J. S. A new time-of-flight SIMS instrument for 3D imaging and analysis. *Surface and Interface Analysis* **2011**, *43*, 506–509.

[21] Rabbani, S.; Fletcher, J. S.; Lockyer, N. P.; Vickerman, J. C. Exploring subcellular imaging on the buncher-ToF J105 3D chemical imager. *Surface and Interface Analysis* **2011**, *43*, 380–384.

[22] Phan, N. T. N.; Munem, M.; Ewing, A. G.; Fletcher, J. S. MS/MS analysis and imaging of lipids across *Drosophila* brain using secondary ion mass spectrometry. *Analytical and Bioanalytical Chemistry* **2017**, *409*, 3923–3932.

[23] Smith, D. F.; Robinson, E. W.; Tolmachev, A. V.; Heeren, R. M.; Pasa-Tolic, L. C60 Secondary Ion Fourier Transform Ion Cyclotron Resonance Mass Spectrometry. *Analytical Chemistry* **2011**, *83*, 9552–9556.

[24] Fisher, G. L.; Bruinen, A. L.; Ogrinc Potočnik, N.; Hammond, J. S.; Bryan, S. R.; Larson, P. E.; Heeren, R. M. A. A New Method and Mass Spectrometer Design for TOF-SIMS Parallel Imaging MS/MS. *Analytical Chemistry* **2016**, *88*, 6433−6440.

[25] Fisher, G. L.; Hammond, J. S.; Larson, P. E.; Bryan, S. R.; Heeren, R. M. A. Parallel imaging MS/MS TOF-SIMS instrument. *Journal of Vacuum Science & Technology B* **2016**, *34*, 03H126.

[26] Fletcher, J. S. Cellular imaging with secondary ion mass spectrometry. *Analyst* **2009**, *134*, 2204–2215.

[27] van der Werff, H. *Sextonia*, a new genus of Lauraceae from South America. *Novon* **1997**, *7*, 436–439.

[28] Madda, J.; Khandregula, S., Bandari, S. K.; Kommu, N.; Yadav, J. S. Stereoselective total synthesis of rubrenolide and rubrynolide. *Tetrahedron: Asymmetry* **2014**, *25*, 1494–1500.

[29] Rodrigues, A. M. S.; Amusant, N.; Beauchêne, J.; Eparvier, V.; Leménager, N.; Baudassé, C., Espíndola, L. S.; Stien, D. The termiticidal activity of Sextonia rubra (Mez) van der Werff (Lauraceae) extract and its active constituent rubrynolide. *Pest Management Science* **2011**, *67*, 1420–1423.

[30] Rodrigues, A. M. S.; Theodoro, P. N. E. T.; Eparvier, V.; Basset, C., Silva, M. R. R.; Beauchêne, J.; Espíndola, L. S.; Stien, D. Search for Antifungal Compounds from the Wood of Durable Tropical Trees. *Journal of Natural Products* **2010**, *73*, 1706–1707.

[31] Falkowski, M.; Jahn-Oyac, O.; Ferrero, E.; Issaly, J.; Eparvier, V.; Rodrigues, A. M. S.; Stien, D.; Houël, E.; Dusfour, I. Assessment of a simple compound-saving method to study insecticidal activity of natural extracts and pure compounds against mosquito larvae. *Journal of the American Mosquito Control Association* **2016**, *32*, 337−340.

[32] Amusant, N.; Migg, M.; Thibaut, B.; Beauchene, J. Diversity of decay resistance strategies of durable tropical woods species: Bocoa prouacencsis Aublet, Vouacapoua americana Aublet, Inga alba (Sw.) Wild. *International Biodeterioration & Biodegradation* **2014**, *94*, 103–108.

[33] Crotti, A. E. M.; Bronze-Uhle, E. S.; Nascimento, P. G. B. D.; Donate, P. M.; Galembeck, S. E.; Vessecchia, R.; Lopes, N. P. Gas-phase fragmentation of γ-lactone derivatives by electrospray ionization tandem mass spectrometry. *Journal of Mass Spectrometry* **2009**, *44*, 1733–1741.

[34] Beritognolo, I.; Magel, E.; Abdel-Latif, A.; Charpentier, J. P.; Jay-Allemand, C.; Breton, C. *Tree Physiology* **2002**, *22*, 291–300.

[35] Saito, K.; Mitsutani, T.; Imai, T.; Matsushita, Y.; Fukushima, K. Discriminating the Indistinguishable Sapwood from Heartwood in Discolored Ancient Wood by Direct Molecular Mapping of Specific Extractives Using Time-of-Flight Secondary Ion Mass Spectrometry. *Analytical Chemistry* **2008**, *80*, 1552–1557.

[36] Hillis, W. E. Formation of robinetin crystals in vessels of *Intsia* species. *IAWA Journal* **1996**, *17*, 405–419.

[37] Nagasaki, T.; Yasuda, S. ; Imai, T. Immunohistochemical localization of agatharesinol, a heartwood norlignan, in *Cryptomeria japonica*. *Phytochemistry* **2002**, *60*, 461–466.

Chapter 4 Biosynthetic investigation and localization of bioactive metabolites in Amazonian tree species *Sextonia rubra* (Lauraceae) by 2D and 3D TOF-SIMS imaging

4.1 Abstract

The biosynthesis of rubrynolide and its analogues has remained disputable since their first isolation in 1971 from the wood of Amazonian tree species *Sextonia rubra* (Lauraceae). To investigate the biosynthetic pathway of these plant metabolites, 2D/3D TOF-SIMS imaging and parallel imaging MS/MS technique were applied to wood samples for *in situ* characterization of putative biosynthetic intermediates and disclosing their cellular localization. The *in vitro* extraction and isolation allow the report for the first time of two new acetylated lactone compounds (butanolides **4** and **5)** along with the presence of isozuihoenalide (**3**) in *S. rubra* sapwood. The *in situ* identification and subsequent 2D and 3D mass spectrometry imaging reveal rubrynolide and rubrenolide are well co-localized with their structurally related putative precursor butanolides **4** and **5** in specific cell types: ray parenchyma cell, tyloses, and oil cell. These results provide new insights in rubrynolide biosynthesis and reveal the intramolecular ring-opening cyclization process of dihydrofuran-2-one in parenchyma cells. Meanwhile, obtusilactone is suggested to arise from the coupling of succinic acid and a *β*-keto carboxylic compound in roots and sapwood. Thus, a new biosynthetic pathway is proposed for the formation of rubrynolide and its analogues in plants.

4.2 Introduction

In response to various environmental stresses such as aggressions from wood destroying organisms, many tropical tree species generate biologically active metabolites for their chemical defense. These metabolites have been selected through the evolution of plant-pathogen interactions [1,2]. Among these species, *Sextonia rubra* (Mez) van der Werff (Lauraceae), initially identified as *Nectandra rubra* (Mez) C.K. Allen and *Ocotea rubra* Mez [3], is a neotropical shade-tolerant rainforest tree species native to South America and one of the most commercially exploited wood for construction in French Guiana owing to its exceptional natural durability. Rubrynolide and rubrenolide natural products were first isolated from the stem wood of *S. rubra* in 1971 [4,5] and the full structures were reported in 1977 [6]. Subsequently these molecules have shown potent antifungal and insecticidal activities [7,8,9,10]. Therefore, it is suggested that the high natural durability of *S. rubra* heartwood is a result of its impregnation with these two bioactive metabolites [11]. Over the years, the total synthesis of rubrynolide and rubrenolide has been achieved leading to revision of their stereochemical structures with the correct configuration (2*S*,4*R*,2'*R*) [12,13,14,15]. In contrast, the biosynthetic process was only discussed by Gottlieb in the 1970s, who proposed the formation of a cyclo-propanone to explain the extrusion of the carbonyl from a normal polyketide precursor [16].

In plant metabolomic studies, gas chromatography (GC) and liquid chromatography (LC) coupled to mass spectrometry are the predominant and most effective approaches to isolate and identify natural products [17,18]. However, solvent extraction of the whole tissue results in the loss of spatial information of the metabolites which is essential in understanding the metabolism and biological functions of specific tissues [19]. Since mass spectrometry imaging (MSI) has been well established for visualizing chemical distribution in biological samples, a number of studies have employed MSI to reveal the spatial information of plant metabolites [20,21]. Particularly, time-of-flight secondary ion mass spectrometry (TOF-SIMS) is now a routine molecular imaging technique with subcellular resolution [22] and has been applied to map metabolite distribution in various wood species [23,24,25]. In addition, versatile sample handling enables TOF-SIMS imaging of high density wood species by analyzing directly the wood block surface [25]. Furthermore, direct three dimensional TOF-SIMS imaging can be realized by dual beam depth profiling method in which a sputter ion beam is utilized to ablate the samples layer by layer, revealing the in-depth distribution of chemical components [26]. Meanwhile, TOF-SIMS prototypes which could provide MS/MS capability are currently available to afford unambiguous and *in situ* identification of the molecules [27,28,29,30].

In order to elucidate the biosynthesis of natural products rubrynolide and rubrynolide in plants, we herein investigated secondary metabolites biosynthesis during heartwood formation of Amazonian tree species *S. rubra* both *in vitro* and *in situ* by solvent extraction/isolation and TOF-SIMS imaging. This original strategy takes fully benefit of the state-of-the-art technologies in mass spectrometry. Parallel MS/MS imaging was performed for *in situ* identification the new metabolites isolated *in vitro*, which allows following 2D/3D TOF-SIMS imaging to localized the bioactive products and their biosynthetic precursors at subcellular level. In this paper we report the presence of newly isolated constituents and their spatial distribution that led to suggest a new biosynthetic route for rubrynolide and its analogues.

4.3 Experimental

4.3.1 Plant material

The samples were taken from two *Sextonia rubra* adult trees (SR1 and SR2) from the Paracou forest in French Guiana (5°15' N, 52°55'W) in December 2015. A wood increment core was taken at breast height and stored in freeze condition (-18 °C) until imaging analysis (ultramicrotoming of wood blocks and extraction of the compounds). The trees were chosen as representative of the species (adult, without damage and with an intact crown) according to the method used by Rutishauser *et al.* [31]. This classification method is based on analysis of the crown structure and its fragmentation degree to evaluate the development of the tree (juvenile or adult specimens, possible damage like headless stem, senescent tree, or intact crown).

4.3.2 Extraction and isolation

Extractions of sapwood and heartwood from *S. rubra* SR1 individual were performed according to previously described procedures [7]. Briefly, 200 g of wood material were extracted three times at room temperature for 48 h with ethyl acetate (3 × 500 mL). The ethyl acetate extracts were then purified by column chromatography (EtOAc).

Preparative chromatography was performed at 15 mL/min with a W600 pump and a W2487 double wavelength UV detector (Waters) using a Discovery C18 column (15 cm x 21.2 mm, 5 µm, Supelco). HPLC analyses were performed on a Discovery C18 column (15 cm × 4.6 mm, 5 µm, Supelco) at 1 mL/min using a Waters HPLC system equipped with a W2996 photodiode array absorbance detector and a W2424 light-scattering detector. Water (HPLC grade) was obtained from a Milli-Q system (Milli-Q plus, Millipore Bedford, MA).

Isolation of isozuihoenalide **3** was carried out on 3 mL of a root extract solution at a concentration of 50 mg/mL in water/acetonitrile 40:60 using a linear gradient of water/acetonitrile (40:60 to 0:100 over 20 min) and remaining at 100% acetonitrile during 10 min. The eluates from the column were monitored at 210 and 240 nm. Fractions containing the same constituents according to analytic chromatographic profiles obtained at 210 and 240 nm and with ELSD detection were gathered and evaporation allowed for isolation of compounds **3** (22 mg) in pure form. Isolation of butanolide **4** and **5** was carried out on 3 mL of a sapwood extract solution at a concentration of 50 mg/mL in water/acetonitrile 40:60 using the same procedure as previously. Compounds **4** (43.4 mg, 28.9% w/w) and **5** (18.1 mg, 12.1% w/w) were both isolated in pure form.

Isolation of heartwood compounds rubrynolide **7** and rubrenolide **8** was carried out with 40 mg of the purified fraction diluted in 1.5 mL of water/acetonitrile 50:50 using a linear gradient of water/acetonitrile (50:50 to 0:100 over 15 min) and remaining at 100% acetonitrile during 5 min. The eluates from the column were monitored at 210 and 240 nm. Fractions containing the same constituents according to analytic chromatographic profiles obtained at 210 and 240 nm and with ELSD detection were gathered and evaporation allowed for isolation of compounds rubrynolide **7** (14.1 mg, 35.2% w/w) rubrenolide **8** (8.1 mg, 20.2% w/w). Both compounds were isolated in pure form.

4.3.3 LC-MS analysis

Purified products from *S. rubra* SR1 individual were prepared at a concentration of 0.1 mg/mL in methanol (Sigma-Aldrich, Saint Quentin-Fallavier, France). LC-MS/MS experiments were performed on a HPLC Ultimate 3000 system (Dionex, Voisins-le-Bretonneux, France) coupled with an Agilent 6540 Q-ToF (Agilent Technologies, Waldbronn, Germany) mass spectrometer. LC separation was achieved with an Accucore RP-MS column (100 × 2.1 mm, 2.6 µm, Thermo Scientific, Courtaboeuf, France) with a mobile phase consisting of water with 0.1 % formic acid (A) and acetonitrile with 0.1 % formic acid (B). Compounds were eluted at a flow rate of 0.4 mL/min with a gradient from 5 % B to 100 % B in 25 min and then 100 % B for 3 min. Injection volume was fixed at 5 µL for all the analyses. Mass spectra were recorded with an electrospray ion source in positive ion mode with the following parameters: spray voltage set at 3.5 kV, capillary temperature at 325 °C, capillary voltage at 45 V and fragmentor voltage at 120 V. The collision energy was optimized and fixed at 15 eV for all the MS/MS fragmentation acquisitions except that 30 eV was chosen for alkalized molecular ions. Internal calibration was achieved with two calibrants (*m/z* 121.0509 and *m/z* 922.0098) providing a high mass accuracy of approximately 2 ppm. Mass resolution (FWHM, full width at half maximum) is 20,000 in MS and MS/MS spectra.

4.3.4 NMR analysis

^{1}H NMR spectra were recorded at 400 MHz and ^{13}C NMR spectra at 100.6 MHz on a Varian 400 NMR spectrometer equipped with a 5 mm inverse probe (Auto X PGF 1H/15N-13C). Samples were dissolved in deuterated chloroform ($CDCl_3$) in 5 mm tubes as stated. Chemical shifts are in ppm downfield from tetramethylsilane (TMS), and coupling constants (J) are in Hz (s stands for singlet, d for doublet, t for triplet, q for quartet, m for multiplet, br for broad). NMR analyses were all performed on *S. rubra* SR1 individual. For the structural determination of isolated compound, two 5 mm NMR tubes containing 8 mg and 25 mg of pure molecule dissolved in deuterated chloroform ($CDCl_3$) were prepared for 1H and 2D

sequences respectively. All sequences 1H (64 scans), 13C (2560 scans), gCOSY (4 scans × 256 increments), gHSQCAD (4 scans × 512 increments), gHMBC (4 scans × 512 increments) were recorded with an acquisition time of 1.0 s, a relaxation delay of 1.0 s for a 45° pulse sequence. All NMR spectra were phased and baseline corrected with MestReNova 9.0 (Mestrelab Research) before being processed.

Quantitative NMR analyses were performed as follows. Wood extracts (14 mg) and the standard for quantitative NMR (TraceCERT®) 1,2,4,5-tetrachloro-3-nitrobenzene (CAS: 117-18-0, Sigma-Aldrich Ref 40384, 7 mg) are dissolved in deuterated chloroform ($CDCl_3$, 400 µL) in a 2 mL vial before transferring the solution into a 5 mm NMR tube. NMR acquisition time was set at 2.55 s with a spectral width of 6410.3 Hz and 16 scans were recorded with a relaxation delay of 5×T1 (85 s) for a 45° pulse sequence. ^{1}H spectra were processed with MestReNova 9.0 (Mestrelab Research) software to perform phase and baseline corrections. For quantification of isozuihoenalide **3**, ^{1}H signals corresponding to protons (7.09, 5.26 and 4.72 ppm) were manually integrated and the mean value of the integrations was used to calculate the concentration of isozuihoenalide **3** in samples. For quantification of butanolides **4** and **5**, ^{1}H signals corresponding to protons (4.33, 4.24 and 4.02 ppm) were manually integrated, the mean value of the integrations and the mean molecular mass (M= 381.22 g.mol^{-1}) were used to calculate the concentration of butanolides **4** and **5** in samples. For quantification of rubrynolide **7** and rubrenolide **8**, ^{1}H signals corresponding to protons (3.80, 3.64 and 3.49 ppm) were manually integrated, the mean value of the integrations and the mean molecular mass (M = 297.22 g·mol^{-1}) were used to calculate the concentration of rubrynolide **7** and rubrenolide **8** in samples.

4.3.5 Ultramicrotoming of wood samples for TOF-SIMS imaging

The wood increment cores of *S. rubra* SR2 individual were cut by an electric saw into small wood blocks (~ 0.7 cm × 0.7 cm × 0.7 cm) corresponding to sapwood, transition zone and heartwood, respectively. Each block was then trimmed with a razor blade to generate a transverse cutting surface of approximately 1 mm × 2.5 mm which was left to be cut with an ultramicrotome (EM UC6, Leica Microsystèmes, SAS, Nanterre, France) using a diamond knife (DIATOME Cryotrim 45°, Leica Microsystèmes, SAS, Nanterre, France). A high cutting speed of 50 mm/s was used considering the dense transverse wood surface and the cutting feed was set at 200 nm. The clearance angle was kept constant at 6° during the sectioning. Optical images of the wood surfaces were acquired at 10 × magnification with an Olympus BX51 microscope (Rungis, France) using extended focal imaging (EFI) scanning mode.

4.3.6 TOF-SIMS analysis

Mass spectrometry imaging acquisitions were performed with a commercial TOF-SIMS IV (ION-TOF GmbH, Münster, Germany) mass spectrometer equipped with a bismuth liquid metal ion gun and an argon cluster ion source. Mass spectra and ion density images were recorded using Bi_3^+ cluster ions as the primary ion beam with a kinetic energy of 25 keV. In order to simultaneously obtain high spatial and high mass resolution on wood surface bearing a diversity of topographic attributes, the so-called burst alignment ion focusing mode has been applied with a delayed extraction of secondary ions as previously described [32]. The primary ion pulse duration was set at 100 ns and the current measured at 10 kHz was 0.07 pA. After the extraction delay, secondary ions were extracted and first accelerated to a kinetic energy of 2 keV and then post-accelerated to 10 keV before reaching a hybrid detector composed of a single microchannel plate followed by a scintillator and a photomultiplier. A low energy pulsed electron flood gun (20 eV) was applied to neutralize the charges accumulated on the insulating wood surface. 2D imaging acquisitions were performed on areas of 400 μm × 400 μm with 1024 × 1024 pixels, thus a pixel size of 400 nm × 400 nm, and an ion dose of 3×10^{12} ions/cm^2. 3D imaging was achieved with dual beam depth profiling method with 25 keV Bi_3^+ as analysis beam and 10 keV Ar_{1000}^+ as sputter beam, respectively. Depth profile in positive polarity was acquired by alternatively analyzing 200 μm × 200 μm area (divided by 512 × 512 pixels) and sputtering 500 μm × 500 μm area. The sputter depth was calibrated by a 20 μm thick transverse wood section of *S. rubra* (Figure S29). Data processing was performed using SurfaceLab 6.5 (ION-TOF GmbH, Münster, Germany), and the primary ion beam shift during the acquisitions were corrected by 'lateral shift correction' function in the software. Due to the extraction delay, the relationship between time-of-flight and the square root of *m/z* can no longer be considered linear as otherwise generally agreed in mass calibration of secondary ions with low initial kinetic energy distribution [33]. Internal mass calibration was therefore achieved by taking advantage of the lignin and polysaccharide fragments derived from the wood samples [34].

4.3.7 *In situ* MS/MS analysis

In situ MS/MS identification was performed on the parallel MS/MS imaging mass spectrometer which is based on a PHI nanoTOF II TOF-SIMS instrument (Physical Electronics, Minnesota, U.S.A.) [30]. In this prototype spectrometer, a precursor selector is positioned after the TRIFT analyzer, allowing the deflection of a desired proportion of precursor ions into a collision cell where argon is introduced as collision gas. The resulting fragment ions as well as the remaining precursors are then mass resolved by a linear TOF analyzer. This instrumental design enables simultaneous recording of MS and MS/MS spectra. Noticeably, the typical precursor selection window is about 1 Da, which could

effectively eliminate possible interferences and simplify the MS/MS spectra. For the MS/MS analyses, 30 keV Bi_3^+ ion beam is operated in a continuous mode to guarantee maximum emission efficiency of the metabolites. The ion images and spectra were collected over an area of 150 µm × 150 µm with 256 × 256 pixels and an ion dose of 2×10^{13} ions/cm^2. To avoid charge accumulation on the insulating surface, low energy electrons were employed for charge compensation. Mass spectra were acquired over a mass range of 0−1000 in positive ion mode and mass calibration was achieved with internal fragments. Data processing was performed using PHI TOF-DR (Physical Electronics, Minnesota, U.S.A.) software.

4.4 Results

4.4.1 Isolation, identification and quantification of new metabolites in *S. rubra*

In the course of understanding *S. rubra* heartwood formation process, and along with the isolation of the well-known compounds rubrynolide and rubrenolide from heartwood, three additional compounds were isolated from the ethyl acetate extract of roots and sapwood from *S. rubra* SR1 individual. NMR and MS data reveal that they are isozuihoenalide **3** and butanolides **4** and **5** (Figure 1). Isozuihoenalide **3** was isolated from the root extract as colorless oil. The molecular formula was determined to be $C_{23}H_{40}O_3$ by MS (ESI) ($[M+H]^+$, *m/z* 365.3051). The ^{1}H and ^{13}C NMR of **3** was similar to that of zuihoenalide [35], indicating the same *β*-hydroxy-*γ*-methylene-*α,β*'-unsaturated-*γ*-lactone skeleton. However, contrary to the *Z* double bond of zuihoenalide, the *E* geometry of the trisubstituted double bond was confirmed by comparing the values of ^{1}H NMR chemical shifts of the olefinic *β*-proton [δ 7.09 (1H, td, *J* = 7.8, 1.8 Hz, H-1')] with related butanolides isoobtusilactone A and lincomolide D [36,37,38]. The presence of a broad singlet δ 1.26 (28H, br s, H-4'−17') was attributed to protons in the long methylene chain. The exocyclic olefinic protons appeared at δ 4.96, 4.72 (each 1H, d, *J* = 1.5 Hz, H_Z-1", H_E-1") and one hydroxymethine proton located at δ 5.26 (1H, br s, H-4). Thus, the structure of isozuihoenalide was elucidated as (3*E*)-4-hydroxy-5-methylene-3-octadecylidenedihydrofuran-2-one, which was further confirmed by COSY and gHSQCAD experiments.

Table 1: NMR data of isozuihoenalide **3**.

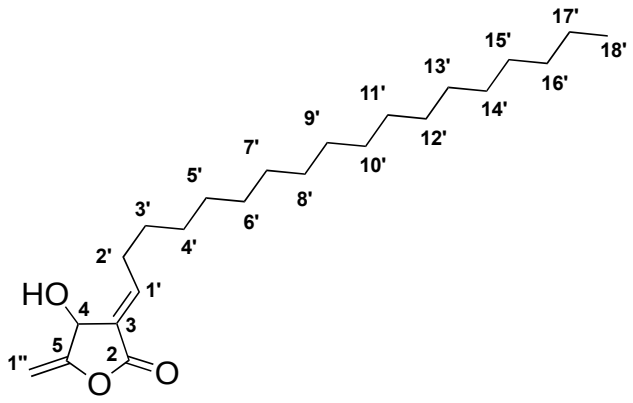

N°	^{13}C (δ)	^{1}H (δ)	gCOSY (^{1}H-^{1}H)
2	168.8 (C)		
3	127.3 (C)		
4	66.6 (CH)	5.26 (1H, br s)	H2'-H1"
5	157.8 (C)		
1'	91.4 (CH)	7.09 (1H, td, *J* = 7.8, 1.8 Hz)	H2'-H4
2'	29.8-28.4 (CH2)	2.46 (2H, m)	H1'-H1"-H3'-H4
3'	29.8-28.4 (CH2)	1.53 (2H, t, *J* = 7.2 Hz)	H2'
4'-15'	29.8-28.4 (CH2)	1.26 (28H, br s)	
16'	32.0 (CH2)	1.26 (28H, br s)	
17'	22.8 (CH2)	1.26 (28H, br s)	
18'	14.2 (CH2)	0.88 (3H, t, *J* = 6.9 Hz)	
1"	150.3 (C)	4.96 (1H, d, *J* = 1.5 Hz, H_Z-1") 4.72 (1H, d, *J* = 1.5 Hz, H_E-1")	H4 - H2'

Butanolides **4** and **5** were isolated from the sapwood extract as colorless oil. Their molecular formula were determined to be $C_{21}H_{32}O_6$ (MS (ESI), *m/z* 381.2283 $[M+H]^+$, *m/z* 403.2107 $[M+Na]^+$, *m/z* 783.4299 $[2M+Na]^+$) and $C_{21}H_{34}O_6$ (MS (ESI), *m/z* 383.2417 $[M+H]^+$, *m/z* 405.2240 $[M+Na]^+$, *m/z* 787.4603 $[2M+Na]^+$) respectively. The ^{1}H and ^{13}C NMR of butanolides **4** and **5** were very similar to that of butaloide previously isolated from a marine actinomycete [39]. The ^{1}H chemical shifts and multiplicity in combination with the gHSQC spectra indicates the presence of two carbinols (C-1 at 65.2 ppm and C-2" at 69.2 ppm) with one (C-1) in α position of an asymmetric carbon (C-2 at 79.2 ppm) bearing an oxygen atom in γ-lactone ring. The lactone is substituted in C-4 (37.9 ppm) position with an aliphatic chain containing either a terminal triple bond or a terminal double bond in C-11 position in butanolides **4** and **5** respectively. Both carbinol oxygen atoms are acetylated as

indicated by the double CH_3 singlet signal at 2.06 ppm and the double ^{13}C signals 170.8 ppm. Thus, the structure of butanolides **4** and **5** were elucidated as (4-(2-acetoxydodec-11-yn-1-yl)-5-oxotetrahydrofuran-2-yl)-methyl acetate and (4-(2-acetoxydodec-11-en-1-yl)-5-oxotetrahydrofuran-2-yl)-methyl acetate respectively, which was further confirmed by COSY and gHSQCAD experiments.

Table 2: NMR data of butanolides **4** and **5**.

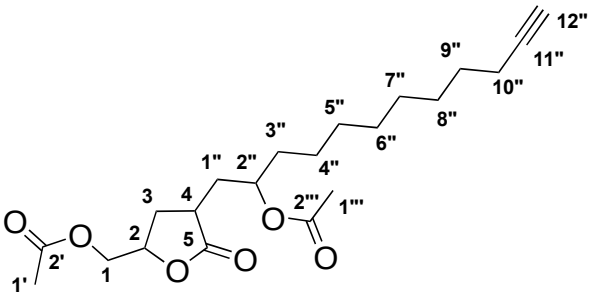

(**4**)

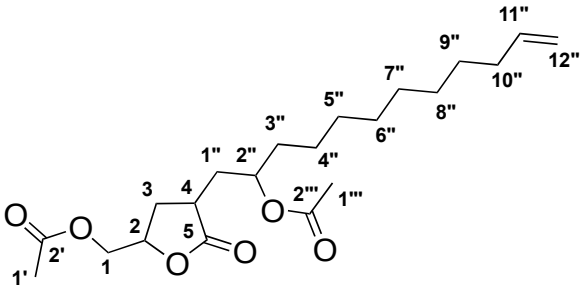

(**5**)

N°	^{13}C (δ)		^{1}H (δ)	
	Butanolide **4**	Butanolide **5**	Butanolide **4**	Butanolide **5**
1	65.2 (CH2)		4.24 (1H, dd, *J* = 11.9, 1.4 Hz, H-1a) 4.02 (1H, dd, *J* = 11.8, 1.4 Hz, H-1b)	4.26 (1H, dd, *J* = 11.9, 3.6 Hz, H-1a) 4.04 (1H, dd, *J* = 11.9, 6.4 Hz, H-1b)
2	79.2 (CH)		5.13 (1H, br s)	
3	32.1 (CH2)		2.53 (1H, m, H-3a) 1.72 (1H, m, H-3b)	
4	37.9 (CH)		2.60 (1H, m)	
5	178.1 (C)			
1’	21.1 (CH3)		2.08 (3H, s)	
2’	170.8 (C)			
1”	35.7 (CH2)		2.33 (1H, t, *J* = 11.7 Hz, H-1”a) 1.59-1.38 (1H, m, H-1”b)	2.34 (1H, ddd, *J* = 14.7, 10.5, 3.3 Hz, H-1”a) 1.65-1.42 (5H, m, H-1’b)
2”	69.2 (CH)		4.33 (1H, br s)	4.35 (1H, m)
3”	35.5 (CH2)		1.59-1.38 (2H, m)	1.65-1.42 (2H, m)
4”	25.3 (CH2)		1.45-1.25 (10H, br s, H-4”−8”)	1.42-1.25 (10H, br s, H-4”−8’)
5”	29.5-28.5 (CH2)		1.45-1.25 (10H, br s, H-4”−8”)	1.42-1.25 (10H, br s, H-4”−8’)
6”-7”	29.5-28.5 (CH2)		1.45-1.25 (10H, br s, H-	1.42-1.25 (10H, br s,

			4”−8”)	H-4”−8’)
8”		29.5-28.5 (CH2)	1.45-1.25 (10H, br s, H-4”−8”)	1.42-1.25 (10H, br s, H-4”−8’)
9”		29.5-28.5 (CH2)	1.59-1.38 (2H, m)	1.65-1.42 (2H, m)
10”	18.4 (CH2)	33.9 (CH2)	2.17 (2H, t, *J* = 7.06 Hz)	2.05 (2H, m)
11”	84.8 (C)	139.3 (CH)		5.82 (1H, m)
12”	68.2 (CH)	114.3 (CH2)	1.93 (1H, s)	5.00 (1H, d, *J* = 17.7, H_E-12”) 4.92 (1H, d, *J* = 10.1, H_Z-12”)
1”’		20.8 (CH3)	2.06 (3H, s)	
2”’		170.8 (C)		

By performing LC-Q-TOF MS on sapwood, heartwood, bark and leaf extracts from SR2 (Figure S1), additional metabolites were detected and identified by comparing the MS/MS spectra with those of obtusilactone analogue **1,** rubrynolide **7** and rubrenolide **8**. Obtusilactone analogues **1** (Figure S2) were detected in trace amount the sapwood extract, along with compounds **4, 5** (Figure S4-5). It is worth noticing that butanolide **6** and rubranolide **9**, both having no terminal insaturation, were detected for the first time in *S. rubra* in trace amount (Figure S6 and S9). The chemical structures of identified metabolites in *S. rubra* are summarized in Figure 1.

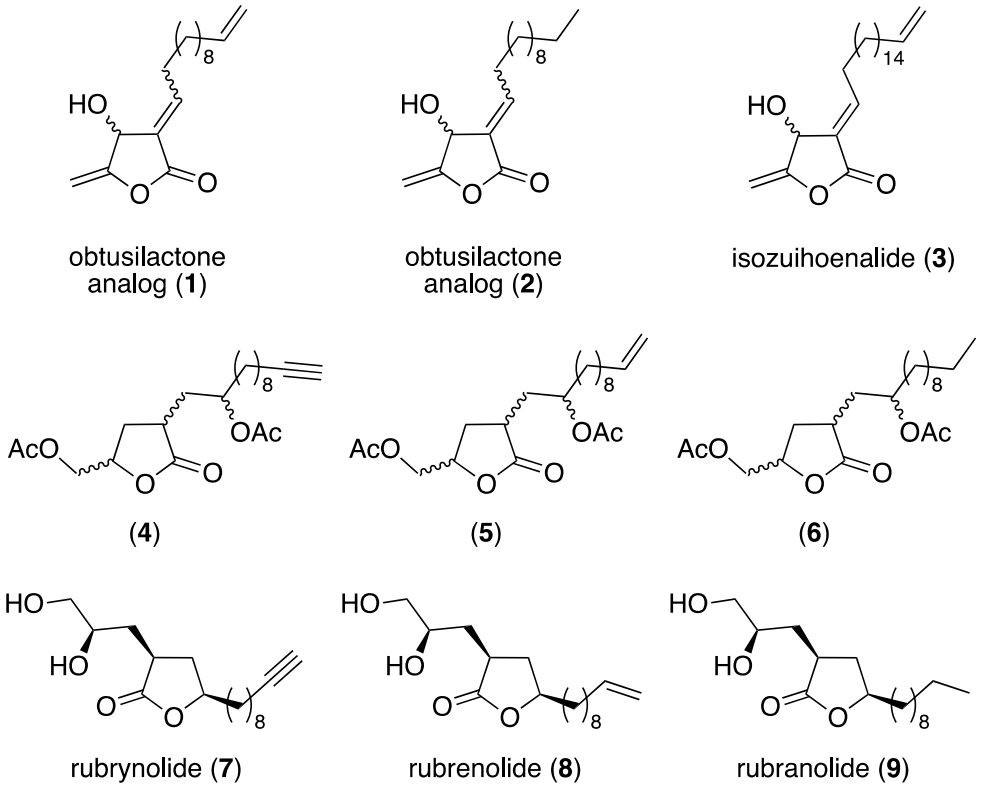

Figure 1: Secondary metabolites in *Sextonia rubra*.

Quantification of some metabolites in different plant organs of *S. rubra* were assessed in SR1 individual by quantitative NMR spectroscopy (Table 3, Figure S20-24). Interestingly, a large variation in quantity and distribution occurs among the different organs. Whereas isozuihoenalide **3** and butanolides **4** and **5** are abundant in roots and sapwood they are absent or detected in low concentration in heartwood, bark and leaf. On the other hand, rubrynolide **7** and rubrenolide **8** compose most the heartwood extract mass but are absent in other organs. Noticeably, roots, sapwood, and heartwood extracts are relatively not complex mixtures composed of few metabolites whereas leaf and bark extracts are complex mixtures of different metabolites as show in ^{1}H NMR spectra in Figure S20-24.

Table 3: Metabolite extraction yields in roots, sapwood, bark and heartwood measured by qNMR.

Material	Extraction yield (%)*				
	Roots	Sapwood	Heartwood	Bark	Leaf
crude extract	8.7	8.1	9.2	1.7	3.7
compound **3**	2.1	1.9	0.4	nd.	0.2
compounds **4**-**5**	6.0	5.3	nd.	0.2	un.
compounds **7**-**8**	nd.	nd.	8.1	un.	un.

*Measurements were performed SR1 individual in $CDCl_3$ using 1,2,4,5-tetrachloronitrobenzene as internal standard. nd.: not detected. un.: unknown, cannot be determined due to the overlap with interference peaks.

In the next section the spatial distribution of metabolites by TOF-SIMS imaging were investigated within sapwood, heartwood and transition zone tissues.

4.4.2 *In situ* identification of diacetylobtusilactones (butanolides 4 and 5)

With the parallel MS/MS imaging technique previously applied to *in situ* identification of rubrenolide (**8**) and rubrynolide (**9**) in chapter 3, butanolides **4** and **5** were further identified directly on a SR2 sapwood surface without any pretreatment. MS/MS imaging analyses were performed on a 150 µm × 150 µm analytical area where an oil cell was present (Figure 2a). TOF-SIMS MS/MS spectra of precursors at *m/z* 381 $[M+H]^+$ (butanolide **4**) and *m/z* 383 $[M+H]^+$ (butanolide **5**) are illustrated in Figure 2e and 2f, respectively. The low mass fragments display regular occurrence of 12 Da or 14 Da mass intervals, which is a typical phenomenon resulted from fragmentation of long hydrocarbon chains. While the high mass range spectra show the protonated precursor ions as well as the characteristic fragments originated from the loss of acetic function groups: -18 Da ($-H_2O$); -42 Da ($-CH_2=C=O$); -60 Da ($-CH_3CO_2H$). The *in situ* MS/MS data is consistent with *in vitro* Q-TOF analysis where the peak attributions are made within 5 ppm mass accuracy (Figure S4-S5). Ion images of precursors at *m/z* 381 and *m/z* 383 were obtained by collecting all the fragment ions and the remaining precursors after the CID collision. It is demonstrated that butanolides **4** and **5** are co-localized in the oil cell on the analyzed area (Figure 2c and 2d). Analyses of their corresponding alkalized (Na^+ and K^+) products further confirmed the structure and lateral distribution of these two diacetylobtusilactones (Figure S25-26).

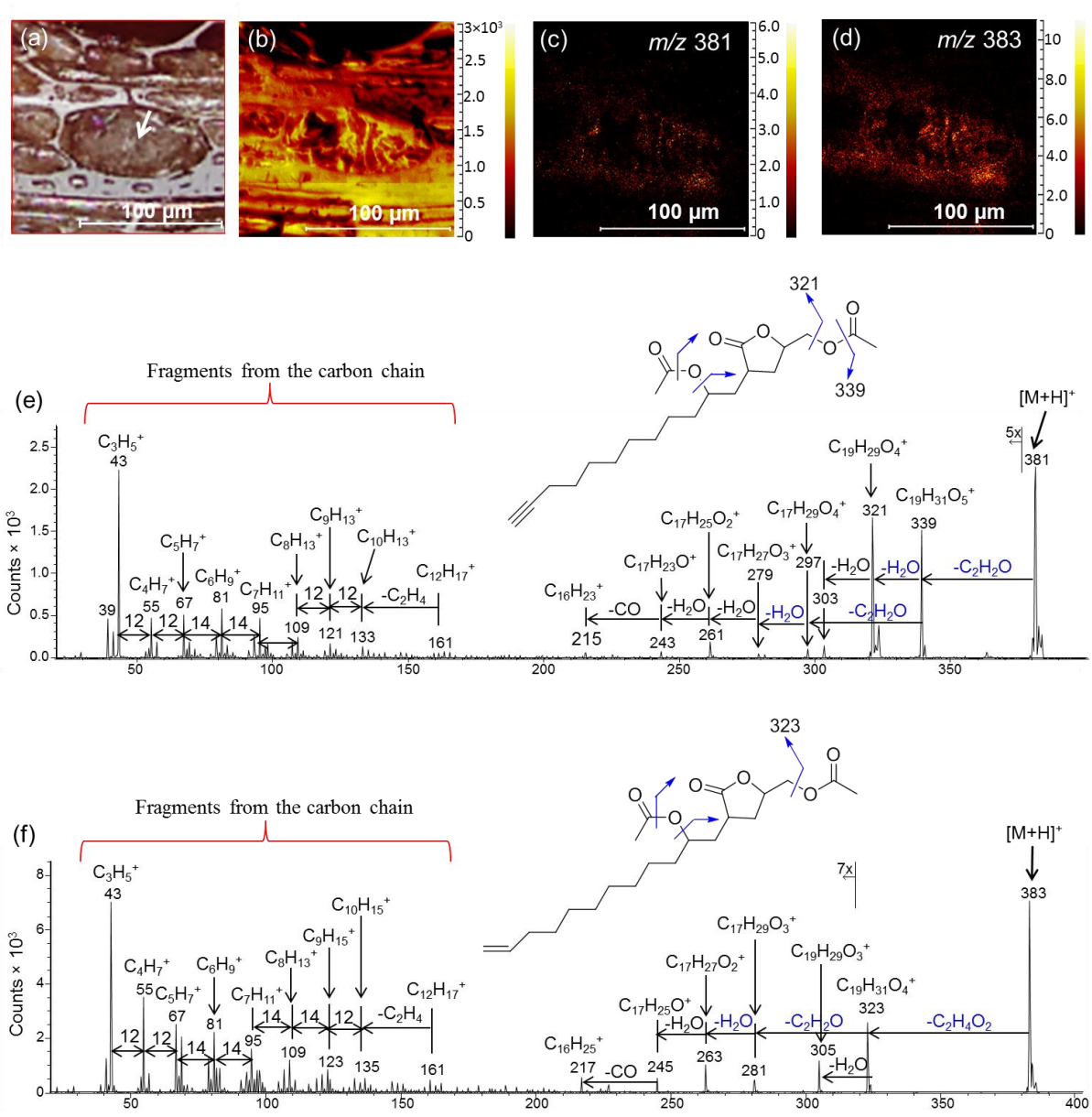

Figure 2: Tandem MS/MS TOF-SIMS imaging. (a) Optical image of sapwood surface with an oil cell (indicated by the white arrow). (b) Total MS^1 ion image collected on the area shown in (a). (c) Total MS^2 ions of precursor ion at *m/z* 381 (compound **4**). (d) Total MS^2 ions of precursor ion at *m/z* 383 (compound **5**). (e) Tandem mass spectrum of the precursor ion at *m/z* 381 (compound **4**). (f) Tandem mass spectrum of precursor ion at *m/z* 383 (compound **5**).

4.4.3 Localization of metabolites in the stem wood of *S. rubra*

It is generally recognized that heartwood is transformed from sapwood along with the death of parenchyma cells [40]. Therefore, to study the production of the metabolites in the stem of *S. rubra*, the wood surface from sapwood to heartwood were chemically mapped by TOF-SIMS with a high lateral resolution of ~400 nm. The optical and ion images displayed in

Figure 3 were recorded on analytical areas of 400 µm × 400 µm of sapwood, transition zone and heartwood, respectively. Not surprisingly, molecular ion images of rubrynolide (**7**) (*m/z* 297) and rubrenolide (**8**) (*m/z* 299) have identical distribution and are present throughout the stem wood surface. The summed ion images of these two metabolites show their particular localization in ray parenchyma cell and tyloses in sapwood, oil cell in transition zone, and tyloses in heartwood, respectively (Figure 3d-3f).

After confirming the same cellular localization of individual compounds (Figure S28), molecular ion images of the **1**-**2, 4**-**6** are summed and highlighted (red) in the two-color overlay with the ion images of lignin fragments (green). It is revealed that compounds **1**-**2, 4**-**6** are co-localized in the same cell types as rubrynolide (**7**) and rubrenolide (**8**) except that they are barely present in the heartwood (Figure 3g-3i, Figure S27), which is in accordance with the NMR analysis.

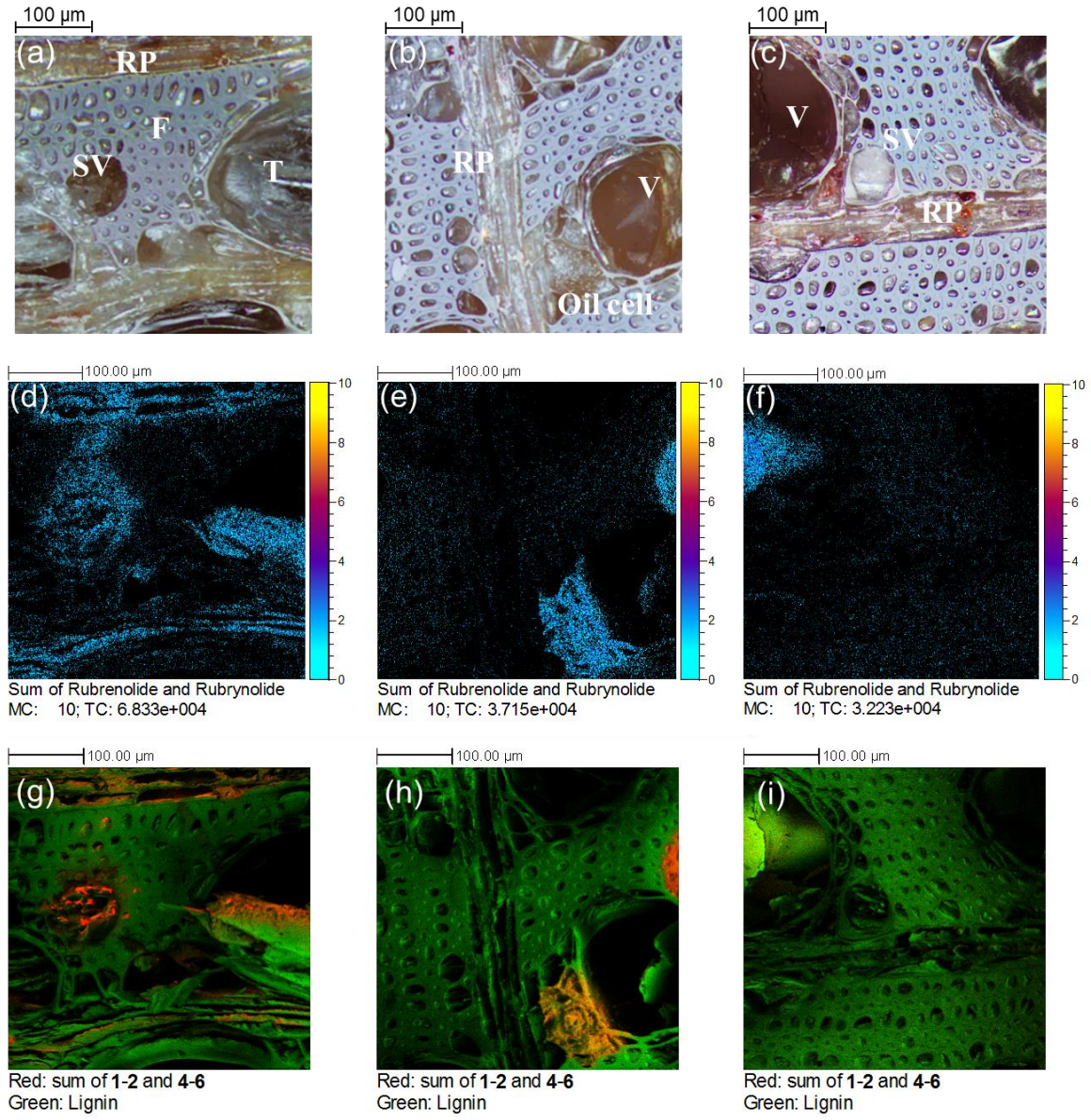

Figure 3: Distribution of secondary metabolites from sapwood to heartwood. a-c: Optical images of sapwood (a), transition zone (b), and heartwood (c). RP: Ray parenchyma cell; F: Fiber; SV: small vessel; V: Vessel; T: Tyloses. d-f: Ion images of rubrynolide (**7**) and rubrenolide (**8**) in sapwood (d), transition zone (e), and (f). The images were compressed to 512 × 512 pixels to increase the contrast. g-i: Two-color overlay ion images of compounds **1-2, 4-6** and lignin fragments in sapwood (g), transition zone (h) and heartwood (i). Ion images summed for compounds **1-2, 4-6**: compound **1**, *m/z* 279, $[M+H]^+$; compound **2**, *m/z* 281, $[M+H]^+$; compound **4**, *m/z* 381, $[M+H]^+$, *m/z* 403, $[M+Na]^+$; *m/z* 419, $[M+K]^+$; compound **5**, *m/z* 383, $[M+H]^+$, *m/z* 405, $[M+Na]^+$; *m/z* 421, $[M+K]^+$; compound **6**, *m/z* 385, $[M+H]^+$, *m/z* 407, $[M+Na]^+$; *m/z* 423, $[M+K]^+$.

4.4.4 3D distribution of the metabolites

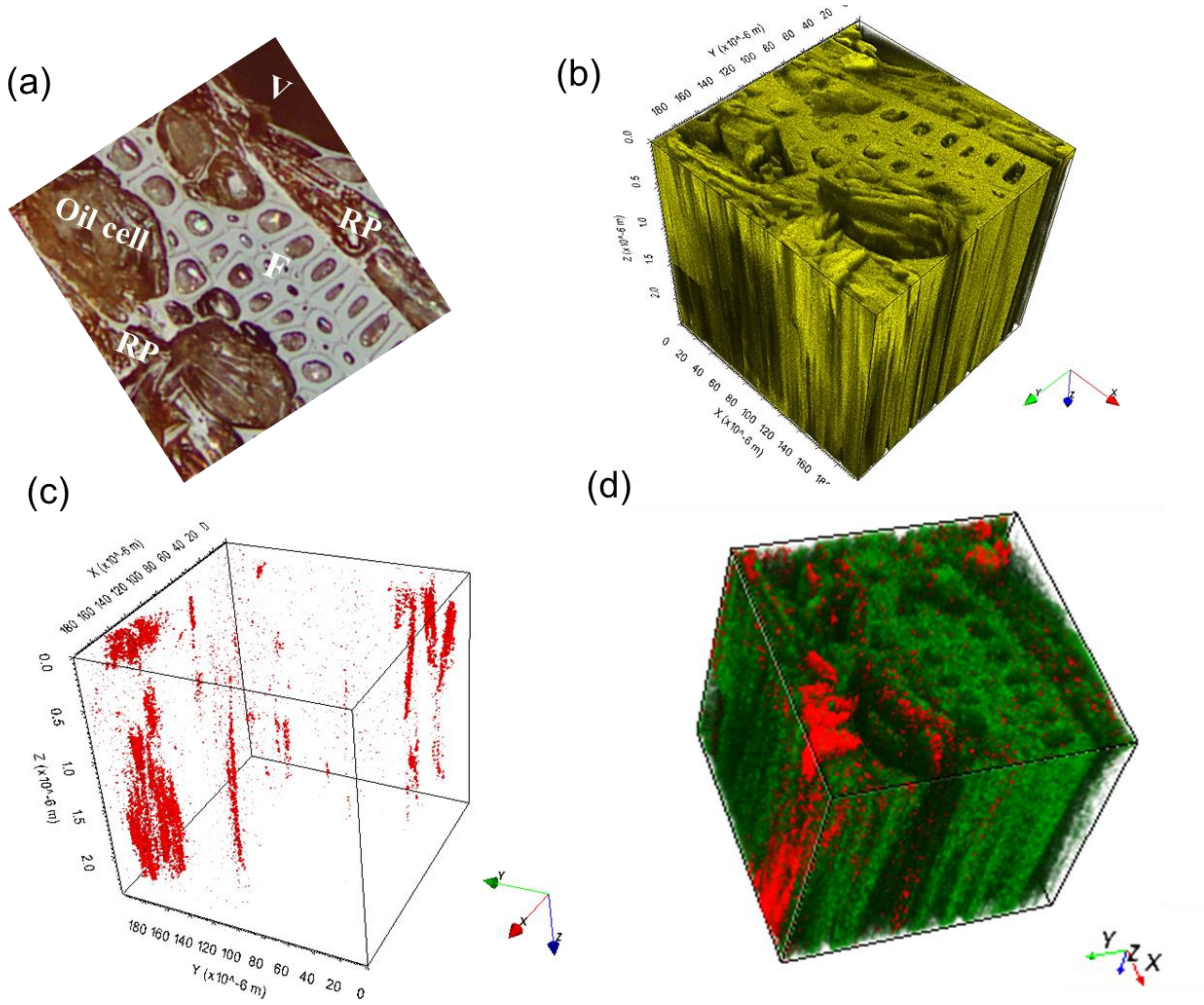

Figure 4: 3D distribution of compound **5**. (a) Optical image of the wood sample from transition zone. (b) 3D reconstruction of total ions. (c) 3D reconstruction of the ion at *m/z* 421 $[M+K]^+$ (compound **5)**. (d) Two-color overlay of ion at *m/z* 421 $[M+K]^+$ compound **5** and lignin fragment $C_4H_3^+$. Red: *m/z* 421; Green: $C_4H_3^+$.

In order to track the in-depth distribution of these metabolites in the stem wood, three dimensional analyses were carried out on the transition zone wood sample using dual beam TOF-SIMS imaging. A 200 µm × 200 µm area comprises various cell types was chosen for the analysis (Figure 4a) and the resulting total ion images is depicted in Figure 4b. During argon cluster sputtering, sample surface was slightly modified due to the erosion rate difference of the cells (Figure S30). However, owing to the large number of constituents in the argon clusters, the impact energy of individual atoms is extremely low, leading to minimum damage of the samples. Therefore, the wood structure and all the cell types are readily recognizable even after a sputter dose of 1.38 $\times 10^{16}$ ions/cm^2 and dislocations of the metabolites can be negligible. The 3D volume reconstruction of the ion at *m/z* 421 ($[M+K]^+$, compound **5**) (Figure 4c) as well as its overlay with lignin fragment $C_4H_3^+$ Figure 4d)

illustrate its distribution in ray parenchyma cell and oil cell, which corresponds well with the lateral distributions.

4.5 Discussion

The Lauraceae family comprises 2850 known plant species in about 45 genera and has a wide distribution in tropical and subtropical regions. Human beings have been using Lauraceae plants for various purposes (construction, food, drugs, spices and perfume). The chemical diversity of metabolites isolated from Lauraceae plants are relatively diverse including alkaloids, arylpropanoids, nitro-derivatves, 2-pyrones, flavonoids, benzophenones, terpenoids, fatty acids and butanolides [41]. In the latter chemical family, several obtusilactone analogues have been previously found in various genus, such as *Lindera* [42], *Machilus* [43] and *Cinnamomum* [44,45]. Obtusilactones analogues have attracted attention due to their cytotoxic *in vitro* and *in vivo* activities against HeLa cell line and several cancer cell lines [39, 40, 41,46,47,48]. On the other hand, rubrenolide **7** and rubrynolide **8** originally isolated by Gottlieb in 1972 in *S. rubra* wood [3] and recently identified in *Mezilaurus* genus [49], does not show any significant cytotoxic activity against human cells (unpublished results). Only their antifungal and antitermite activities are known, thus demonstrating the ecological role of these metabolites to protect the wood against wood pathogens. We report herein for the first time the presence of obtusilactone derivatives **1**-**3** and butanolides **4**-**6** in *S. rubra* roots and sapwood along with rubrynolide **7**, rubrenolide **8**, rubranolide **9** mostly present in the heartwood. Our results prompt the questioning of biosynthesis of rubrynolide **7** and its analogues.

Parallel MS/MS imaging experiments provided unambiguous *in situ* identification of related constituents and facilitated the attribution of corresponding mass peaks. Subsequent 2D and 3D TOF-SIMS imaging thus enabled spatial examination of the metabolites in the stem wood of *S. rubra*. Molecular ion images reveal that all the detected and isolated constituents are co-localized in three different cell types in sapwood and transition zone: ray parenchyma cells, oil cells and tyloses (vessels), indicating that those constituents maybe biosynthetically related. In heartwood, tyloses are principally arisen from ray parenchyma cells before expanding into the adjacent vessel through cell wall pits [50]. And in Lauraceae, oil cells are enlarged or vertical ray parenchyma cells [51]. Therefore, it is confirmed that ray parenchyma cells are responsible for the biosynthesis of the above metabolites, in agreement with previous observations that wood metabolites are produced in ray parenchyma cell during heartwood formation before being transferred to other tissues [24,52,53].

The earlier biosynthesis pathway proposed by Gottlieb involved a polyketide precursor which could yield the γ-lactone products through a Favorsky-type rearrangement (Figure 5). This

polyketide route had satisfactorily explained many natural products with terminal alkene-alkyne pairs from Lauraceae and it was considered that rubrynolide shall be biosynthetically analogous to those constituents [11]. However, the structural determination of isolated isozuihoenalide (**3**) along with our MS detection of butanolides **4**, **5**, **6** suggest that the polyketide pathway is probably not an appropriate route. An alternative route involves two precursors: a succinic acid derivative formed through the citric acid cycle and a *β*-keto acid entity synthesized via acetyl-CoA metabolism. In this case, the rubrynolide biosynthesis starts with the formation of an ester, followed by an aldol type ring closure process between the enol form of the *β*-keto acid and the succinic acid carboxyl group (Figure 5). This pathway is similar to that of a number of natural products containing tetronic acid nucleus [54], substituted lactones and butanolides [55,56] and to the biosynthesis of carolic and carlosic acids in *Penicillium Charlesii* demonstrated using ^{14}C isotopic enrichment [57].

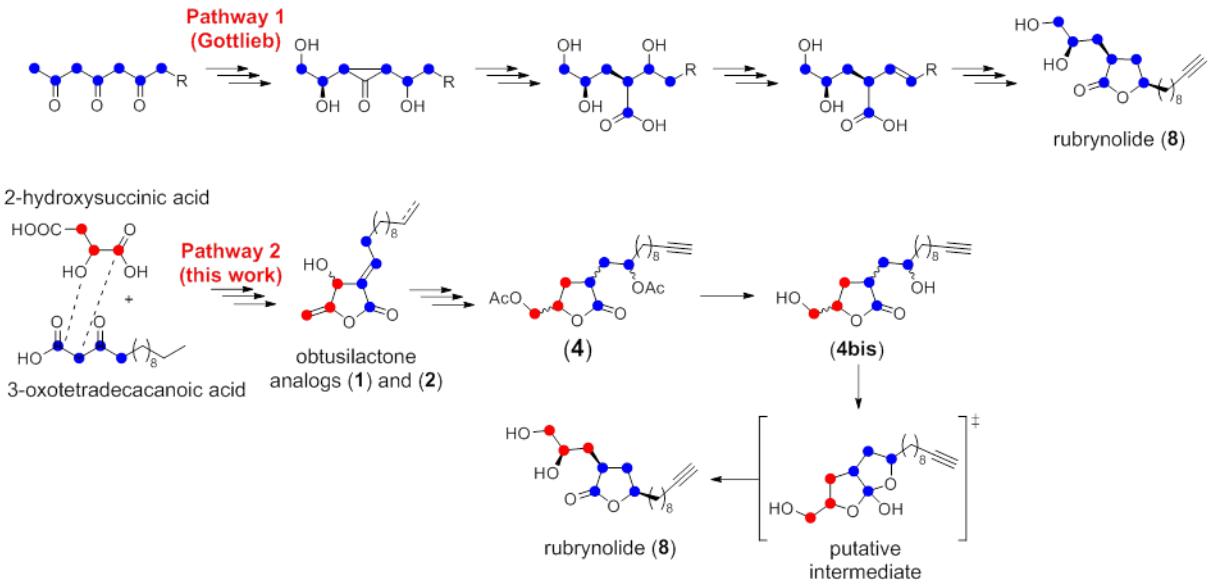

Figure 5: Possible biosynthetic pathways for the formation of rubrynolide and its derivatives. Top: polyketide pathway proposed by Gottlieb; bottom: biosynthesis pathway proposed in this report.

Many chemical entities found in the Lauraceae family such as 2-pyrones, chalcones, and avocatins are believed to be derived from polyketide chains [16], so that the terminal alkene-alkyne pairs can be readily generated by decarboxylation of the precursor as suggested by Gottlieb. However, the enzymatic formation of the terminal triple bond should be considered as many acetylenase have been sequenced recently after being isolated from plants, insects and microorganisms [58].

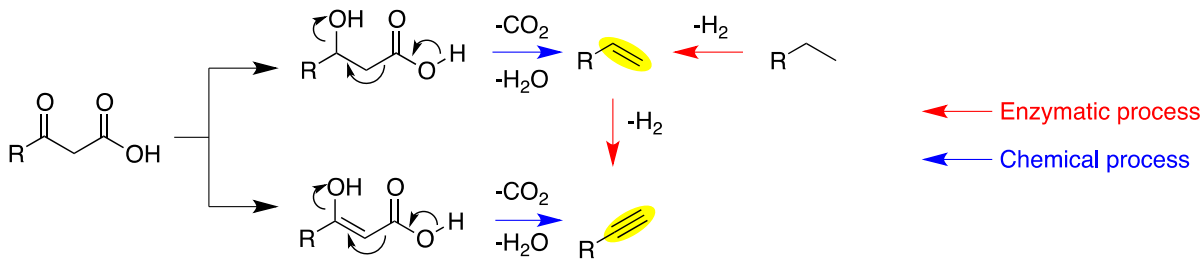

Figure 6: Possible formation of the terminal double and triple bonds.

Nevertheless, 2-hydroxysuccinic acid and β-keto acid precursors shown in the proposed pathway were not able to be detected, therefore there are still controversial aspects in the biosynthesis of rubrynolide and rubrenolide as well as their analogues such as obtusilactone derivatives [59]. Further investigation of tree species from Lauraceae family will be essential to prove the biosynthetic pathways, using either isotopic enrichment with ^{13}C-labelled 2-hydroxysuccinic acid or using ^{13}C NMR at natural abundance to potentially measure isotopic differences between carbons in the lactone and in the 1propane 1,2-diol moiety suggesting the coupling of two precursors [60].

4.6 Conclusion

Reinvestigation of the stem wood of *S. rubra* led to the isolation of isozuihoenalide **3** and butanolides **4**, **5** which are structurally related to bioactive metabolites rubrynolide and rubrenolide. TOF-SIMS imaging provided spatial information of the related metabolites by *in situ* identification and multidimensional mapping of the corresponding quasi molecular ions and the salt adducts. These results indicate that the biosynthesis of rubrynolide and rubrenolide is probably not derived from a single polyketide. Therefore, a new biosynthetic pathway involving an aldol type ring closure and a penta-lactone ring rearrangement in the ray parenchyma cell is proposed for the genetic formation of rubrynolide and its analogues. This new biosynthetic route is in good accordance with the presence of the trace intermediates detected in high resolution LC-MS/MS and would provide new insights in the genetic production of other related natural products. Nevertheless, further investigation using isotopic enrichment method will be beneficial to decipher the whole biosynthetic process.

4.7 Acknowledgements

This work was supported by the Agence Nationale de la Recherche (grant ANR-2015-CE29-0007-01 DEFIMAGE), and has benefited from an “Investissement d’Avenir” grant managed by Agence Nationale de la Recherche (CEBA, ref. ANR-10-LABX-25-01). TF would like to acknowledge financial support from China Scholarship Council (CSC, No. 201406310013).

This work has benefited from the facilities and expertise of the Electron Microscopy facilities of Imagerie-Gif (http://www.i2bc.parissaclay.fr/spip.php?article282).

4.8 Supporting information

4.8.1 LC-Q-TOF MS analysis of ethyl acetate extracts of leaves, bark, sapwood and heartwood of *S. rubra*

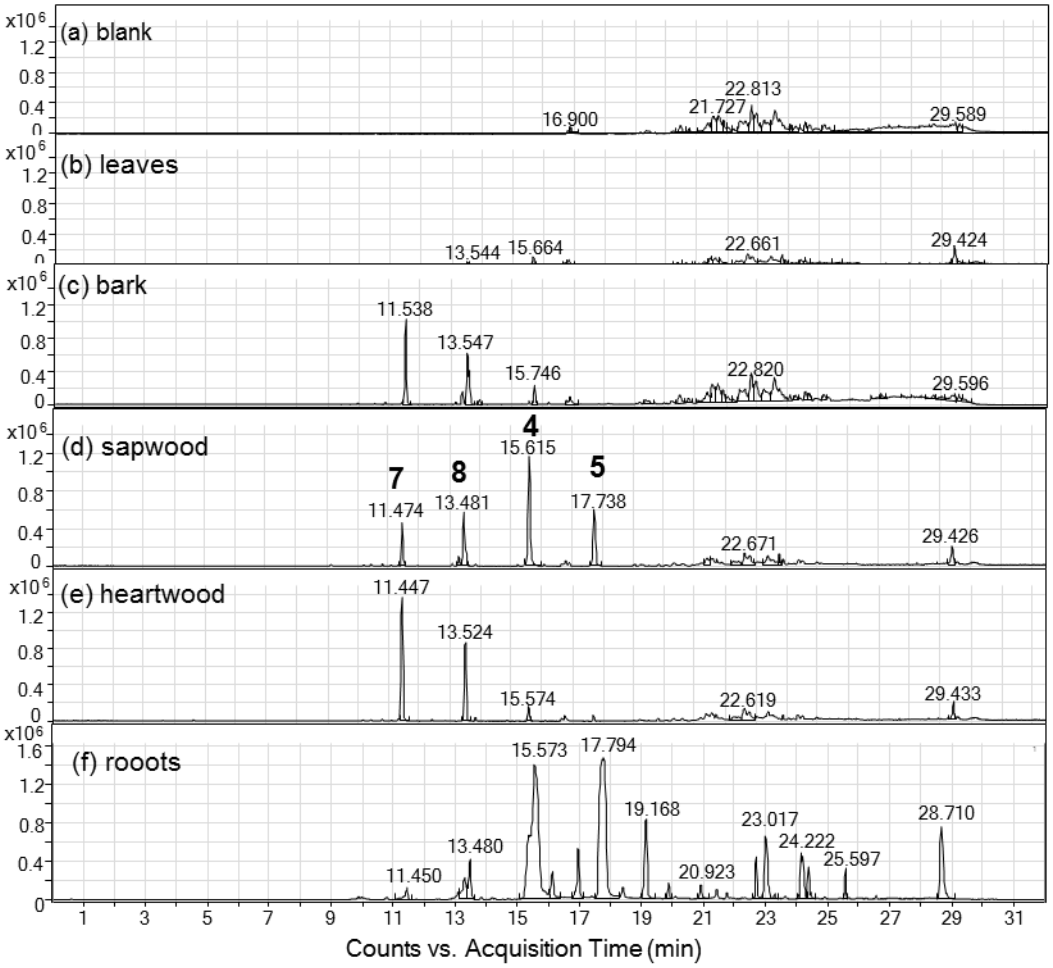

Figure S1: Liquid chromatogram of ethyl acetate extracts of leaves, bark, sapwood, heartwood, and roots of *S. rubra*. The main components are indicated in (d).

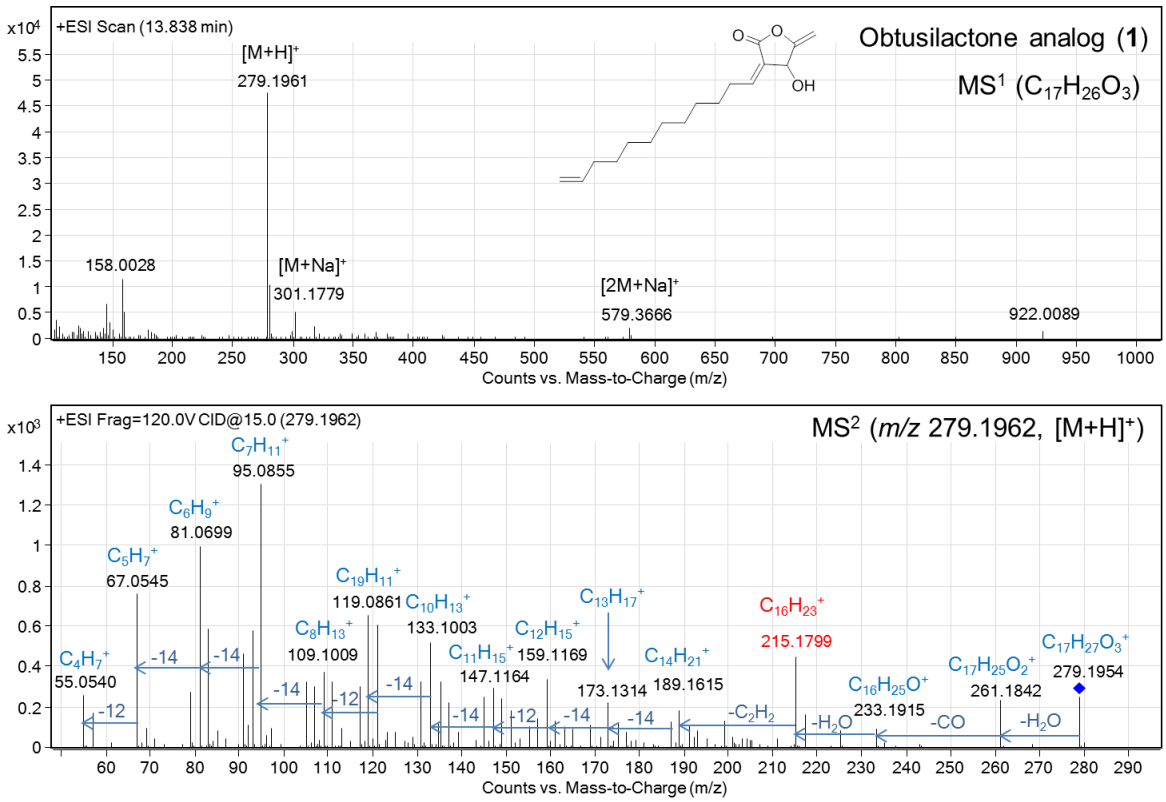

Figure S2: MS^1 and MS^2 spectra of obtusilactone analog (**1**) from sapwood extract (RT=13.838 min)

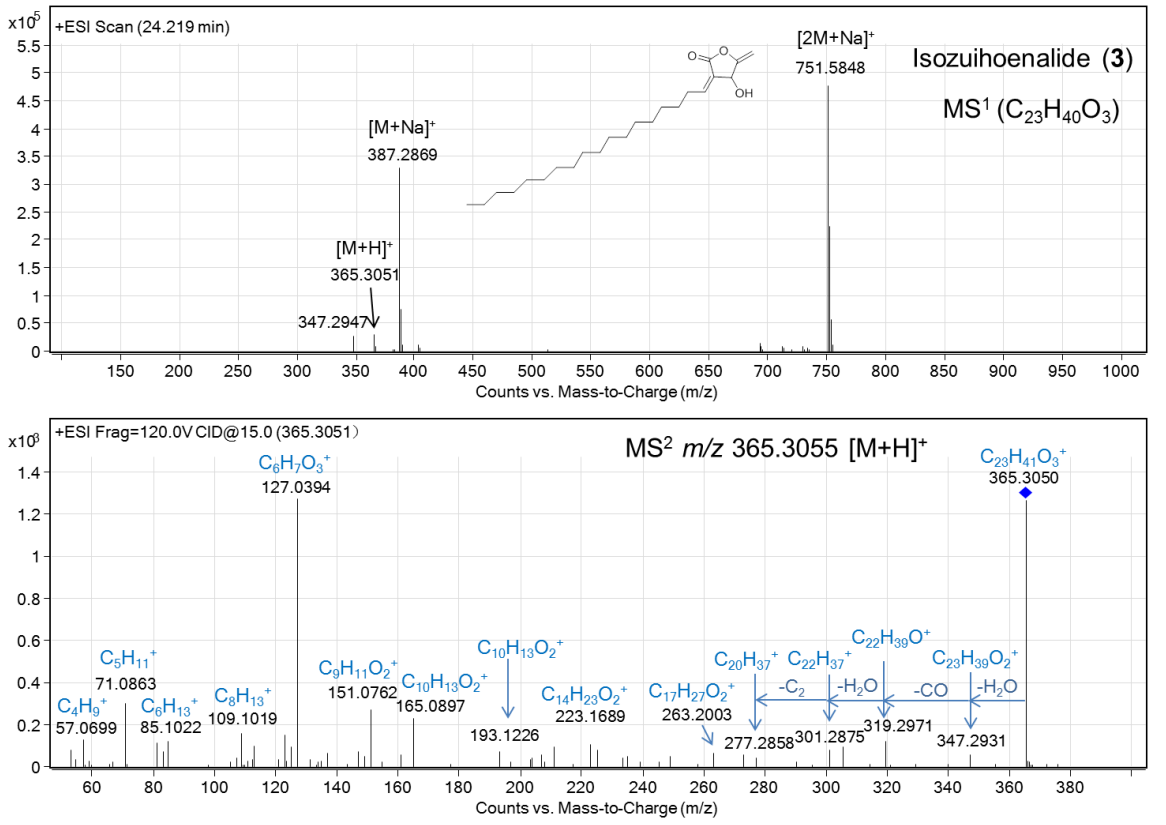

Figure S3: MS^1 and MS^2 spectra of isozuihoenalide (**3**) from roots extract (RT=24.219 min).

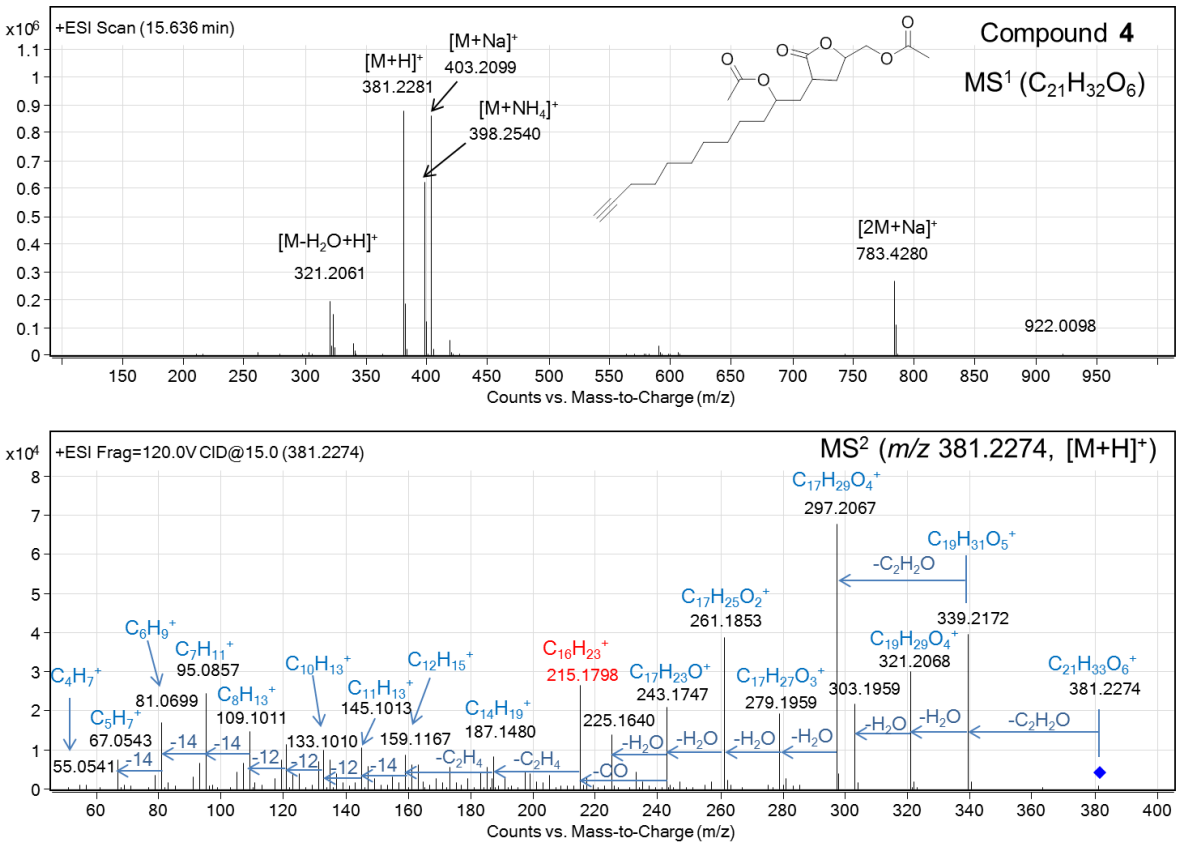

Figure S4: MS^1 and MS^2 spectra of compound **4** from sapwood extract (RT=15.615 min).

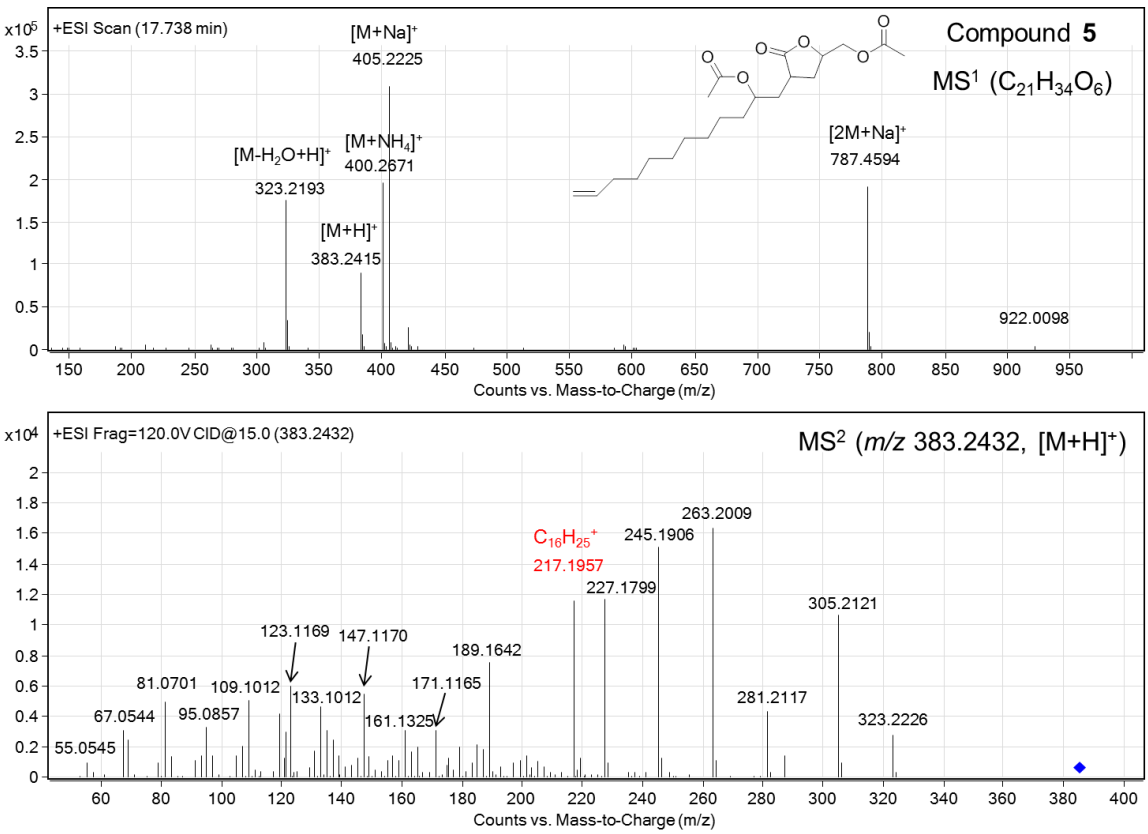

Figure S5: MS^1 and MS^2 spectra of compound **5** from sapwood extract (RT=17.738 min).

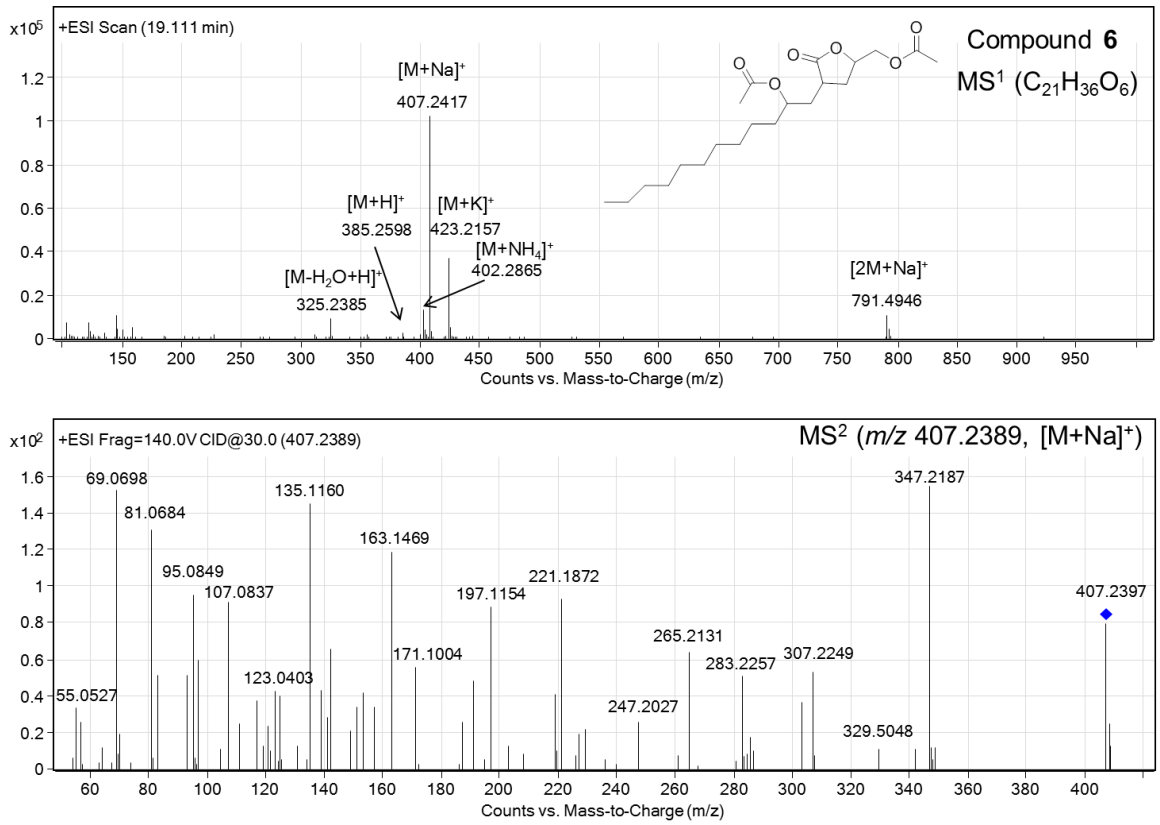

Figure S6: MS^1 and MS^2 spectra of compound **6** from sapwood extract (RT=19.111 min).

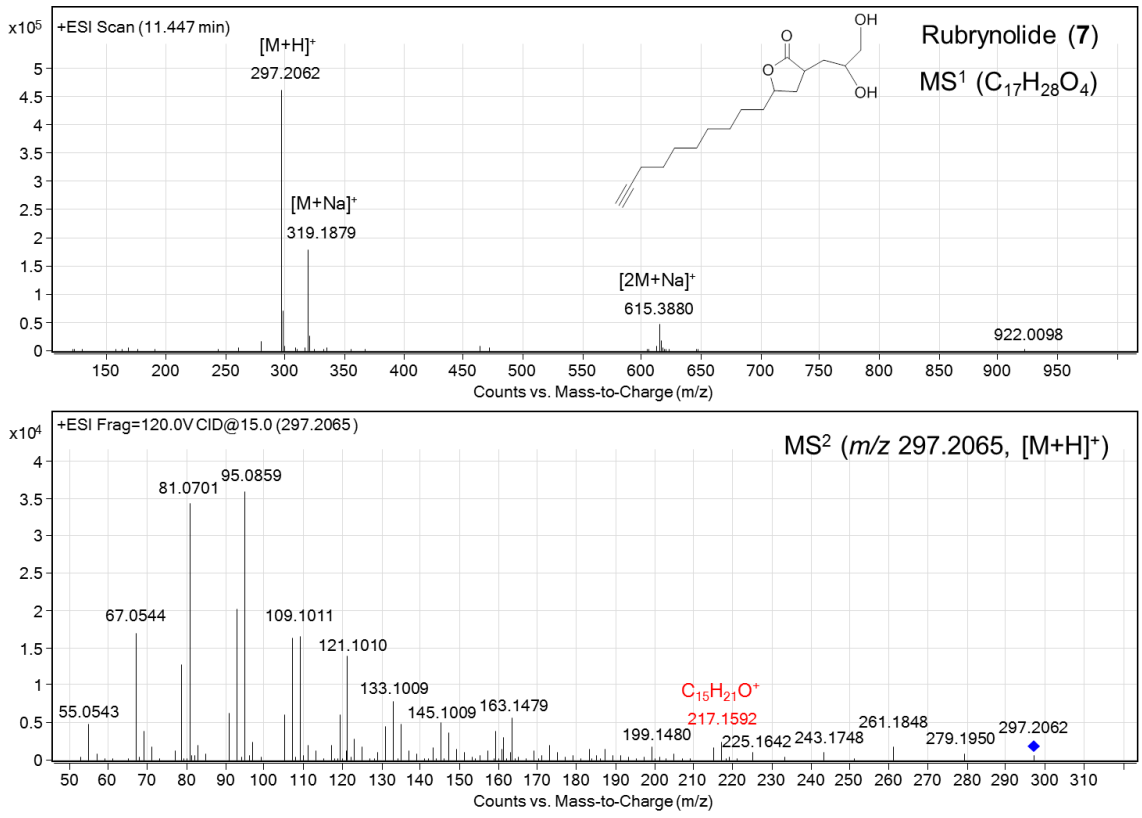

Figure S7: MS^1 and MS^2 spectra of rubrynolide (**7**) from heartwood extract (RT=11.447 min)

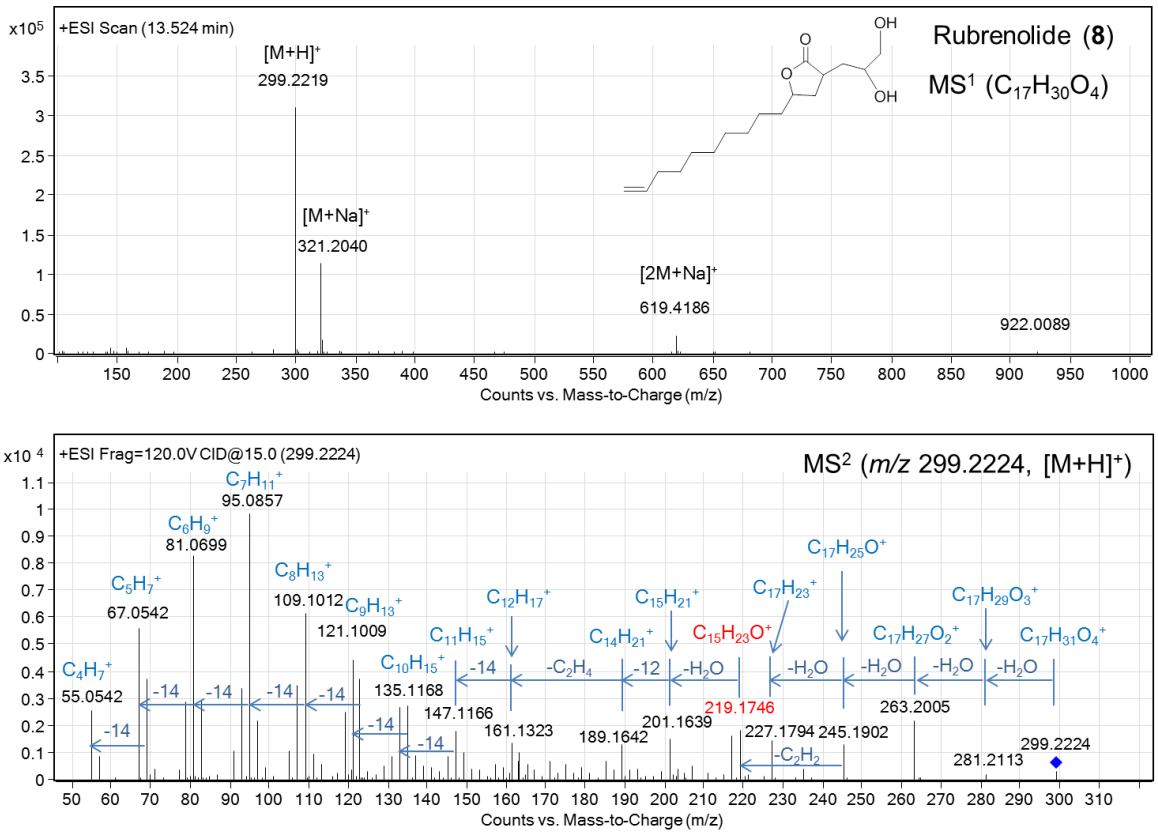

Figure S8: MS^1 and MS^2 spectra of rubrenolide (**8**) from heartwood extract (RT=13.524 min).

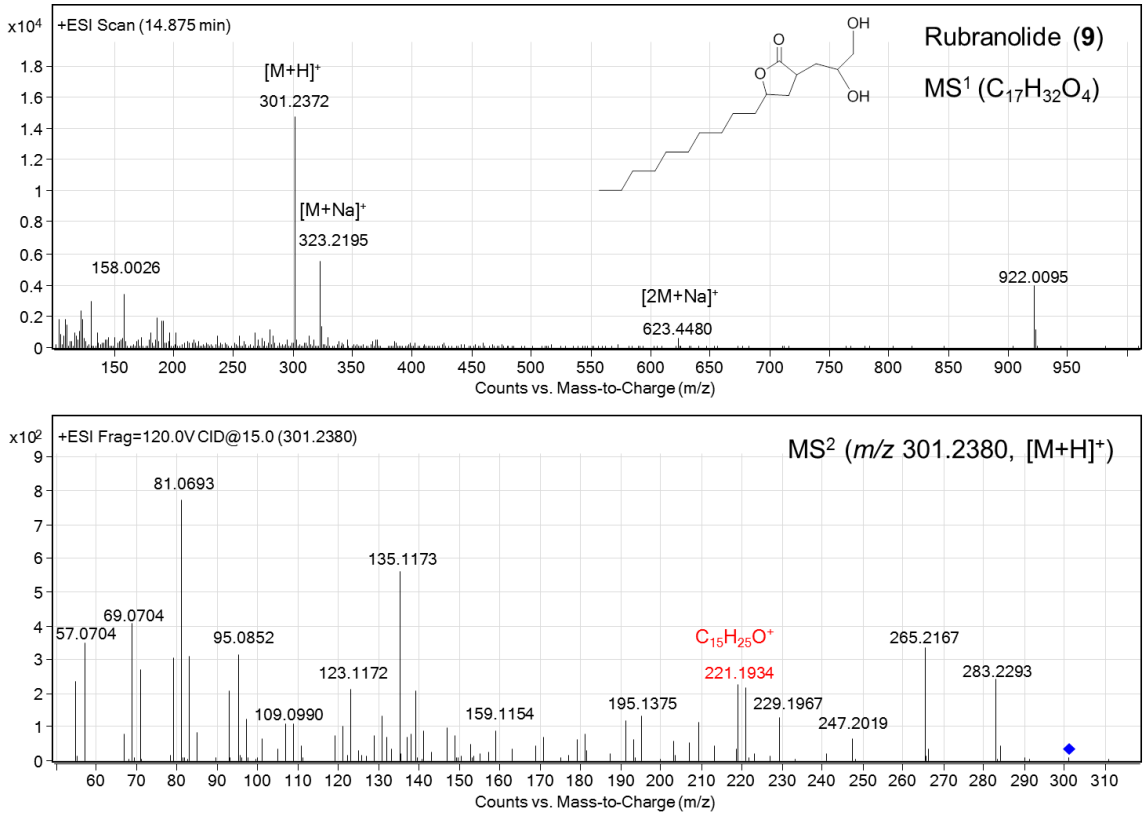

Figure S9: MS^1 and MS^2 spectra of rubranolide (**9**) from heartwood extract (RT=14.880 min).

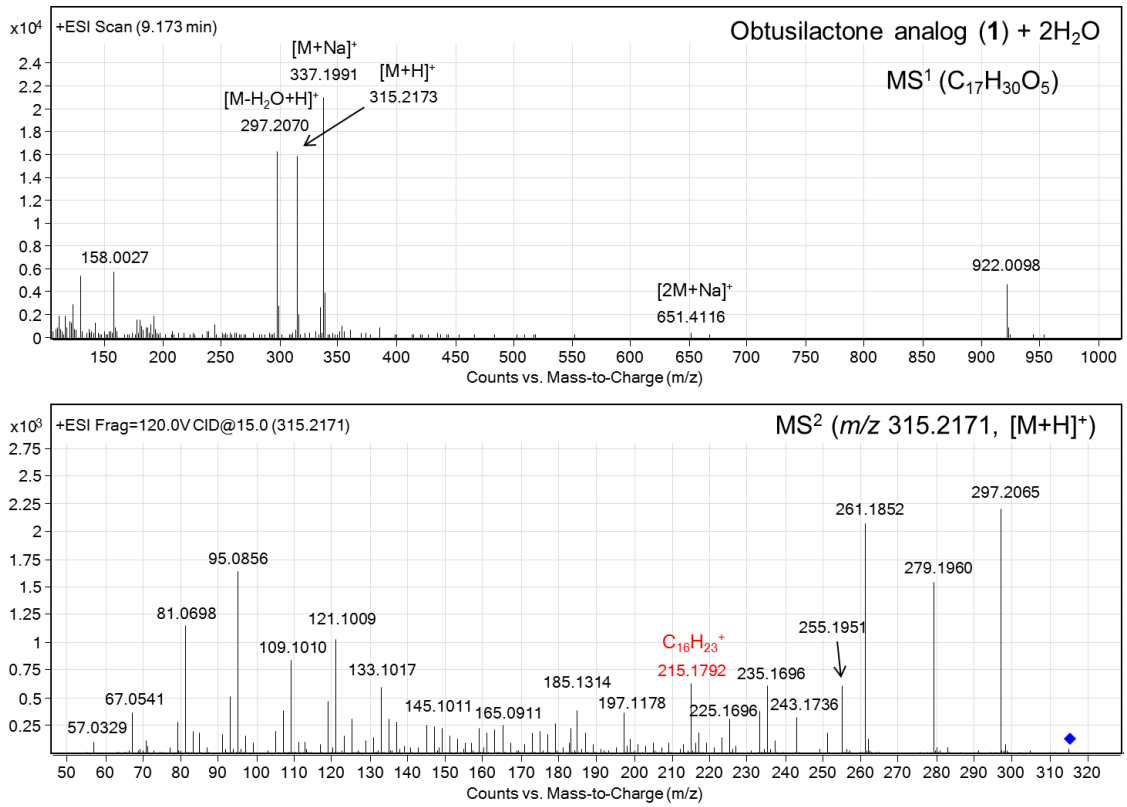

Figure S10: MS^1 and MS^2 spectra of protonated ion at *m/z* 315.2173 from sapwood extract (RT=9.173 min). Proposed as obtusilactone analog (**1**) + $2H_2O$.

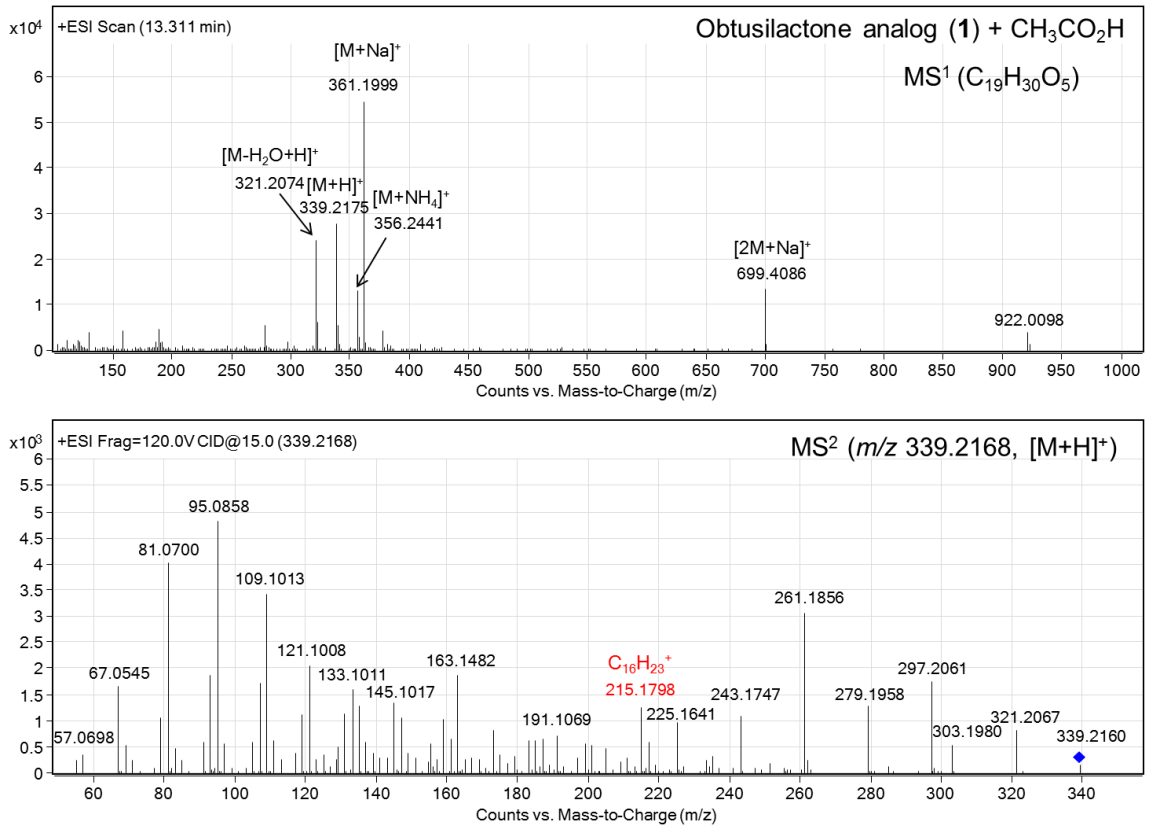

Figure S11: MS^1 and MS^2 spectra of protonated ion at *m/z* 339.2175 from sapwood extract (RT=13.311 min). Proposed as obtusilactone analog (**1**) + CH_3CO_2H.

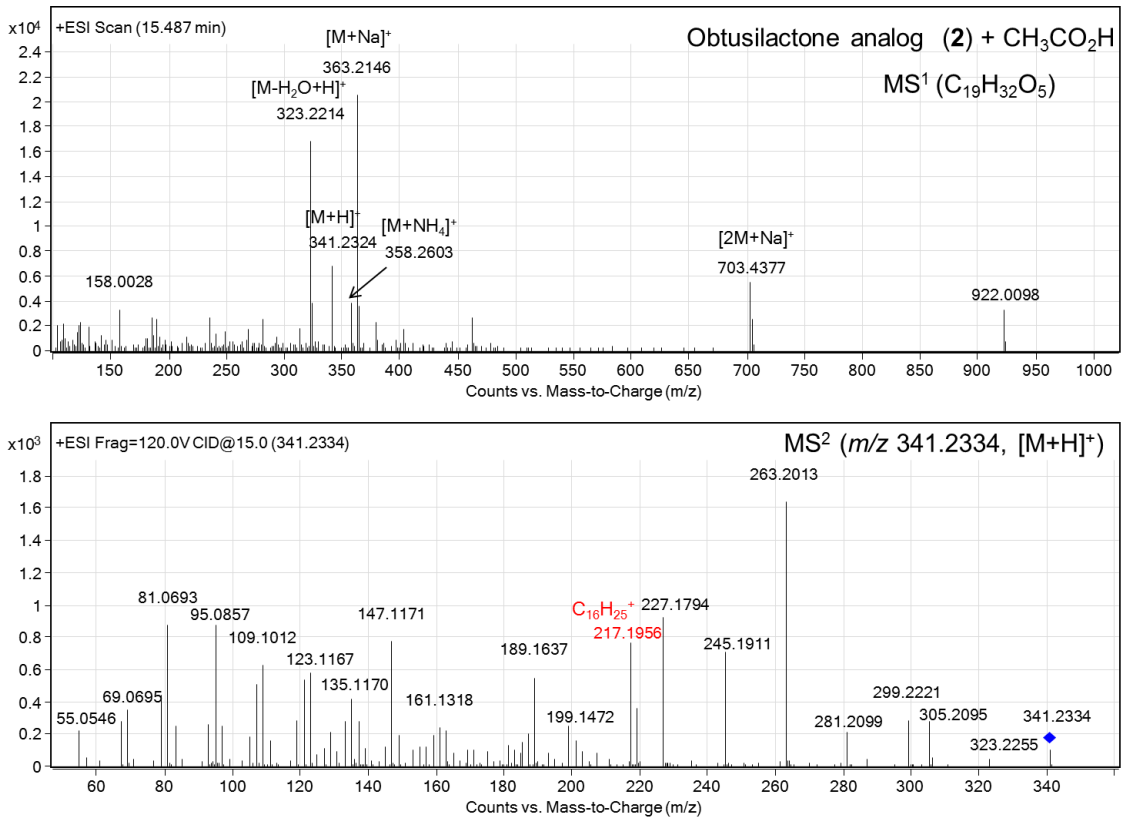

Figure S12: MS^1 and MS^2 spectra of protonated ion at *m/z* 341.2324 from sapwood extract (RT=15.487 min). Proposed as obtusilactone analog (**2**) + CH_3CO_2H.

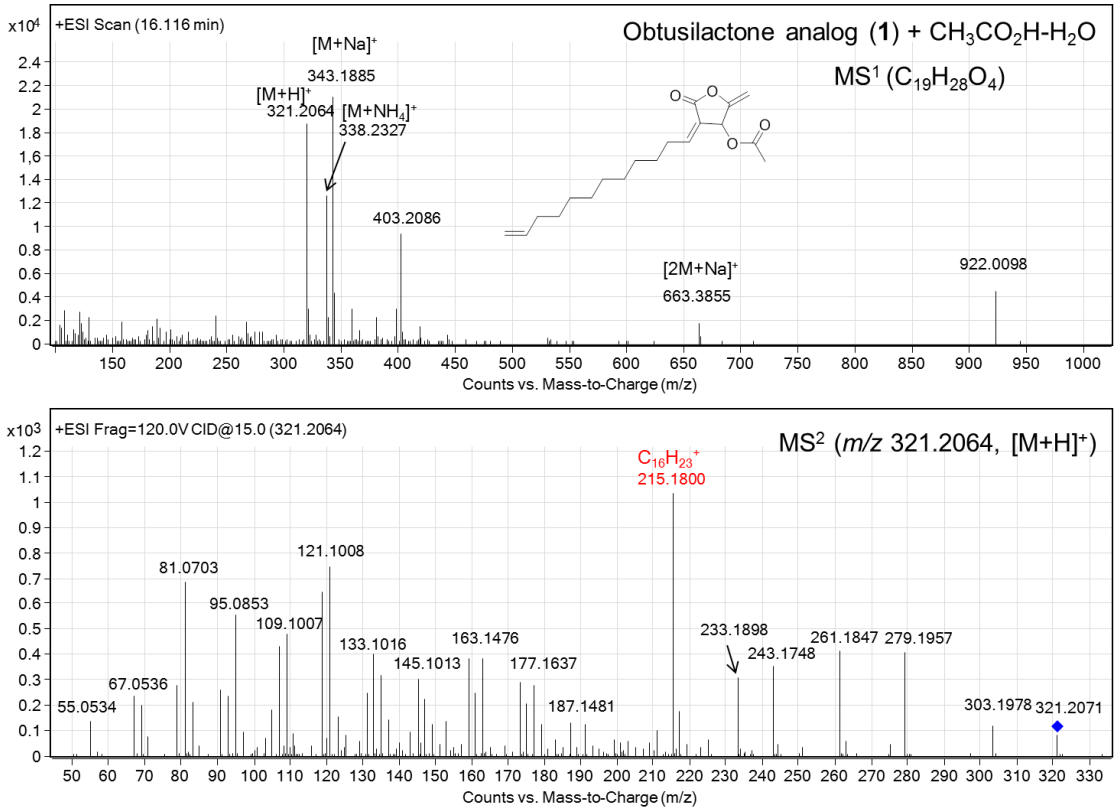

Figure S13: MS^1 and MS^2 spectra of protonated ion at *m/z* 321.2064 from sapwood extract (RT=16.116 min). Proposed as obtusilactone analog (**1**) + CH_3CO_2H-H_2O.

4.8.2 1H NMR and 13C spectra of isozuihoenalide (3), butanolides 4 and 5.

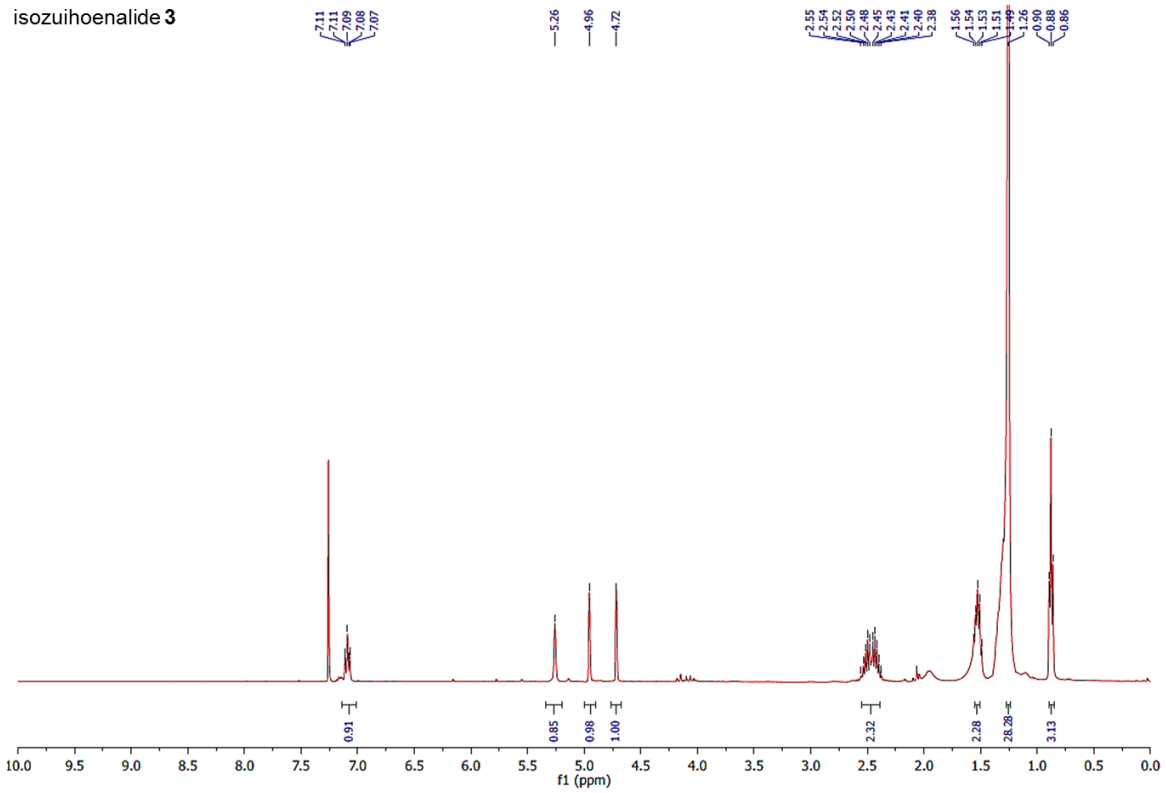

Figure S14: 1H NMR spectrum of isozuihoenalide (**3**).

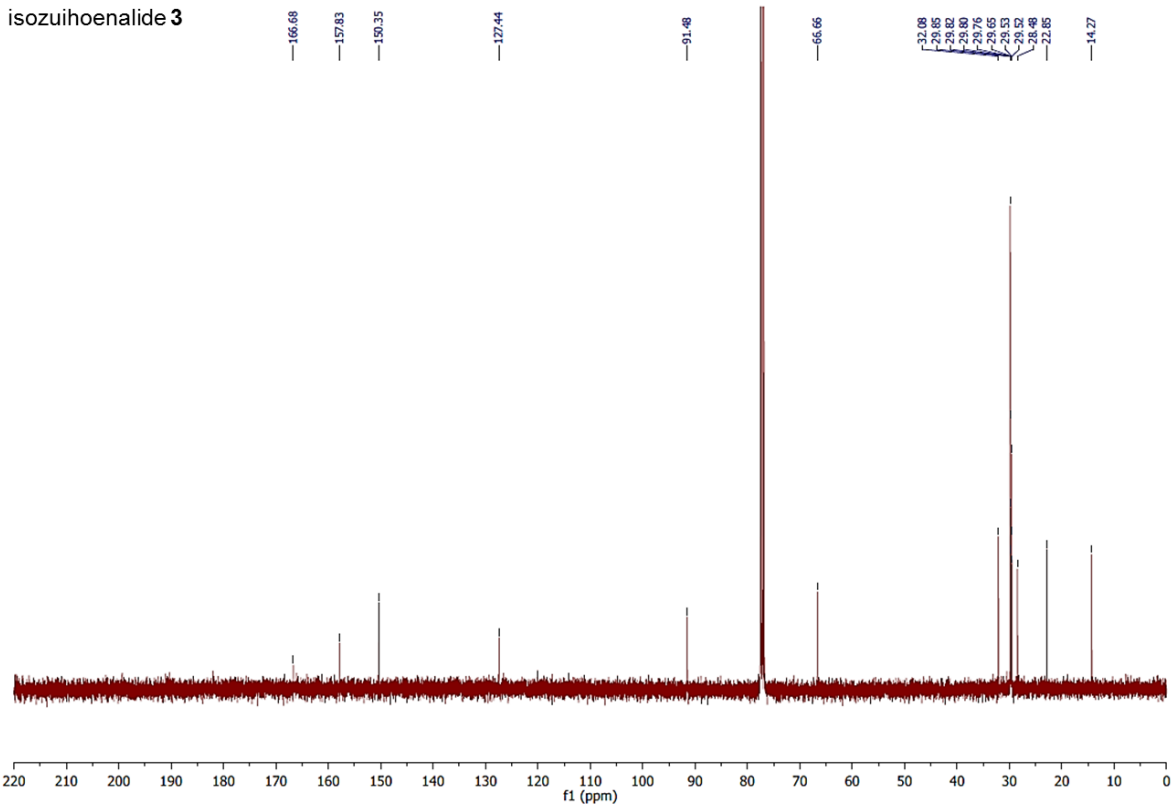

Figure S15: 13C NMR spectrum of isozuihoenalide (**3**).

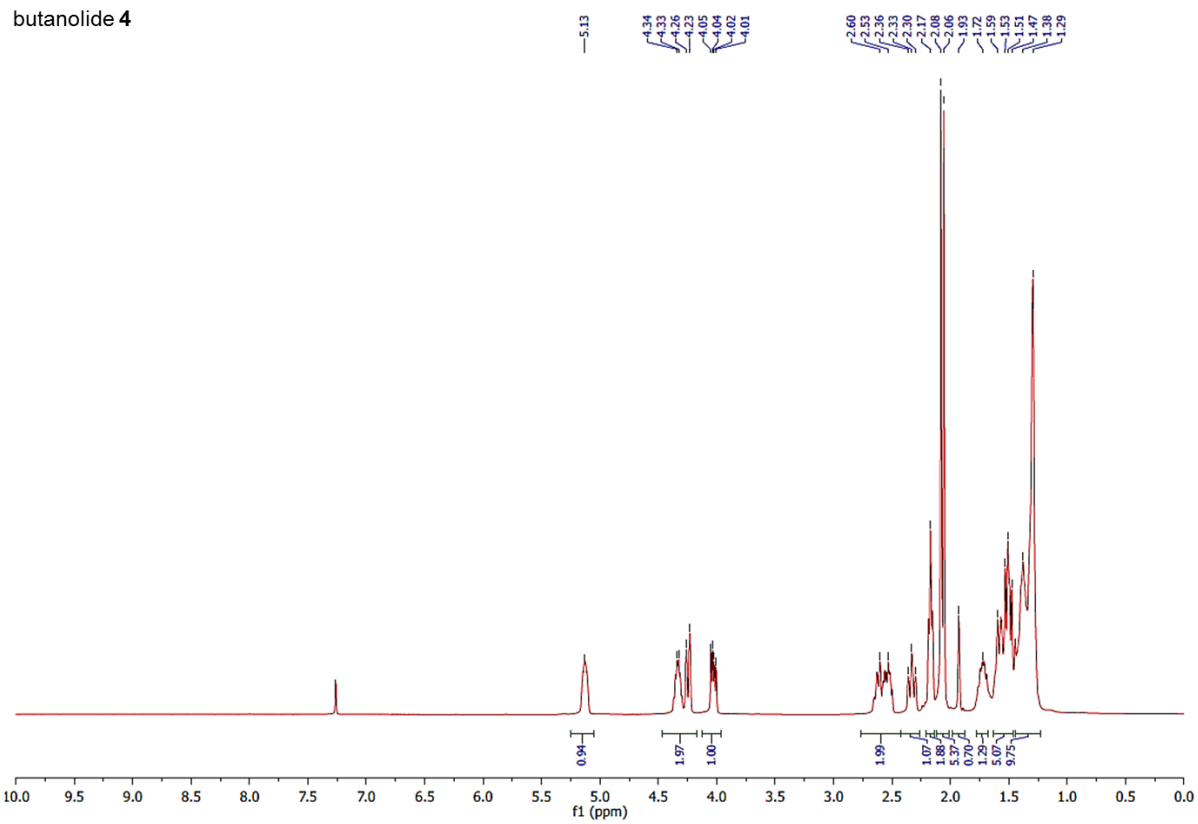

Figure S16: 1H NMR spectrum of butanolide **4**.

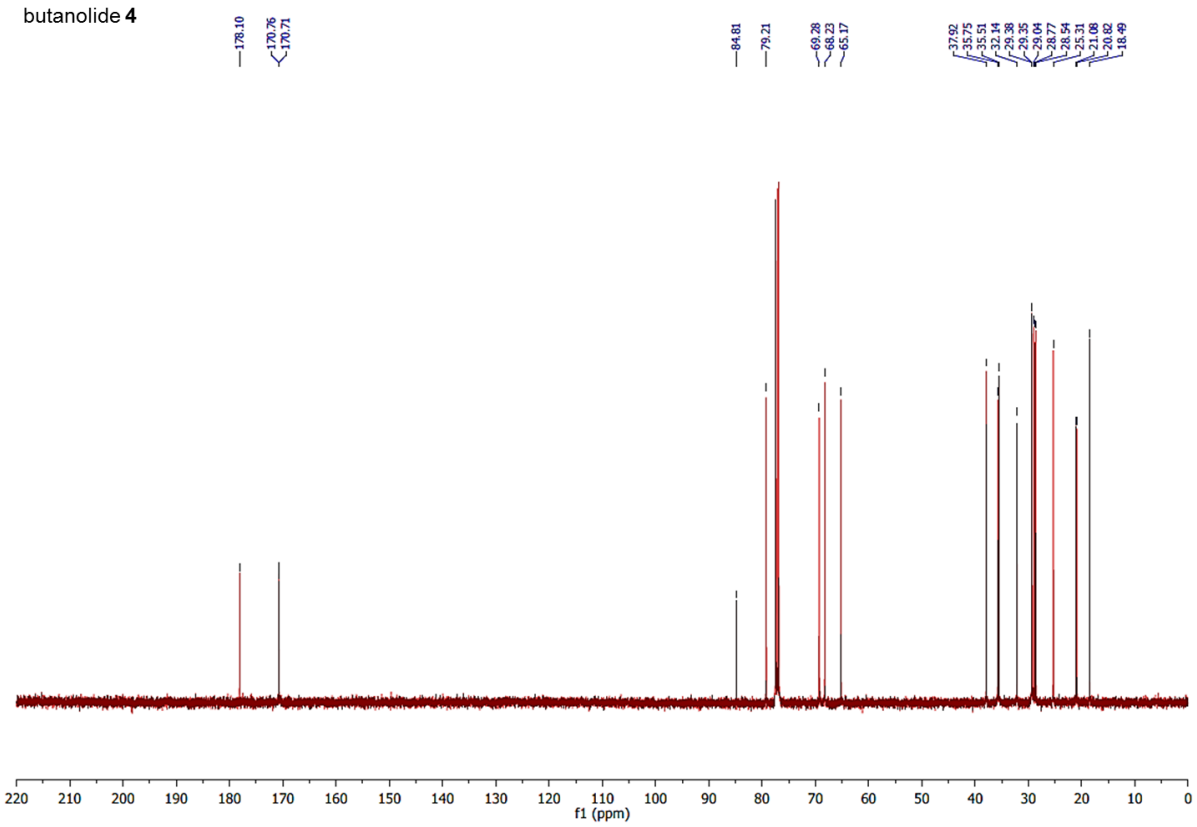

Figure S17: 13C NMR spectrum of butanolide **4**.

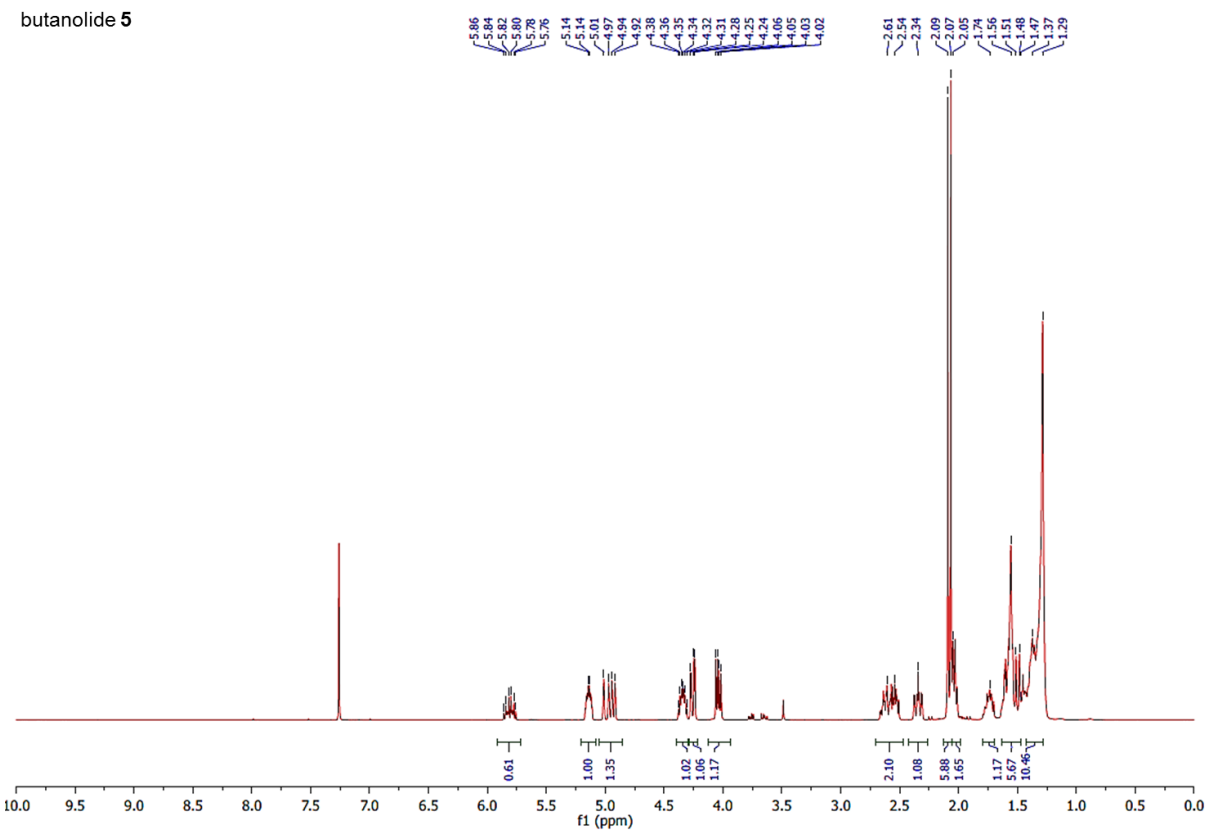

Figure S18: 1H NMR spectrum of butanolide **5**.

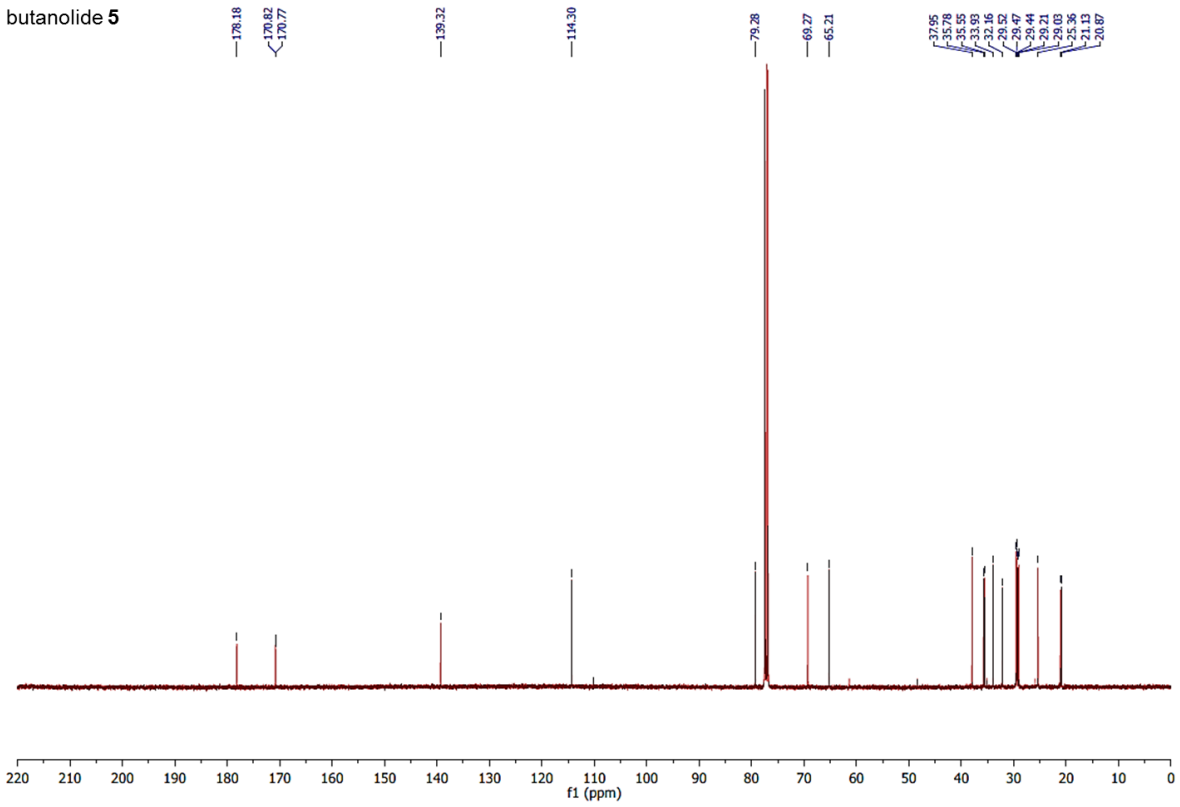

Figure S19: 13C NMR spectrum of butanolide **5**

4.8.3 Quantitative NMR analysis of crude ethyl acetate extracts from different organs of *S. rubra*

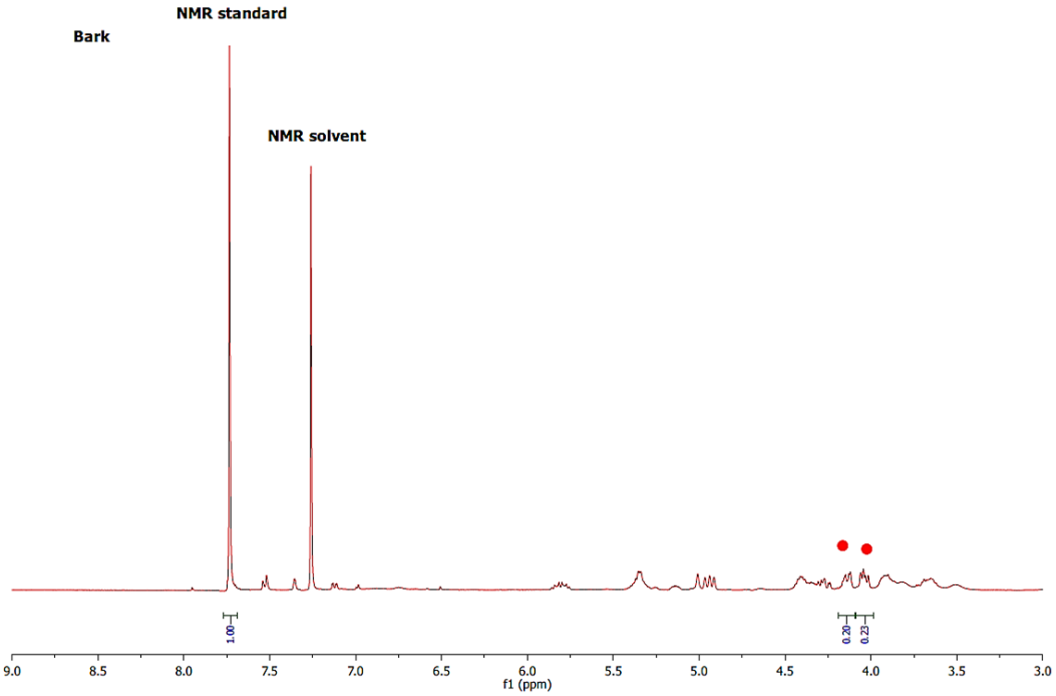

Figure S20: ^{1}H NMR spectra of bark extracts. Red dots show proton ^{1}H NMR signals used for the quantification of metabolites **4**-**5.**

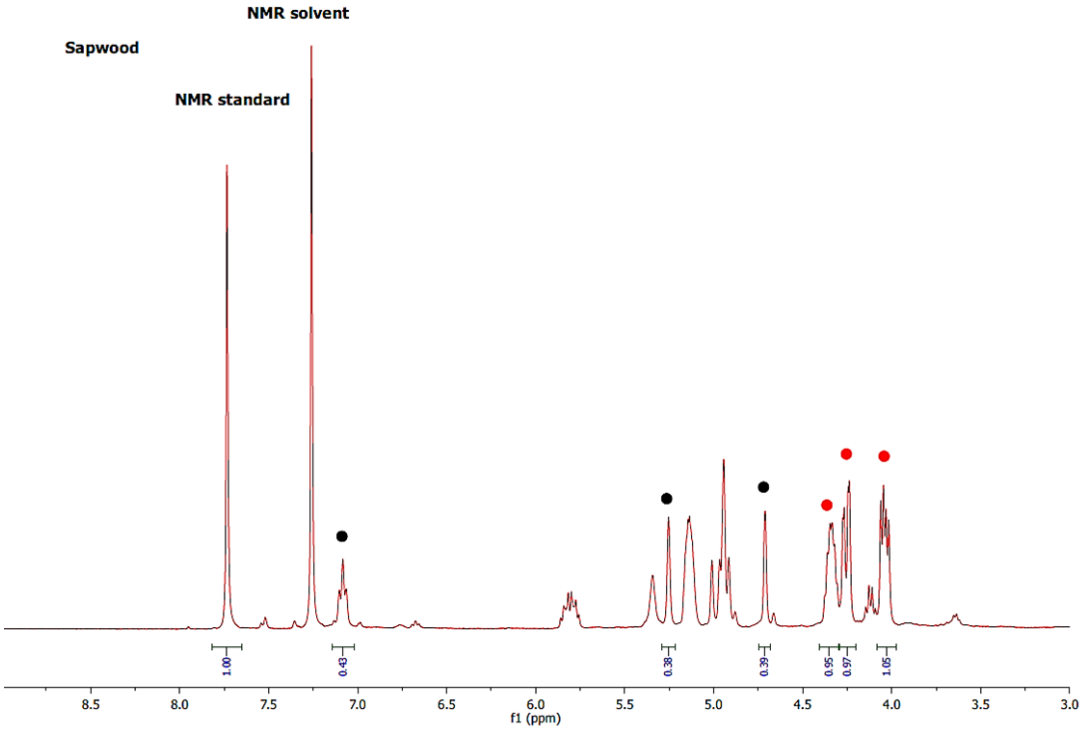

Figure S21: ^{1}H NMR spectra of sapwood extracts. Black and red dots show proton ^{1}H NMR signals used for the quantification of metabolites **3** and **4**-**5**.

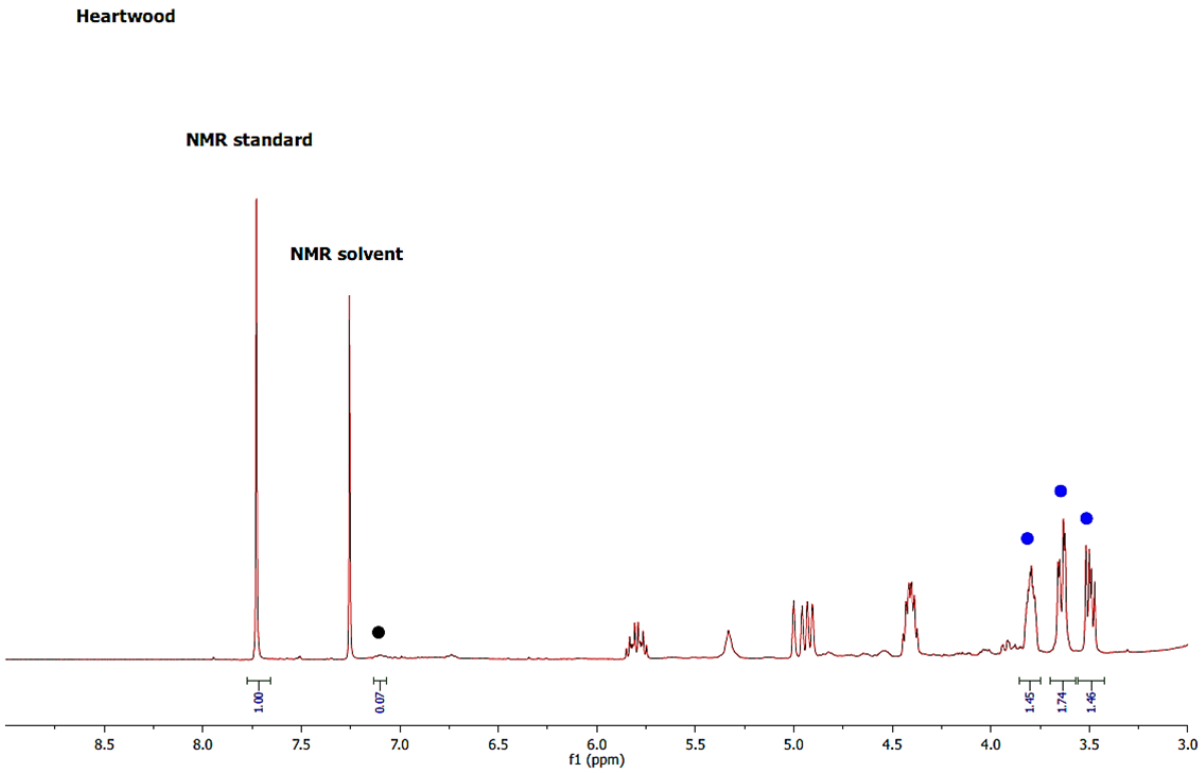

Figure S22: ^{1}H NMR spectra of heartwood extracts. Black and blue dots show proton ^{1}H NMR signals used for the quantification of metabolites **3** and **7**-**8**.

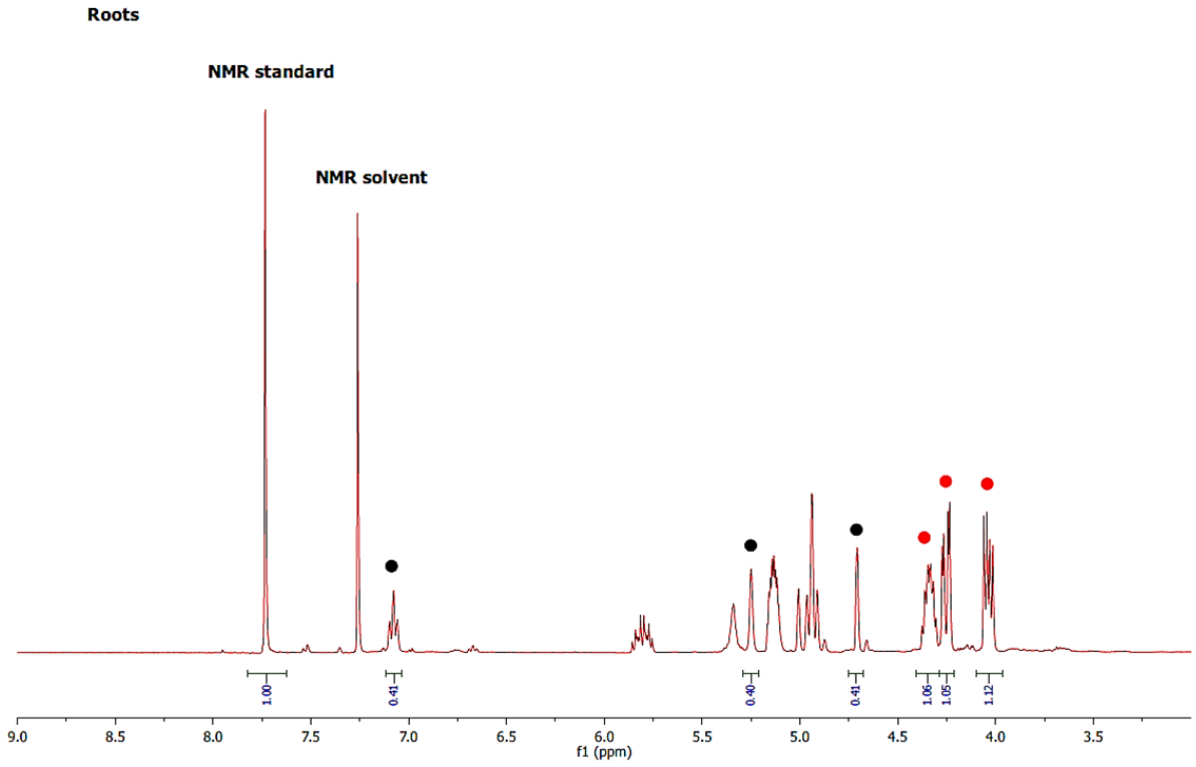

Figure S23: ^{1}H NMR spectra of root extracts. Black and red dots show proton 1H NMR signals used for the quantification of metabolites **3** and **4**-**5**.

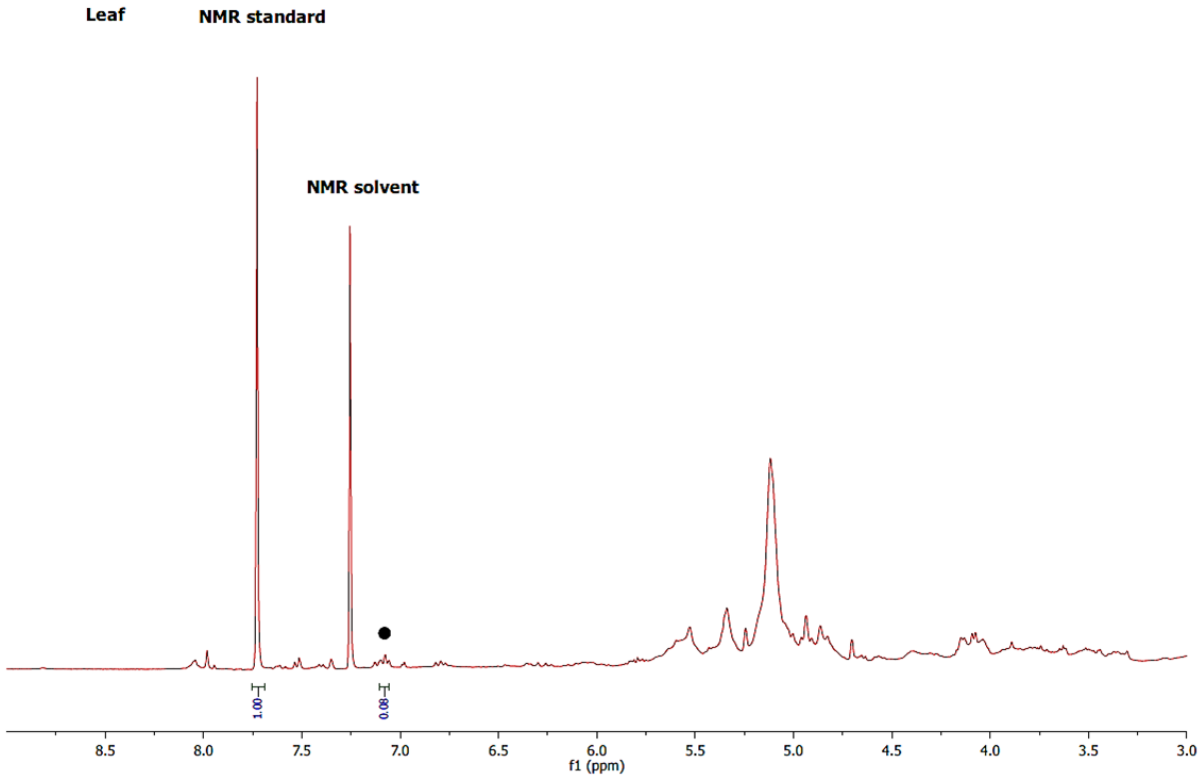

Figure S24: ^{1}H NMR spectra of leaf extracts. Black show proton ^{1}H NMR signals used for the quantification of metabolites **3**.

4.8.4 In situ MS^2 identification of sodium and potassium cationized molecules of butanolides 4 and 5

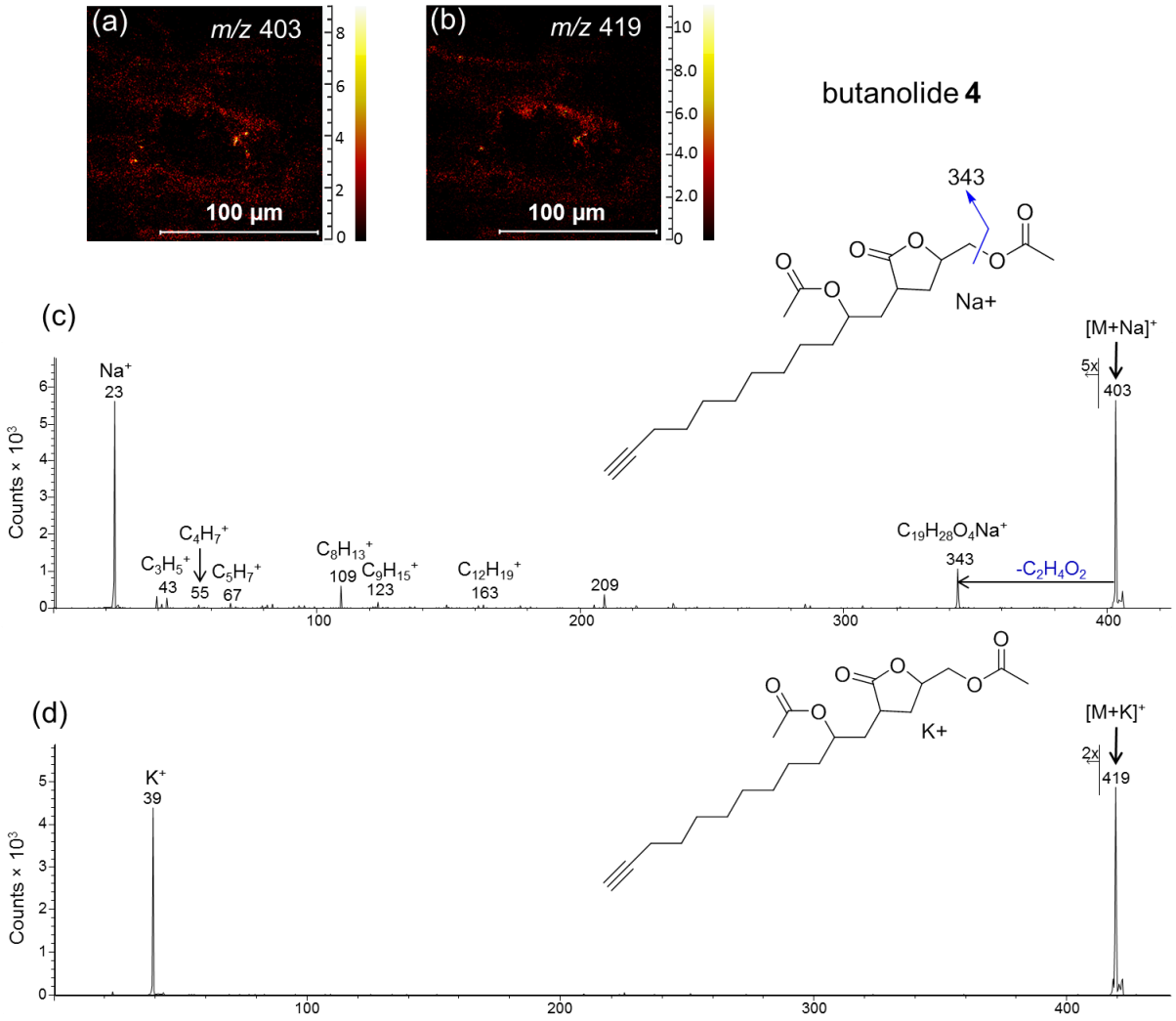

Figure S25: Tandem TOF-SIMS of precursors at *m/z* 403 $[M+Na]^+$ and *m/z* 419 $[M+K]^+$, compound **4**. (a) Total MS^2 ion image of precursor at *m/z* 403 $[M+Na]^+$. (b) Total MS^2 ion image of precursor at *m/z* 419 $[M+Na]^+$. (c) MS/MS spectrum of precursor at *m/z* 403 $[M+Na]^+$. (d) MS/MS spectrum of precursor at *m/z* 419 $[M+K]^+$.

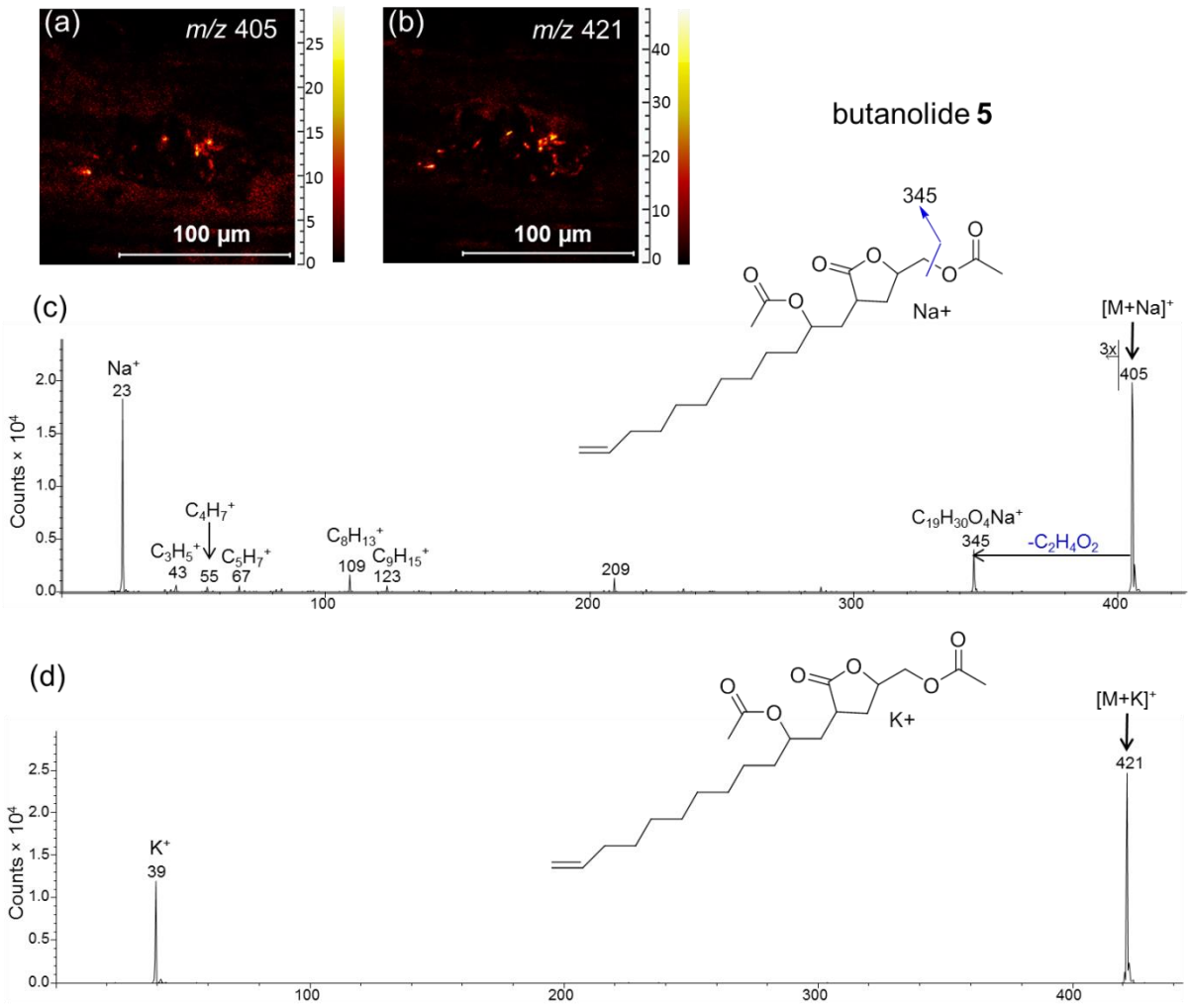

Figure S26: Tandem TOF-SIMS of precursors at *m/z* 405 $[M+Na]^+$ and *m/z* 421 $[M+K]^+$, compound **5**. (a) Total MS^2 ion image of precursor at *m/z* 405 $[M+Na]^+$. (b) Total MS^2 ion image of precursor at *m/z* 421 $[M+Na]^+$. (c) MS/MS spectrum of precursor at *m/z* 405 $[M+Na]^+$. (d) MS/MS spectrum of precursor at *m/z* 421 $[M+K]^+$.

4.8.5 Distribution of compounds 4-6 in the stem wood of *S. rubra*

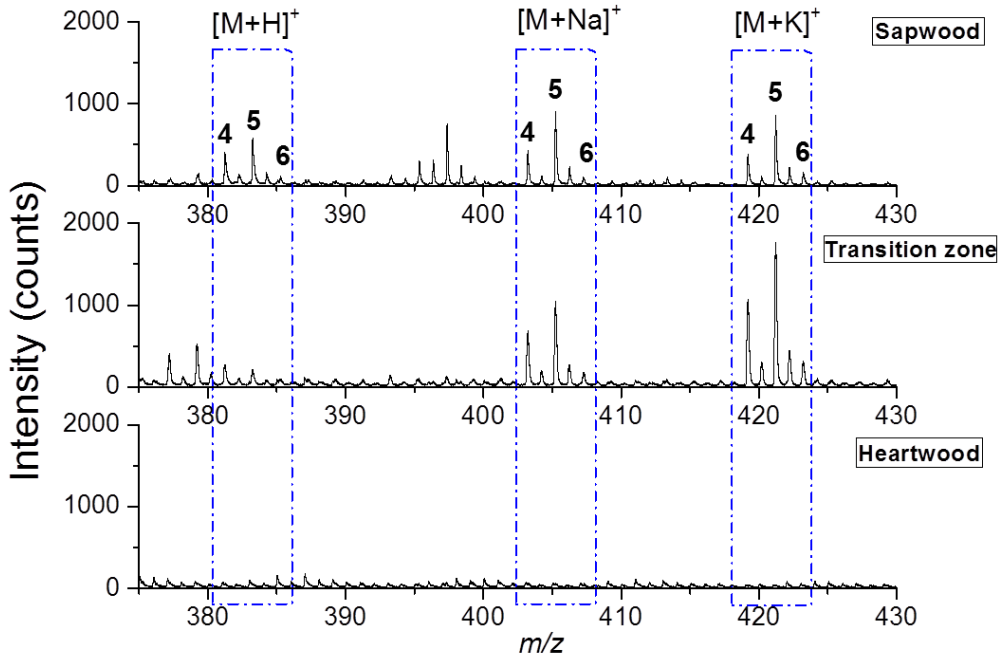

Figure S27: Partial TOF-SIMS spectra showing the detection of compounds **4**-**6** in sapwood and transition zone but not in heartwood. Compound **4**: *m/z* 381 $[M+H]^+$, *m/z* 403 $[M+Na]^+$, *m/z* 419 $[M+K]^+$; Compound **5**: *m/z* 383 $[M+H]^+$, *m/z* 405 $[M+Na]^+$, *m/z* 421 $[M+K]^+$; Compound **6**: *m/z* 385 $[M+H]^+$, *m/z* 407 $[M+Na]^+$, *m/z* 423 $[M+K]^+$.

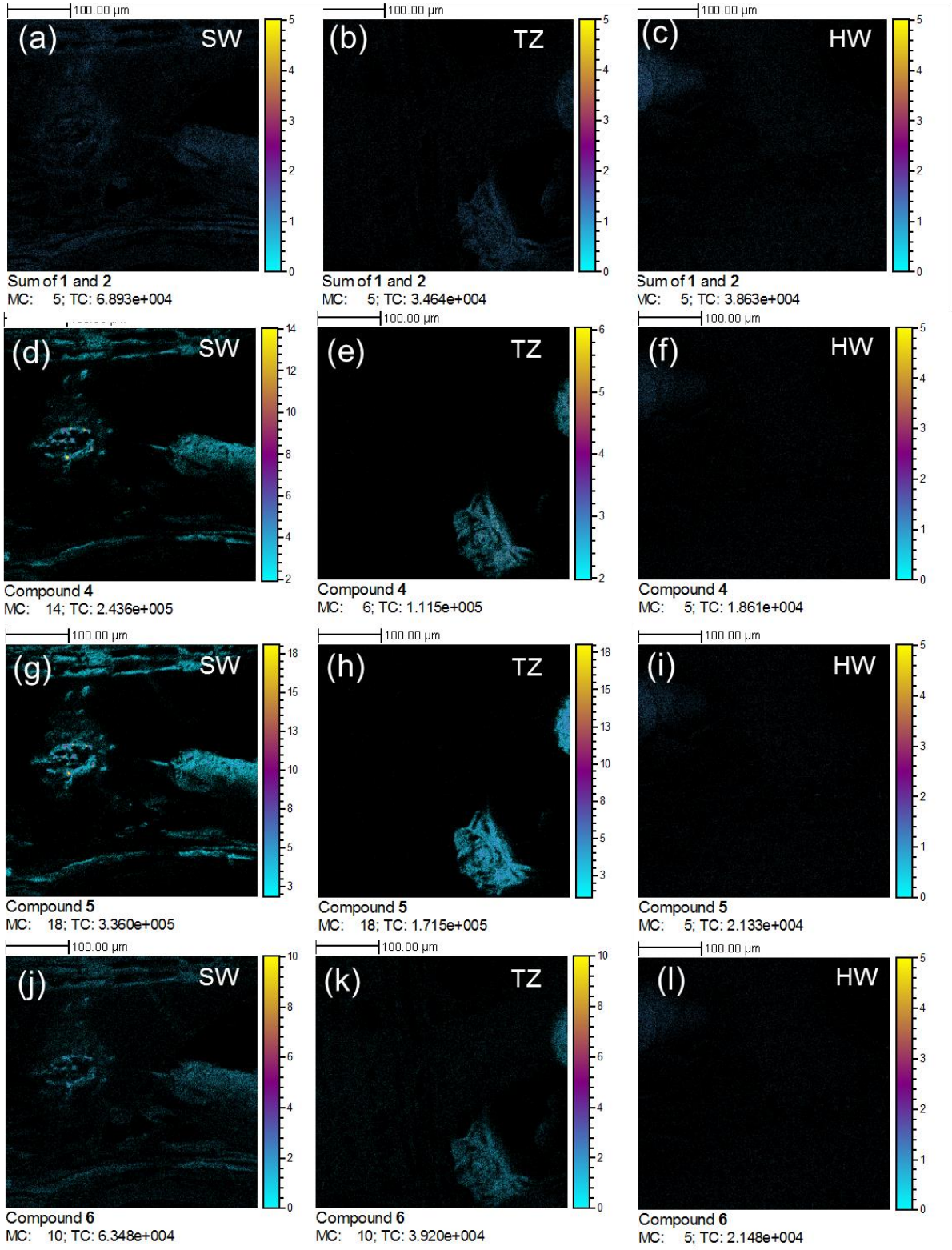

Figure S28: Distribution of compounds **1-2, 4-6** in sapwood (SW), transition zone (TZ) and heartwood (HW), respectively. (a)-(c) Compounds **1** and **2**. (d)-(f) Compound **4**. (g)-(i) Compound **5**. (j)-(l) Compound **6**.

4.8.6 Sputter depth measurement

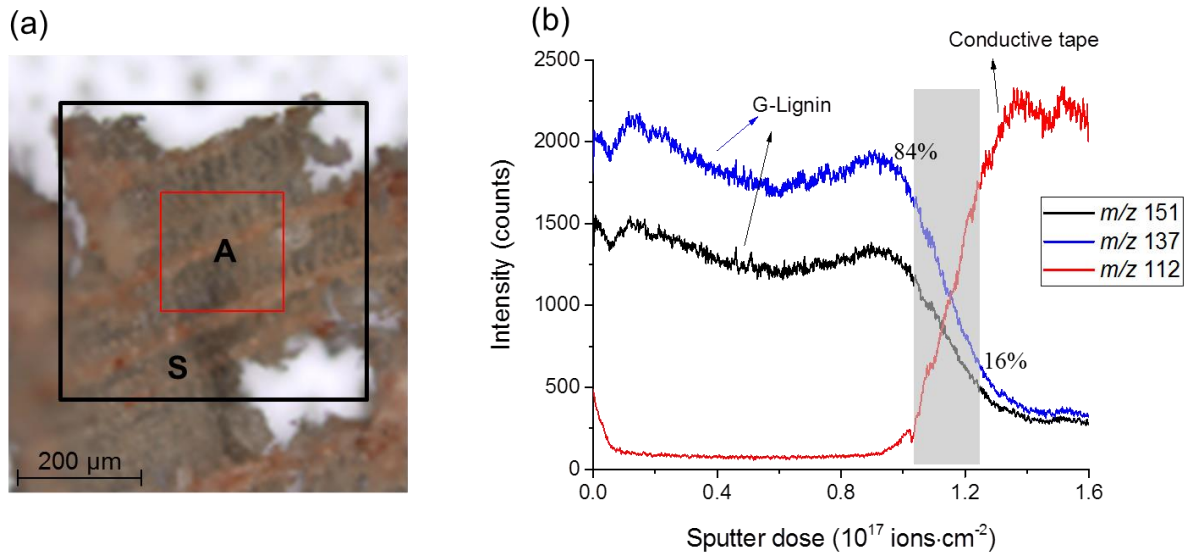

Figure S29: Argon cluster sputter depth measurement. (a) Optical image of a 20 µm thick *Sextonia rubra* wood section fixed on double side conductive tape. A: Analytical area. S: Sputter area. (b) Depth profile of the wood section fixed on the tape.

4.8.7 Surface modification by argon clusters

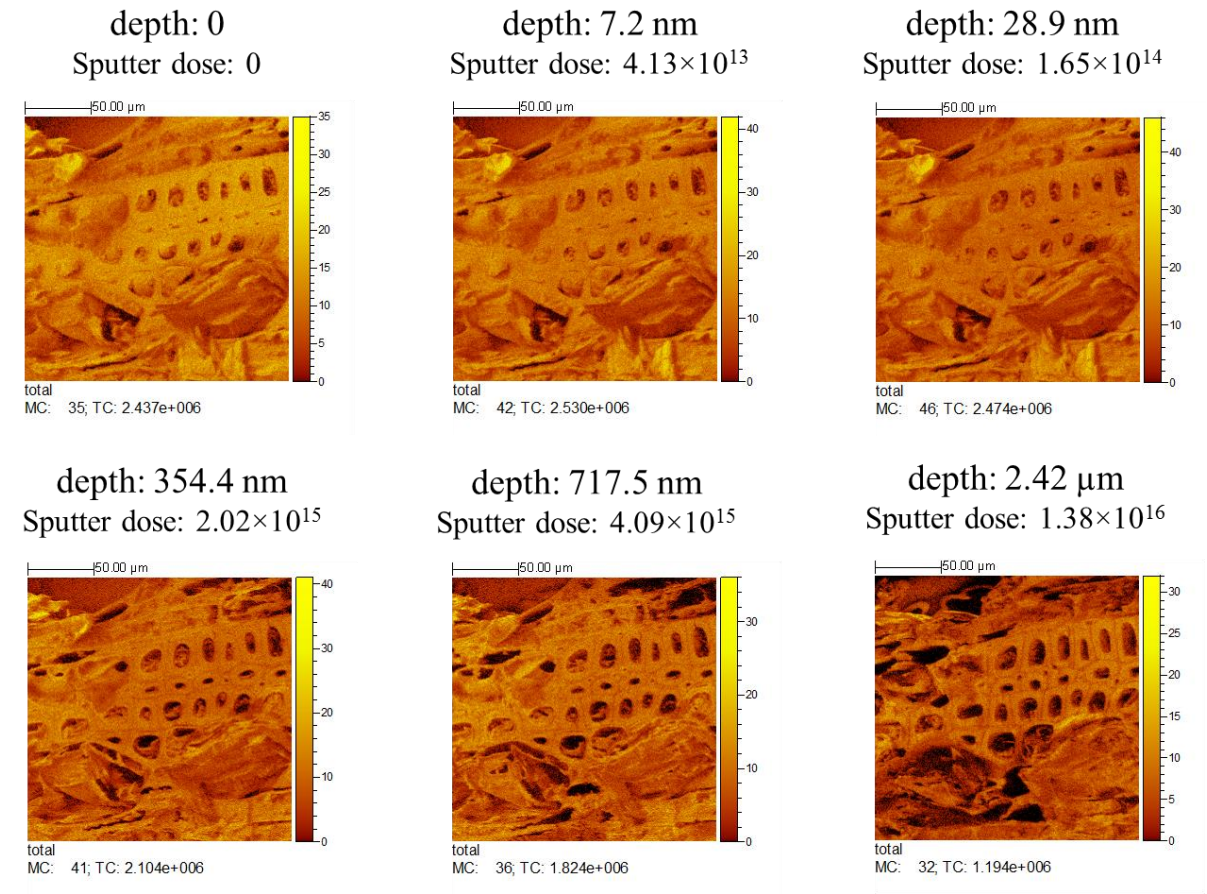

Figure S30: Total ion images of the analytical area at different depth during the argon cluster sputtering. Images are extracted from the 3D stack image displayed in Figure 4.

References

[1] Amusant, N.; Moretti, C.; Richard, B.; Prost, E.; Nuzillard, J. M.; Thévenon, M. F. Chemical compounds from *Eperua falcata* and *Eperua grandiflora* heartwood and their biological activities agains twood destroying fungus (*Coriolus versicolor*). *Holz Roh Werkst* **2007**, *65*, 23–28.

[2] Amusant, N.; Migg, M.; Thibaut, B.; Beauchene, J. Diversity of decay resistance strategies of durable tropical woods species: *Bocoa prouacencsis* Aublet, *Vouacapoua americana* Aublet, *Inga alba* (*Sw.*) Wild. *International Biodeterioration & Biodegradation* **2014**, *94*, 103–108.

[3] van der Werff, H. Sextonia, a new genus of Lauraceae from South America. *Novon* 1**997**, *7*, 436–439.

[4] Franca, N. C.; Gottlieb, O. R.; Coxon, D. T.; Ollis, W. D. Chemistry of brazilian Lauraceae. xVII. constitution of rubrenolide and rubrynolide in Nectandra rubra. *Acad Brasil Cienc An* **1971**, *43*, 123–125.

[5] Franc, N. C.; Gottlieb, O. R.; Coxon, D. T.; Ollis, W. D. Constitutions of Rubrenolide and Rubrynolide: an Alkene-Alkyne Pair from Nectandra rubra. *Journal of the Chemical Society, Chemical Communications* **1972**, 514–515.

[6] Franca, N. C.; Gottlieb, O. R.; Coxon, D. T. Rubrenolide and rubrynolide: An alkene-alkyne pair from Nectandra rubra. *Phytochemistry* **1977**, *16*, 257–262.

[7] Rodrigues, A. M. S.; Theodoro, P. N. E. T.; Eparvier, V.; Basset, C., Silva, M. R. R.; Beauchêne, J.; Espíndola, L. S.; Stien, D. Search for Antifungal Compounds from the Wood of Durable Tropical Trees. *Journal of Natural Products* **2010**, *73*, 1706–1707.

[8] Rodrigues, A. M. S.; Amusant, N.; Beauchêne, J.; Eparvier, V.; Leménager, N.; Baudassé, C., Espíndola, L. S.; Stien, D. The termiticidal activity of *Sextonia rubra* (Mez) van der Werff (Lauraceae) extract and its active constituent rubrynolide. *Pest Management Science* **2011**, *67*, 1420–1423.

[9] Houël, E.; Rodrigues, A. M. S.; Nicolini, E.; Ngwete, O.; Duplais, C.; Stien, D.; Amusant, N. Natural durability of Sextonia rubra, an Amazonian tree species: description and origin. IRG/WP 17-10887, Proceedings IRG Annual Meeting (ISSN 2000−8953)

[10] Falkowski, M.; Jahn-Oyac, O.; Ferrero, E.; Issaly, J.; Eparvier, V.; Rodrigues, A. M. S.; Stien, D.; Houël, E.; Dusfour, I. Assessment of a simple compound-saving method to study insecticidal activity of natural extracts and pure compounds against mosquito larvae. *Journal of the American Mosquito Control Association* **2016**, *32*, 337−340.

[11] Rodrigues, A. M. S.; Royer, M.; Amusant, N.; Beauchêne, J.; Herbette, G.; Eparvier, V.; Thibaut, A.; Espindola, L. S.; Thibaut, B.; Stien, D. Antinomic natural self-protection mechanism in long-lasting woods: a case study with three tropical species from French

Guiana. IRG/WP 09-10696. The International Research Group on Wood Protection **2009**, Beijing.

[12] Taylor, S. K.; Hopkins, J. A.; Spangenberg, K. A.; McMillen, D. W.; Grutzner, J. B. Synthesis of (±)-rubrynolide and a revision of its reported stereochemistry. *Journal of Organic Chemistry* **1991**, *56*, 5951–5955.

[13] Thijs, L.; Zwanenburg, B. Rubrenolide, total synthesis and revision of its reported stereochemical structure. *Tetrahedron*, **2004**, *60*, 5237-5252.

[14] Fujioka, H.; Ohba, Y.; Hirose, H.; Nakahara, K.; Murai, K.; Kita, Y. Facile formation of tetrahydrofurans with multiple chiral centers using double iodoetherification of σ-symmetric diene acetals: short asymmetric total synthesis of rubrenolide and rubrynolide. *Tetrahedron* **2008**, *64*, 4233–4245.

[15] Madda, J.; Khandregula, S.; Bandari, S. K.; Kommu, N.; Yadav, J. S. Stereoselective total synthesis of rubrenolide and rubrynolide. *Tetrahedron: Asymmetry* **2014**, *25*, 1494–1500.

[16] Gottlieb, O. R. Chemosystematics of the lauraceae. *Phytochemistry* **1972**, *11*, 1537–1570.

[17] Lisec, J.; Schauer, N.; Kopka, J.; Willmitzer, L.; Fernie, A. R. Gas chromatography mass spectrometry–based metabolite profiling in plants. *Nature protocols* **2006**, *1*, 387–396.

[18] Allwood, J. W.; Goodacre, R. An introduction to liquid chromatography–mass spectrometry instrumentation applied in plant metabolomic analyses. *Phytochemical Analysis* **2010**, *21*, 33–47.

[19] Lee, Y. J.; Perdian, D. C.; Song, Z.; Yeung, E. S.; Nikolau, B. J. Use of mass spectrometry for imaging metabolites in plants. *The Plant Journal* **2012**, *70*, 81–95.

[20] Bjarnholt, N.; Li, B.; D'Alvise, J.; Janfelt, C. Mass spectrometry imaging of plant metabolites –principles and possibilities. *Nature Product Report* **2014**, *31*, 818–837.

[21] Dong, Y.; Li, B.; Malitsky, S.; Rogachev, I.; Aharoni, A., Kaftan, F.; Svatoš, A.; Franceschi, P. Sample preparation for mass spectrometry imaging of plant tissues: A review. *Frontiers in Plant Science* **2016**, *7*, 60.

[22] Ostrowski, S. G.; Van Bell, C. T.; Winograd, N.; Ewing, A. G. Mass spectrometric imaging of highly curved membranes during *Tetrahymena* mating. *Science* **2004**, *305*, 71–73.

[23] Imai, T.; Tanabe, K.; Kato, T.; Fukushima, K. Localization of ferruginol, a diterpene phenol, in Cryptomeria japonica heartwood by time-of-flight secondary ion mass spectrometry. *Planta* **2005**, *211*, 549–556.

[24] Saito, K.; Mitsutani, T.; Imai, T.; Matsushita, Y., Fukushima, K. Discriminating the indistinguishable sapwood from heartwood in discolored ancient wood by direct molecular

mapping of specific extractives using time-of-flight secondary ion mass spectrometry. *Analytical Chemistry* **2008**, *80*, 1552–1557.

[25] Vanbellingen, Q. P.; Fu T.; Bich, C.; Amusant, N.; Stien, D.; Della-Negra, S.; Touboul, D.; Brunelle, A. Mapping Dicorynia guianensis wood constituents by submicron resolution cluster-TOF-SIMS Imaging. *Journal of Mass Spectrometry* **2016**, *51*, 412–423.

[26] Jung, S.; Foston, M.; Kalluri, U. C.; Tuskan, G. A.; Ragauskas, A. J. 3D chemical image using TOF-SIMS revealing the biopolymer component spatial and lateral distributions in biomass. *Angewandte Chemie International Edition* **2012**, *51*, 12005–12008.

[27] Carado, A.; Passarelli, M. K.; Kozole, J.; Wingate, J. E.; Winograd, N.; Loboda, A.V. C60 secondary ion mass spectrometry with a hybrid quadrupole orthogonal time-of-flight mass spectrometer. *Analytical Chemistry* **2008**, *80*, 7921–7929.

[28] Fletcher, J. S.; Rabbani, S.; Henderson, A.; Blenkinsopp, P.; Thompson, S. P.; Lockyer, N. P.; Vickerman, J. C. A new dynamic in mass spectral imaging of single biological cells. *Analytical Chemistry* **2008**, *80*, 9058–9064.

[29] Smith, D. F.; Robinson, E. W.; Tolmachev, A. V.; Heeren, R. M.; Pasa-Tolic, L. C60 secondary ion fourier transform ion cyclotron resonance mass spectrometry. *Analytical Chemistry* **2011**, *83*, 9552–9556.

[30] Fisher, G. L.; Bruinen, A. L.; Ogrinc Potočnik, N.; Hammond, J. S.; Bryan, S. R.; Larson, P. E.; Heeren, R. M. A. A new method and mass spectrometer design for TOF-SIMS parallel imaging MS/MS. *Analytical Chemistry* **2016**, *88*, 6433−6440.

[31] Rutishauser, E.; Barthélémy, D.; Blanc, L.; Eric-André, N. Crown fragmentation assessment in tropical trees: Method, insights and perspectives. *Forest ecology and management* **2011**, *461*, 400–407.

[32] Vanbellingen, Q. P.; Elie N.; Eller, M. J.; Della-Negra, S.; Touboul D.; Brunelle A. Time-of-flight secondary ion mass spectrometry imaging of biological samples with delayed extraction for high mass and high spatial resolutions. *Rapid Communications in Mass Spectrometry* **2015**, *29*, 1187–1195.

[33] Touboul, D.; Brunelle, A.; Halgand, F.; De La Porte S.; Laprévote, O. Lipid imaging by gold cluster time-of-flight secondary ion mass spectrometry: application to Duchenne muscular dystrophy. *Journal of Lipid Research* **2005**, *46*, 1388–1395.

[34] Goacher, R. E.; Jeremic, D.; Master, E. R. Expanding the library of secondary ions that distinguish lignin and polysaccharides in time-of-flight secondary ion mass spectrometry analysis of wood. *Analytical Chemistry* **2011**, *83*, 804–812.

[35] Cheng, M. J.; Tsai I. L.; Lee, S. J.; Jayaprakasam, B.; Chen, I. S. Steryl epoxide, secobutanolide and butanolides from the stem wood of Machilus zuihoensis. *Phytochemistry* **2005**, *66*, 1180–1185.

[36] Niwa, M.; Iguchi, M.; Yamamura, S. Three new obtusilactones from *Lindera obtusiloba* Blume. *Chemical letters* **1975**, 655–658.

[37] Karikome, H.; Mimaki, Y.; Sashida, Y. A butanolide and phenolics from *Machilus Thunbergii*. *Phytochemistry* **1991**, *30*, 315−319.

[38] Tsai, I. L.; Hung, C. H.; Duh, C. Y.; Chen, I. S. Cytotoxic butanolides and secobutanolides from the stem wood of formosan *Lindera communis*. *Planta Medica* **2002**, *68*, 142−145.

[39] Pathirana, C.; Dwight, R.; Jensen, P. R.; Fenical, W.; Delgado, A.; Brinen, L. S.; Clardy, J. Structure and synthesis of a new butanolide from a marine actinomycete. *Tetrahedron Letters* **1991**, *32*, 7001−7004.

[40] Taylor, A. M.; Gartner, B. L.; Morrell, J. J. Heartwood formation and natural durability - a review. *Wood and fiber science* **2002**, *34*, 587–611.

[41] Grecco, S. S.; Lorenzi, H.; Tempone, A. G.; Lago, J. H. G. Update: biological and chemical aspects of Nectandra genus (Lauraceae). *Tetrahedron: Asymmetry* **2016**, *27*, 793–810.

[42] Anderson, J. E.; Ma, W.; Smith, D. L.; Chang, C. J. Biologically active γ-lactones and methylketoalkenes from *Lindera benzoin*. *Journal of Natural Products* **2009**, *72*, 2145–2152.

[43] Cheng, W.; Zhu, C.; Xu, W.; Fan, X.; Yang, Y.; Li, Y.; Chen, X.; Wang, W.; Shi, J. Chemical constituents of the bark of *Machilus wangchiana* and their biological activities. *Journal of Natural Products* **2009**, *72*, 2145–2152.

[44] Chen C. H.; Lo W. L.; Liu, Y. C.; Chen, C.Y. Chemical and cytotoxic constituents from the leaves of *Cinnamomum kotoense*. *Journal of Natural Products* **2006**, *69*, 927–33.

[45] Lin, R. J.; Cheng, M. J.; Huang, J. C.; Lo, W. L.; Yeh, Y. T.; Yen, C. M.; Lu, C. M.; Chen, C. Y. Cytotoxic Compounds from the Stems of *Cinnamomum tenuifolium*. *Journal of Natural Products* **2009**, *72*, 1816–1824.

[46] Tsai, I. L.; Hung, C. H.; Duh, C. Y.; Chen, I. S. Cytotoxic butanolides and secobutanolides from the stem wood of formosan *Lindera communis*. *Planta Medica* **2002**, *68*, 142−145.

[47] Tanaka, H.; Takaya, Y.; Toyoda, J.; Yasuda, T.; Sato, M.; Murata, J.; Murata, H.; Kaburagi, K.; Iida, O.; Sugimura, K.; Sakai, E. Two new butanolides from the roots of *Litsea acuminata*. *Phytochemistry Letter* **2015**, *11*, 32−36.

[48] Kuo, P. L.; Chen, C. Y.; Hsu, Y. L. Isoobtusilactone A induces cell cycle arrest and apoptosis through reactive oxygen species/apoptosis signal-regulating kinase 1 signaling pathway in human breast cancer cells. *Cancer Research* **2007**, *67*, 7406−7420.

[49] Tófoli, D.; Martins, L. A. V.; Matos, M. F. C.; Garcez, W. S.; Garcez, F. R. Antiproliferative Butyrolactones from Mezilaurus crassiramea. *Planta Medica Letters* **2016**, *3*, e14–e16.

[50] De Micco, V.; Balzano, A.; Wheeler, E. A. Baas, P. Tyloses and gums: a review of structure, function and occurrence of vessel occlusions. *IAWA Journal* **2016**, *37*, 186–205.

[51] Dadswell, H. E.; Hillis, W. E. Wood. In *Wood extractives and their significance to the pulp and paper industries*; Hillis, W. E., Ed.; Academic press inc. London, **1962**, pp 3−49.

[52] Hillis, W. E. Formation of robinetin crystals in vessels of Intsia species. *IAWA Journal* **1996**, *17*, 405–419.

[53] Nagasaki, T.; Yasuda, S. ; Imai, T. Immunohistochemical localization of agatharesinol, a heartwood norlignan, in Cryptomeria japonica. *Phytochemistry* **2002**, *60*, 461–466.

[54] Filho, R. B.; Diaz, P. P.; Gottlieb, O. R. Tetronic acid and diarylpropanes from *Iryanthera elliptica*. *Phytochemistry* **1980**, *19*, 455–459.

[55] Kato, J. A.; Funa, N.; Watanabe, H.; Ohnishi, Y.; Horinouchi, S. Biosynthesis of butyrolactone autoregulators that switch on secondary metabolism and morphological development in Streptomyces. *Proceedings of the National Academy of Sciences* **2007**, *104*, 2378−2383.

[56] Schulz, S.; Hötling, S. The use of lactone motif in chemical communications. *Nature Product Report* **2015**, *32*, 1042−1066.

[57] Lybing, S.; Reio, L. Degradation of 14C-Labelled Carolic and Carlosic acids from *Penicillium Charlessi G. Smith*. *Acta Chemica Scandinavica* **1958**, *12*, 1575–1584.

[58] Ross, C.; Scherlach, K.; Kloss, F.; Hertweck, C. The molecular basis of conjugated polyyne biosynthesis in phytopathogenic bacteria. *Angewandte Chemie International Edition* **2014**, *53*, 7794−7798.

[59] Juan, C.; Martinez, V.; Yoshida, M.; Gottlieb, O. R. Six groups of ω-ethyl-, ω-ethenyl- and ω-ethynyl-α-alkylidene- γ-lactones. *Tetrahedron Letters* **1979**, 1021–1024.

[60] Romek, K. N.; Nun, P.; Rémaud, G. S.; Silvestre, V.; Taïwe, G. S.; Lecerf-Schmidt, F.; Boumendjel.; De Waard, M.; Robins, R. A retro-biosynthetic approach to the prediction of biosynthetic pathways from position-specific isotope analysis as shown for tramadol. *Proceedings of the National Academy of Sciences* **2015**, *112*, 8296−8301.

Chapter 5 Radial distribution of wood extractives in European larch *Larix decidua* by TOF-SIMS imaging

5.1 Abstract

Wood extractives in the branch heartwood of European larch *Larix decidua* was mapped by Time-of-flight secondary ion mass spectrometry (TOF-SIMS) imaging, which allows the radial distribution of both mineral and lipophilic extractives in the heartwood be scrutinized with high spatial resolution for the first time. Results show that all the components are inhomogeneously distributed across the annual ring. Mineral nutrients including Na^+, K^+, Ca^+, Cl^- exhibit no preferential localization between earlywood and latewood, whereas PO_3^- is exclusively present in the ray cells, indicating it may be related to acid phosphatase. Lipophilic extractives were found more abundant in the inner heartwood. Ion images with 400 nm spatial resolution reveal that fatty acids, triglycerides and phytosterols are co-localized principally in the earlywood within the first annual ring. Resin acids prove to be the main components in the resin canal of the branch heartwood and are distributed in the outer heartwood.

5.2 Introduction

Wood extractives are solvent extractable components in wood tissues, comprising of a variety of compounds such as fatty acid, sterols, phenols, and so on [1]. These extractives play an important role in decay resistance to termite, fungi, and environmental stress.

European larch (*Larix decidua*) is an important conifer species native to mountainous and alpine forests in central Europe. The fast-growing nature and good durability make it a valuable timber tree of which the wood is widely used in carpentry, especially in making waterproof objects that can be used outdoors [2]. It has been revealed that, as a property shared by many hardwood and softwood trees, the natural durability of larch wood is due to its decay resistance to microbial deterioration. The quantity and composition of heartwood extractives varies dramatically among different larch species, and there is a close correlation between extractive contents and natural durability [3,4]. In addition, heartwood extractives could also affect the wood quality including mechanical property [5] and stability [6,7].

Conventionally, the extractives were roughly classified into organic solvent extractives, water extractives and phenolics which were then determined by solvent extraction or more rapidly by Fourier transform near infrared (FTNIR) spectroscopy [8]. Nevertheless, precise characterization of the chemical composition of some larch species has also been performed with gas chromatography (GC) [9]- and liquid chromatography (LC) [10]-mass spectrometry (MS). However, very few studies concerning the spatial distribution of the extractives have been carried out. Spatial distribution of the extractives is very important in understanding heartwood formation and it largely determines the wood quality [11]. Radial distribution of

European larch extractives have been examined by Gierlinger *et al* [12] through micro-sampling of wood blocks which were subsequently analyzed by FTIR. Their results have shown that in mature larch the amount of the wood extractives increase linearly from pith to the heartwood/sapwood boundary. Similar sampling method followed by GC analyses was also applied to scrutinize the chemical compositional difference in earlywood and latewood of spruce [13] and radial distribution of extractives in scots pine wood [14]. However, this manual sampling method leads to limited spatial resolution and could not provide cellular localization of the extractives, let alone the time consuming extraction with toxic solvents.

Time-of-flight secondary ion mass spectrometry (TOF-SIMS) is a surface analytical technique which is recognized by its high spatial resolution. By dividing a certain analytical area into pixels and recording mass spectra from each pixel, TOF-SIMS provides simultaneously chemical and spatial information of the sample surface. Although traditionally employed for analysis of inorganic materials, TOF-SIMS has been gaining its reputation in biological imaging since the development of cluster ion beams (for example, Bi_3^+, Au_3^+, C_{60}^+) which has effectively improved the capability of providing direct molecular information up to *m/z* 1500 [15,16,17]. Concurrently, the number of studies using TOF-SIMS to map chemical constituents in wood tissues is also increasing. In addition to inorganic ions [18] and fragments of wood structural polymer lignin and polysaccharides [19,20], specific extractives such as diterpene phenol [21], hinokinin and its derivatives [22], and tryptamine [23] in various wood species have been mapped by TOF-SIMS.

In this study, TOF-SIMS was employed to investigate the spatial distribution of heartwood extractives in the branch wood of European larch (*Larix decidua*). Large area analysis of the heartwood was performed to examine the radial distribution of wood extractives from the pith towards the heartwood/sapwood boundary. Meanwhile, cellular localization of the extractives in earlywood and latewood within different annual rings was revealed with a high spatial resolution of 400 nm. Different localization patterns were observed for mineral ions and organic extractives, whereas both extractive species are heterogeneously distributed in the branch heartwood.

5.3 Experimental

5.3.1 Plant material

Larch samples are from the upper part of the Vallouise valley, in the small valley of torrent de Saint-Pierre in France (area of Pelvoux village, exact GPS coordinates 6°26’31’’ E and 44°53’49’’ N) [24], at an altitude of 1572 m. The branch wood was collected from a several-year-old larch tree in the August of 2015, and had been conserved under ambient

environment afterwards. Previous reports have shown that the branch heartwood contains relatively more extractives than the stem wood [25,26].

5.3.2 Wood surface preparation

Before analysis, the bark was removed and the remaining stem was trimmed with a razor blade to generate a small block of about 1 cm × 1 cm × 1 cm. A transverse surface of approximately 1 mm × 3 mm was obtained with ultramicrotome (EM UC6, Leica Microsystèmes, SAS, Nanterre, France) using diamond knife (DIATOME Cryotrim 45°, Leica Microsystèmes, SAS, Nanterre, France). The cutting was performed at a speed of 2 mm/s with a fixed cutting feed of 200 nm. The clearance angle was kept constant at 6° during the sectioning. Optical images of wood surfaces were acquired at ×10 magnification with an Olympus BX51 microscope (Rungis, France) using extended focal imaging (EFI) scanning mode.

5.3.3 TOF-SIMS imaging analysis

Mass spectrometry imaging experiments were performed with a commercial TOF-SIMS IV (ION-TOF GmbH, Münster, Germany) mass spectrometer equipped with a bismuth liquid metal ion gun (LMIG). Mass spectra and ion density images were acquired using Bi_3^+ cluster ions as primary ion beam with a kinetic energy of 25 keV. Large area imaging was carried out with the so called high current bunched ion focusing mode where the current measured at 10 kHz was 0.38 pA. The imaged area was 3000 µm × 500 µm divided by 768 pixels × 128 pixels, resulting in a spatial resolution of about 4 µm. The ion dose applied was 1.25×10^{10} ions/cm^2. High resolution images were recorded with burst alignment ion focusing mode to obtain a high lateral resolution of 0.4 µm. In this case, the primary ion pulse duration was set at 100 ns and the current measured at 10 kHz was 0.074 pA. An extraction delay of the secondary ions was employed to improve mass resolution [27]. The attainable mass resolution was ~ 6000 at *m/z* 279.2 ($C_{18}H_{31}O_2^-$). Three individual areas of 400 µm × 400 µm were imaged with 1024 × 1024 pixels and an ion dose of 3×10^{12} ions/cm^2, respectively. A low energy pulsed electron flood gun (21 eV) was applied to neutralize the charges accumulated on the insulating surface. Data processing was performed using SurfaceLab 6.5 (ION-TOF GmbH, Münster, Germany), and the primary ion beam shift during the acquisitions were corrected by 'lateral shift correction' function in the software. Mass spectra were calibrated to lignin and polysaccharides fragment ions [28] such as $C_7H_7^+$, $C_7H_9^+$, $C_7H_{11}^+$, $C_8H_7^+$, $C_8H_{11}^+$, $C_9H_{11}^+$, $C_{10}H_{11}^+$, $C_{11}H_9O_3^+$ in positive ion mode and light fragments C_4H^-, $C_4H_3^-$, $C_3H_3O^-$, $C_3H_5O^-$, $C_3H_3O_2^-$ in negative ion mode.

5.4 Results and discussion

5.4.1 Large area imaging and distribution of mineral nutrients

To examine the radial distribution of wood extractives from pith towards heartwood/sapwood boundary in the larch branch, a large area of 3000 µm × 500 µm was first mapped by TOF-SIMS. Although wood extractives generally refer to extractable organic components, mineral elements also constitute an important part of the extractives and different translocation patterns of mineral elements have been observed in heartwood formation [11]. Therefore, the mineral ions in the branch heartwood were also investigated in addition to the organic constituents. Figure 1 illustrates the distributions of mineral ions in the heartwood as well as in the pith. It is found that very few amounts of Cl^- and Na^+ are present in the heartwood. Also interesting to note is that Cl^- is well co-localized with Na^+, indicating that Cl^- is mainly associated with Na^+ in larch wood, although K^+ turns out to be more abundant than Na^+ in the larch branch. Calcium shows similar distribution to K^+, however with lower intensity. Calcium has low mobility in plant tissues and plays an important role in physiological process and environmental response [29]. Phosphate was exclusively detected in the ray cells and is probably related to acid phosphatase which is believed to facilitate the transport of carbohydrates in wood tissues through phosphorylation/dephosphorylation process [30]. The ion images demonstrate that except from the ray cell-specific phosphate, all the other minerals show heterogeneous distribution in the heartwood and no obvious preferential distribution between earlywood and latewood. In all the cases, minimum amount of mineral nutrients is present in the pith. Besides endogenous mechanisms [31], variations in the concentration of the minerals across the annual rings may also reflect the environmental influence [32].

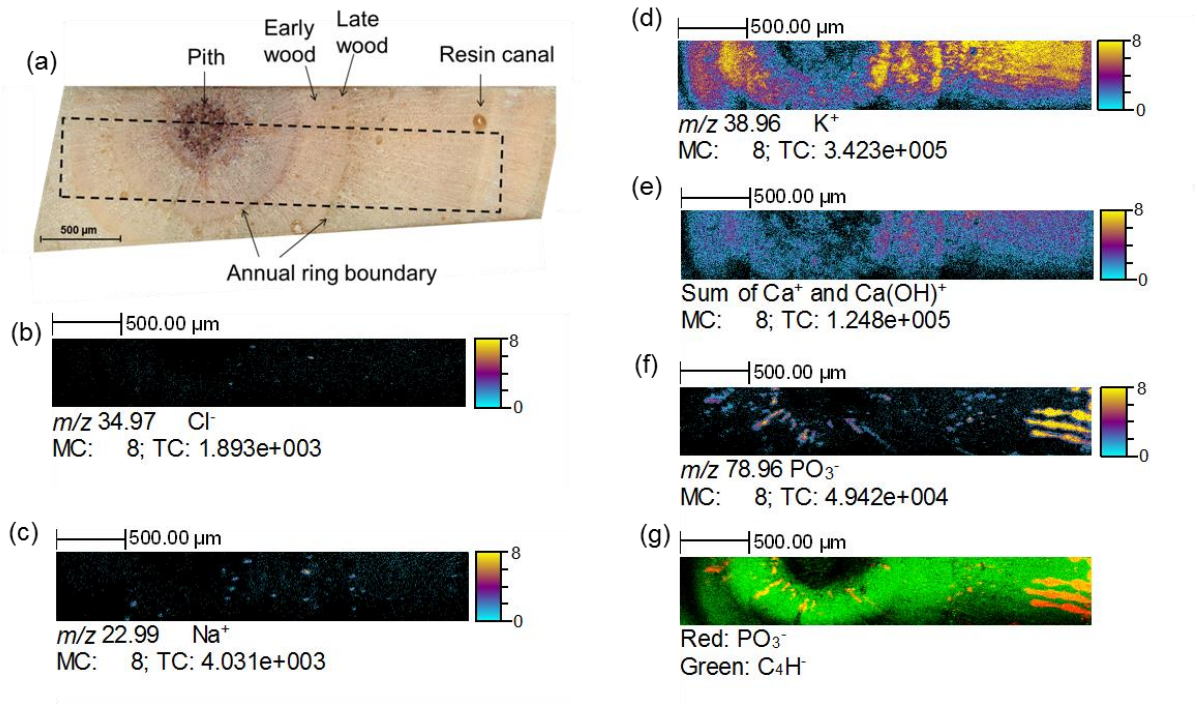

Figure 1: Radial distribution of mineral ions in the branch heartwood of *Larix decidua*. (a) Microscopic image of the transverse surface of the branch heartwood. The black rectangular indicates the area imaged by TOF-SIMS. (b) Ion image of Cl^-. (c) Ion image of Na^+. (d) Ion image of K^+. (e) Ion image of the sum of Ca^+ and $Ca(OH)^+$. (f) Ion image of PO_3^-. (d) Two-color overlay image of PO_3^- (Red) and C_4H^- (Green) fragment ion representing the background.

5.4.2 Radial distribution of lipophilic extractives

Organic extractives are more abundant than inorganic minerals in wood. They constituent an important proportion of wood chemistry and comprise a wide range of non-structural lipophilic compounds. To scrutinize the precise localization of the organic components, three different regions presenting wood tissue within different annual rings including in the branch heartwood were mapped with high spatial resolution of 0.4 µm (Figure 2a). Figure 2b illustrates TOF-SIMS mass spectra obtained from the three different analyzed areas in both positive and negative polarities. Similar to the inhomogeneous distribution of mineral nutrients, the comparison of spectra from the three different regions indicate the abundance of the organic extractive also vary dramatically throughout the heartwood surface. The composition and radial distribution of fatty acids, glycerides, flavonoid and phytosterols will be discussed in detail in the following paragraphs. The ion peaks at *m/z* 502.3 in the positive mass spectrum and *m/z* 501.4 in the negative spectrum were not able to be characterized. In addition, the most abundant phenol compound taxifolin in the knotwood of *Larix decidua* [33] was not detected here, probably due to compositional variation in different anatomic plant parts.

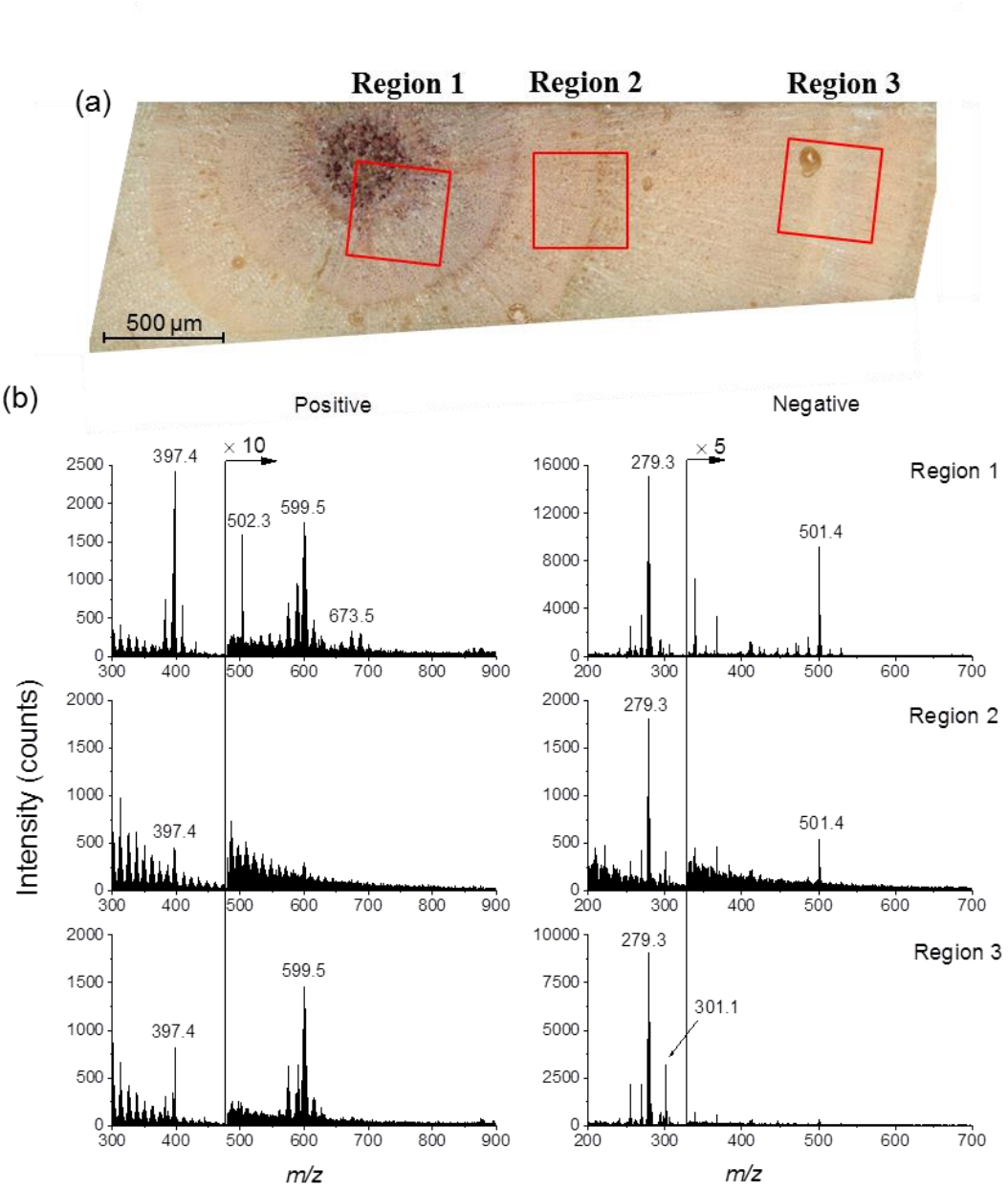

Figure 2: High resolution TOF-SIMS imaging of the branch heartwood of *Larix decidua*. (a) Optical image of the three regions analyzed with 0.4 µm spatial resolution. (b) Partial TOF-SIMS mass spectra showing organic composition in the three regions.

Glycerides and fatty acids

Glycerides and fatty acids are common extractives present in various wood species. As shown in Figure 2b, ion peaks corresponding to fatty acids were observed in the negative mass spectra: *m/z* 255.3 ($C_{16}H_{31}O_2^-$, palmitic acid), *m/z* 269.3 ($C_{17}H_{33}O_2^-$, heptadecanoic acid), *m/z* 277.3 ($C_{18}H_{29}O_2^-$, α-linoleic acid), *m/z* 279.3 ($C_{18}H_{31}O_2^-$, linoleic acid), and *m/z* 281.28 ($C_{18}H_{33}O_2^-$, oleic acid). Meanwhile, triglycerides were mainly detected as diglycerides fragments in the positive mass spectra [18]: *m/z* 573.5 ($C_{37}H_{65}O_4^+$, DG34:3),

m/z 575.5 ($C_{37}H_{67}O_4^+$, DG34:2), *m/z* 577.5 ($C_{37}H_{69}O_4^+$, DG34:1), *m/z* 595.5 ($C_{39}H_{63}O_4^+$, DG36:6), *m/z* 597.5 ($C_{39}H_{65}O_4^+$, DG36:5), *m/z* 599.5 ($C_{39}H_{67}O_4^+$, DG36:4), *m/z* 601.5 ($C_{39}H_{69}O_4^+$, DG36:3), *m/z* 603.5 ($C_{39}H_{71}O_4^+$, DG36:2). Figure 3 displays the radial distribution of fatty acids and triglycerides in the branch heartwood. Ion images of fatty acids and triglycerides were summed up respectively, revealing that they have identical localization mainly in the earlywood within the first annual ring around the pith (Figure 3a and 3b). Triglycerides make up the main composition of fats in wood and serve as energy source for the cells. However, hydrolysis of triglycerides will occur when heartwood is formed, which partly explains their low abundance apart from the low ionization/desorption efficiency and fragmentation during SIMS analysis. High resolution images further show the accumulation of fatty acids and triglycerides in the inner earlywood and their diffusion into the surrounding cells (Figure 3c-3h). Nevertheless, fatty acids and triglycerides are also present in the resin canal in a noticeable amount.

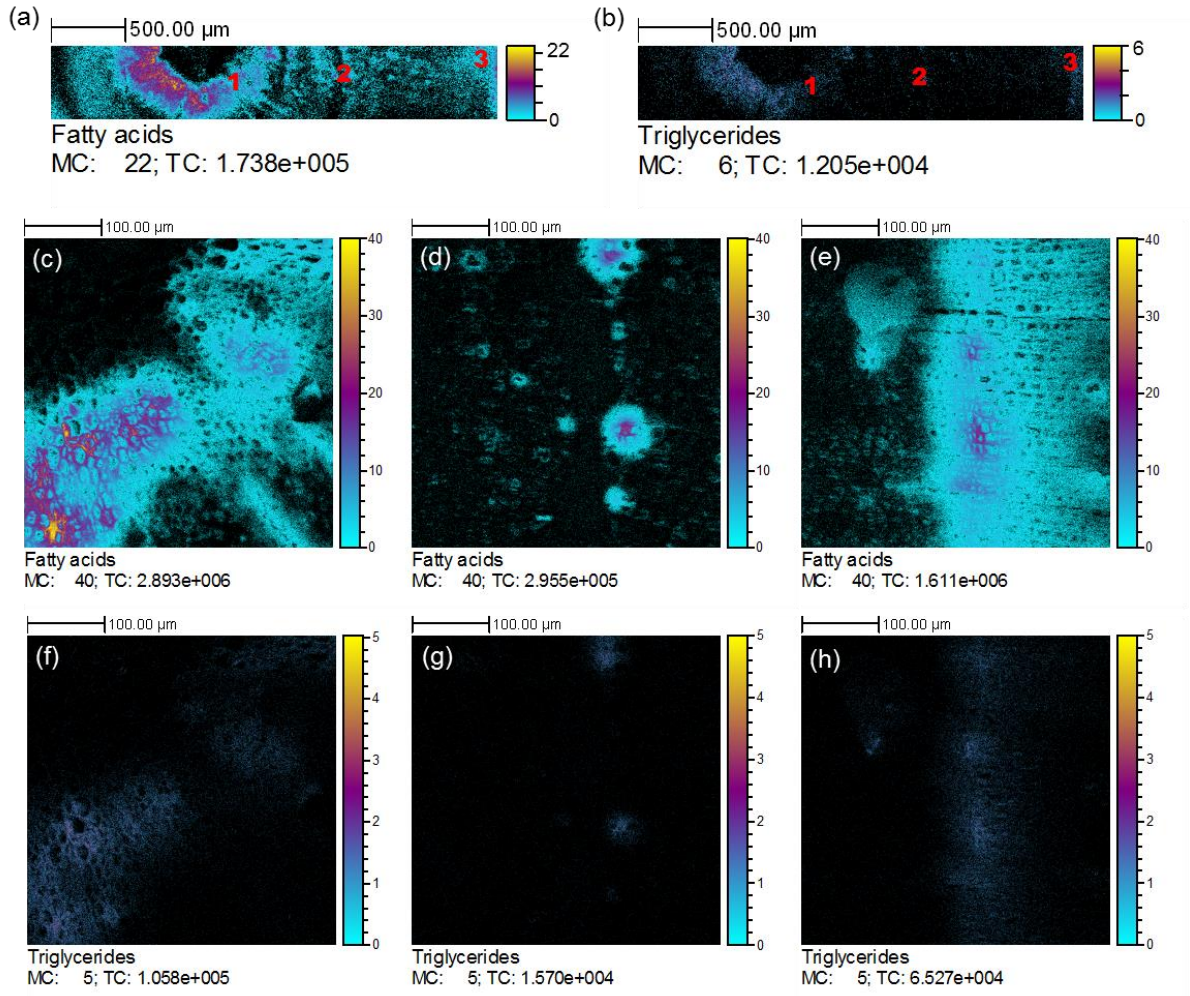

Figure 3: Radial distribution of fatty acids and triglycerides in branch heartwood of *Larix decidua*. (a) Summed ion images of fatty acids from large area analysis. (b) Summed ion

images of triglycerides from large area analysis. c-e: high resolution localization of fatty acids in region 1 (c), region 2 (d) and region 3 (e). f-h: high resolution localization of fatty acids in region 1 (f), region 2 (g) and region 3 (h). The three regions are indicated in Figure 2.

Resin acids

Apart from phenolic compounds, resin acids also contribute significantly to protecting the wood from insects and microbial deterioration [34]. Comparing the high resolution mass spectra recorded in the three regions leads to the differentiation of the specific presence of the ion at *m/z* 301.2 in region 3 (Figure 2b). Reconstruction of the ion image in Figure 4 reveals that this compound is almost exclusively located in the resin canal. Therefore, the ion at *m/z* 301.2 is attributed to resin acid ($C_{20}H_{30}O_2$, MW 302.2) which is probably a mixture of abietic-type acids and pimaric-type acids since they are both predominantly present in European larch [9,10]. Noticeably, abietic acid and isopimaric acid (Figure 4) which represent the two types of resin acids, respectively, are the most abundant resin acids in larch. The three-color overlay of ion images from resin acids (blue), fatty acids (red) and low molecular fragment (green) directly illustrates the distinct localizations of these two lipophilic extractives (Figure 4c). Chemical composition of the resin canal was further examined by manually selecting a region of interest of this specific structure. The corresponding mass spectrum is illustrated in Figure 4d, showing that apart from a minimum amount of fatty acids, resin acid is the main components of the resin canal.

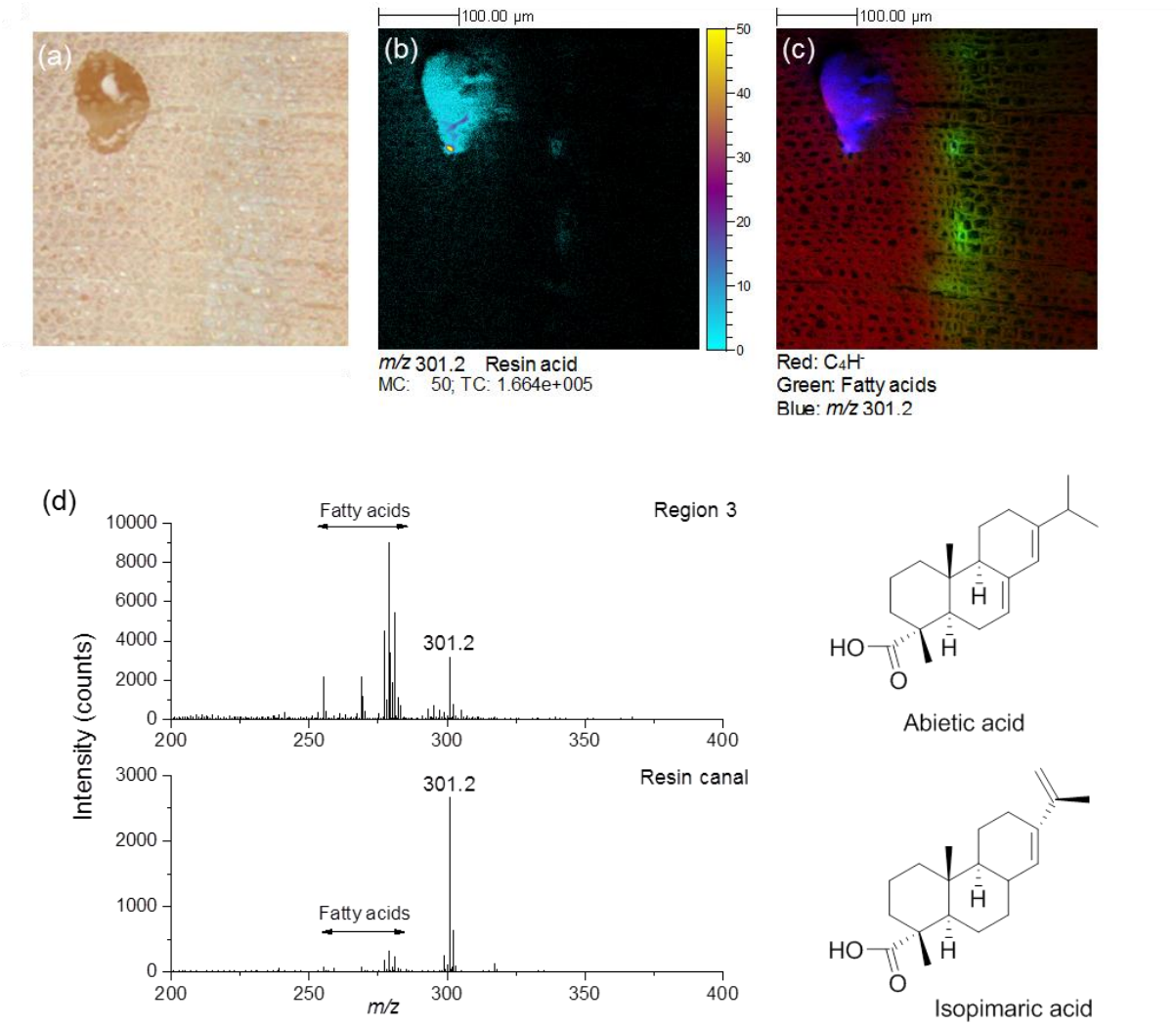

Figure 4: Localization of resin acids in the resin canal. (a) Optical image of region 3 with a resin canal. (b) High resolution ion image of resin acids in region 3. (c) Three color overlay of C_4H^- (Red) representing the background, fatty acids (Green) and resin acid (Blue) (*m/z* 301.2). (d) TOF-SIMS spectra of the whole region 3 (upper) and region of interest (ROI) of the resin canal (bottom). Structures of representative resin acids abietic acid and pimaric acid are shown in the bottom right.

Phytosterols

Phytosterols are plant sterols which are essential components of plant cell membrane in the same way as cholesterol in mammalian cells [35]. Figure 5 displays the main phytosterols detected in TOF-SIMS. In accordance with previous study [9], *β*-sitosterol is found the most abundant in the branch heartwood and was detected as dehydrated fragment ion at *m/z* 397.4 ($C_{29}H_{49}^+$) [18]. The neighbor ion peaks at *m/z* 381.3 ($C_{28}H_{45}^+$), 383.3 ($C_{28}H_{47}^+$), 395.3 ($C_{29}H_{47}^+$), 409.4 ($C_{30}H_{49}^+$) are attributed to brassicasterol, campesterol, stigmasterol and cycloartenol, respectively. The radial distribution of phytosterols is illustrated in Figure 6.

The large area chemical map (Figure 6a) shows that phytosterols concentrate in the earlywood within the first annual ring and they are rarely present in the outer heartwood. High resolution ion images (Figure 6b-6d) reveal that phytosterols are well co-localized with fatty acids and triglycerides in the inner earlywood in all the three analyzed regions. In addition, the ion images demonstrate that inner heartwood comprise higher amount of lipophilic extractives (fatty acids, glycerides, and phytosterols) than the outer heartwood. Detailed radial distribution of wood extractives within a few annual rings in larch has not been investigated before. These results revealed that their distribution patterns are similar to other softwood species such as Norway spruce [13] and Scots pine [14].

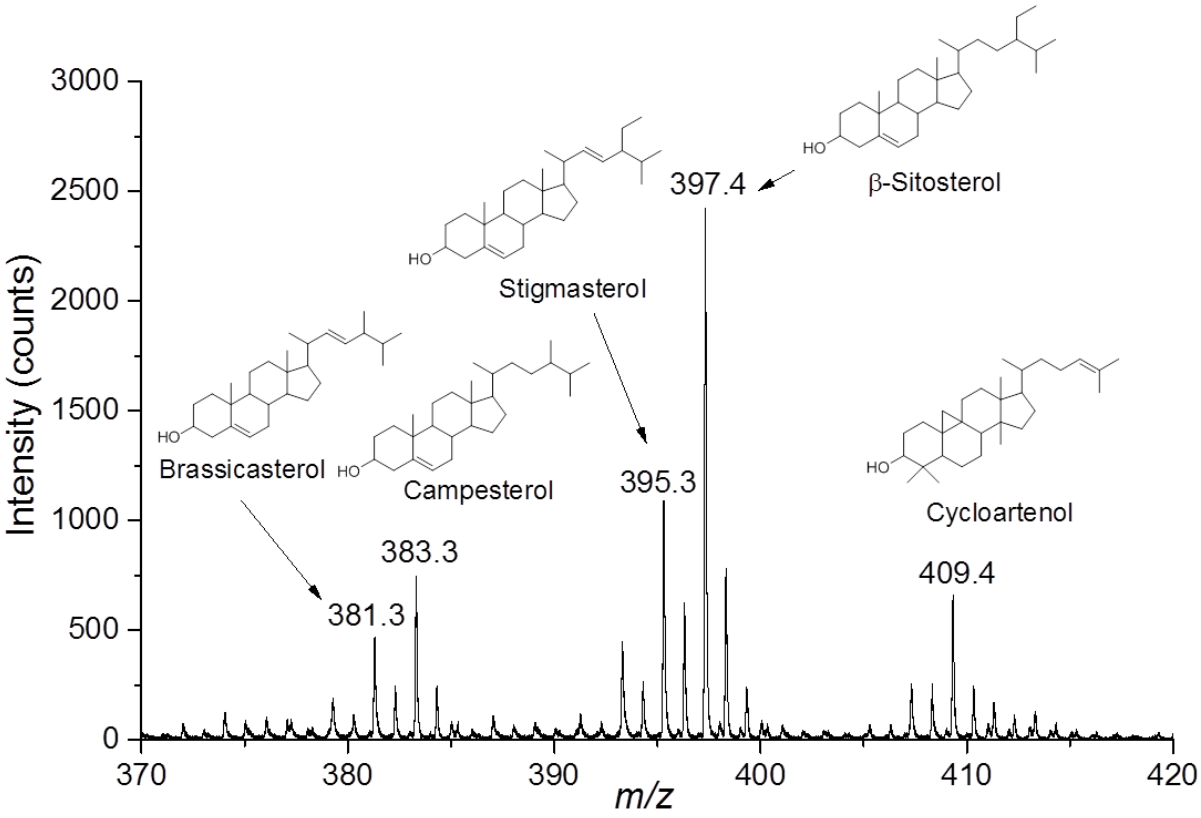

Figure 5: Partial positive TOF-SIMS spectrum obtained from region 1 showing the ion peaks corresponding to phytosterols, with chemical structures indicated above.

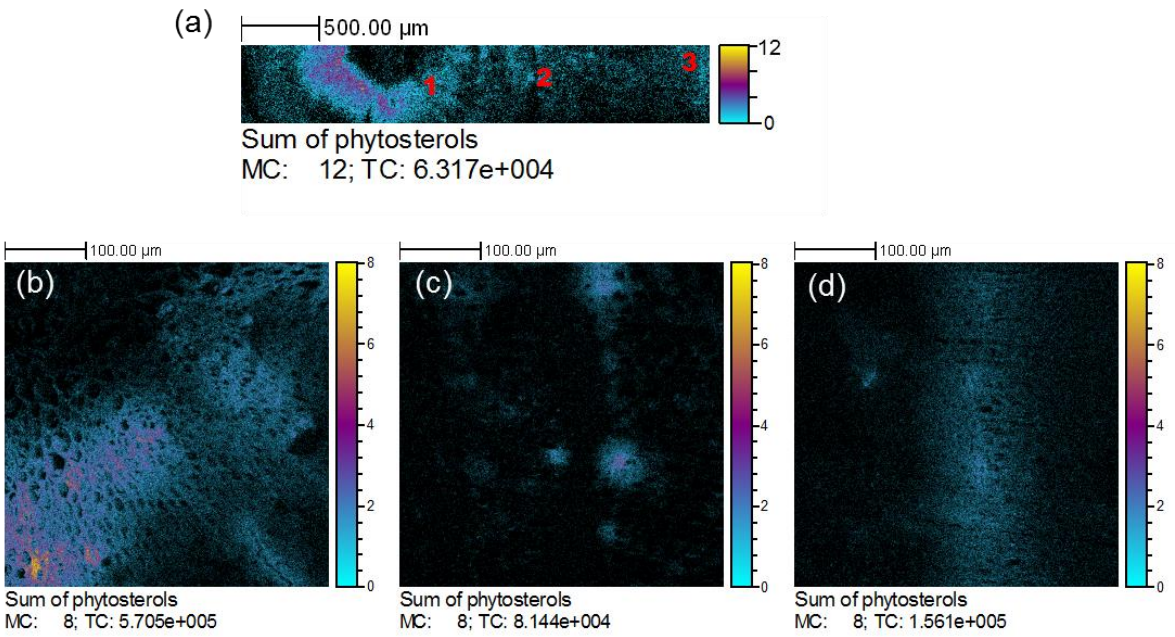

Figure 6: Radial distribution of phytosterols. (a) Summed ion images of phytosterols from large area analysis. b-d: high resolution localization of phytosterol in region 1 (b), region 2 (c) and region 3 (d).

5.5 Conclusion

TOF-SIMS imaging was applied to reveal the chemical composition and their radial distribution in the branch heartwood of European larch *Larix decidua*. The *in situ* characterization of the extractives proves to be a precise and rapid analytical tool in examining the radial distribution of wood extractives. High resolution mapping of both inorganic and organic extractives establish the inhomogeneous distribution of the chemical contents. Mineral nutrients exhibit no preferential localization except phosphate which is probably involved in the phosphorylation/dephosphorylation process to facilitate the transport of carbohydrates in wood. Examination of the mineral contents and their radial distribution may help to study the environment change in the growing sites. Lipophilic extractives including fatty acids, glycerides and phytosterols were found more abundant in the inner heartwood, whereas resin acids were mostly found in the outer heartwood due to their specific localization in the resin canal. In contrary to inorganic compounds, all the lipophilic compounds are revealed to be mainly localized in the earlywood. The results indicate that in addition to the main chemical constituents, the distribution pattern is also similar to other conifer genera such as pine and spruce. Lipophilic extractives are essential metabolites responsible for the endogenous metabolism and natural decay resistance of the wood. Thus scrutiny of radial distribution of the extractives will contribute to a better understanding of heartwood formation and wood quality control.

5.6 Acknowledgements

Fruitful discussions with Stéphane Dumarcay (INRA, Nancy, France) are greatly appreciated. We acknowledge an Investissement d'Avenir grant of the Agence Nationale de la Recherche (CEBA: ANR-10-LABX-25-01). TF would like to acknowledge financial support from China Scholarship Council (CSC, No. 201406310013). This work has benefited from the facilities and expertise of the Electron Microscopy facilities of Imagerie-Gif (http://www.i2bc.parissaclay.fr/spip.php?article282).

References

[1] Rowell, R. M.; Pettersen, R.; Han, J. S.; Rowell, J. S.; Tshabalala, M. A. Cell wall chemistry. In *Handbook of wood chemistry and wood composites*; Rowell, R. M., Ed.; CRC press, Boca Raton, Florida, **2005**.

[2] Da Ronch, F.; Caudullo, G.; Tinner, W.; de Rigo, D. Larix decidua and other larches in Europe: distribution, habitat, usage and threats. In *European atlas of forest tree species*; San-Miguel-Ayanz, J.; de Rigo, D.; Caudullo, G.; Houston Durrant, T.; Mauri, A., Ed.; Publication Office of the European Union, Luxembourg, **2016**, pp 108−110.

[3] Windeisen, E.; Wegener, G.; Lesnino, G.; Schumacher, P. Investigation of the correlation between extractives content and natural durability in 20 cultivated larch trees. *Holz als Roh- und Werkstoff* **2002**, *60*, 373−374.

[4] Gierlinger, N.; Jacques, D.; Schwanninger, M.; Wimmer, R.; Pâques, L. E. Heartwood extractives and lignin content of different larch species (Larix sp.) and relationships to brown-rot decay-resistance. *Trees* **2004**, *18*, 230–236.

[5] Grabner, M.; Müller, U.; Gierlinger, N.; Wimmer, R. Effects of heartwood extractives on mechanical properties of larch. *IAWA Journal* **2005**, *26*, 211–220.

[6] Pandey, K. K. A note on the influence of extractives on the photo-discoloration and photo-degradation of wood. *Polymer Degradation Stability* **2005**, *87*, 375−379.

[7] Shebani, A. N.; van Reenen, A. J.; Meincken, M. The effect of wood extractives on the thermal stability of different wood species. *Thermochimica Acta* **2008**, *471*, 43–50.

[8] Gierlinger, N.; Schwanninger, M.; Hinterstoisser, B.; Wimmer, R. Rapid determination of heartwood extractives in *Larix* sp. by means of Fourier transform near infrared spectroscopy. *Journal of Near Infrared Spectroscopy* **2002**, *10*, 203–214.

[9] Zule, J.; Čufar, K.; Tišler, V. Lipophilic Extractives in Heartwood of European Larch (*Larix decidua* Mill.). *Drvna industrija* **2015**, *66*, 305−313.

[10] Ostroukhova, L. A.; Raldugin, V. A.; Babkin, V. A.; Onuchina, N. A.; Levchuk, A. A. Investigation of the chemical composition of larch wood resin. *Russian Journal of Bioorganic Chemistry* **2012**, *38*, 775–779.

[11] Taylor, A. M.; Gartner, B. L.; Morrell, J. J. Heartwood formation and natural durability–A review. *Wood and Fiber Science* **2002**, *34*,587–611.

[12] Gierlinger, N.; Wimmer, R. Radial distribution of heartwood extractives and lignin in mature European larch. *Wood and Fiber Science* **2004**, *36*, 387–394.

[13] Bertaud, F.; Holmbom, B. Chemical composition of earlywood and latewood in Norway spruce heartwood, sapwood and transition zone wood. *Wood Science and Technology* **2004**, *38*, 245–256.

[14] Ekeberg, D.; Flæte, P. O.; Eikenes, M.; Fongen, M.; Naess-Andresen, C. F. Qualitative and quantitative determination of extractives in heartwood of Scots pine (*Pinus sylvestris* L.) by gas chromatography. *Journal of Chromatography A* **2006**, *1109*, 267−272.

[15] Winograd, N. The Magic of Cluster SIMS. *Analytical Chemistry* **2005**, *77*, 142A–149A.

[16] Brunelle, A.; Touboul, D.; Laprévote, O. Biological tissue imaging with time-of-flight secondary ion mass spectrometry and cluster ion sources. *Journal of Mass Spectrometry* **2005**, *40*, 985–999.

[17] Bich, C.; Touboul, D.; Brunelle, A. Cluster TOF-SIMS imaging as a tool for micrometric histology of lipids in tissue. *Mass Spectrometry Reviews* **2014**, *33*, 442–451.

[18] Tokareva, E. N.; Fardim, P.; Pranovich, A. V.; Fagerholm, H.-P.; Daniel, G.; Holmbom, B. Imaging of wood tissue by ToF-SIMS: Critical evaluation and development of sample preparation techniques. *Applied Surface Science* **2007**, *253*, 7569–7577.

[19] Saito, K.; Watanabe, Y.; Shirakawa, M.; Matsushita, Y.; Imai, T.; Koike, T.; Sano, Y.; Funada, R.; Fukazawa, K.; Fukushima, K. Direct mapping of morphological distribution of syringyl and guaiacyl lignin in the xylem of maple by time-of-flight secondary ion mass spectrometry. *The Plant Journal* **2012**, *69*, 542–552.

[20] Jung, S.; Foston, M.; Kalluri, U. C.; Tuskan, G. A.; Ragauskas, A. J. 3D chemical image using TOF-SIMS revealing the biopolymer component spatial and lateral distributions in biomass. *Angewandte Chemie International Edition* **2012**, *51*, 12005–12008.

[21] Imai, T.; Tanabe, K.; Kato, T.; Fukushima, K. Localization of ferruginol, a diterpene phenol, in Cryptomeria japonica heartwood by time-of-flight secondary ion mass spectrometry. *Planta* **2005**, *211*, 549–556.

[22] Saito, K.; Mitsutani, T.; Imai, T.; Matsushita, Y., Fukushima, K. Discriminating the indistinguishable sapwood from heartwood in discolored ancient wood by direct molecular mapping of specific extractives using time-of-flight secondary ion mass spectrometry. *Analytical Chemistry* **2008**, *80*, 1552–1557.

[23] Vanbellingen, Q. P.; Fu T.; Bich, C.; Amusant, N.; Stien, D.; Della-Negra, S.; Touboul, D.; Brunelle, A. Mapping Dicorynia guianensis wood constituents by submicron resolution cluster-TOF-SIMS Imaging. *Journal of Mass Spectrometry* **2016**, *51*, 412–423.

[24] https://www.google.fr/maps/place/44%C2%B053'49%22N+6%C2%B026'31%22E/@44.8965408,6.4231335,4855m/data=!3m1!1e3!4m5!3m4!1s0x0:0x0!8m2!3d44.8970556!4d6.4421389?hl=fr

[25] Morikawa, T.; Ashitani, T.; Sekine, N.; Kusumoto, N.; Takahashi, K. Bioactivities of extracts from *Chamaecyparis obtusa* branch heartwood. *Journal of Wood Science* **2012**, *58*, 544−549.

[26] Wen-jie, W.; Xue-ying, L.; Yuan-gang, Z. Dynamic feature of flavonoids content in different organs of larch (*Larix gmelinii*). *Journal of Forest Research* **2005**, *16*, 89−92.

[27] Vanbellingen, Q. P.; Elie N.; Eller, M. J.; Della-Negra, S.; Touboul, D.; Brunelle, A. Time-of-flight secondary ion mass spectrometry imaging of biological samples with delayed extraction for high mass and high spatial resolutions. *Rapid Communications in Mass Spectrometry* **2015**, *29*, 1187–1195.

[28] Goacher, R. E.; Jeremic, D.; Master, E. R. Expanding the library of secondary ions that distinguish lignin and polysaccharides in time-of-flight secondary ion mass spectrometry analysis of wood. *Analytical Chemistry* **2011**, *83*, 804–812.

[29] McLaughlin, S. B.; Wimmer, R. Calcium physiology and terrestrial ecosystem processes. *New Phytologist* **1999**, *142*, 373–417.

[30] Sauter, J. J. Respiratory and phosphatase activities in contact cells of wood rays and their possible role in sugar secretion. *Zeitschrift für Pflanzenphysiologie* **1972**, *67*, 135−145.

[31] Chun, L.; Hui-yi, H.; Tree-ring element analysis of Korean pine (*Pinus koraiensis* Sieb. Et Zucc.) and Mongolian oak (*Quercus mongolica* Fisch. ex Turcz.) from Changbai Mountain, northeast China. *Trees* **1992**, *6*, 103–108.

[32] Penninckx, V.; Glineur, S.; Gruber, W.; Herbauts, J.; Meerts, P. Radial variations in wood mineral element concentrations: a comparison of beech and pedunculate oak from the Belgian Ardennes. *Annals of Forest Science* **2001**, *58*, 253–260.

[33] Kebbi-Benkeder, Z.; Colin, F.; Dumarçay, S.; Gérardin, P. Quantification and characterization of knotwood extractives of 12 European softwood and hardwood species. *Annals of Forest Science* **2015**, *72*, 277–284.

[34] Harju, A. M.; Kainulainen, P.; Venäläinen, M.; Tiitta, M.; Viitanen, H. Differences in resin acid concentration between brown-rot resistant and susceptible scots pine heartwood. *Holzforschung* **2002**, *56*, 479–486.

[35] Piironen, V.; Lindsay, D. G.; Miettinen, T. A.; Toivo, J.; Lampi, A.-M. Plant sterols: biosynthesis, biological function and their importance to human nutrition. *Journal of the science of food and agriculture* **2000**, *80*, 939–966.

Chapter 6 Conclusions

6.1 Conclusions

In this thesis, fundamental study of ion production under impact of massive argon clusters, and biological application of TOF-SIMS imaging in mapping plant metabolites have been performed.

First we investigated the ion production in SIMS by examining the internal energy distribution of the secondary ions (SIs) with survival yield method. Average internal energy of the SIs represents the softness of the ionization process. The study of the fragmentation rate under various incident conditions (energy and cluster size) leads to the conclusion that the decisive factor of internal energy distribution of secondary ions is the velocity of the primary ions. It is also established that fragmentation behavior varies with incident velocity: at $E/n < 5$ eV, very few fragmentation was observed, indicating a soft ionization process takes place; between 2.0 eV/atom and 10 eV/atom, internal energy increase rapidly with primary ion velocity; at $E/n > 10$ eV, fragmentation reaches a plateau and will not change even when further increasing the incident velocity. Thus it is possible to realize soft ionization analysis with controlled beam velocity. In addition, argon clusters induce minimum sample damage during the analysis.

Biological applications include TOF-SIMS imaging of both hard wood and soft wood species. In the analysis of hard wood species *Sextonia rubra* (Lauraceae), structural characterization of the metabolites were carried out with the newly designed PHI *nano*TOF II which enables parallel imaging MS/MS. We first assessed the performance of this new instrumentation by analyzing the known bioactive metabolites rubrenolide and rubrynolide in the heartwood of *S. rubra*. The results demonstrated that the MS/MS capability could provide unambiguous identification of the metabolites. Moreover, the MS/MS images could better reveal the localization of these metabolites due to the exclusion of background interferences. These results suggested the parallel MS/MS imaging spectrometer a powerful tool in identification and localization natural products in complex biological samples.

The parallel imaging MS/MS technique was then applied to perform *in situ* identification of related metabolites which were previously identified in vitro by NMR and LC-MS/MS. The MS/MS fragmentation of protonated and alkalized precursors gave unambiguous identification of metabolites butanolides **4** and **5**. High resolution TOF-SIMS imaging (~ 400 nm) of sapwood, transition zone and heartwood revealed the co-localization of the bioactive metabolites (rubrynolide **7** and rubrenolide **8**, see figure 3 in Chapter 4) and their structurally related metabolites (obstusilactone analogues **1**−**2** and butanolides **4**−**5**) in ray parenchyma cells, tyloses and oil cells. 3D imaging of the transition zone wood sample further confirmed their spatial localization in ray parenchyma and oil cells. The identification

of the new metabolites and investigation of their spatial distribution result in the proposal of new biosynthetic pathway for the formation of rubrynolide and its analogues in plants.

As another application in mapping plant metabolites, TOF-SIMS imaging was used to study the chemical variation in the branch heartwood of European larch *Larix decidua* to get better understanding of heartwood formation. In large area imaging analysis, mineral nutrients Na^+, K^+, Ca^+, Cl^- showed no preferential localization and were found inhomogeneously distributed across the annual rings from pith to sapwood/heartwood boundary, whereas PO_3^- was exclusively detected in the ray cells. Radial distributions of lipophilic extractives were revealed on large areas with moderate spatial resolution (~ 4 µm) and on micro areas with high resolution (400 nm). Fatty acids, glycerides and phytosterols were found co-localized in the heartwood and were mostly abundant within the first annual ring surrounding the pith. Resin acids were almost exclusive located in the resin canal.

6.2 Perspectives

In the fundamental study, we have investigated two available ion beams, argon cluster and bismuth cluster. To examine the scope and applicability of the relationship between cluster ion velocity and the molecular fragmentation established in this thesis, a wider range of projectiles need to be examined. Obviously such study would require extensive collaboration in the SIMS community. Regarding this, a good example is the VAMAS Interlaboratory Study [1,2,3] launched by National Physical Laboratory (NPL, UK). Alternatively, with various modeling methods being developed [4], computational calculations and simulations can be combined with the experimental results to disclose the facts that behind the phenomena and observations.

For biological application, despite the improvement achieved in the past years, there is still a long way to go to make it powerful and sensitive enough for analysis of complex biological systems.

As to the sensitivity, large gas cluster ion sources have proven beneficial in improving secondary ion yield. Ar_n^+ cluster ion source has also been successfully applied for TOF-SIMS imaging of biological tissues [5,6,7]. Although the samples are currently limited to mammalian tissues, one can expect that it will be expanded to other biological systems. Furthermore, other new sources have been developed to further enhance the ion yield by increasing the ionization efficiency. For example, H_2O cluster ions [8] have shown ion yield enhancement when compared with C_{60}^+ clusters. The lifetime of this H_2O GCIB was later improved by using water doped Ar GCIB [9], from which the ion yield enhancement is about 4−10 times compared with Ar clusters. The uses of other dopants for the sake of improved

ionization have also been reported [7,10]. These developments open a new way to improve the sensitivity by using the chemistry of mixed clusters. It can even be reasoned that a particular dopant can be selected to enhance the intensity of a considered species. Future developments will need to focus on the improvement of stability and spatial resolution of these GCIBs.

In analysis of organic compounds, high mass resolution and MS/MS analysis is required for molecular identification. The new development in instrumentation summarized in the introduction will certainly contribute to solving the current issues in identification of biomolecules. For example, the J105−3D Chemical Imager has been applied to identify intact lipids in *Drosophila* brain by MS/MS fragmentation [11]; the PHI nano TOF II has been used in this thesis for *in situ* identification of various plant metabolites; the SIMS-FTICR has shown excellent mass resolution and MS/MS capability on rat brain tissues [12]. We hope future improvement in transmission efficiency and sensitivity will find them broad applications.

Other considerations including matrix effect, quantification, and data analysis method also need to be taken into account in future development [13].

---

[1] Gilmore, I. S.; Seah, M. P.; Green, F. M. Static TOF-SIMS—a VAMAS interlaboratory study. Part I. Repeatability and reproducibility of spectra. *Surface and Interface Analysis* **2005**, *37*, 651−672.

[2] Gilmore, I. S.; Green, F. M; Seah, M. P. Static TOF-SIMS. A VAMAS interlaboratory study. Part II—accuracy of the mass scale and G-SIMS compatibility. *Surface and Interface Analysis* **2007**, 39, 817−825.

[3] Shard, A. G.; Havelund, R.; Seah, M. P.; Spencer, S. J.; Gilmore, I. S.; Winograd, N.; Mao, D.; Miyayama, T.; Niehuis, E., Rading, D., Moellers, R. Argon cluster ion beams for organic depth profiling: results from a VAMAS interlaboratory study. *Analytical Chemistry* **2012**, *84*, 7865−7873.

[4] Postawa, Z.; Rzeznik, L.; Paruch, R.; Russo, M. F.; Winograd, N.; Garrison, B. J. Depth profiling by cluster projectiles as seen by computer simulations. *Surface and Interface Analysis* **2011**, *43*, 12−15.

[5] Angerer, T. B.; Blenkinsopp, P.; Fletcher, J. S. High energy gas cluster ions for organic and biological analysis by timeof-flight secondary ion mass spectrometry. *International Journal of Mass Spectrometry* **2015**, *377*, 591–598.

[6] Shon H. K.; Yoon, S.; Moon, J. H.; Le, T. G. Improved mass resolution and mass accuracy in TOF-SIMS spectra and images using argon gas cluster ion beams. *Biointerphases* **2016**, *11*, 02A321.

[7] Angerer, T. B.; Magnusson, Y.; Landberg, G.; Fletcher, J. S. Lipid heterogeneity resulting from fatty acid processing in the human breast cancer microenvironment identified by GCIB-ToF-SIMS Imaging. *Analytical Chemistry* **2016**, *88*, 11946–11954.

[8] Berrueta Razo, I.; Sheraz, S.; Henderson, A.; Lockyer, N. P.; Vickerman, J. C. Comparing C_{60}^+ and $(H_2O)_n^+$ clusters for mouse brain tissue analysis. *Surface and Interface Analysis* **2014**, *46*, 136–139.

[9] Berrueta Razo, I.; Sheraz, S.; Henderson, A.; Lockyer, N. P.; Vickerman, J. C. Mass spectrometric imaging of brain tissue by time-of-flight secondary ion mass spectrometry–How do polyatomic primary beams C_{60}^+, Ar_{2000}^+, water-doped Ar_{2000}^+ and $(H_2O)_{6000}^+$ compare? *Rapid Communications in Mass Spectrometry* **2015**, 29, 1851–1862.

[10] Wucher, A.; Tian, H.; Winograd, N.; A mixed cluster ion beam to enhance the ionization efficiency in molecular secondary ion mass spectrometry. *Rapid Communications in Mass Spectrometry* **2014**, *28*, 396–400.

[11] Phan, N. T. N.; Munem, M.; Ewing, A. G.; Fletcher, J. S. MS/MS analysis and imaging of lipids across Drosophila brain using secondary ion mass spectrometry. *Analytical and Bioanalytical Chemistry* **2017**, *409*, 3923–3932.

[12] Smith, D. F.; Robinson, E. W.; Tolmachev, A. V.; Heeren, R. M.; Pasa-Tolic, L. C60 secondary ion fourier transform ion cyclotron resonance mass spectrometry. *Analytical Chemistry* **2011**, *83*, 9552–9556.

[13] Mahoney, C. M. Cluster secondary ion mass spectrometry: principles and applications. John Wiley & Sons, Inc., Hoboken, New Jersey, **2013**.

Appendices

I. List of figures

Chapter 1:

Chapter 2:

Chapter 4:

Chapter 5:

II. List of tables

Chapter 2:

Chapter 4:

III. Résumé français de la thèse

Introduction et objectifs

L'imagerie par spectrométrie de masse fournit simultanément des informations chimiques et spatiales d'une grande variété d'échantillons, des semi-conducteurs aux tissus biologiques jusqu'aux cellules individuelles. Parmi les différentes techniques d'imagerie basées sur la spectrométrie de masse, la spectrométrie de masse d'ions secondaires induits par bombardement ionique (SIMS, Secondary Ion Mass Spectrometry), en association avec la technique de temps de vol (TOF, Time of Flight), est la première technique utilisée pour l'imagerie de surface. Après des décennies de développement, cette technique baptisée TOF-SIMS s'impose pour l'imagerie biologique grâce à sa grande résolution spatiale et la préparation minimale des échantillons. Cette forte implication dans l'analyse des composés organiques a été favorisée par l'utilisation de nouvelles sources d'ions délivrant des faisceaux d'ions agrégats. Actuellement, les faisceaux du bismuth et d'or permettent une analyse de routine de diverses molécules organiques et biologiques comme les lipides, les métabolites dans des échantillons naturels et les produits pharmaceutiques dans des échantillons biologiques ; ces analyses s'effectuent avec une sensibilité élevée et une bonne résolution spatiale autour du micron ou moins. L'utilisation récente de faisceaux d'agrégats d'argon dans les instruments TOF-SIMS offre de nouvelles possibilités pour l'imagerie ionique grâce l'ionisation douce des analytes, donc une fragmentation moindre des molécules, l'amélioration de la sensibilité et l'imagerie 3D.

En dépit des applications en plein développement du TOF-SIMS dans différents domaines scientifiques, de nombreux aspects concernant le processus d'ionisation/désorption sont encore mal compris. Si les améliorations techniques se poursuivent, des études fondamentales doivent être entreprises malgré leurs complexités pour définir tous les paramètres influençant l'émission ionique. C'est ainsi que la première partie de cette thèse vise à comprendre la production d'ions sous impact ionique en mesurant la distribution d'énergie interne transférée aux molécules émises en fonction du type des ions incidents, de leurs vitesses, et de leurs masses.

La deuxième partie porte sur les applications biologiques de la technique TOF-SIMS avec la cartographie des métabolites dans les plantes, lesquels jouent un rôle important dans diverses activités biologiques telles que la protection des plantes, la communication avec l'environnement, *etc*. La détermination de leur distribution spatiale est essentielle pour comprendre le métabolisme des plantes et le processus biologique correspondant dans les tissus spécifiques. Pour obtenir une identification sans ambiguïté et *in situ* des métabolites, les capacités parallèles de MS/MS et d'imagerie du prototype de spectromètre de masse PHI

nano TOF II ont été évaluées avec succès sur les espèces d'arbre Amazonien *Sextonia rubra*. Ensuite, l'imagerie TOF-SIMS a été appliquée pour étudier la production biosynthétique de deux métabolites bioactifs, rubrénolide et rubrynolide, dans *Sextonia rubra*. Enfin, une dernière étude a porté sur le mélèze européen *Larix decidua* dans le but de comprendre les variations chimiques associées à la formation du duramen du bois.

Distribution d'énergie interne transférée dans les molécules sous l'impact d'agrégats d'argon et de bismuth

Au cours de l'impact de l'ion primaire, l'énergie est transférée au milieu et conduit à l'excitation des molécules, donc à l'accroissement de leur énergie interne. Cette augmentation de l'énergie interne induit la fragmentation de ces molécules et ce taux de fragmentation est directement relié à l'énergie interne. Ainsi, la détermination de la distribution d'énergie interne permettrait d'évaluer le transfert d'énergie conduisant aux processus d'émission-ionisation sous impact ionique. Pour effectuer cette mesure, une série de molécules de benzylpyridium a été sélectionnée. Elles ont la particularité d'avoir une seule voie de fragmentation, dont l'énergie de dissociation est connue : ce sont des « thermomètres » de l'interaction. L'énergie interne est obtenue par la détermination du rendement de survie de ces molécules, lequel est déterminé en utilisant la formule $SY = I(M^+)/[I(M^+) + I(F^+)]$, où $I(M^+)$ est l'intensité de l'ion moléculaire et $I(F^+)$ celle du fragment. Ces rendements SYs sont ensuite tracés en fonction des énergies de dissociation de chaque molécule, une fonction sigmoïde est ajustée sur ces données, et la différenciation de la courbe sigmoïdale donne la distribution d'énergie des ions « thermomètres » désorbés.

Des agrégats d'argon Ar_n^+ avec des énergies cinétiques entre 10 et 20 keV et des tailles d'agrégats allant de 500 à 10000 ont été utilisés afin d'établir l'influence de la taille, de l'énergie et donc aussi de la vitesse de l'agrégat sur la distribution d'énergie interne transférée aux molécules. Les résultats montrent que le paramètre déterminant pour le transfert d'énergie est la vitesse des ions primaires. Il est établi que le taux de fragmentation varie avec la vitesse de l'ion incident: à $E/n < 5$ eV (énergie cinétique par atome d'argon de l'agrégat), très peu de fragmentations sont observées, ce qui indique un processus d'émission-ionisation doux ; entre 2 eV/atome et 10 eV/atome, le taux de fragmentation, et donc l'énergie interne, augmente rapidement avec la vitesse des ions primaires; à $E/n > 10$ eV, la fragmentation atteint un plateau et ne change plus, même en continuant à augmenter la vitesse de l'ion incident (*Figure 2*). Le contrôle de la vitesse des ions permet donc de déterminer des conditions pour effectuer une analyse de surfaces moléculaires dans des conditions d'émission-ionisation douce avec une fragmentation limitée.

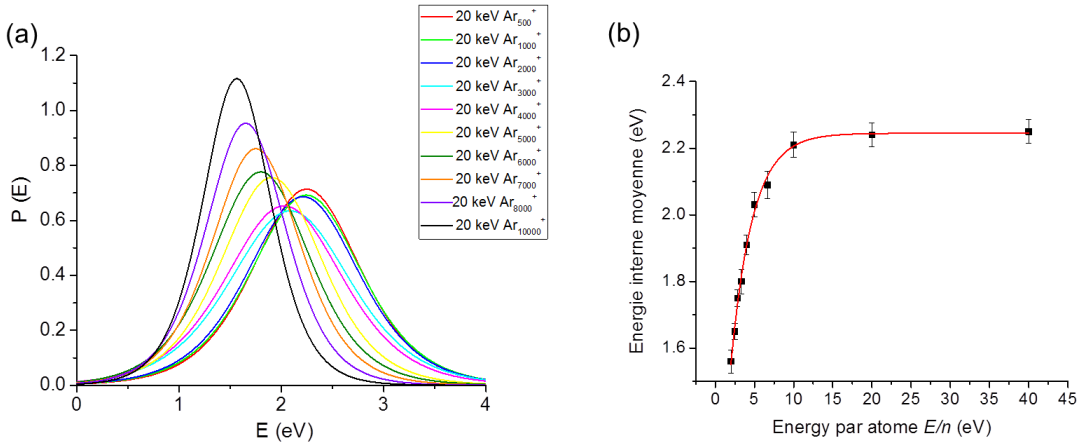

Figure 2(a) Distribution d'énergie interne des molécules émises sous l'impact d'agrégats d'argon à 20 keV. (b) L'énergie interne moyenne des molécules en fonction de l'énergie par atome des projectiles.

Dans le cas des agrégats de bismuth Bi_n^{q+} d'énergie de 25 qkeV, il a été mesuré une énergie interne moyenne entre 2,2 et 2,4 eV (*Tableau 1*), ce qui correspond aux valeurs obtenues dans le cas d'impacts d'agrégats d'argon de forte énergie par atome (E/n > 10 eV) où l'énergie interne moyenne reste constante autour de 2,24 eV. Il faut noter que les rendements d'émission des ions moléculaires obtenus avec les agrégats de bismuth ou d'argon sont identiques au niveau de ce plateau. Cependant, la section efficace d'endommagement des molécules est beaucoup plus faible sous le bombardement des agrégats d'argon. Ainsi cette section efficace induite par l'agrégat Ar_{2000}^+ de 20 keV est plus de 20 fois plus petite que celle du bombardement en l'agrégat Bi_5^+ de 25 keV, ce qui donne une efficacité ionique secondaire beaucoup plus élevée de $3{,}47 \times 10^{12}$ cm^{-2}.

Tension	Ions primaires	Y	σ (cm^2)	E (cm^{-2})	IE moyenne (eV)
25 kV	Bi^+	$5{,}49\times10^{-4}$	$3{,}87\times10^{-14}$	$1{,}42\times10^{10}$	2,29 ± 0.02
	Bi^{2+}	$4{,}52\times10^{-3}$	$3{,}03\times10^{-14}$	$1{,}49\times10^{11}$	2,21 ± 0.02
	Bi_3^+	$4{,}40\times10^{-2}$	$1{,}62\times10^{-13}$	$2{,}72\times10^{11}$	2,37 ± 0.01
	Bi_3^{2+}	$6{,}02\times10^{-2}$	$2{,}58\times10^{-13}$	$2{,}34\times10^{11}$	2,38 ± 0.02
	Bi_5^+	$2{,}55\times10^{-2}$	$9{,}17\times10^{-14}$	$2{,}78\times10^{11}$	2,41 ± 0.04
	Bi_5^{2+}	$4{,}18\times10^{-2}$	$7{,}38\times10^{-14}$	$5{,}66\times10^{11}$	2,46 ± 0.03
	Bi_7^+	$4{,}48\times10^{-2}$	$1{,}11\times10^{-13}$	$4{,}04\times10^{11}$	2,38 ± 0.03
20 kV	Ar_{2000}^+	$1{,}54\times10^{-2}$	$4{,}44\times10^{-15}$	$3{,}47\times10^{12}$	2,21 ± 0.04

Tableau 1 Rendement Y, section efficace d'endommagement σ, efficacité ionique secondaire E et énergie interne (IE) moyenne pour l'ion p-méthylbenzylpyridinium (m/z 184,11) sous l'impact d'agrégats de bismuth et d'argon.

L'imagerie en Tandem MS et l'identification *in situ* des métabolites du bois bioactif dans les espèces d'arbres amazoniennes *Sextonia rubra*

Malgré l'importance croissante du TOF-SIMS dans l'analyse biochimique, les applications actuelles sont limitées par le manque de capacité tandem MS/MS pour la caractérisation structurale permettant de lever les ambiguïtés liées à la résolution en masse limitée autour de 10 000. Ce point est crucial lorsqu'il s'agit d'identifier les molécules dans des échantillons biologiques complexes où les interférences en masse peuvent être nombreuses. Dans cette optique, un nouveau spectromètre MS/MS d'imagerie parallèle TOF-SIMS (PHI *nano* TOF II) a récemment été développé par Physical Electronics (Minnesota, États-Unis). Ce prototype de spectromètre est basé sur un analyseur TRIFT (temps de vol avec un triple analyseur électrostatique), sur lequel a été ajouté un dispositif de sélection de précurseur après le troisième analyseur électrostatique. Ce déflecteur électrostatique permet la sélection d'ions précurseurs avec une fenêtre d'une largeur d'environ 1 Da. Le précurseur sélectionné est dévié vers une cellule de collision où est induite la fragmentation, suivie d'un analyseur TOF linéaire et d'un détecteur standard constitué de galettes de microcanaux (voir *Figure 3*).

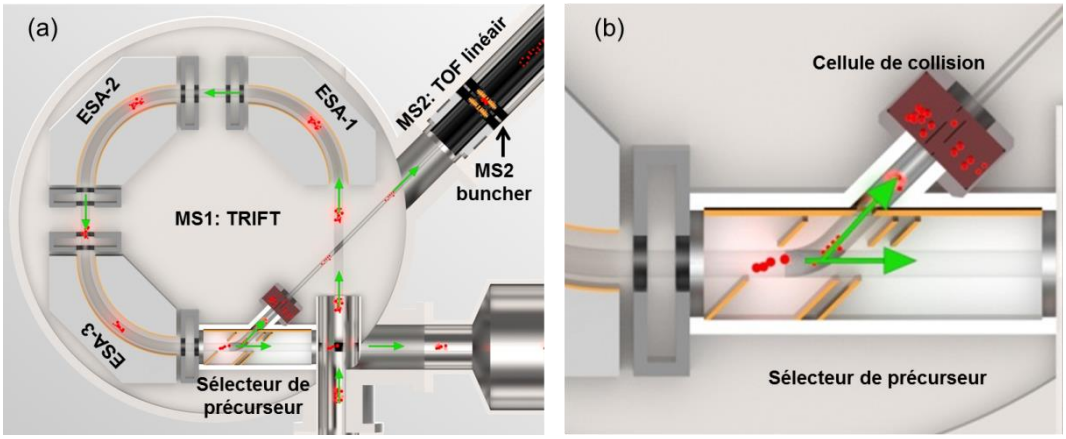

Figure 3 Illustration schématique du spectromètre MS/MS d'imagerie parallèle TOF-SIMS.

Les avantages de ce nouveau développement de spectrométrie d'imagerie MS/MS pour l'étude des produits naturels ont été démontrés par l'identification *in situ* des métabolites bioactifs rubrynolide et rubrénolide, dans les espèces d'arbres amazoniennes *Sextonia rubra*, grâce aux spectres de fragmentations spécifiques. La fragmentation MS/MS a permis une identification sans équivoque des métabolites. De plus, l'imagerie en tandem renforce ces attributions en minimisant les interférences de masse et révèle une localisation spécifique de ces métabolites dans les cellules du parenchyme radial (*Figure 4*). Cette étude permet de conclure que ce nouveau spectromètre d'imagerie MS/MS parallèle est un outil puissant de caractérisation, d'identification et de localisation de produits naturels en faible abondance dans des échantillons biologiques complexes.

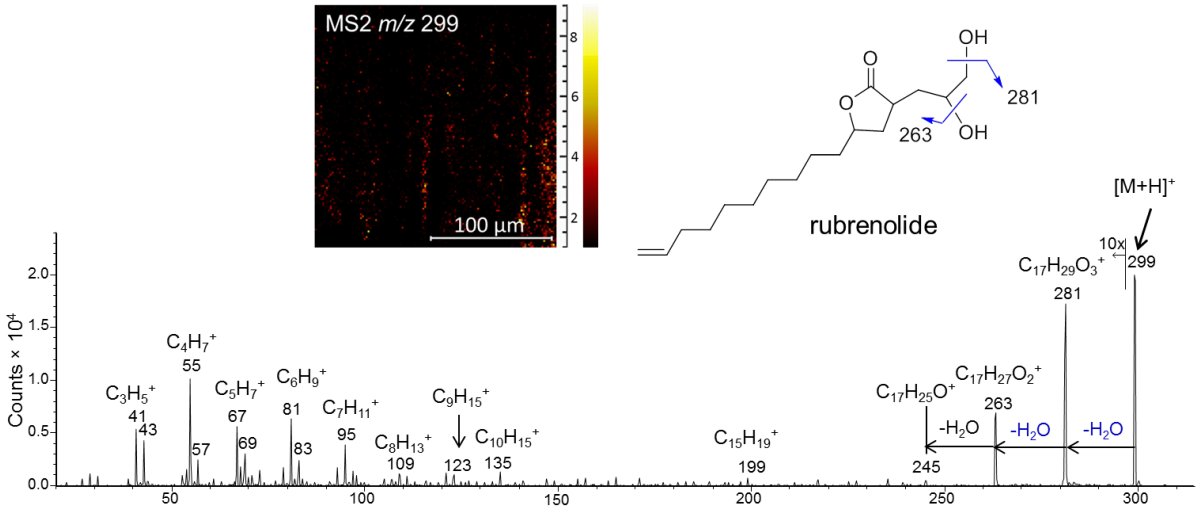

Figure 4 Spectre MS/MS, structure chimique, et image ionique du rubrenolide.

L'étude de la biosynthèse et la localisation des métabolites bioactifs chez *Sextonia rubra (Lauraceae)* par l'imagerie TOF-SIMS 2D et 3D

Sextonia rubra est l'une des espèces forestières les plus exploitées commercialement pour la construction en Guyane française en raison de sa durabilité naturelle exceptionnelle. Les produits naturels bioactifs rubrynolide et rubrénolide sont suggérés pour être responsables de l'excellente durabilité du duramen de ce bois. La biosynthèse du rubrynolide et de ses analogues est demeurée incertaine depuis son premier isolement en 1971. Pour étudier le processus de biosynthèse de ces métabolites végétaux, une MS/MS parallèle et une imagerie TOF-SIMS 2D/3D ont été réalisés pour identifier *in situ* les précurseurs potentiels et localiser ces métabolites dans les tissus de bois au niveau subcellulaire.

L'extraction et l'isolement *in vitro* ont été effectués par des collaborateurs d'Ecologie des Forêts de Guyane (ECOFOG), ce qui a permis de trouver pour la première fois deux nouveaux composés de lactone acétate (butanolides **4** et **5**) ainsi que la présence d'isozuihoenolide (**3**) dans l'aubier de S*extonia rubra*. L'identification structurale des métabolites apparentés (*Figure 5*) a été réalisée par LC-MS/MS, par RMN *in vitro* et avec l'imagerie MS/MS parallèle *in situ*.

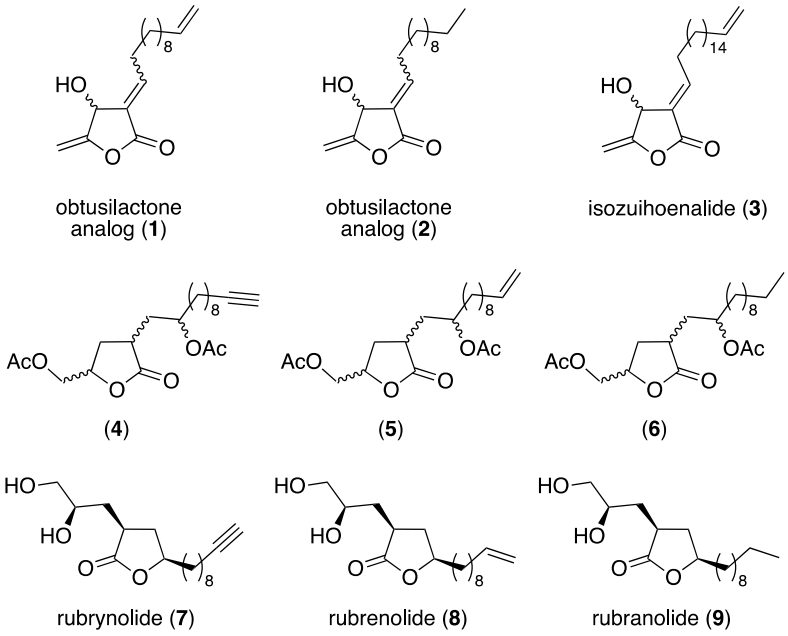

Figure 5 Métabolites secondaires chez Sextonia rubra.

L'imagerie TOF-SIMS à haute résolution (~ 400 nm) de l'aubier, de la zone de transition et du duramen révèle la colocalisation des métabolites bioactifs rubrynolide **7** et rubrenolide **8** et des métabolites structurellement apparentés (analogues de obstusilactone **1**−**2** et butanolides **4**−**5**) dans les cellules de parenchyme radial, tyloses et « oil cell » (figure 5). L'imagerie 3D de l'échantillon de bois de la zone de transition a confirmé leur localisation spatiale dans le parenchyme radial et les « oil cell ».

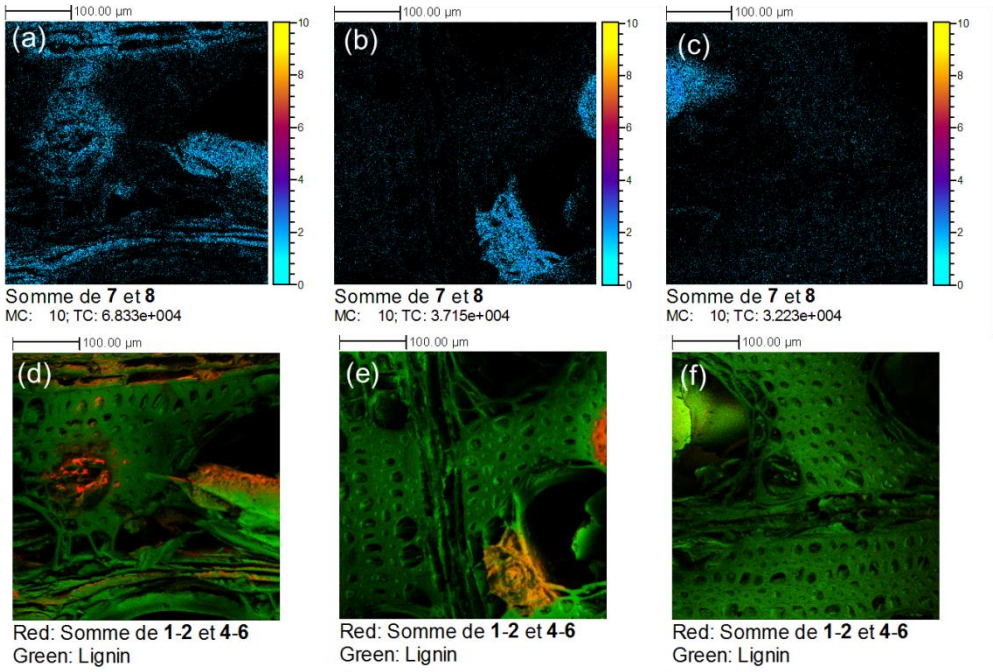

Figure 6 Distribution spatiale des métabolites apparentés dans S. rubra. a & d: Aubier; b & e: Zone de transition; c & f: Duramen.

L'identification des nouveaux métabolites et l'étude de leurs distributions spatiales conduisent à la proposition d'une nouvelle voie biosynthétique pour la formation du rubrynolide et de ses analogues (*Figure 7*). La biosynthèse commence par la formation d'un ester, suivie d'un processus de fermeture du cycle de type aldol entre la forme énol du *β*-céto-acide et du groupe carboxyle d'acide succinique.

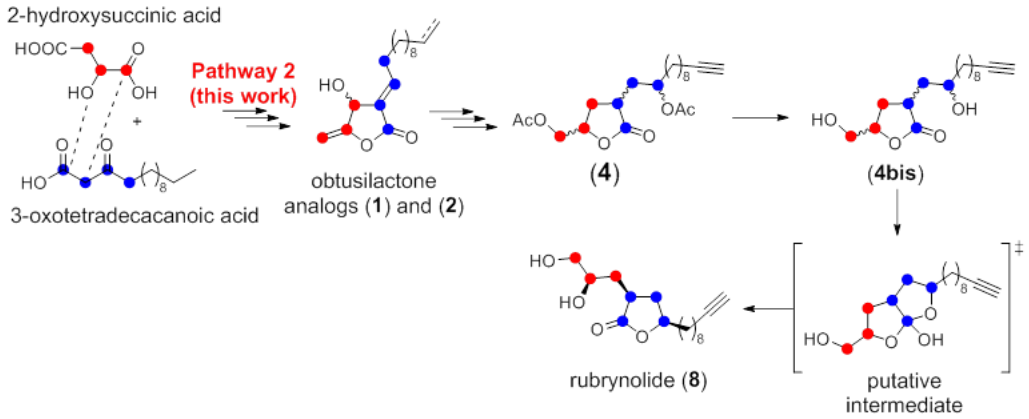

Figure 7 Possibilité de voies de biosynthèses pour la formation de rubrynolide et ses dérivés.

Distribution radiale des extraits de bois du mélèze européen *Larix decidua* par imagerie TOF-SIMS

Les extraits de bois sont des composants extractibles aux solvants à partir du bois. Ils jouent un rôle important dans la résistance à l'attaque des termites, aux champignons et au stress environnemental. Le mélèze européen (*Larix decidua*) est un arbre dont le bois est largement utilisé dans la menuiserie, et en particulier dans la fabrication d'objets qui peuvent être soumis aux intempéries. Pour comprendre la variation de la composition chimique associée à la formation du duramen du bois, l'imagerie TOF-SIMS a été employée pour examiner la distribution radiale des extraits minéraux et lipophiles dans le bois d'une branche de *Larix decidua*.

L'analyse d'une grande surface par imagerie ionique (présentée sur la figure 7) n'a pas montré de localisation préférentielle pour les nutriments minéraux K^+ et Ca^+ qui sont répartis de façon inhomogène à travers les anneaux annuels de la moelle à la limite de l'aubier/ duramen, tandis que l'ion PO_3^-, qui peut être impliqué dans le processus de phosphorylation/déphosphorylation, a été détecté exclusivement dans les cellules radiales.

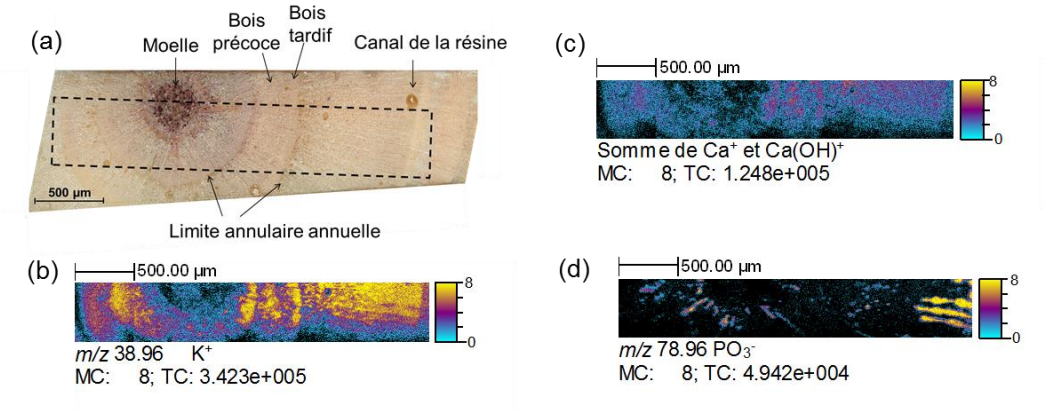

Figure 8 Distribution spatiale des nutriments minéraux.

Les distributions radiales d'extraits lipophiles ont été mesurées à la fois sur de grandes surfaces avec une résolution spatiale modérée (~ 4 µm) et sur des micro-zones à haute résolution (~ 400 nm). Les acides gras, les glycérides et les phytostérols ont été localisés localement dans le duramen et ils étaient principalement abondants dans le premier anneau annuel autour de la moelle (figure 8). Les images à haute résolution révèlent également que les composés lipophiles sont principalement localisés dans le bois précoce. En effet, une analyse avec une grande résolution spatiale (régions 2 et 3 de la figure 8) montre que ces lipophiles sont aussi localisés de manière discontinue ou homogène sur le bord des anneaux au début de leur croissance.

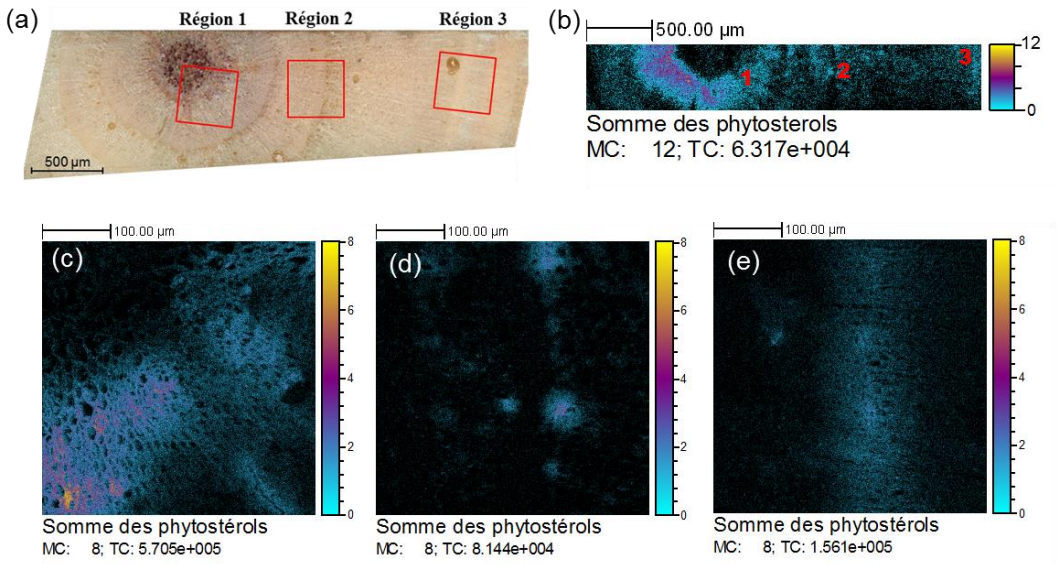

Figure 9 Distributions radiales de phytostérols. (c) Région 1; (d) Région 2; (e) Région 3.

Au contraire, les acides résineux se trouvent surtout dans le bois de cœur extérieur en raison de leur localisation spécifique dans les canaux à résine. Les extraits lipophiles sont des métabolites essentiels responsables du métabolisme endogène et de la résistance à la dégradation naturelle du bois. Ainsi, l'examen minutieux de la distribution radiale des extraits

contribuera à une meilleure compréhension de la formation du duramen et du contrôle de la qualité du bois.

Conclusions et perspectives

L'étude de la production d'ions moléculaires sous l'impact d'agrégats d'argon massifs révèle que le taux de fragmentation des ions moléculaires, ou l'énergie interne transférée aux molécules, atteint une valeur de saturation sous impact d'agrégats lorsque la vitesse devient grande, similaire à ceux mesuré avec des agrégats de bismuth. Par contre, il est possible de réaliser une analyse dans des conditions d'émission-ionisation « douce » avec un faible taux de fragmentation à faible vitesse avec ces agrégats très lourds. Pour examiner la portée et l'applicabilité de la relation entre la vitesse des ions et la fragmentation moléculaire établie dans cette thèse, une plus large gamme de projectiles doit être examinée. En outre, la modélisation de l'impact et du transfert d'énergie dans le solide et les molécules le constituant permettrait avec les molécules thermomètres de mieux appréhender les processus de désorption-ionisation en reproduisant les observations expérimentales.

L'imagerie TOF-SIMS 2D/3D a été appliquée avec succès pour cartographier les métabolites des plantes dans différentes espèces de bois avec une résolution spatiale élevée pour comprendre la biosynthèse des métabolites importants et les variations de compositions chimiques pendant la formation du duramen. Les applications futures sur des systèmes biologiques complexes nécessiteront une meilleure sensibilité et l'identification de la structure. Les sources à gaz produisant des ions agrégats massifs se sont avérées bénéfiques pour améliorer le rendement des ions secondaires. La source d'ions d'agrégats d'argon Ar_n^+ a également été utilisée avec succès pour l'imagerie TOF-SIMS sur des tissus biologiques. D'autres nouvelles sources délivrant des agrégats d'eau ont été développées pour améliorer le rendement ionique en augmentant l'efficacité de l'ionisation. Cette voie consistant à ajouter une molécule ionisante sur les agrégats lourds d'argon doit être suivie avec attention car elle ouvre des possibilités d'ionisation spécifique par le choix de cette molécule additionnelle. Du point de vue instrumental, les nouveaux développements comme l'Orbi-SIMS contribueront à résoudre les problèmes actuels d'identification des biomolécules, en fournissant une résolution en masse élevée, ainsi qu'une excellente précision et une capacité MS/MS. Une meilleure compréhension de l'effet de matrice, du développement en quantification et de la méthode d'analyse des données facilitera grandement les applications biologiques de l'imagerie TOF-SIMS.

Titre : Imagerie par spectrométrie de masse micrométrique en 3D et haute sensibilité

Mots clés : Imagerie par spectrométrie de masse; TOF-SIMS; énergie interne; métabolites du bois

Résumé : L'imagerie par spectrométrie de masse est d'un grand intérêt pour aborder les questions biologiques en fournissant simultanément des informations chimiques et spatiales. En particulier, la spectrométrie de masse baptisée TOF-SIMS est bien reconnue par sa haute résolution spatiale (< 1 µm), qui est essentielle pour révéler l'information chimique dans une zone submicronique. L'emploi croissant de cette technique dans la caractérisation des échantillons biologiques a bénéficié du développement de nouvelles sources d'ions d'agrégats. Cependant, les processus d'ionisation/désorption des analytes sous les impacts d'agrégats lourds sont encore mal compris. D'un autre côté, techniquement, les instruments TOF-SIMS commerciaux actuels ne peuvent pas fournir une résolution en masse suffisante ni une précision sur la détermination de la masse pour l'identification moléculaire, ce qui rend les analyses de systèmes biologiques complexes très difficiles, et nécessite le recours à la fragmentation MS/MS. Cette thèse vise à mieux comprendre la production d'ions sous l'impact d'agrégats lourds et à explorer la capacité MS/MS du spectromètre de masse par temps de vol combiné à l'imagerie ionique en utilisant le spectromètre de masse PHI *nano*TOF II. Ce dernier point a été réalisé en cartographiant en haute résolution spatiale des métabolites importants de bois.

Pour comprendre la production d'ions sous les impacts d'agrégats d'argon massifs, l'énergie interne des ions secondaires a été mesurée en utilisant la mesure du taux de survie d'une série d'ions benzylpyridinium. L'étude de diverses conditions d'impact (énergie, vitesse, taille des agrégats) a montré que la vitesse joue le rôle majeur dans la distribution d'énergie interne et la fragmentation moléculaire dans le régime à faible énergie par atome (E/n < 10 eV).

Les capacités de la fragmentation MS/MS et d'imagerie en parallèle du spectromètre PHI *nano*TOF II nouvellement conçu ont été évalués par cartographie MS/MS in situ des métabolites bioactifs rubrynolide et rubrenolide dans les espèces amazoniennes de bois *Sextonia rubra*, ainsi qu'une identification *in situ* des métabolites précurseurs. L'imagerie TOF-SIMS 2D et 3D a permis de localiser les cellules où cette biosynthèse s'effectue. Les résultats ont conduit à la proposition d'une voie possible de biosynthèse des deux métabolites. Pour étendre l'application de l'imagerie TOF-SIMS dans l'analyse chimique du bois, la distribution radiale des extraits de bois dans le duramen du bois du mélèze européen a également été étudiée.

Title : 3D and high sensitivity micrometric mass spectrometry imaging

Keywords : Mass spectrometry imaging; TOF-SIMS, internal energy; wood metabolites

Abstract : Mass spectrometry imaging has been shown of great interest in addressing biological questions by providing simultaneously chemical and spatial information. Particularly, TOF-SIMS is well recognized for its high spatial resolution (< 1 µm) which is essential in disclosing chemical information within a submicron area. The increasing use of TOF-SIMS in characterizing biological samples has greatly benefited from the introduction of new cluster ion sources. However, the ionization/desorption of the analytes under impacts of large clusters is still poorly understood. On the other hand, technically, current commercial TOF-SIMS instruments generally cannot provide sufficient mass resolution or mass accuracy for molecular identification, making analyses of complex biological systems especially challenging when no MS/MS fragmentation is available. Thus this thesis is aimed to get a better understanding of ion production under cluster impacts, to explore the MS/MS capability of the parallel imaging MS/MS Spectrometer (PHI *nano*TOF II), as well as to apply TOF-SIMS to map important wood metabolites with high spatial resolution.

In order to understand ion production under impacts of massive argon clusters, internal energy distributions of secondary ions were measured using survival yield method which involves the analyses of a series of benzylpyridinium ions. Investigation of various impacting conditions (energy, velocity, cluster size) suggested that velocity of the clusters play a major role in internal energy distribution and molecular fragmentation in the low energy per atom regime (E/n < 10 eV).

The MS/MS fragmentation and parallel imaging capabilities of the newly designed PHI *nano*TOF II spectrometer were evaluated by *in situ* MS/MS mapping of bioactive metabolites rubrynolide and rubrenolide in Amazonia wood species *Sextonia rubra*. Then this parallel imaging MS/MS technique was applied to perform in situ identification of related precursor metabolites in the same tree species. 2D and 3D TOF-SIMS imaging were carried out to target the plant cells that biosynthesize rubrynolide and rubrenolide. The results led to the proposal of a possible biosynthesis pathway of these two metabolites. In addition, to expand the application of TOF-SIMS imaging in wood chemistry analysis, radial distribution of wood extractives in the heartwood of European larch was also investigated.

Université Paris-Saclay
Espace Technologique / Immeuble Discovery
Route de l'Orme aux Merisiers RD 128 / 91190 Saint-Aubin, France